LEVEL

AD A071193

RADC-TR-79-15
Final Technical Report
May 1979

MEASUREMENTS OF BISTATIC CLUTTER CROSS SECTION

Environmental Research Institute of Michigan

DDC
RECEIVED
JUL 16 1979
C

Sponsored by
Defense Advanced Research Projects Agency (DoD)
ARPA Order No. 3071

APPROVED FOR PUBLIC RELEASE; DISTRIBUTION UNLIMITED

DDC FILE COPY

The views and conclusions contained in this document are those of the authors and should not be interpreted as necessarily representing the official policies, either expressed or implied, of the Defense Advanced Research Project Agency or the U. S. Government.

ROME AIR DEVELOPMENT CENTER
Air Force Systems Command
Griffiss Air Force Base, New York 13441

79 07 16 00

MEASUREMENTS OF BISTATIC CLUTTER CROSS SECTION

R. W. Larson
F. Smith
A. Fromm
A. Maffett
R. C. Heimiller

Contractor: Environmental Research Institute of Michigan
Contract Number: F30602-77-C-0145
Effective Date of Contract: 15 August 1977
Contract Expiration Date: 31 July 1978
Short Title of Work: Measurements of Bistatic Clutter Cross Section
Program Code Number: 7E20
Period of Work Covered: Aug 77 - Jun 78

Principal Investigator: R. W. Larson
Phone: (313) 994-1200

Project Engineer: Robert G. Polce
Phone: (315) 330-2814

Approved for public release; distribution unlimited.

This research was supported by the Defense Advanced Research Projects Agency of the Department of Defense and was monitored by Robert G. Polce (OCSA), Griffiss AFB NY 13441 under Contract F30602-77-C-0145.

SECURITY CLASSIFICATION OF THIS PAGE (When Date Entered)

REPORT DOCUMENTATION PAGE

READ INSTRUCTIONS BEFORE COMPLETING FORM

1. REPORT NUMBER: RADC-TR-79-15	2. GOVT ACCESSION NO. / 3. RECIPIENT'S CATALOG NUMBER
4. TITLE (and Subtitle): MEASUREMENTS OF BISTATIC CLUTTER CROSS SECTION	5. TYPE OF REPORT & PERIOD COVERED: Final Technical Report, 21 Sep 77 - 30 Jun 78 6. PERFORMING ORG. REPORT NUMBER: 130300-15-F
7. AUTHOR(s): R. W. Larson, F. Smith, A. Fromm, A. Maffett, R. C. Heimiller	8. CONTRACT OR GRANT NUMBER(s): F30602-77-C-0145
9. PERFORMING ORGANIZATION NAME AND ADDRESS: Environmental Research Institute of Michigan, P O Box 8618, Ann Arbor MI 48107	10. PROGRAM ELEMENT, PROJECT, TASK AREA & WORK UNIT NUMBERS: 62301E, C0710104
11. CONTROLLING OFFICE NAME AND ADDRESS: Defense Advanced Research Projects Agency, 1400 Wilson Blvd, Arlington VA 22209	12. REPORT DATE: May 1979 13. NUMBER OF PAGES: 230
14. MONITORING AGENCY NAME & ADDRESS(if different from Controlling Office): Rome Air Development Center (OCSA), Griffiss AFB NY 13441	15. SECURITY CLASS. (of this report): UNCLASSIFIED 15a. DECLASSIFICATION DOWNGRADING SCHEDULE: N/A

16. DISTRIBUTION STATEMENT (of this Report)

Approved for public release; distribution unlimited.

ERIM 130300-15-F

17. DISTRIBUTION STATEMENT (of the abstract entered in Block 20, if different from Report)

Same

18. SUPPLEMENTARY NOTES

RADC Project Engineer: Robert G. Polce (OCSA)

19. KEY WORDS (Continue on reverse side if necessary and identify by block number)

Bistatic
Radar Cross-Section Density
Reflection
Coefficient

20. ABSTRACT (Continue on reverse side if necessary and identify by block number)

The work reported utilized the air-ground bistatic instrumentation developed previously under Contract F30602-76-C-0037, ~~and reported in RADC-TR-77-389.~~ Empirical data have been obtained from which estimates of the bistatic reflection coefficient have been determined. Measurements were made over snow covered terrain and over an orchard with snow cover. The snow covered terrain area was the same area of tall weeds and rough ground utilized during the 1976 measurements. Data were obtained at incident and reflective angles of 80°, 70° → next page

DD FORM 1 JAN 73 1473

UNCLASSIFIED

SECURITY CLASSIFICATION OF THIS PAGE (When Date Entered)

and 60 deg (low grazing angles) and 0-180 deg azimuth angle. Measurements were made at 3 cm and 23 cm wavelength with horizontal polarization. Both like and orthogonal polarizations were received at each wavelength; four channels of data were recorded. The measurement technique utilized an aircraft with 3 cm and 23 cm pulsed transmitters and four channel receivers on a ground based tower. Coherent signals were recorded by utilizing a separate air-ground link for the receiver local oscillator signal. Approximately 146 data curves are given.

PREFACE

This technical report describes the experimental program for the measurement of bistatic scattering coefficients funded under contract F30602-77-C-0145. This effort is a continuation of the work performed and funded under contract F30602-76-C-0037. The research reported herein was carried out by members of the Radar and Optics Division, Environmental Research Institute of Michigan (ERIM) during the period 21 September 1977 to 30 June 1978.

This contract was monitored by Mr. Robert Polce and Mr. Richard Schneible of Rome Air Development Center, Rome, New York. The DARPA Program Director was Dr. D. Walsh, DARPA, STO.

The principal investigators for the program at ERIM were Messrs. R.W. Larson and R.C. Heimiller. In addition, the following persons contributed to this program: Mr. A. Fromm, Mr. F. Smith, Prof. A. Moffett, Mr. B. DiTullio, Mr. A. Gillies, Mr. R. Hamilton and Mr. L. Kottke. The report was typed by Mrs. D. Clarke and Mrs. A. Sadlowski. This effort was conducted in ERIM's Radar and Optics Division, directed by Dr. A. Kozma.

TABLE OF CONTENTS

1. INTRODUCTION AND SUMMARIES 9
   1.1 Introduction 9
   1.2 Summary of Advantages of Spotlight Scanning Technique 12
   1.3 Report Summary 12

2. DESCRIPTION OF TEST SITES 19
   2.1 Site II (Dec. 16, 1977) 19
   2.2 Site II (Feb. 15, 17, 18, & 19, 1978) 19
   2.3 Site III (Mar. 17 & 18, 1978) 28

3. DATA ANALYSIS 35
   3.1 Processing Techniques 35
   3.2 Incident Power Corrections 42

4. ERROR ANALYSIS 53
   4.1 Instrumentation Errors 53
   4.2 Sampling Error 56
   4.3 Application of Error Estimates to Data Sets 56

5. BISTATIC RECEIVER MODIFICATIONS 59
   5.1 PRF Sync Receiver, 77 Modification 59
   5.2 Bistatic Receiver Response 63
   5.3 Circuit Board Modifications 67
   5.4 Incident Power Receiver 71

6. CONCLUSIONS AND RECOMMENDATIONS 77
   6.1 Conclusions 77
   6.2 Recommendations 78

APPENDIX A: MEASUREMENT DATA 83

REFERENCES 81

Accession For
NTIS GRA&I
DDC TAB
Unannounced
Justification
By
Distribution/
Availability Codes
Dist | Avail and/or special
A

LIST OF ILLUSTRATIONS

1. Basic Bistatic Geometry 10

2. Functional Block Diagram of Complete System 11

3. Test Site II: 16 Dec 77 System Test: View Looking East Over Scattering Area 20

4. Test Site II: 15, 17, 18, and 19 Feb 78: View Toward East Over Scattering Area (Snow-Covered Weeds) 21

5. Test Site II: 15, 17, 18, and 19 Feb 78: View Toward Northeast Over Scattering Area (Snow-Covered Weeds) . . . 22

6. Test Site II: 17, 18, and 19 Feb 78: View Toward Northwest Over Scattering Area (Snow-Covered Weeds) 23

7. Test Site II: 17, 18, and 19 Feb 78: View Toward Southwest Over Scattering Area (Snow-Covered Weeds) . . . 24

8. Cross Section of Snow Pit in Test Site II (15, 17, 18, and 19 Feb 78) 26

9. Test Site III: 17 and 18 Mar 78: Aerial Photograph of Test Site (Forest-Orchard Area) Showing Receiving Antenna Coverage 29

10. Test Site III: 17 and 18 Mar 78: View Looking Northwest 30

11. Test Site III: 17 and 18 Mar 78: View Looking West . . . 31

12. Test Site III: 17 and 18 Mar 78: View Looking Southwest 32

13. Test Site III: 17 and 18 Mar 78: View of Receiver Van and Crane-Tower Location 34

14. σ_o vs. φ_s (Upper) for Eight Receiver Scans and (Lower) as Averaged Over a 5° Interval (Linear and Logarithmic Regressions are Shown) 37

15a. Computer-Generated Data Set 15-F 39

15b. Computer-Generated Data Set 15-S 40

16. Computed σ_o Data: (Upper) Graphed Data Set and (Lower) Averaged Data Set 41

17. Test Site III: σ_o vs. θ_s for Fixed θ_i, L-Parallel (·) and L-Cross (x) 47

18. Test Site III: σ_o vs. θ_i for Fixed θ_s, L-Parallel (·) and L-Cross (x) 48

19. Test Site III: σ_o vs. θ_s for Fixed θ_i, X-Parallel (·) and X-Cross (x) 49

PAGE 2 IS BLANK

PRECEDING PAGE BLANK-NOT FILMED

LIST OF ILLUSTRATIONS
(Continued)

20. Test Site III: σ_o vs. θ_i for Fixed θ_o, X-Parallel (·) and X-Cross (x) 50

21. Test Site III: X and L Forward-Scatter and Backscatter Data 51

22. PRF Receiver Block Diagram 61

23. Change in Sync Delay (ΔT_d) vs. Input Power (S) 62

24. PRF Sync Receiver Input Power vs. Range 64

25. X-Band Receivers Frequency Response, L.O. Freq. = 9452 MHz 65

26. L-Band Receivers Frequency Response 66

27. X-Band Receivers Frequency Response, L.O. Freq. = 9472 MHz 68

28. X-L Incident Power Receiver 72

29. X-Band Incident Power Receiver Frequency Response 74

30. L-Band Incident Power Receiver Frequency Response 75

31. Comparison of 1976 and 1978 Results for 23 cm Wavelength at Site II 79

LIST OF TABLES

I. Summary of Bistatic Data Obtained 15

II. Summary of Bistatic Measurement Angles for Which Data Were Used 17

III. Summary of Ground Measurements at Test Site II for 17, 18, and 19 February 1978 27

IV. Corrections Applied to Incident Power Values Due to Geometry and Incident Power Receiver Antenna 44

V. Estimates of Random Errors 54

VI. Estimates of Systematic Errors 55

1
INTRODUCTION AND SUMMARIES

1.1 INTRODUCTION

During the period 1 October 1975 through 30 September 1976, a program was conducted for the Defense Advanced Research Projects Agency (DARPA) and monitored by the Rome Air Development Center (RADC, OCSA) for the design and construction of air-to-ground instrumentation for the measurement of bistatic scattering coefficients. Also, as part of that program, empirical data were obtained from which estimates of the scattering coefficient, σ_o, have been determined. These results are reported in the Final Technical Report, November 1977 [1].

It is the objective of this present effort to utilize the instrumentation developed and demonstrated in the previous program to obtain additional bistatic data and to use the empirical data to determine bistatic scattering coefficients. During this program, several modifications were made to improve and facilitate operation of the existing air-to-ground bistatic instrumentation. The geometrical situation used in the measurements is given in Figure 1. A functional block diagram of the complete system is given in Figure 2; a complete description of the measurements instrumentation is given in Reference 1.

Following the submission of this final report to RADC for sponsor approval, additional data analysis was accomplished as an ERIM IR&D program. This analysis (1) verified proper operation of the computer analysis program, (2) identified several errors in parameter inputs used in the recently completed data processing, (3) provided improved incident power illumination corrections for all passes, and (4) reviewed ancillary recorded data parameters to increase the usability of the February X-band data. Results from this IR&D program have been presented to the sponsor and are included this report.

PRECEDING PAGE BLANK-NOT FILMED

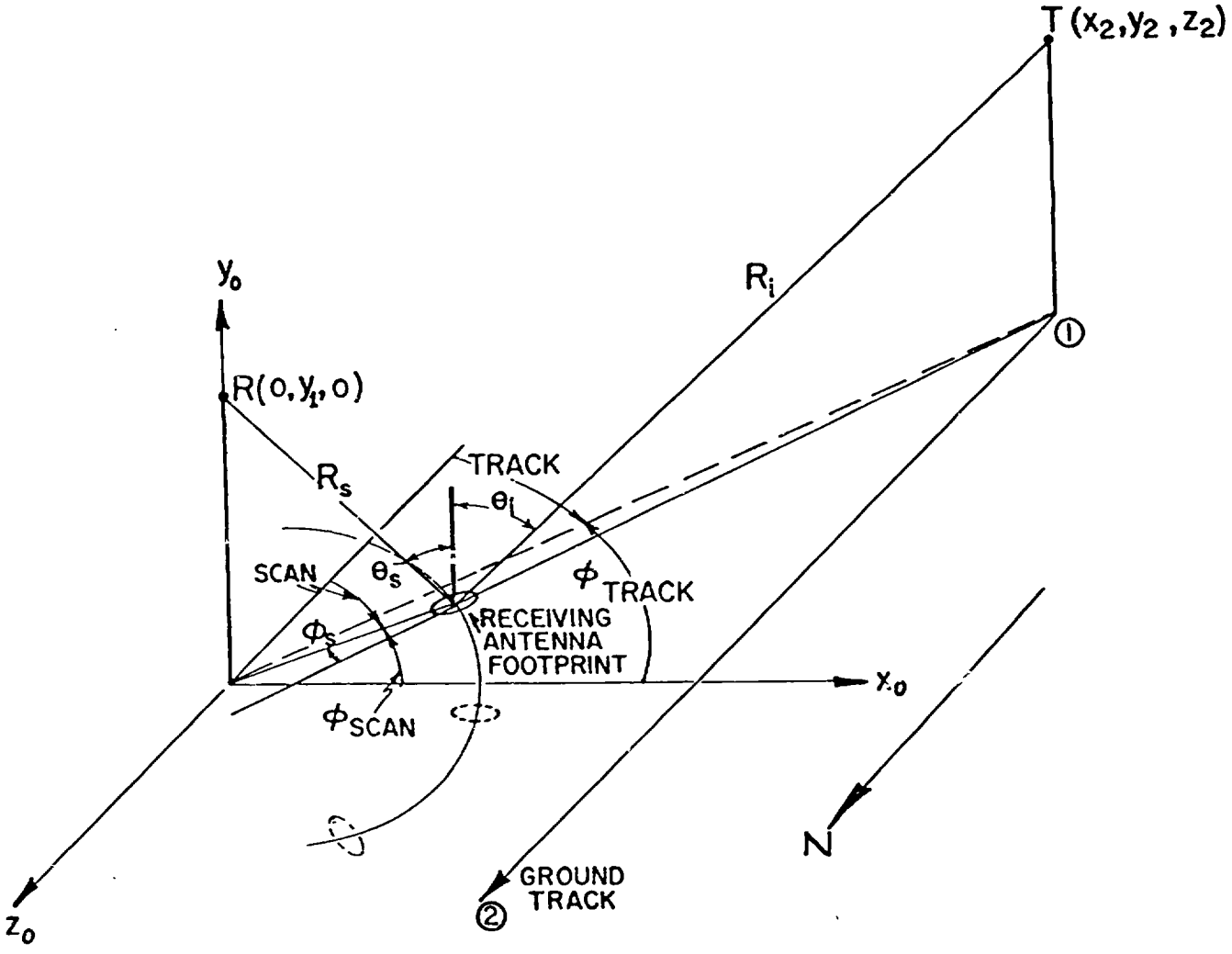

Figure 1. Basic Bistatic Geometry

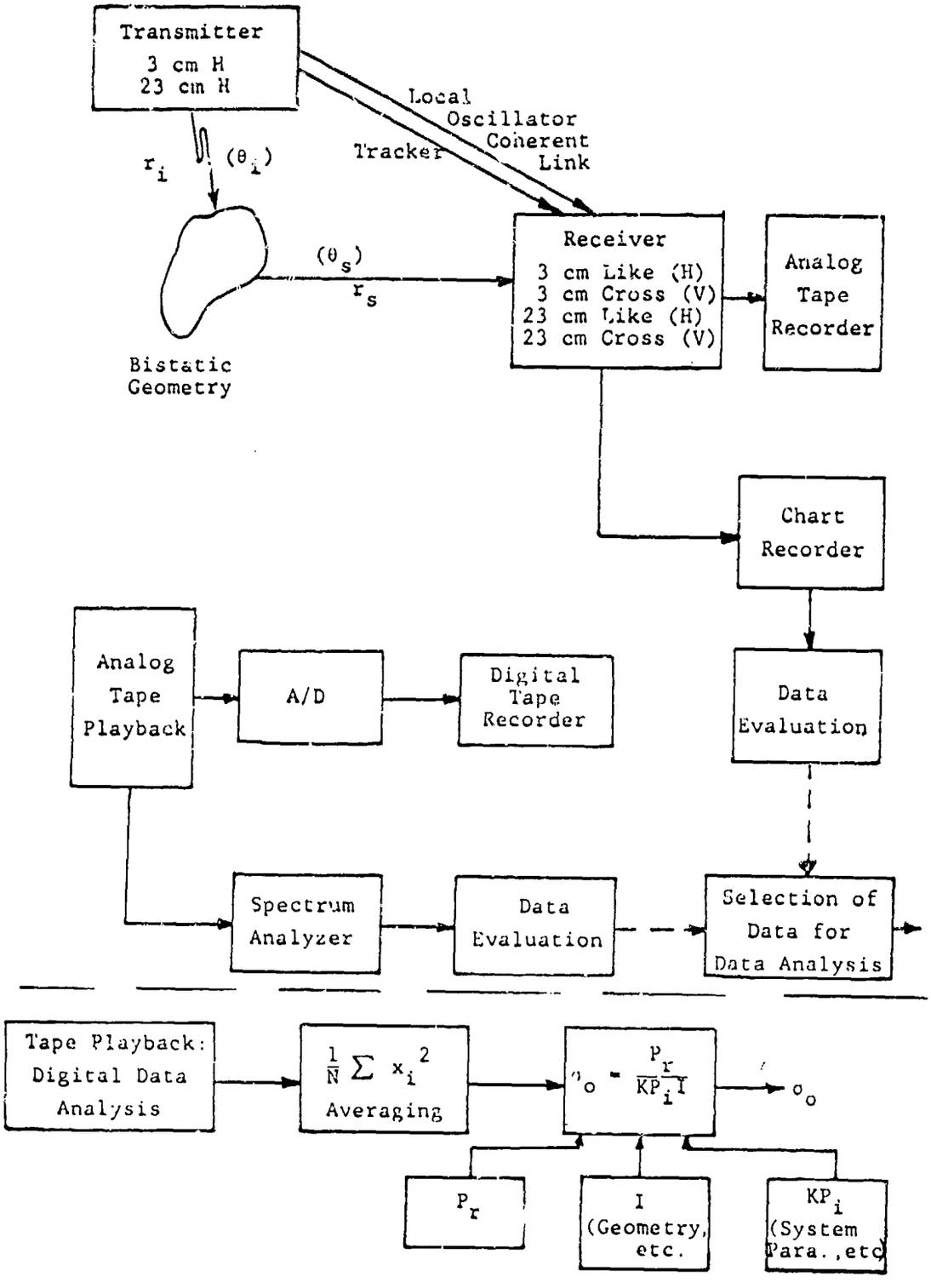

Figure 2. Functional Block Diagram of Complete System

1.2 SUMMARY OF ADVANTAGES OF SPOTLIGHT SCANNING TECHNIQUE

The area near the receiver is spotlighted to increase the time on target, and the receiving antenna is scanned back and forth several times during a pass. A given terrain patch is sampled at different φ_s values during each scan; hence, samples are obtained from many different ensemble points during a single pass. Data from an ensemble of patches is preferable to several independent samples from a single patch, unless the terrain is very uniform.

Since the receiving antenna is scanned several times during each fly-by, Doppler spread and wind motion do not increase the number of independent samples from a single ensemble point. If the receiving antenna were to scan only once during a fly-by, these factors would significantly increase the number of independent samples at 3 cm but not at 23.5 cm. More independent samples at one ensemble point give a more accurate mean value of the cross section density for that point.

1.3 PROGRAM SUMMARY

This report describes work which was performed during the period from 1 September 1977 to 30 June 1978. Results obtained from additional effort performed between 1 October 1978 to 31 December 1978 as an ERIM IR&D program are also included in this report. The objective of this program was to utilize instrumentation developed previously to collect empirical data from which to obtain an accurate estimate of bistatic scattering coefficient for two different terrain types. This program was conducted in three phases:

1. Modification of existing instrumentation,
2. Data gathering, and
3. Reduction of empirical data.

Simultaneous empirical data were obtained at 3.14 cm and 23.5 cm wavelengths. The transmitted polarization was horizontal;

horizontally- and vertically-polarized energy was received at both operating wavelengths. The instrumentation provided coherent data, sampled and revealed on a pulse-by-pulse basis on each of the four receiving channels. The instrumentation used matches the typical operational bistatic system, except that an aircraft and ground tower were utilized for transmitting and receiving, respectively, instead of two aircraft.

The following tasks were completed during this program:

1. Modification of the parallel-polarization receivers.
2. Installation of isolation switches in the cross-polarization receivers.
3. Design, construction, and utilization of a receiver to obtain the PRF reference from the signal received via the direct transmitter-receiver path.
4. Provision of two receivers, 3 cm and 23.5 cm, for the measurement of absolute value of power incident on the test area.
5. System test.
6. Data gathering at the test sites.
7. Digitization of data.
8. Reduction and analysis of data to obtain scattering coefficient.
9. Documentation of modification to instrumentation.
10. Graphical presentation of the bistatic scattering coefficients and error estimate.
11. Provision of copies of digitized data tapes to the sponsor.

The measurement technique utilized is illustrated in Figure 1 and is completely described in Reference 1. Receiving apertures are

mounted on a tower and their field of view is scanned through an azimuth angular interval SCAN. The scattering area is illuminated using the radar transmitters in ERIM's C-46 aircraft as sources. Radiation at two wavelengths is transmitted simultaneously and horizontal polarization is used in both transmitter channels. As the aircraft flies along a path 1-2 (Figure 1), the transmitter antennas are scanned so as to spotlight the scattering area. The receiving antenna scan rate is adjusted so that one scan is completed during a period in which the transmitted illumination angle changes by approximately 5 degrees. Measurements were made for the bistatic angles listed in Table 1; priorities for the selection of angles θ_i and θ_s were determined by sponsor representatives.

To obtain estimates of the values of σ_o, empirical values of received power are substituted into the bistatic equation (see Equation 3 in Reference 1) along with the experimental geometrical parameters, and the equation is solved for σ_o as a function of bistatic angle. During data analysis, values of received power are averaged over approximately 5 degrees of azimuth angle. It is assumed that the function σ_o is a slowly-varying function of azimuth angle and that therefore the 5-degree truncation does not obscure any fine-scale structure in the σ_o characteristics. This assumption is based on a consideration of available data [2].

The aircraft carrying the transmitter was tracked during each data pass and the nominal illumination angle (that is, the TRACK angle) at the receiver site was recorded. Similarly, the receiving antenna azimuth angle SCAN was recorded. The difference between these two angles is the bistatic azimuthal, or out-of-plane, angle φ_s. Based on the results of an error analysis (discussed in Section 4), the estimated error in σ_o values obtained is 4 dB.

A description of the modifications to the existing instrumentation is included as Section 5. A summary of the bistatic data

TABLE I. SUMMARY OF BISTATIC DATA OBTAINED

DATA GATHERING FLIGHT DATE	DATA ON ANALOG TAPE	DIGITIZED DATA
16 December 1977	All Passes: 1-8 3 Calibrations	None
15 February 1978	All Passes: 1-3 2 Calibrations	Pass 2 2 Calibrations
17 February 1978*	All Passes: 1-10 2 Calibrations	All Passes 2 Calibrations
18 February 1978*	All Passes: 1-9 3 Calibrations	All Passes 3 Calibrations
19 February 1978*	All Passes: 1-13 3 Calibrations	All Passes 2 Calibrations
17 March 1978	All Passes: 1-11 2 Calibrations	All Passes 2 Calibrations
18 March 1978	All Passes: 1-21 4 Calibrations	All Passes 4 Calibrations

*X-band data calibration questionable; values of σ_o not included.

obtained is given in Table I and a summary of bistatic measurement angles is given in Table II. A complete collection of σ_o versus φ_s plots can be found in Appendix A.

TABLE II. SUMMARY OF BISTATIC MEASUREMENT ANGLES FOR WHICH DATA WERE USED

SITE TERRAIN	θ_s	θ_i	ϕ_s
Site II - Dec. (system test)	80°	70°	0-90°
Rough ground, dry weeds		60°	
85% snow cover			
6 inches			
Site II - Feb.	80°	80°	0-180°
Snow cover; 12"-20"	70°	70°	
snow depth	60°	65°	
		60°	
Site III - March	84°		
Tree-orchard; snow	80°	80°	0-180°
covered ground, 6" deep	70°	70°	
Wet ground	60°	60°	

2
DESCRIPTION OF TEST SITES

The bistatic clutter measurements described in this report were conducted at two locations. These locations are designated as Site II and Site III, consistent with the test sites utilized in the previous bistatic clutter measurements program.

2.1 SITE II (Dec. 16, 1977)

This site is located at the Willow Run airport, Ypsilanti, Michigan and is the same location at which bistatic data were obtained during the measurements conducted in the summer of 1976. Photographs taken at site II during the measurements period are given in Figures 3 through 7.

December 16, 1977 Data

Measurements conducted during December 1977 were obtained as a part of the overall system final testing; data obtained are summarized in Table I. Figure 3 is a photograph of the test site. The following is a description of the site and other relevant conditions existing during the data taking period.

Surface Conditions

Dry weeds on surface of rough terrain; snow melting, about 25% snow cover with snow depths of 3-6 inches. Ground wet.

Temperature	40°F
Sky	Clear
Wind	Light, 10 kts

2.2 SITE II (Feb. 15, 17, 18 & 19, 1978)

The complete site was snow covered; average snow depth was 16 inches with variations in depth from 12 inches to 20 inches.

PRECEDING PAGE BLANK-NOT FILMED

Figure 3. Test Site II: 16 Dec 77 System Test: View Looking East Over Scattering Area

Figure 4. Test Site II: 15, 17, 18 & 19 Feb 78: View Toward East Over Scattering Area (Snow-Covered Weeds)

Figure 5. Test Site II: 15, 17, 18 & 19 Feb 78: View Toward Northeast Over Scattering Area (Snow-Covered Weeds)

Figure 6. Test Site II: 17, 18 & 19 Feb 78: View Toward Northwest Over Scattering Area (Snow-Covered Weeds)

Figure 7. Test Site II: 17, 18 & 19 Feb 78: View Toward Southwest Over Scattering Area (Snow-Covered Weeds)

Surface of snow was very smooth with respect to X-band (3 cm) with very gradual slopes. There were scattered regions throughout the area where dry weeds were visible over the top of the snow, several inches high. Also, as shown in Figure 4, some tall weeds were scattered throughout the area, extending 1 to 2 feet above the snow surface. These general conditions existed during the entire test period. The temperature did not exceed 25°F during the three-day data taking period. Photographs of test site II are given in Figures 4 through 7.

17 February

Temperature	20°F
Sky	Clear to 2000 feet, widely-scattered clouds
Wind	5-10 kts West

18 February

Temperature	18°F
Sky	Clear, very bright
Wind	5-10 kts West

19 February

Temperature	20°F
Sky	Clear
Wind	Calm

Surface Measurements

Measurements were made at various locations within the test site. These included: (1) snow depth and snow characterization obtained from snow pits, (2) electrical measurements (dielectric constant) and (3) snow temperature and density. Results from these measurements are summarized in Figure 8 and Table III. Measurements of the dielectric constant were made at random locations throughout the test site. Also, measurements were made in two rectangular grids, one each on the north and south sections of the test site.

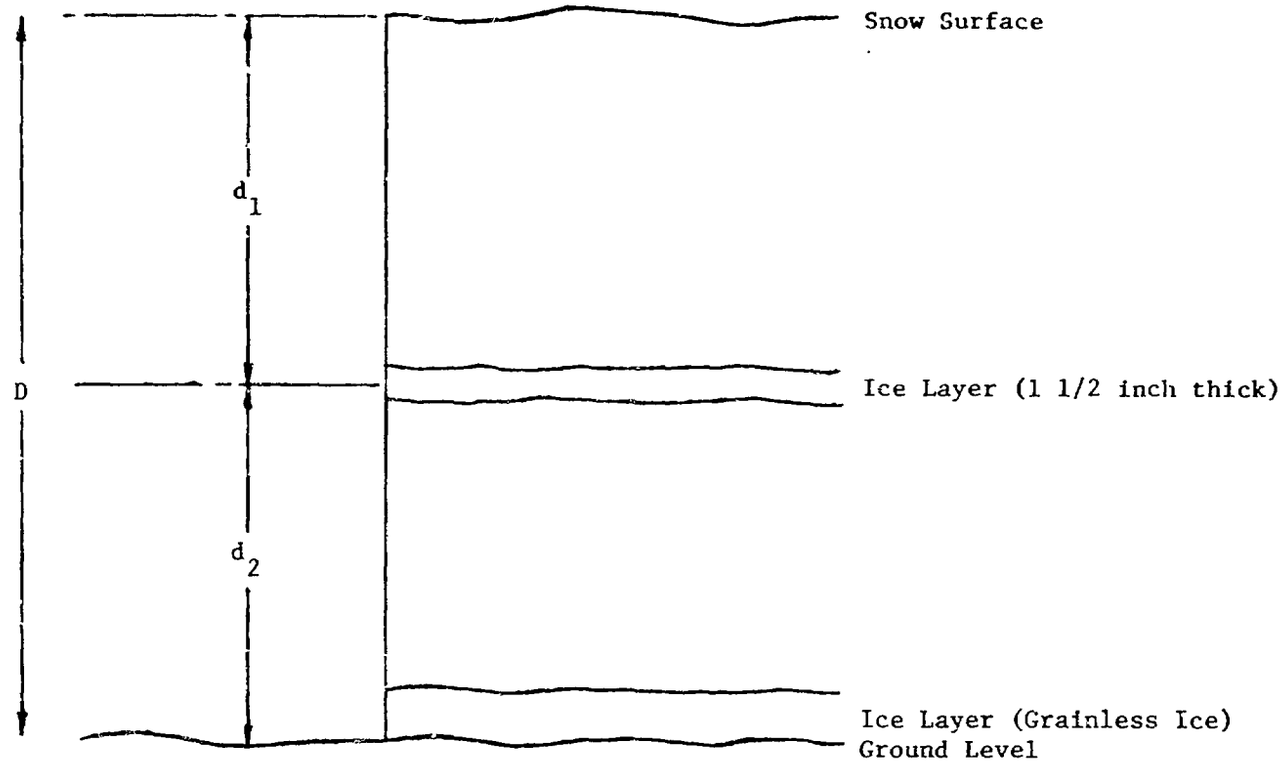

Total Snow Depth: $12" \leq D \leq 23"$

Surface to Middle Ice Layer: $4" \leq d_1 \leq 10"$

Middle Ice Layer to Ground: $8" \leq d_2 \leq 13"$

Figure 8. Cross Section of Snow Pit in Test Site II (15, 17, 18 & 19 Feb 78)

TABLE III. SUMMARY OF GROUND MEASUREMENTS AT TEST SITE II FOR 17, 18, AND 19 FEBRUARY 1978

Parameter	Date - February 17	18	19
Dielectric Constant (ϵ_r)			
Top 10 inches	1.95	1.71	1.84
Bottom 10 inches	2.25	2.03	2.1
Snow Temperature			
Surface	-8°C	-8°C	-7°C
Bottom	-2°C	-1°C	-2°C
Snow Density			
Surface		0.1 gm/cm^3	
Bottom		0.3 gm/cm^3	

Each grid consisted of two parallel north-south lines with four measurements made along each line. Space between measurements was 100 feet; the lines were spaced by 250 feet. The dielectric constant values measured were within the 25% estimated accuracy of the instrumentation. Measurements were made using a portable "Q" meter instrument and an operating frequency of 100 MHz. The frequency dependence of the dielectric constant of snow is well documented [3]. Measurements were made to give average values and to show any spatial variation. Average values are given in Table III; all spatial variations observed were within the error of the instrumentation. A drawing showing the snow profile in the Test Site II area is given in Figure 8.

2.3 SITE III (Mar. 17 & 18, 1978)

Test Site III consisted of an apple orchard located northwest of Ann Arbor, Michigan. An aerial photograph of the test site is included as Figure 9. Several ground photographs showing the test area as seen from the receiver location are given in Figures 10, 11, and 12. The average height of the trees was 25 feet; the ground was snow covered with wet snow; the dielectric constant of the snow was greater than 3.15, the maximum value that can be measured using the portable instrumentation. Snow depth was 6 to 10 inches.

Weather conditions for the 17th & 18th of March were:

17 March

Data taking period 5pm - 7pm

Temperature	20°F
Sky	Clear
Wind	Light

18 March

Data taking period 12pm - 4pm

Figure 9. Test Site III: 17 and 18 Mar 78: Aerial Photograph of Test Site (Forest-Orchard Area) Showing Receiving Antenna Coverage

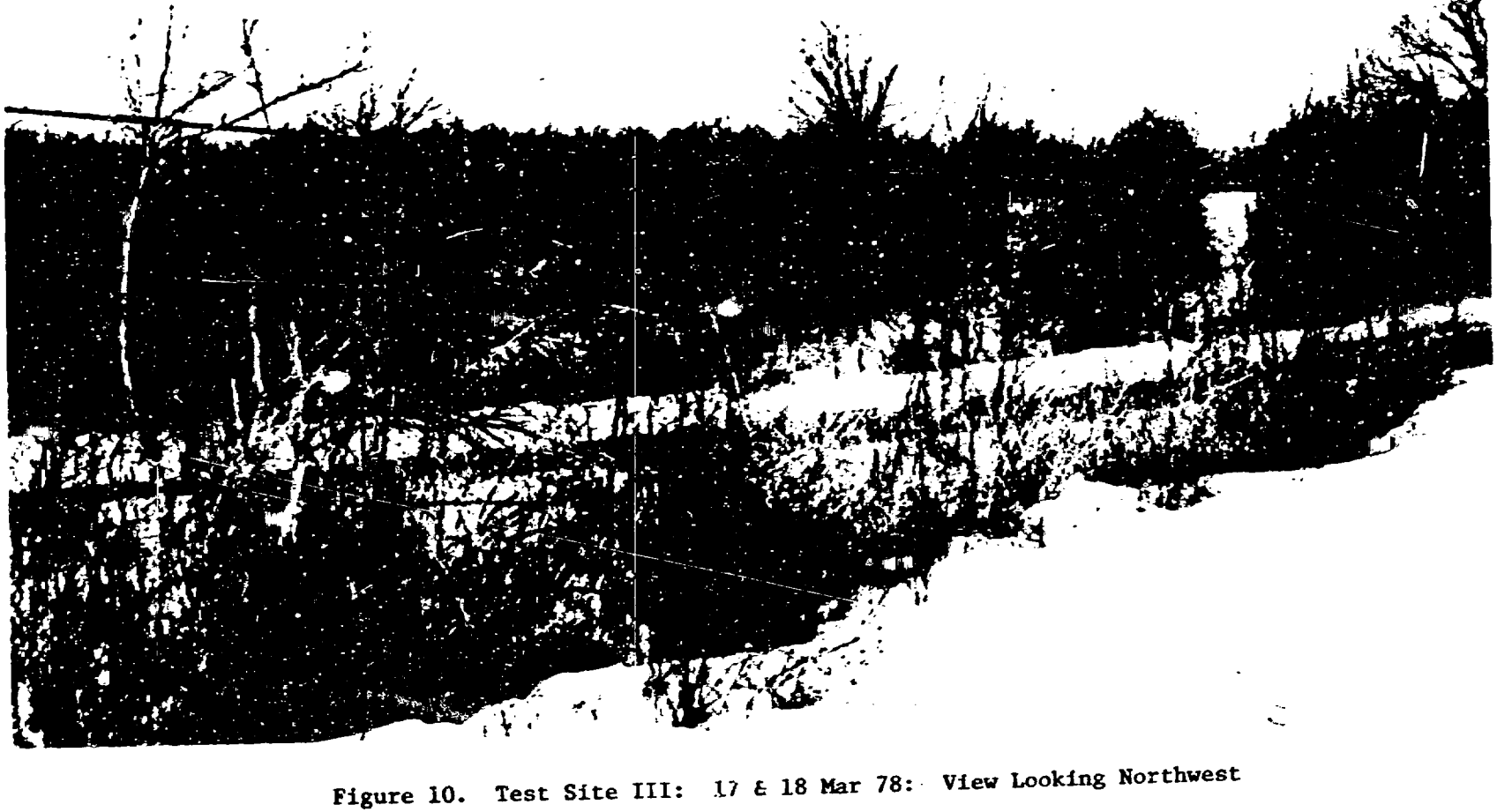

Figure 10. Test Site III: 17 & 18 Mar 78: View Looking Northwest

Figure 11. Test Site III: 17 & 18 Mar 78: View Looking West

Figure 12. Test Site III: 17 & 18 Mar 78: View Looking Southwest

Temperature	33°F - 20°F
Sky	High overcast
Wind	15 - 20 kts, gusty to 35 kts
	Ground wet - then frozen

A photograph of the receiving location at Site III is shown in Figure 13.

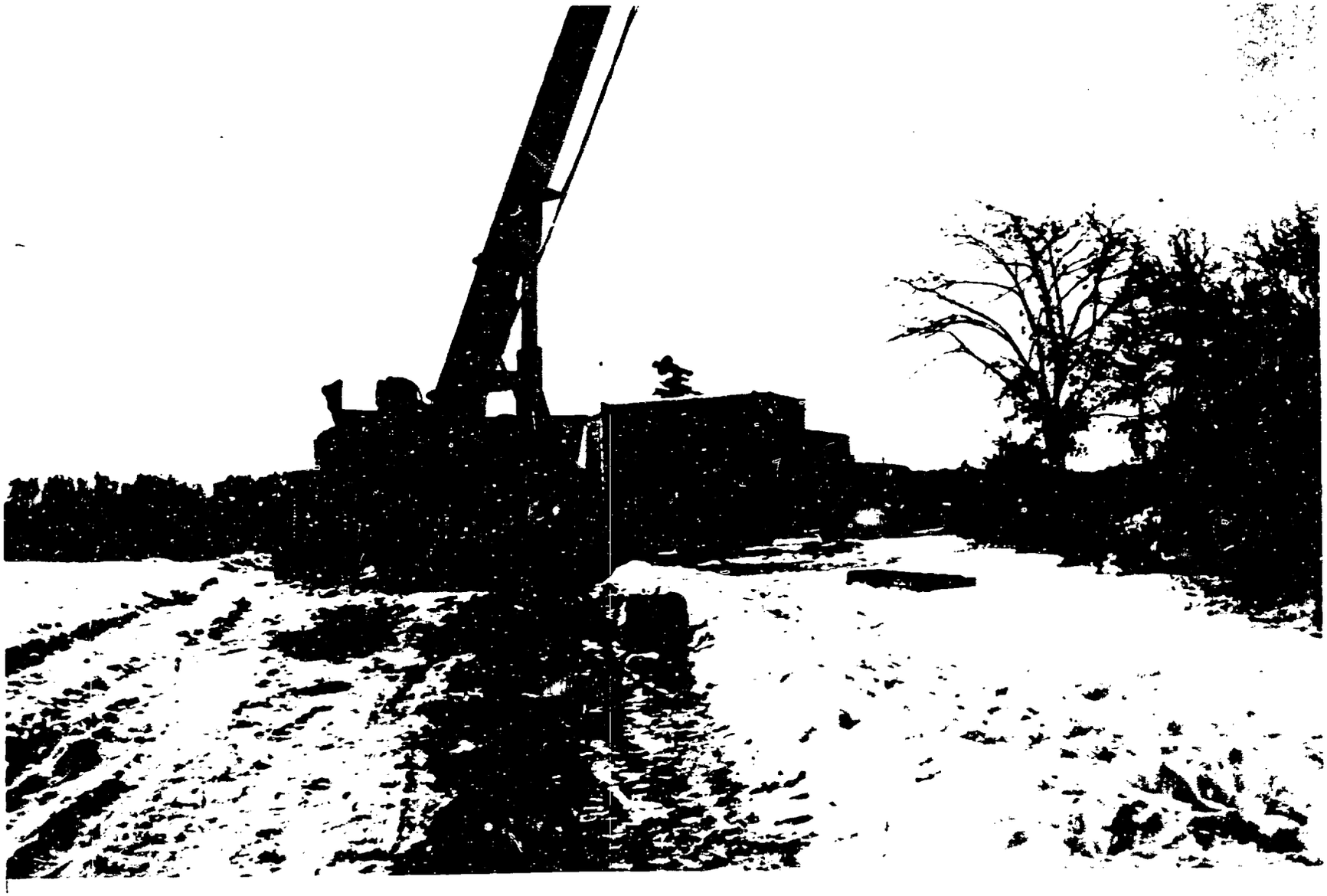

Figure 13. Test Site III: 17 & 18 Mar 78: View of Receiver Van and Crane-Tower Location

3
DATA ANALYSIS

After the terrain scattering data were collected and analyzed, it became apparent that the σ_o-results could be improved by a more detailed account of variations in incident power with additional corrections using other recorded parameters. Section 3.1 contains the basic data processing techniques used. The corrections developed for incident power modification are given in Section 3.2. These developments were carried out as an ERIM internal research and development program. In those passes where the corrections were small, or essentially like those used previously, the re-run data and graphs are essentially identical to those previously obtained. Results are discussed from various viewpoints in Section 3.3.

3.1 PROCESSING TECHNIQUES

The processing techniques and notation used to analyze the bistatic data gathered during flights made in February and March of 1978 are identical to those explained in Section 5.6 of Reference 1. For the reader's convenience, coordinate and angle definitions are repeated in Figure 1 (from Ref. 1).

One small change in geometric arrangement of transmitter and receiver may be noted. In Reference 1, the backscattering measurements were accomplished by rotating the receiving arrangement through 180^o (to face basically in the $-x_o$ direction) and by having the transmitter repeat its forward scattering flight path (as shown in Figure 1). In the current program for Site III, the backscattering measurements used the same receiver arrangement but changed the transmitter flight path to the $-x_o$ side of the $y_o z_o$ plane, i.e., "behind" the receiver. Thus, in Reference 1, the terrain areas viewed in forward scattering and backscattering measurements are

different; in the current program, they are the same. However, this procedural change requires no modification of the basic argument concerning independence of samples in the bistatic data collection (see Section 2.4 of Ref. 1).

As the receiver scans back and forth over the terrain spotlighted by the aircraft transmitter, the track-scan angle combinations cause all values of the "azimuth" angle φ_s to be repeated many times. A sample of power scattered by the illuminated terrain is thus obtained for each repeated φ_s value. To follow the process more easily, the computer processing program can be specially modified to show σ_o values obtained throughout each scan and for all scans. Figure 14 (upper plot) shows the result of 8 scans made by the receiver during a single pass of the transmitter. The variation of σ_o during the 5th scan, for example, can be followed by tracing the numeral 5 through the maze of data. Data are then averaged over a 5^o interval; Figure 14 shows that many samples are available for each average calculation. The lower plot of Figure 14 is the result of the 5^o averaging.

The averaging used is an arithmetic average of the (normalized) power values. This type of average gives most weight to the higher values of σ_o. It is of interest to see how this type of averaging compares with other measures of central tendency of the original data set. Consider, for example, linear or logarithmic regressions of the data. Using a linear regression of the form $y = a + bx$, one finds $a = -0.23$ and $b = -0.07$ with a correlation coefficient r^2 of only 0.07. A linear regression of the averaged data yields $a = 0.49$ and $b = -0.06$ with an $r^2 = 0.54$. Figure 14 shows that the latter falls approximately 2 dB above (roughly 1 dB at the ordinate axis) the former. This result confirms the statement above that the type of average used favors the higher σ_o values. A logarithmic regression produces a similar result.

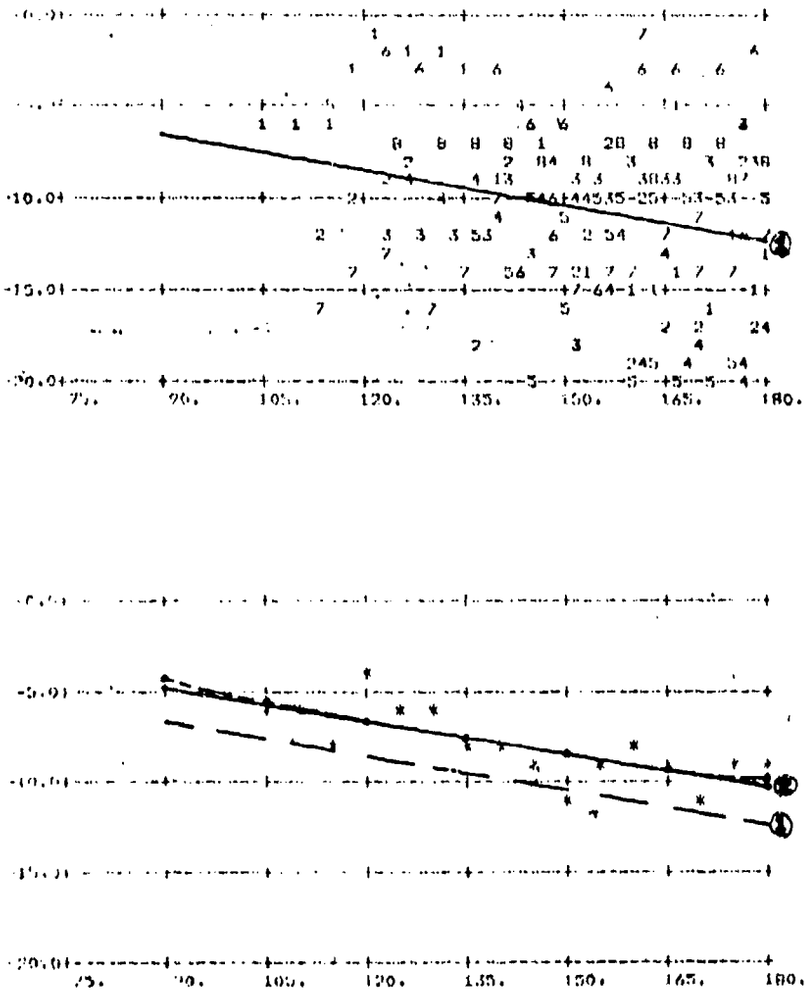

Regressions:

1. Linear
   (y = a + bx)

   r^2 = 0.07
   a = -0.23
   b = -0.07

2. Linear (•)

   r^2 = 0.54
   a = 0.49
   b = -0.06

2. Log (•)

   r^2 = 0.55
   a = 33.25
   b = -8.33

Figure 14. σ_o vs ϕ_s (Upper) for Eight Receiver Scans and (Lower) as Averaged Over a 5° Interval (Linear and Logarithmic Regressions Are Shown)

It is of some interest to note that each operation of the data analysis can be carefully traced for any pass. In addition to the graphical data illustrated by Figure 14, the computer program can be made to output two sets of numerical data. One, labeled 15-F, displays the computation results for the SCAN and TRACK angles (in degrees) arising from the digitized data tapes. The azimuth angle φ_s is computed for each (SCAN, TRACK) pair. Corresponding also to this pair are the received power outputs (in dBm) for the parallel and cross polarization channels at each of the two frequencies of interest (L:23.5 cm wavelength and X:3 cm wavelength). In addition, there is a correction column (COR) which is used to obtain the actual amount of incident power at the angle pair in question. Derivation and discussion of all quantities which make up the total correction COR is given in Section 3.2. Finally, a line number is assigned to the line of data for each angle pair.

The line number is carried over to a second output labeled S where the integral KI is computed for the illuminated area A_{gd} corresponding to the (SCAN, TRACK) angle pair of that particular line. From this result, σ_o is computed and plotted on the upper data graph for that pass. A partial data set for Pass 2 of the 3/17/78 Flight is shown in Figures 15a and 15b as an example. Figure 15a shows the F-data, Figure 15b shows the S-data, and Figure 16 shows the graphed data set (upper) and averaged data set (lower).

Let us follow line 17 as an example. A count of 4132 individual power samples produces an X-parallel received power of -65.8 dBm, as determined relative to a calibration level of 7 given in parentheses to the right of the X-parallel power value. Incident power is nominally 60 dBm but must be corrected according to the record of actual radiated power (Section 3.2). The computed corrections to be applied to the 60 dBm incident power are listed in the "correction" column; for line 17, the value is -1.8 dB.

SCAN = FORWARD
SCAN = 89.8700 + -0.6740 X
TRACK = 1.0526 + 0.1895 X
X-BAND = -73.7200 + 0.9340 X -76.5900 + 1.0320 X
L-BAND = -71.9800 + 0.8540 X -76.2500 + 1.0590 X
THRESHOLD = 400
RANGE = -360. 360. (SCAN) -45. 45. (TRACK)
POWER CORRECTION ANGLE POINTS -45.0 -2.0 13.0 32.0 38.0 45.0 0.0 0.0 0.0 0.0 0.0 0.0 0.0 0.0 0.0
POWER CORRECTIONS -13.0 -1.0 -9.0 -14.0 -11.0 -11.0 0.0 0.0 0.0 0.0 0.0 0.0 0.0 0.0 0.0

	COUNT	SCAN	TRACK	PHI-S	X-PAR	X-CROSS	L-PAR	L-CROSS	CORRECTION
1	1709	-38.9(19)	-0.6(-11)	38.3	-56.3(74)	-59.3(87)	-45.3(1338)	-51.6(245)	-1.7
2	2876	-34.3(18)	-0.6(-11)	33.6	-50.3(321)	-53.0(199)	-44.5(973)	-49.6(336)	-1.7
3	932	-29.6(17)	-0.6(-10)	29.1	-50.0(385)	-52.2(230)	-48.0(644)	-55.1(100)	-1.8
4	1702	-24.9(16)	-0.6(-11)	24.3	-61.8(21)	-63.6(18)	-46.9(863)	-53.1(152)	-1.7
5	1612	-20.2(15)	-0.6(-10)	19.8	-65.3(8)	-68.8(14)	-52.3(202)	-55.8(98)	-1.8
6	1836	-15.6(14)	-0.6(-10)	15.1	-58.9(104)	-58.5(139)	-51.7(238)	-60.4(30)	-1.8
7	1673	-10.9(13)	-0.6(-11)	10.3	-50.6(299)	-52.5(218)	-48.9(506)	-53.7(136)	-1.7
8	1823	-6.2(12)	-0.6(-11)	5.6	-51.7(229)	-57.5(70)	-50.6(373)	-56.3(283)	-1.7
9	1659	-1.5(11)	-0.6(-11)	0.9	-55.1(99)	-55.7(105)	-48.0(645)	-48.0(804)	-1.7
10	1700	3.1(10)	-0.6(-10)	3.6	-61.2(22)	-55.6(108)	-47.8(755)	-49.6(331)	-1.8
11	1528	7.8(9)	-0.6(-11)	8.4	-65.3(8)	-66.7(9)	-48.6(559)	-56.8(69)	-1.7
12	1895	12.5(8)	-0.6(-11)	13.1	-60.8(10)	-69.8(5)	-50.6(317)	-57.7(57)	-1.7
13	1733	17.2(7)	-0.6(-11)	17.8	-60.8(10)	-69.8(5)	-55.5(144)	-51.4(116)	-1.7
14	1965	21.8(6)	-0.6(-11)	22.5	-61.8(23)	-57.9(65)	-57.8(51)	-56.2(93)	-1.7
15	2179	26.5(5)	-0.7(-10)	26.9	-59.7(32)	-56.0(100)	-54.3(88)	-51.5(142)	-1.8
16	2746	31.2(4)	-0.6(-11)	31.8	-70.9(2)	-67.3(8)	-56.7(62)	-52.1(52)	-1.7
17	4132	35.8(3)	-0.8(-10)	36.3	-65.8(7)	-62.9(21)	-59.9(30)	-60.8(29)	-1.6
18	2533	31.2(4)	-0.6(-11)	31.8	-68.8(9)	-73.5(2)	-60.8(24)	-60.2(33)	-1.7
19	1569	26.5(5)	-0.8(-10)	26.9	-68.0(11)	-70.4(8)	-59.8(39)	-57.8(88)	-1.8
20	1899	21.8(6)	-0.6(-11)	22.5	-65.8(7)	-69.8(5)	-57.1(55)	-56.9(67)	-1.7
21	1612	17.2(7)	-0.8(-10)	17.6	-60.5(26)	-57.1(78)	-59.9(101)	-54.8(89)	-1.8
22	1377	12.5(8)	-0.6(-11)	13.1	-66.5(6)	-60.1(43)	-51.1(278)	-49.9(307)	-1.7
23	1124	7.8(9)	-0.8(-10)	8.2	-101.7(0)	-73.5(2)	-49.5(432)	-48.8(395)	-1.8
24	1341	3.1(10)	-0.8(-10)	3.6	-101.7(0)	-76.6(1)	-47.8(866)	-47.8(888)	-1.8
25	1432	-1.5(11)	-0.6(-11)	0.9	-57.2(58)	-60.9(33)	-42.7(2658)	-49.8(313)	-1.7
26	1326	-6.2(12)	-0.8(-10)	5.8	-56.3(74)	-60.2(39)	-42.2(3106)	-53.2(156)	-1.8
27	1656	-10.9(13)	-0.8(-10)	10.8	-65.8(7)	-61.2(31)	-44.1(1832)	-52.8(179)	-1.8
28	2123	-15.6(13)	-0.6(-11)	14.9	-63.3(13)	-62.3(24)	-42.6(2770)	-48.1(370)	-1.7
29	2101	-20.2(15)	-0.6(-11)	19.6	-65.8(7)	-70.4(8)	-46.9(864)	-51.7(208)	-1.7
30	1789	-24.9(16)	-0.6(-11)	24.3	-61.2(22)	-56.0(99)	-41.5(3715)	-51.5(228)	-1.7
31	2792	-29.6(17)	-0.8(-10)	29.1	-73.7(1)	-73.5(2)	-43.5(2148)	-50.6(262)	-1.8
32	4119	-34.3(18)	-0.8(-10)	33.8	-59.8(34)	-60.2(39)	-45.6(1225)	-51.4(223)	-1.8

Figure 15a. Computer-Generated Data Set 15-F

X-BAND
RECEIVER DEPRESSION= 88.
RECEIVER HEIGHT= 100.
TRANSMITTER HEIGHT= 9000.
TRANSMITTER DISTANCE= 15000.
ANGULAR OFFSET= 60.0
UNACCEPTABLE RESPONSE APPENDED WITH "*"

BW = 6.70 D/LAMDA = 10.92 PI = 60.0 K = 0.037

PHIS	PT	PO=FR PARALLEL	PO=FR CROSS	RI	COR	SIGMA PARALLEL	SIGMA CROSS	STR-SCAN	STR-TRACK	LINE
38.3	60.0	-56.3	-59.3	-104.7	-1.7	-7.9	-10.9	38.9	0.6	1
33.6	60.0	-50.3	-53.9	-104.1	-1.7	-2.5	-5.1	38.3	0.4	2
29.1	60.0	-50.0	-52.2	-105.7	-1.8	-2.5	-4.7	29.4	0.4	3
24.5	60.0	-61.8	-63.4	-104.9	-1.7	-14.7	-17.0	24.9	0.4	4
19.8	60.0	-65.3	-68.8	-104.5	-1.8	-18.9	-18.4	20.2	0.4	5
15.1	60.0	-58.9	-58.5	-103.9	-1.8	-9.1	-8.7	15.6	0.4	6
10.3	60.0	-50.4	-52.5	-103.6	-1.7	-5.3	-7.1	10.9	0.6	7
5.6	60.0	-51.7	-57.5	-103.3	-1.7	-6.6	-12.5	6.2	0.6	8
0.9	60.0	-55.1	-55.7	-103.2	-1.7	-10.2	-10.8	1.5	0.6	9
3.5	60.0	-61.2	-55.6	-103.2	-1.8	-14.1	-10.6	-3.1	0.4	10
8.4	60.0	-65.3	-64.7	-103.5	-1.7	-20.1	-21.5	-7.8	0.6	11
13.1	60.0	-68.4	-69.8	-103.8	-1.7	-18.9	-23.9	-12.5	0.6	12
17.8	60.0	-68.8	-69.8	-104.3	-1.7	-18.3	-23.3	-17.2	0.4	13
22.5	60.0	-61.0	-57.9	-104.7	-1.7	-14.5	-11.8	-21.8	0.4	14
26.9	60.0	-59.7	-51.0	-105.3	-1.8	-12.5	-4.4	-26.5	0.4	15
31.8	60.0	-70.0	-67.3	-105.9	-1.7	-23.2*	-10.6	-31.2	0.4	16
36.3	60.0	-65.8	-62.9	-106.3	-1.8	-17.7	-14.8	-35.8	0.4	17
31.8	60.0	-68.8	-73.5	-105.9	-1.7	-17.1	-25.8*	-31.2	0.6	18
26.9	60.0	-68.0	-70.4	-105.3	-1.8	-16.8	-23.2*	-26.5	0.3	19
22.5	60.0	-65.8	-69.8	-104.7	-1.7	-19.8	-22.0	-21.8	0.4	20
17.8	60.0	-60.5	-57.1	-104.3	-1.8	-18.4	-16.8	-17.2	0.4	21
13.1	60.0	-64.5	-60.1	-103.8	-1.7	-20.8	-16.5	-12.5	0.6	22
8.8	60.0	-57.2	-60.9	-103.2	-1.7	-12.3	-16.0	1.5	0.6	25
5.8	60.0	-54.3	-60.2	-103.3	-1.8	-11.1	-15.0	6.2	0.4	26
10.4	60.0	-65.8	-61.2	-103.6	-1.8	-20.8	-15.8	10.9	0.4	27
15.9	60.0	-63.3	-62.3	-103.8	-1.7	-17.7	-16.7	15.6	0.6	28
19.6	60.0	-65.8	-70.4	-104.5	-1.7	-19.6	-24.1*	20.2	0.6	29
24.3	60.0	-61.2	-56.0	-104.9	-1.7	-18.5	-9.8	24.9	0.6	30
33.8	60.0	-59.4	-60.2	-106.2	-1.8	-11.9	-12.2	34.5	0.4	32

Figure 15b. Computer-Generated Data Set 15-S

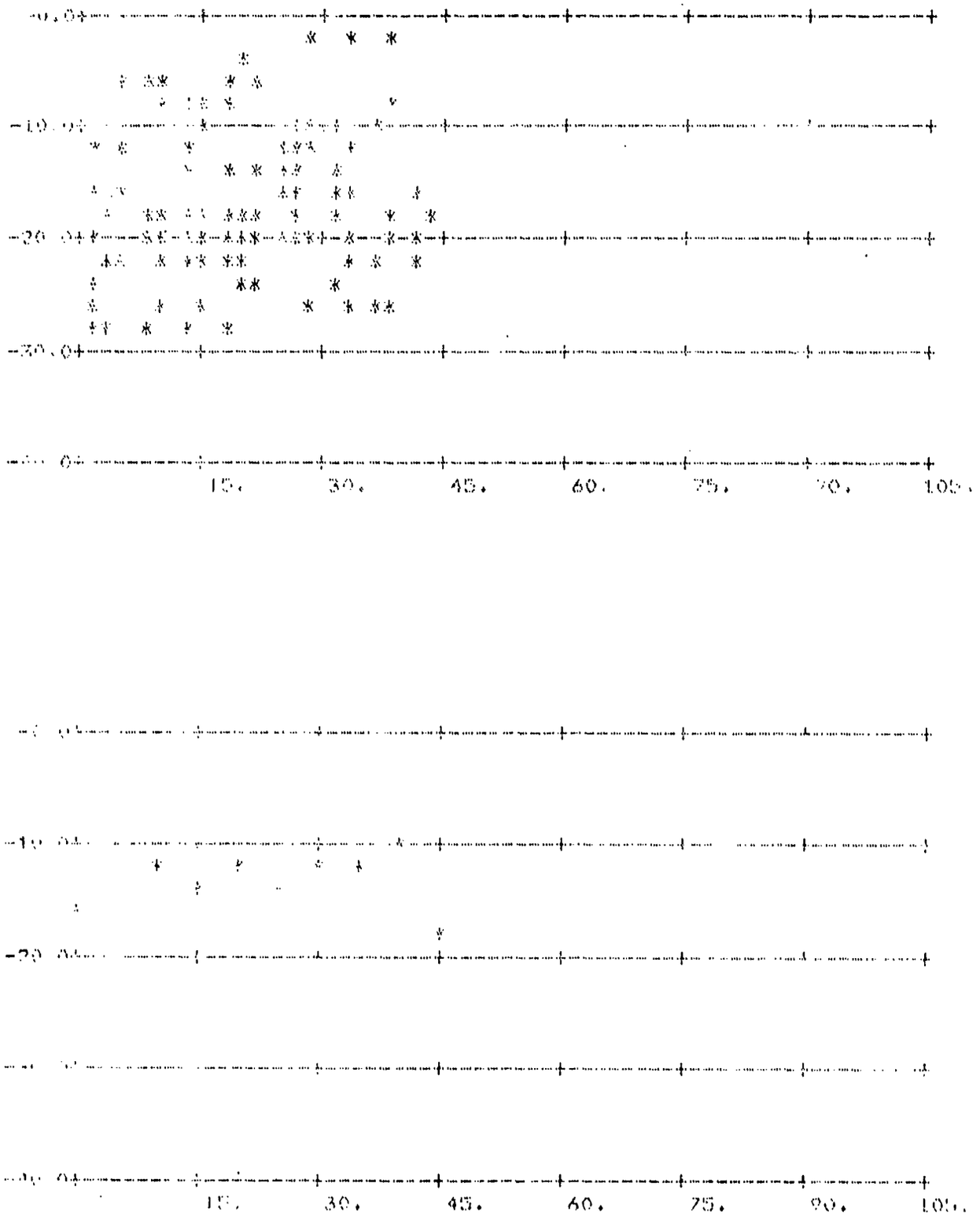

Figure 16. Computed σ_o Data: (Upper) Graphed Data Set and (Lower) Average Data Set

On the same F-sheet, SCAN and TRACK angles (degrees) are computed from their digital tape values, recorded in the accompanying parentheses. For line 17, a SCAN angle of 35.8° is computed from a tape value of 3 (which is converted to degrees by the SCAN equation at the top of the sheet). PHI-S (φ_s) is then determined from SCAN and TRACK; for line 17, PHI-S = 36.3°.

The X-PAR and X-CROSS powers are carried from the F- to the S-data sheet for X-BAND and recorded in the PARALLEL and CROSS POWER columns. The correction is also carried along in the COR column. SIM-SCAN and SIM-TRACK are transformations of SCAN and TRACK angles into angles in a standard mathematical coordinate system. Using these angles, together with a receiver depression angle value (84° for Figure 15) and a transmitter depression angle value computed from transmitter height and distance, the integral KI is computed for suitable parameter values. For the Figure 15 example, the receiver antenna beamwidth (at 10-dB points) is 8.70°, the antenna diameter-to-wavelength ratio, D/LAMBDA, is 14.42, and the constant K is 0.037. The integral I is the weighted area common to the antenna footprints of the transmitter and receiver (a portion of the correction COR arises from a correction of the transmitter beam position). The line 17 value for KI is -106.3 dB (KI is dimensionless).

Finally, RCS per unit illuminated area, σ_o (SIGMA) in dB is computed from (Eq. 50, Ref. 1)

$$\sigma_o = (\text{X-PAR}) - [(\text{PI} - \text{COR}) + \text{KI}]$$

where all quantities are in dB.

3.2 INCIDENT POWER CORRECTIONS

The incident power receiver was used to record continuous values of power incident on the scattering area. This system is described in Section 5.4. Chart recordings were obtained presenting incident power level as a function of time, with the start and end of each

pass indicated on the chart record. Using internal calibration, these records are converted to absolute value of incident power as a function of time throughout each pass. Before these values of measured power can be used in the calculation of σ_o values, several corrections must be applied to obtain true values of power incident on the scattering area. These corrections are:

1. Variation in incident power values due to geometry. The range dependencies are accounted for in the computation of σ_o.
2. Variation in the incident power receiver antenna pattern.
3. Illumination taper across the scattering area due to the variation in the transmitter antenna gain across the extended scattering area.

The ERIM computer program used to calculate the values of σ_o provides for the input of incident power correction as a function of illumination angle. Values given in Table IV are the corrections as measured or calculated for corrections (1) and (2) as listed above.

The final correction, that due to the variations in the transmitter antenna illumination, is obtained using contour plots of the antenna gain. This correction was found to be necessary because only a single incident power receiver was used in the large scattering area. The measurement provided from the incident power receiver applies only within the region of near constant transmitter gain. Careful examination of the variation of antenna gain over the entire scattering area indicated that compensation was necessary to obtain minimum error in σ_o values. Information regarding transmitter antenna illumination angle was obtained from the antenna angle versus time records made on the aircraft and from the ground tracking angle information. The technique used is identical to that described in the previous report [1].

TABLE IV. CORRECTIONS APPLIED TO INCIDENT POWER VALUES
DUE TO GEOMETRY AND INCIDENT POWER RECEIVER ANTENNA

	Illumination Angle (dB)								
	-45	-37½	-22½	-7.5	0	+7.5	+22½	+37½	+45
Geometrical Correction $\frac{1}{R_i^2}$	3	2	1	0	0	1	2	3	
Incident Power Receiver-Antenna Response	1.5	1.0	0.5	0	0	0.5	1.0	1.5	

Since the three types of corrections are keyed to TRACK angle, a correction computation for the incident power PI is made for every entry of the computation procedure. In the F-computation, the CORRECTION appears as the last column (Figure 15a) and is -1.8 dB for line 17. It is also carried over to the S-computation, for convenience, and appears as COR in the sixth column (Figure 15b).

For site III, data are recorded for three transmitter incidence $\theta_i = 60^\circ$, 70°, and 80°, and four receiver incidence angles, $\theta_s = 60^\circ$, 70°, 80°, and 84°. For each incidence angle pair, there are parallel and cross polarization cases for both forward and backscattering passes. Counting both the 23.5 cm and 3 cm wavelengths, there is therefore a total of 80 plots of σ_o versus φ_s for Site III. These data are organized according to incidence angle pairs and presented in Appendix A.

For Site III terrain scattering at the 23.5 cm wavelength, it can be remarked that, in general, the parallel polarization σ_o exceeds the cross polarization σ_o by some 4 to 8 dB on the average. Taking account of the ± 4 dB error interval for these values, it appears that the parallel return ranges from comparable to marginally higher than the cross return. For the 3 cm wavelength, the distinction is not quite so clear, since there are some cases when the cross return exceeds the parallel. However, on the average, the 3 cm parallel return exceeds the cross by some 2 dB.

For several combinations of values of θ_i and θ_s, one can observe an unexpectedly large saltus between the forward-scattering and the back-scattering returns. For example, Figures A-9 and A-10 show a drop of some 8 dB in going from the forward to the back case. Although the reason for such behavior in this instance is not clear, there are other cases where the paucity of sample points in the vicinity of $\varphi_s = 90^\circ$ places the average value there in doubt. Such situations are observable in Figures A-21, A-22; A-25, and A-26. For example, in Figure A-26, there is but one sample each at the

first two values of φ_s and so the average takes exactly that value at each point.

It is of interest to consider the variation of σ_o with incidence angle pairs for special azimuth values, in particular, the forward ($\varphi_s = 0^\circ$) and back ($\varphi_s = 180^\circ$) scattering cases. In Figure 17, σ_o is plotted as a function of θ_s for fixed values of θ_i in both the forward and back cases at the 23.5 cm wavelength. For a constant θ_i at the forward direction, the trend is from essentially constant to a gentle fall-off with increasing θ_s. For backscattering, the reverse statement is appropriate.

Figure 18 presents the alternative view for 23.5 cm, i.e., for fixed θ_s, σ_o varies with θ_i. The forward cases seem to be essentially flat as a function of θ_i while the backward cases show a "null" at $\theta_i = 70^\circ$, except for the $\theta_s = 84^\circ$ case. Such anomalous behavior might be ascribable to the regularity of the Site III terrain (an orchard consisting of uniform height, uniformly spaced apple trees).

Figure 19 gives the 3 cm data for fixed θ_i and φ_s. The trend for forward scattering is like that at 23.5 cm, but the fall-off is more abrupt. For backscattering, there is a strange reversal of trend from $\theta_s = 80^\circ$ to 84° for $\theta_i = 70^\circ$ and 80°.

Figure 20 gives the alternative viewpoint for fixed θ_s and φ_s for the 3 cm wavelength. The data trends are rather like those of the 23.5 cm wavelength, except for $\theta_s = 84^\circ$ forward. The $\theta_i = 70^\circ$ data are down instead of up. In both Figures 19 and 20, it is clear that the cross return often exceeds the parallel, but never beyond the error interval. Thus, the parallel and cross returns for the forward and backscattering cases may be considered comparable.

In Figure 21, forward and backscattering data are collected for the cases $\theta_s = \theta_i$ at both wavelengths. The data for both

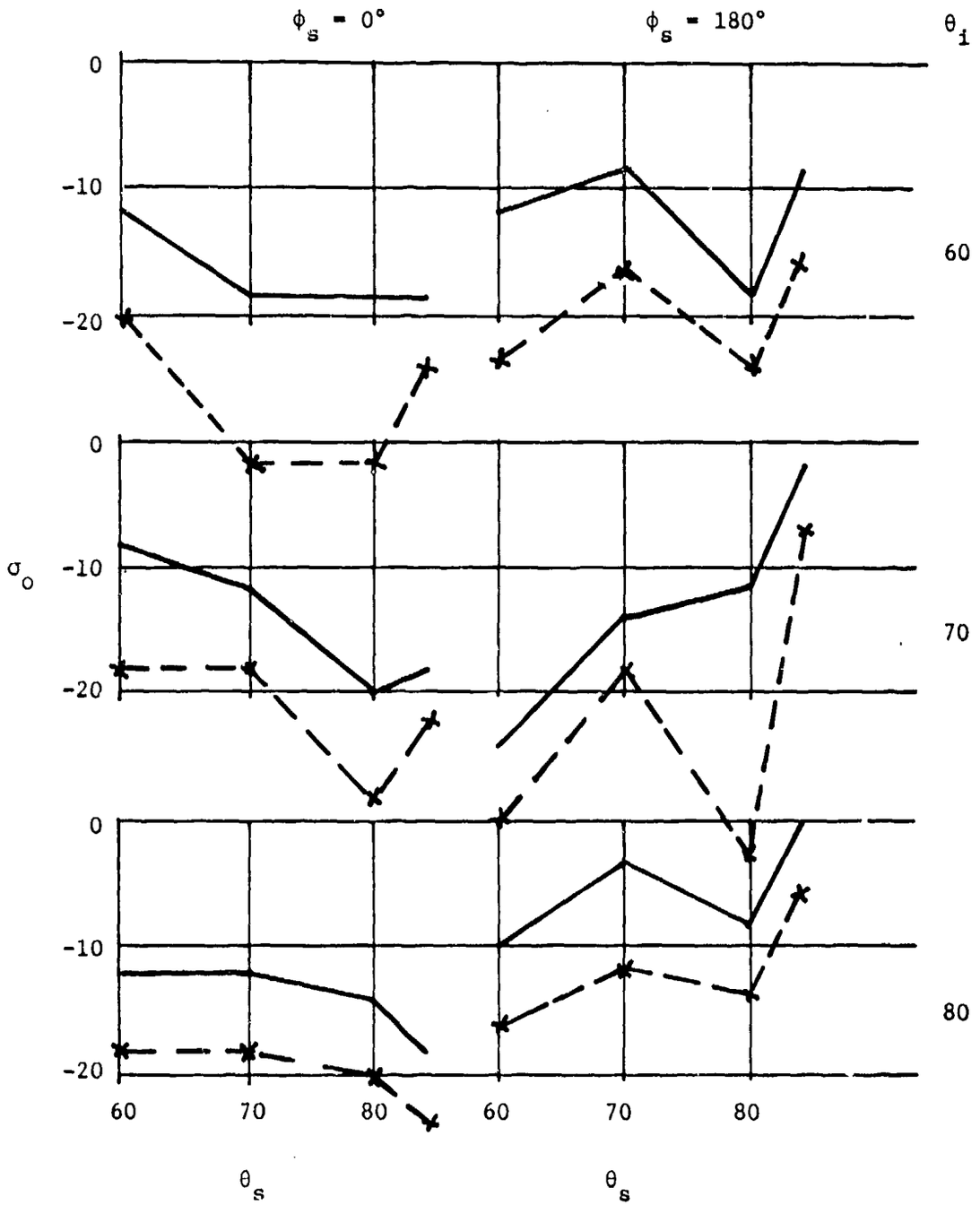

Figure 17. Test Site III: σ_o vs θ_s for Fixed θ_i, L-Parallel (•) and L-Cross (x)

Angles θ_s and θ_i Measured from Surface Normal

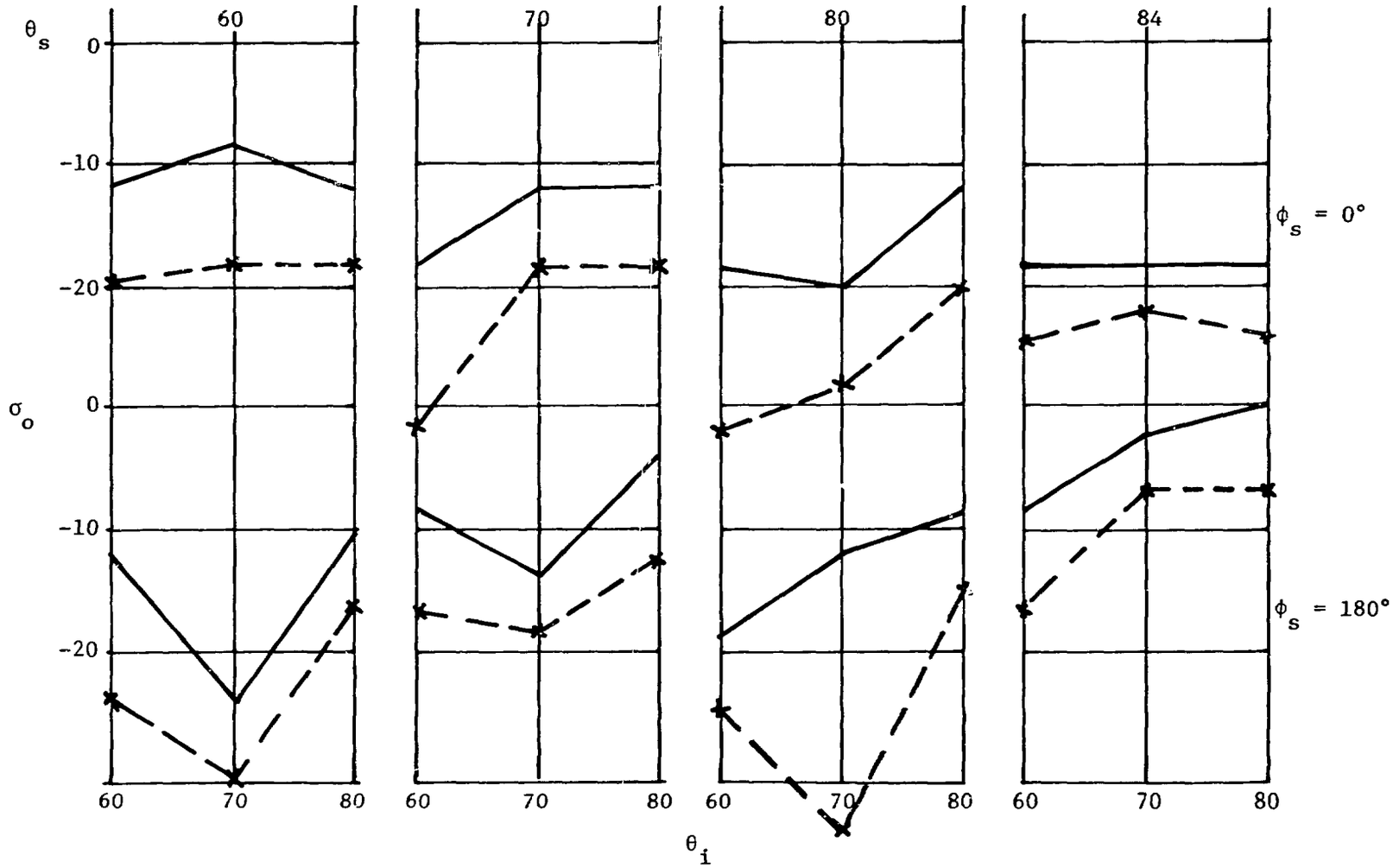

Figure 18. Test Site III: σ_o vs θ_i for Fixed θ_s, L-Parallel (•) and L-Cross (x)
Angles θ_s and θ_i Measured from Surface Normal

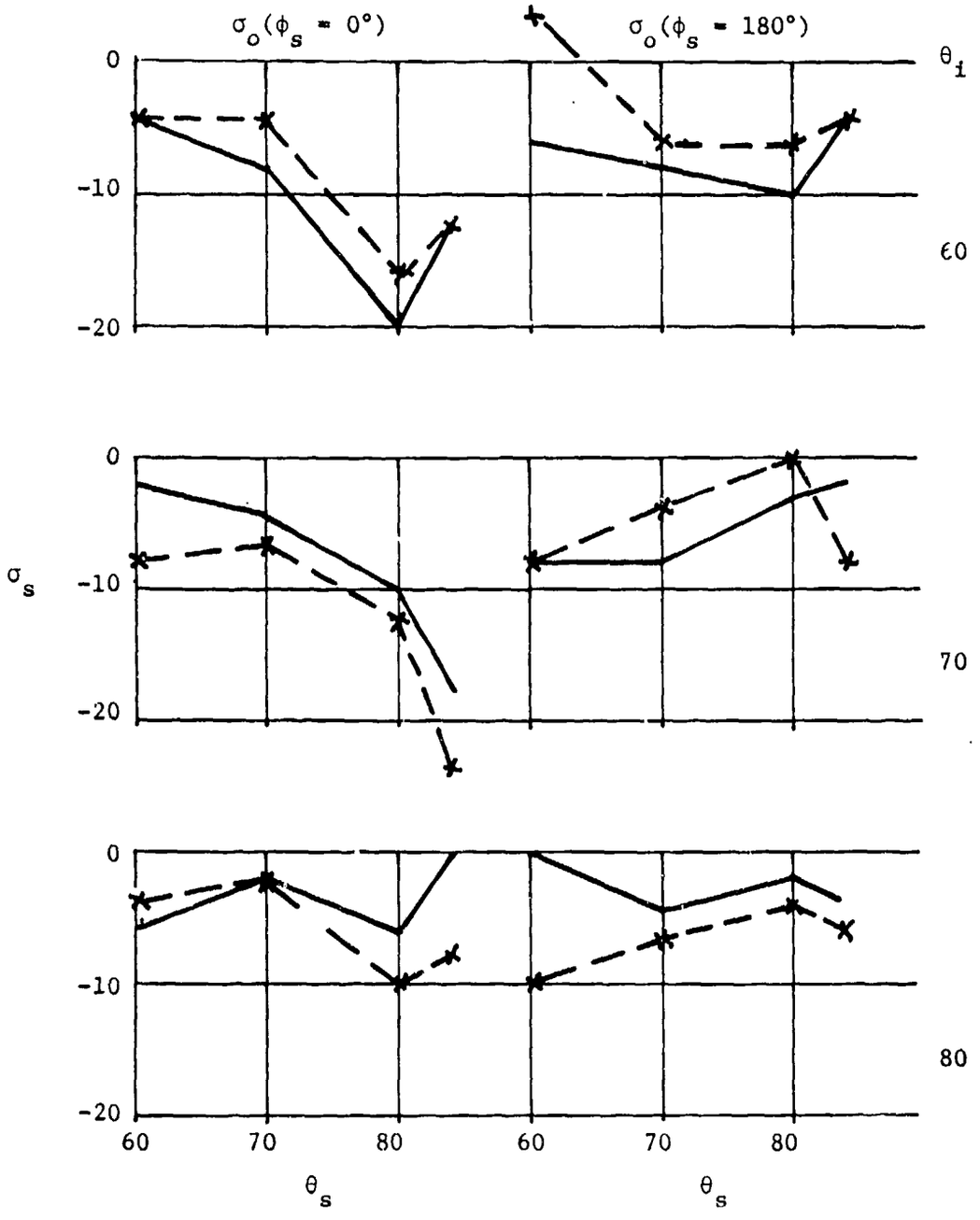

Figure 19. Test Site III: σ_o vs θ_s for Fixed θ_i, X-Parallel (•) and X-Cross (x)

Angles θ_s and θ_i Measured from Surface Normal

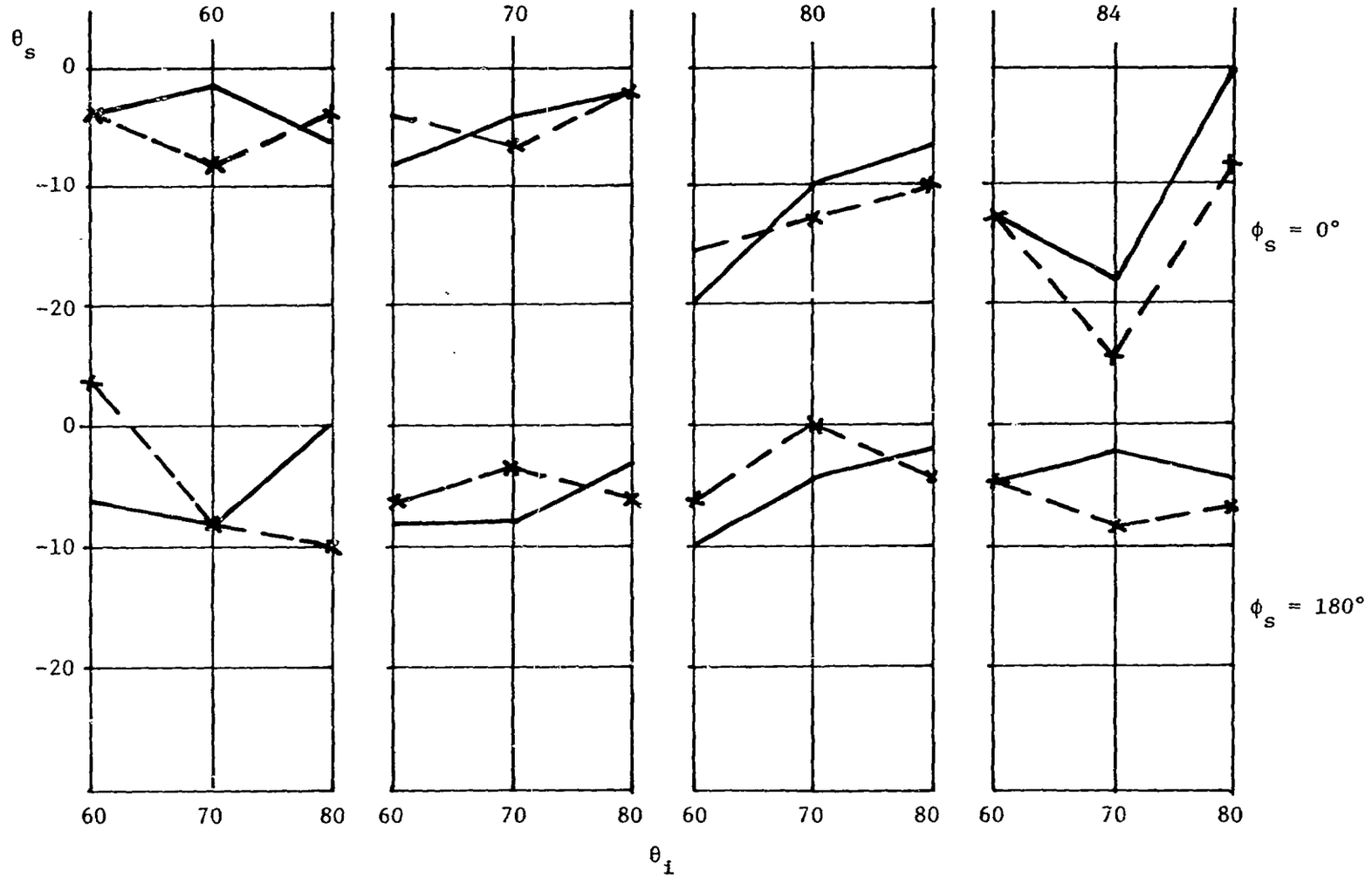

Figure 20. Test Site III: σ_o vs θ_i for Fixed θ_s, X-Parallel (•) and X-Cross (x)
Angles θ_s and θ_i Measured from Surface Normal

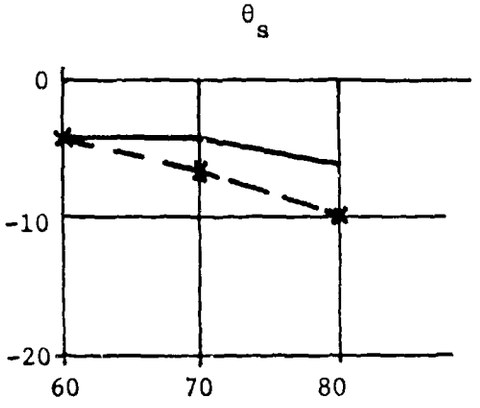

$\sigma_o(\theta_s = \theta_i)$, Site III,
X-Parallel (•) and X-Cross (x)
$\phi_s = 0°$

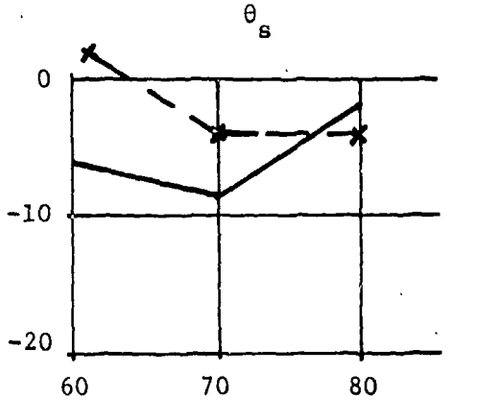

$\sigma_o(\theta_s = \theta_i)$, Site III,
X-Parallel (•) and X-Cross (x)
$\phi_s = 180°$

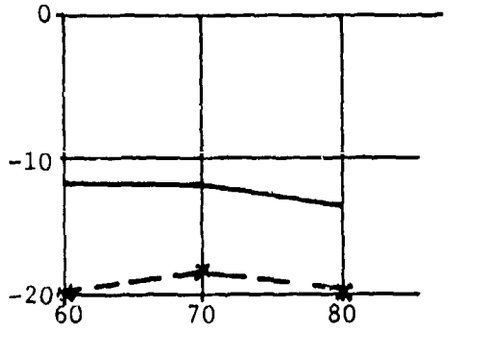

$\sigma_o(\theta_s = \theta_i)$, Site III,
X-Parallel (•) and X-Cross (x)
$\phi_s = 0°$

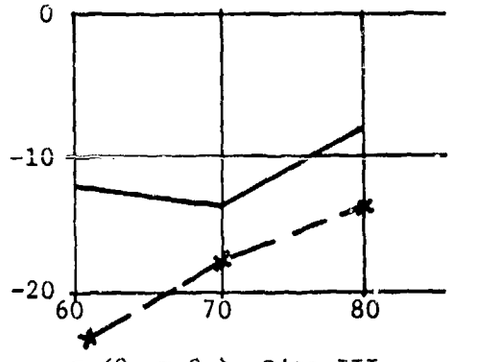

$\sigma_o(\theta_s = \theta_i)$, Site III,
X-Parallel (•) and X-Cross (x)
$\phi_s = 180°$

Figure 21. Test Site III: X and L
Forward-Scatter and Backscatter Data
Angles θ_s and θ_i Measured from Surface Normal

wavelengths show a marked tendency towards features in both the forward and back scattering cases.

The calibration of the X-band data from the February measurements is subject to question and so only a small sample of results is included. Results obtained from the analysis of the February (snow site) X-band indicated inconsistent values of σ_o. A review of the operating conditions during data gathering showed that a shift in frequency occurred, due to the cold weather conditions. As a result of the frequency shift, the system transfer function as measured by the calibration signal is not directly applicable. Attempts have been made to compensate for the frequency shift by making additional measurements of the total system response. The difference between the values so obtained, and the calibration, is used as a correction factor. However, due to uncertainties in the actual value of frequency drift existing as a function of time, the correction factors obtained do not give consistent results. For example, using the calculated corrections for the first half of pass 10, 19 February data, the values of σ_o obtained are given in Figures A-141 and A-142. However, when the correction factor is applied to the data from the complete pass unreasonably large values of σ_o are obtained. The possibility of direct triggering was considered, but this would have affected the L-band channels also, which did not occur. At this time it is assumed that the magnitude of frequency drift is a variable, changing slowly during a pass. It is possible that an analysis of additional (but not normally used) parameters recorded during data gathering with the measurements system would provide adequate information to obtain accurate correction factors for some of the February X-band data.

Although the flight of 15 February was very short, as it was scheduled as a test flight, the complete measurements system operated satisfactorily and the X-band results are included in Figures A-143 and A-144; L-band results are included in Figures A-145 and A-146.

4
ERROR ANALYSIS

A discussion of the error analysis for the complete bistatic instrumentation is given in Section 6, Reference 1. The results of that analysis are summarized in Tables V and VI as those values are applicable to the present data gathering program. However, by including the calibrated receivers for the direct measurement of incident power, accomplished in Phase 1 of this program, the error due to transmitter antenna pointing uncertainties has been reduced. Two receivers, at the two operating wavelengths, were utilized to obtain a calibrated measure of the power incident on the test area. In addition, the incident power receivers are used as insulators for the initiation of the transmitter scan (spotlight operation). The incident power level is recorded during each data pass. These records are used to obtain the value of incident power throughout the pass and these values are used in the data reduction to obtain values of the scattering coefficients σ_o. The total error contribution due to uncertainties in the absolute value of incident power has been determined to be ± 2 dB. This value represents a reduction of 2 dB in the total error over that realized in the previous bistatic data gathering program.

4.1 INSTRUMENTATION ERRORS

Instrumentation errors can be classed as systematic or random. The systematic error is estimated to have a maximum value of 4.7 dB and an RMS value of 2.0 dB; the random error has an estimated RMS value of 2.5 dB. These errors are believed to be realistic since they are based on instrumentation tests and the results of the data-gathering experiments. Transmitter antenna pointing is the largest single source of error. The total error is estimated to be 4 dB; total error was estimated to be 6 dB for the initial data gathering program [1].

TABLE V. ESTIMATES OF RANDOM ERRORS

Source	Magnitude (dB)
Measurement of incident power*	±2.0
Position uncertainty of transmitter	±0.2
Height variation of ground	±0.2
Receiver noise (26 dB S/N after non-coherent processing)	±0.4
Receiver gain error (L.O. power variation and other factors)	±1.0
Sample and hold error (10 nsec jitter)	±1.3
Tape recorder error (noise and jitter)	±0.3
Maximum	= 5.4
RMS Value	= 2.5

*Error due to incident power uncertainties for the 17, 18, 19 February data are ±4 dB giving a total maximum of 7.4 and rms of 3.5

TABLE VI. ESTIMATES OF SYSTEMATIC ERRORS

(Log-normal distributions assumed)

Source	Magnitude (dB)
Transmitter power error	±1.0
Receiver power error	±1.0
Transmitter antenna peak gain error	±0.6
Receiving antenna peak gain error	±0.6
Losses in microwave components, radome, and atmosphere	±1.0
Maximum gain drift with temperature	±0.5
Maximum	= 4.7
RMS Value	= 2.0

The problem of energy entering the receiver sidelobes must be considered for the measurement geometries in the program. Range gating has insured that the specular return was not received through the antenna mainlobe. The average sidelobe response of 24 dB down provides adequate spatial filtering in the specular plane. A limiting factor in the measurement of cross-polarized σ_o is the cross-polarization isolation of the transmitting and receiving antennas; this isolation ranged between 20 and 31 dB for the 3 and 23.5 cm wavelength transmitting and receiving antennas.

Errors due to sampling effects are introduced at different points in the data gathering and analysis process. The finite sampling window of the sample-and-hold detector results in a location ambiguity of 10 nsec or 10 ft of processed error. However, this produces negligible error in the σ_o calculation. The basic timing error in the S-H results in a 1.3 dB error in the output signal. Tape recorder noise will add 0.3 dB to the total error.

4.2 SAMPLING ERROR

Error bounds (or confidence) in the estimate of the mean value of σ_o are a function of the number of independent samples, as discussed in Section 5.5. The average number of independent samples of each 23 cm data point is about 10, giving a 5 dB spread in the 95% confidence interval for the mean value. Similarly, the average number of independent samples for 3 cm data points is 35, giving a 3.5 dB spread in the 95% confidence interval for the mean value.

4.3 APPLICATION OF ERROR ESTIMATES TO DATA SETS

The results of the error analysis summarized in this section are applicable to the values of scattering coefficient obtained under normal operating conditions. However, due primarily to the extreme weather conditions that prevailed during the data gathering period

covered by this report, it is necessary to qualify the error estimate for particular data sets. The error estimate for all reported data obtained from the 16 December 1977, 15 February 1978, and 17, 18 March 1978 data gathering periods is approximately 4 dB as given in Tables V and VI. The data obtained from the 17, 18, 19 February 1978 data gathering period is approximately 6 dB (same as for the data obtained in the 1976 measurements).

It is possible to reduce the total error in all of the present data by a change in the data analysis program. This change would need to provide a means to correct the data on an individual sample (pulse) basis, utilizing the incident power data. This, however, is not possible with the present digitization system developed previously. It is estimated that a further reduction in error of between 1-2 dB is possible using existing data.

5
BISTATIC RECEIVER MODIFICATIONS

Several modifications to the overall bistatic measurements instrumentation were completed as a part of this program. These modifications are: (1) receiver for the pulse repetition frequency for reference synchronization, (2) modification of receiver and receiver response measurements, (3) sync generator modification, and (4) incident power receivers, 3 cm and 23.5 cm. All modifications completed as a part of this program have been designated "77 modifications."

5.1 PRF SYNC RECEIVER, 77 MODIFICATION

A PRF Sync Trigger is necessary to turn on the Bistatic Data Receivers. The Bistatic Data Receivers are held in a high-attenuation off mode by an RF switch in the input of each receiver to avoid measuring the direct-path RF power amplitude. The RF switches attenuate the signal strength by at least 60 dB. Precise alignment of the PRF Sync Receiver allows the RF switches to be triggered on in 10 nanoseconds or longer after the direct path transmitter pulse's trailing edge has passed the receiver location. Both the PRF sync and bistatic receivers are mounted on the crane (tower).

Integrating the PRF sync receiver into the bistatic system has eliminated the transient responses in the X- and L-band L.O. paths experienced in the original design of the system. Multi-PRF triggering occurring at low L.O. power signal strengths in the original design has now been eliminated by employing the PRF Sync Receiver. An easier alignment and more reliable sync delay exists in the PRF Sync Receiver versus the original technique.

PRECEDING PAGE BLANK-NOT FILMED

Implementation of the PRF Sync Receiver is illustrated in Figure 22. An X-band pulsed signal at a PRF of 4 KHz is transmitted from the C-46 aircraft. Each PRF interval consists of two X-band pulses. The first pulse developed is 0.8 μsec in width (the sync pulse) followed by a 50 nanosecond pulse delayed by 2.5 μsec with respect to the sync pulse. The 50 nanosecond pulse is the bistatic illumination pulse which is used for data acquisition.

The X-band pulses operate at a frequency of 9452 MHz and are received by either the front or rear dipole type antenna, depending on the geometry of the flight path. The received RF pulses are amplified by a turnel diode amplifier (TDA) and mixed with a 9512 MHz L.O. frequency. The resulting 60 MHz frequency is amplified by a log amplifier which develops video pulses used to trigger the PRF sync delay logic shown in Figure 22.

A PRF sync delay gate develops when the signal strength exceeds a threshold setting of about 6 dB above the noise. The leading edge of the 0.8 μsec pulse triggers the PRF sync delay gate. The delay's time interval is controlled from the van by observing the monitor logic pulses sent down 200 ft of coax for oscilloscope presentation. A PRF pulse generated in the van for test and calibration purposes is sent up a 200-ft coax to trigger the PRF sync delay logic. This test PRF pulse is used to set the correct delay needed to turn the bistatic RF switches on at the precise time.

Once the leading edge of the 0.8 μsec pulse triggers the PRF sync delay logic, an inhibit triggering gate is formed. This gate's function is to keep the bistatic pulse occurring 2.5 μsec later from retriggering the PRF sync delay logic. The inhibit gate interval is about 5 μsec in duration.

The trailing edge of the PRF sync delay logic triggers the PRF trigger logic shown in Figure 23. A 1-μsec pulse width is generated which is coupled to the X-band data receiver module. The 1-μsec

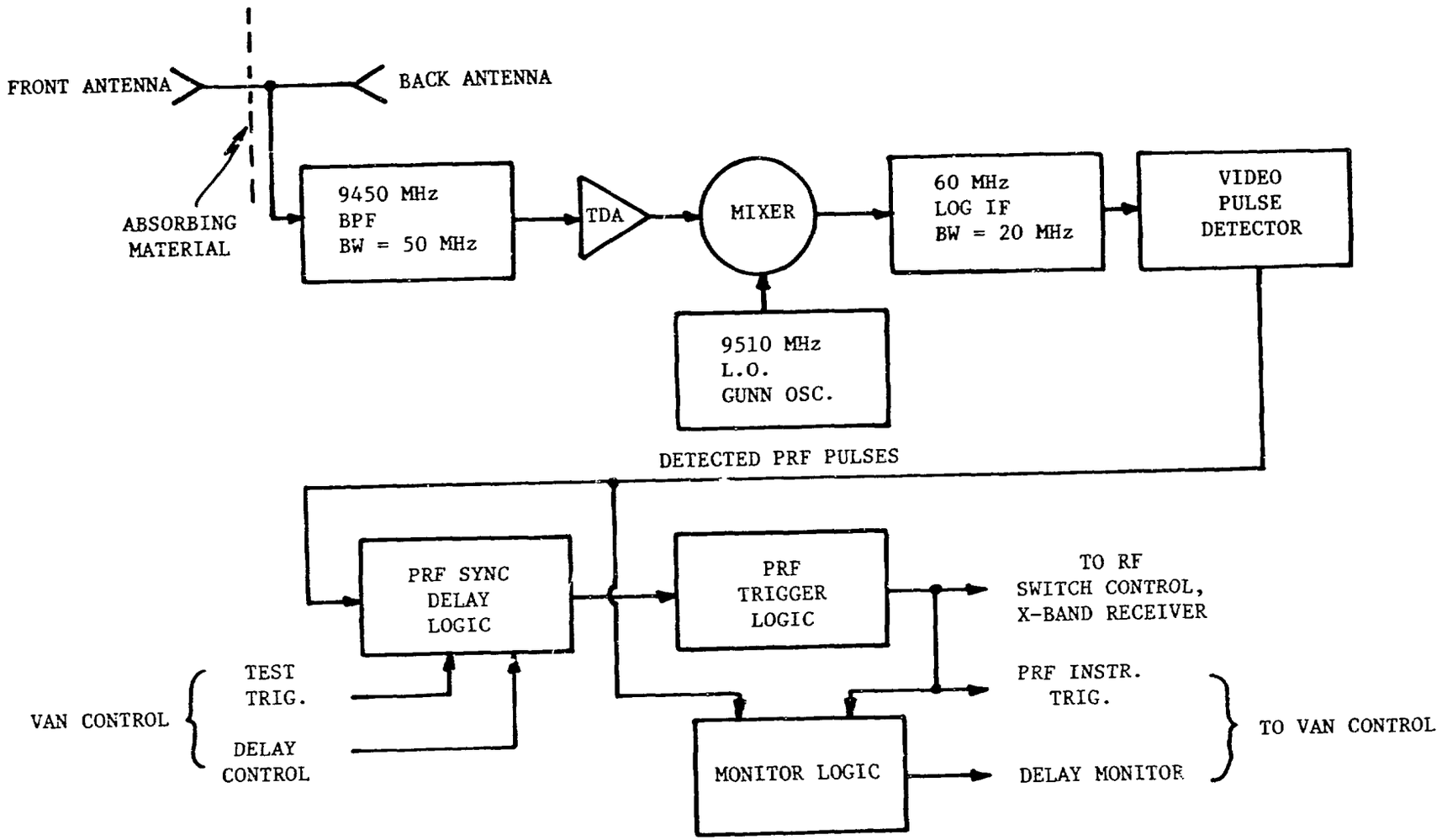

Figure 22. PRF Receiver Block Diagram

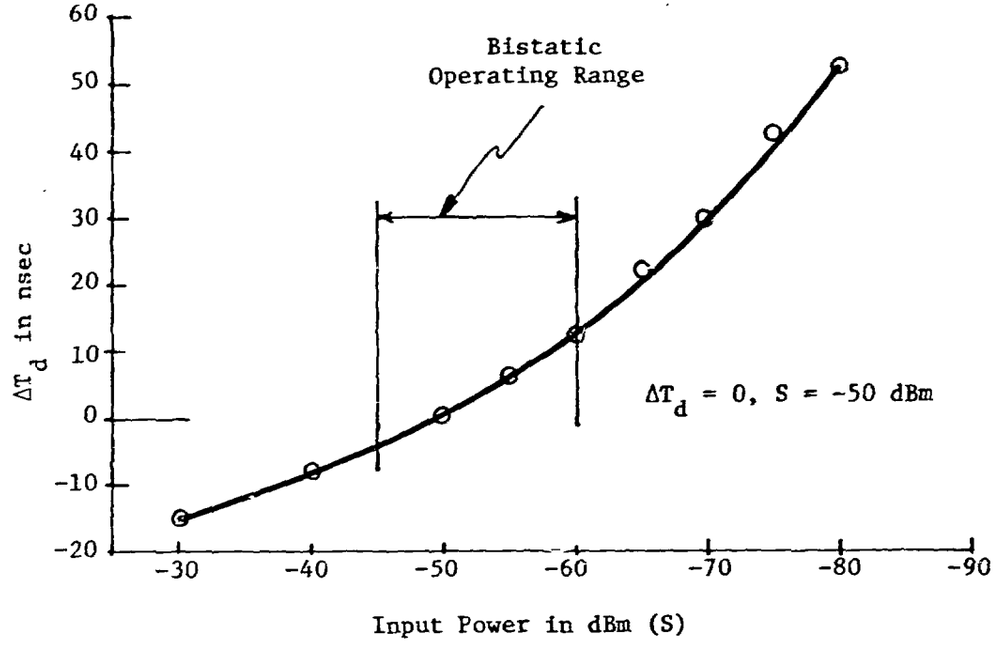

Figure 23. Change in Sync Delay (ΔT_d) vs Input Power (S)

pulse triggers a 5-μsec pulse width generator used to turn all four RF switches on, located in the front ends of the bistatic data receivers. The PRF trigger logic pulse and the detected PRF pulses are ORed in the monitor logic which forms a composite signal to be observed in the van for alignment. The PRF trigger is also directed down a 200-ft coax and used to trigger the PRF instrumentation logic located in the van for recording purposes.

The PRF sync receiver can be triggered with a minimum RF input power level of -83 dBm. Figure 24 is an estimate of the signal strength versus aircraft slant range for the radar parameters used during the bistatic flight tests. It can be seen from this figure that the RF power exceeds the minimum required power of -83 dBm by at least 25 dB. The PRF sync receiver will trigger 90% of the time with an input signal level of -83 dBm. 100% triggering occurs when the signal level is -80 dBm or greater.

The sync delay T_d varies slightly as a function of input power to the PRF sync receiver. Figure 23 shows the change in delay as a function of the input power. The sync delay is aligned with the test PRF trigger. This alignment corresponds to a simulated input power level of -50 dBm and $T_d = 0$. When the signal level is -45 dBm, the sync delay T_d decreases by about 5 nsec, as shown in Figure 23. At a signal level of -60 dBm, the sync delay increases by about 12 nsec. Signal levels between -45 dBm and -60 dBm are the signal strengths to be expected when operating the bistatic system.

5.2 BISTATIC RECEIVER RESPONSE

Figures 25 and 26 are X- and L-band bistatic receiver response curves. All data points plotted in these figures are relative amplitude points with respect to the bistatic transmitter frequencies. A constant input power level was maintained for each frequency change. The response was measured at the output of each sample-hold circuit.

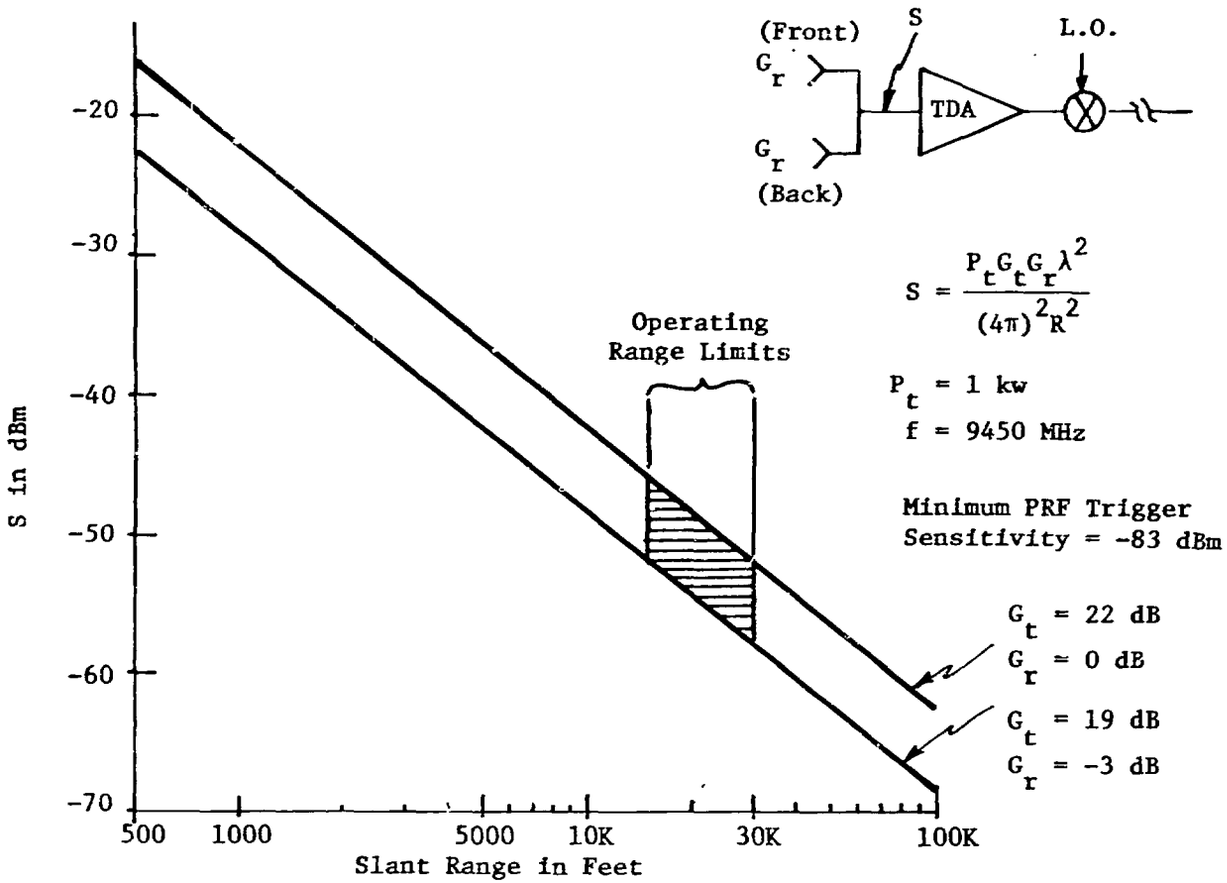

Figure 24. PRF Sync Receiver Input Power vs Range

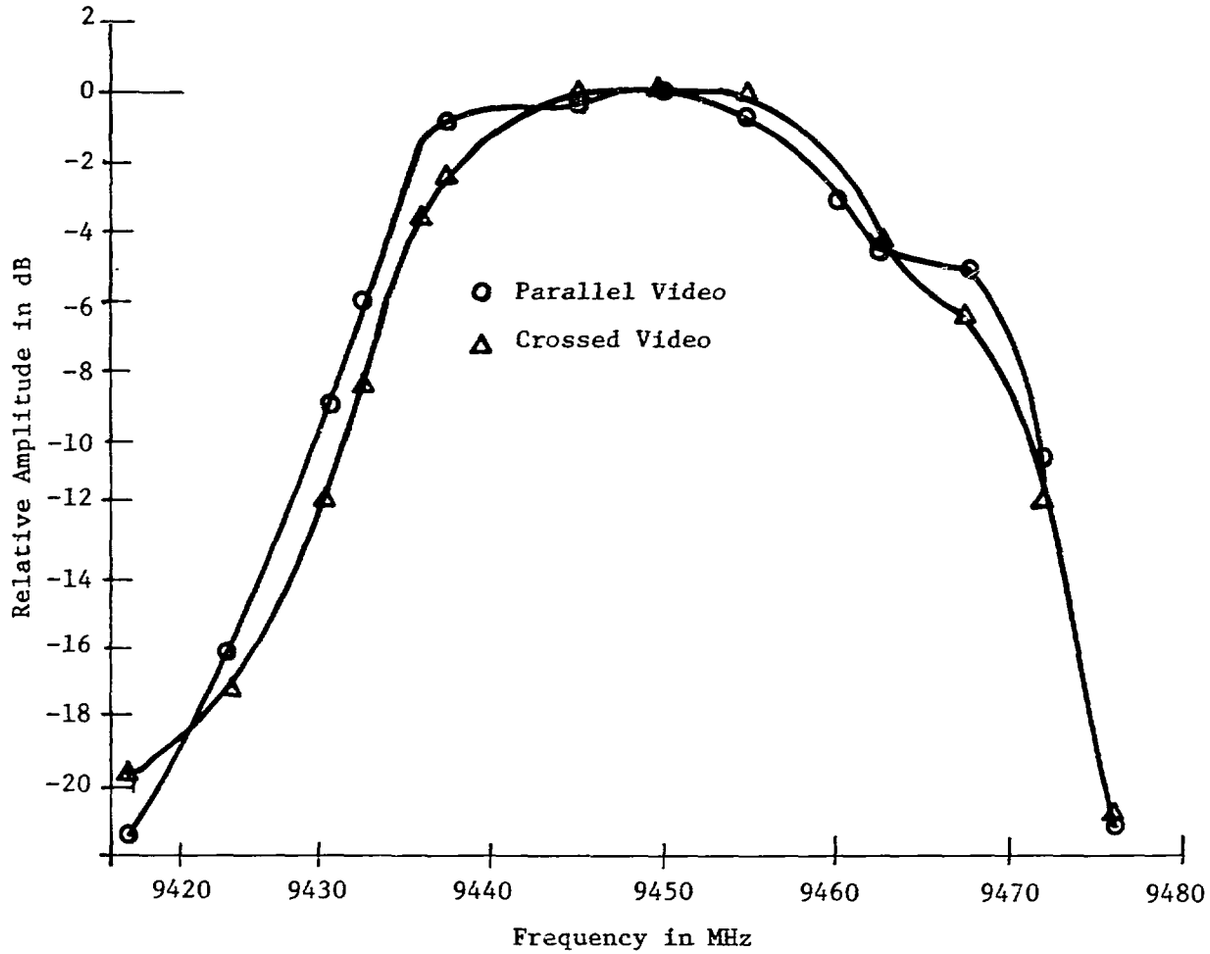

Figure 25. X-Band Receivers Frequency Response,
L.O. Frequency = 9452 MHz

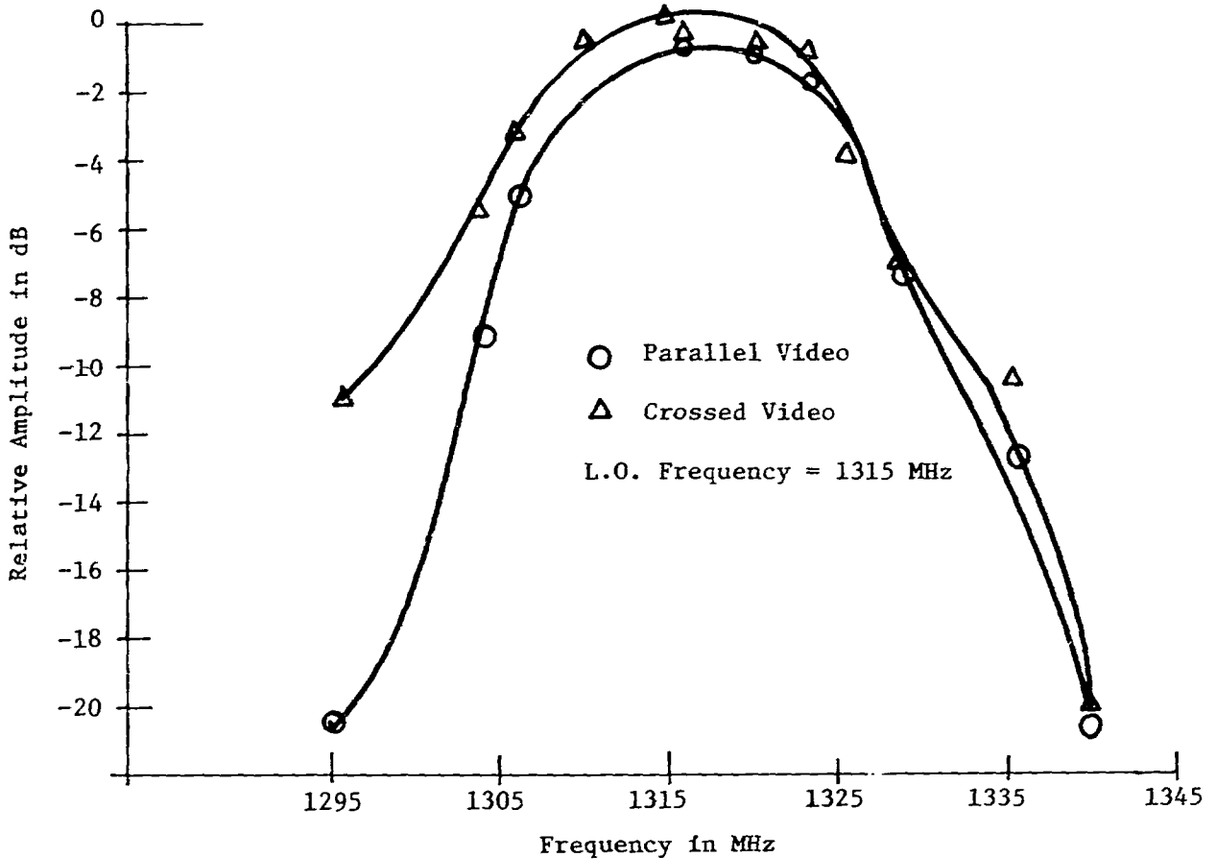

Figure 26. L-Band Receivers Frequency Response

Figure 27 is the X-band bistatic frequency response of the parallel and crossed receivers when the calibrated RF signal is being used. All points are plotted relative to the aircraft transmitter frequency (9452 MHz). Note that, in Figure 27, the parallel receiver response at 9472 MHz is down by 2 dB with respect to the aircraft transmitter frequency. This variation in parallel receiver response has been used in correcting the received powers for the calculation of σ_o. The 9472 MHz frequency is the X-band calibrated frequency offset by 500 Hz, as all received signals are recorded with a 500 Hz offset.

The 9472 MHz calibrated RF signal is 20 MHz greater than the X-band bistatic transmitter frequency. This occurs because the calibrated RF signal is derived from the tracker's L.O. frequency. An L.O. difference frequency of 20 MHz must exist to accommodate the tracker's IF amplifier.

5.3 CIRCUIT BOARD MODIFICATIONS

Board 1: Sync Generator and PRF Instrumentation (77 Mod.)

Board 1 was modified for this series of bistatic tests and replaces the original design, Figure B-9 [1].

Board 1 conditions the received PRF synchronizing pulse via the PRF receiver in order to:

1. Implement a means to monitor the proper delay to trigger the bistatic receivers on,
2. Supply a system PRF trigger for an oscilloscope for alignment and monitoring purposes,
3. Stretch the PRF pulse for recording,
4. Provide a trigger to measure and record the ΔR function.

During test and alignment procedures, a calibration PRF trigger via board 2 is used to perform the above functions. In addition,

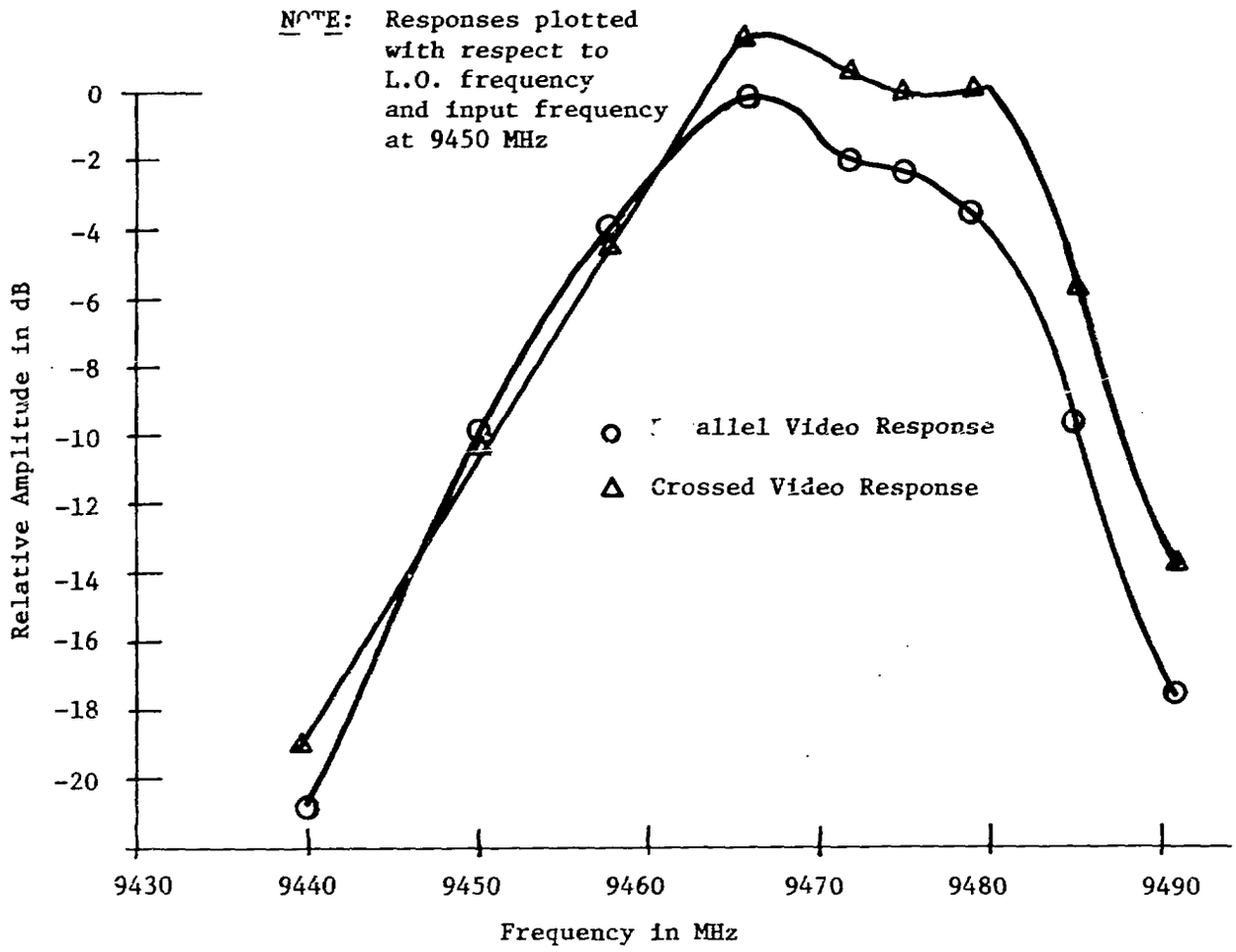

Figure 27. X-Band Receivers Frequency Response,
L.O. Frequency = 9472 MHz

the calibration PRF trigger is used to trigger the Incident Power Receiver via SW-1 and the line driver I-4.

R-1 is the remote sync delay control which is used to adjust the PRF delay necessary to turn on the bistatic receiver located on the crane. TP-1 is used to monitor this function. Logic, timing and driver circuits I5, I6, I7, and I8 function to enable the PRF for recording and to drive LED indicators located on the control panel.

Board 2: Calibration PRF Generator (77 Mod.)

Board 2 contains an internal PRF generator to simulate the received PRF signals when the system is not operating. Its functions include:

1. A basic 4 kHz PRF trigger generator,
2. A sync pulse generator,
3. A 50 nsec pulse width generator to control the RF pulses,
4. Logic to simulate the dual-band PRF alternate pulsing sequence, and
5. A ΔR range delay generator to calibrate the ΔR instrumentation.

R-4 is used to adjust the calibration PRF to match the PRF of the C-46 radar.

R-3 controls the 50 nsec pulse used to trigger the two RF switches in the 3 and 23.5 cm RF calibration paths. The RF pulses simulate the received bistatic data pulses. A range delay control circuit, I-2 and I-3, provides a means to calibrate the ΔR channel. Controls R-1 and R-2 are used to adjust the maximum and minimum range of the calibrated ΔR channel. The maximum range of the ΔR is determined by the last step of the staircase voltage driving I-3.

Logic integration circuits I5 and I6 control alternate sequencing of the dual-band PRF function. One position of the SW-1 control alternates the sequencing of the dual-band PRF function. When SW-1 is in the 1:1 position, a 50 nsec pulse triggers the 3 and 23 cm RF switches at the same time.

When the system control panel switch is in the Operate position, the calibration PRF generator is inhibited. A bias voltage to attenuate the PIN modulators to their maximum (80 dB) via Q1 and Q2 also occurs in the system's operate position. This attenuation function essentially cuts off the RF signal developed from the two 3 cm Gunn oscillators used to simulate the received RF signals from the C-46 aircraft.

Parallel Receivers (77 Mod.)

The X- and L-band receiver circuits were modified to include a retriggering inhibit gate. The retriggering inhibit gate (I-7) prevents more than one sample-hold gate from occurring. Once the leading edge of the bistatic pulse is detected, a sample-hold pulse occurs via the sample delay (I-3). At the same time the sample-hold pulse is generated, a triggering inhibit gate is formed which prevents another sample-hold from occurring. The inhibit gate lasts for about 10 μsec. The purpose of the retriggering inhibit gate is to avoid multi-triggering which may occur from the received bistatic signal. This function assures that the first 50 nsec of the detected video will be sampled.

X-Band Crossed Receiver (77 Mod.)

The X-Band Crossed Receiver circuit board was modified to include 50 Ω line drivers to pulse all four R-F switches located in both the X- and L-band bistatic receivers.

Board 16: X- and L-Band Incident Power Instrumentation (77 Mod.)

The incident power data detected from the Incident Power Receiver is conditioned for recording purposes by this circuit board. A pulse-to-pulse incident power data updating occurs which is recorded on the tape recorder. The incident power is also filtered before being applied to the analog recorder. A tape offset bias control and amplitude controls exist for offsetting voltage adjustments and scaling purposes. See Figure 28.

5.4 INCIDENT POWER RECEIVER

An Incident Power Receiver was implemented to measure the X- and L-band power illuminating the bistatic site. It is capable of measuring the received power on a pulse-to-pulse basis.

Figure 28 is a block diagram of the X-L Incident Power Receiver. The transmitter power radiating from the C46F aircraft is received by the open-ended waveguide antennae. The RF pulses are mixed with the local oscillators generating a 60-MHz IF. The 60-MHz IF is amplified by a log amplifier which generates video output pulses.

The same pulse data acquisition technique is used for the incident power as is used in the bistatic data receivers. That is, the video is split into two paths. One path is used to trigger a sample-hold gate which is delayed long enough to intercept the delayed video at the output of a delay line. The sampled video pulse is held for about 225 μsec before resetting and waits for the next PRF interval to occur. The output of the sample-hold is coupled to the van for signal conditioning before being applied to the tape and analog recorders.

The Incident Power Receiver is also capable of generating X- and L-band calibration pulses. The X-band calibration pulses are also

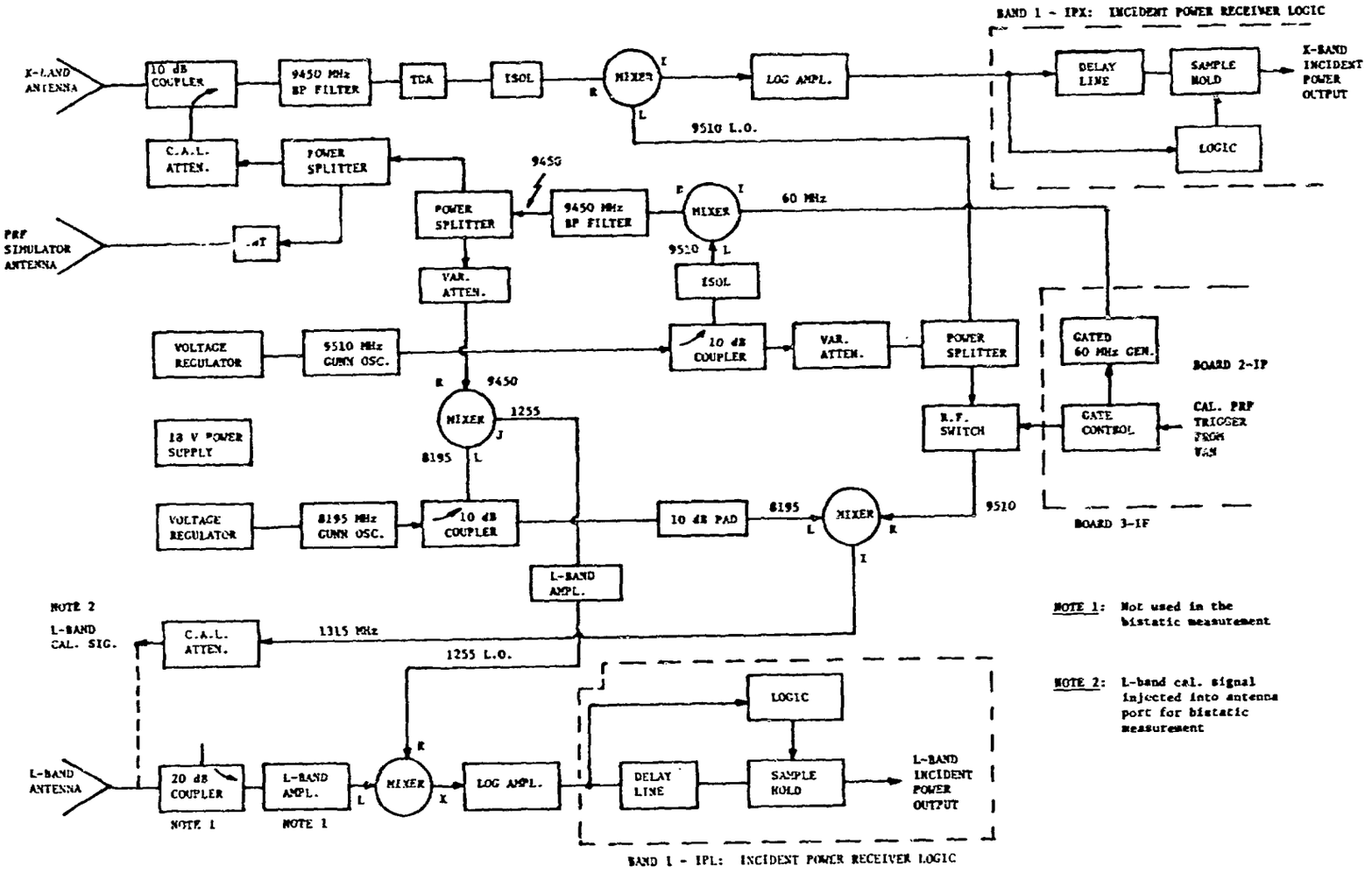

Figure 28. X-L Incident Power Receiver Block Diagram

used to simulate an aircraft transmitter signal to check out the PRF receiver.

Two X-band Gunn oscillators and a 60-MHz generator are used to generate the following:

1. 9512 MHz, X-band L.O. frequency,
2. 1255 MHz, L-band L.O. frequency,
3. 9452 MHz, calibration X-band transmitter frequency, and
4. 1315 MHz, calibration L-band transmitter frequency.

The gate control block shown in Figure 28 is used to generate the same pulse sequences and pulse widths transmitted by the C46F aircraft. The gate control circuits are triggered from the van whenever calibration or PRF receiver checkout procedures are employed.

Frequency response curves are illustrated for both the X-band and L-band receivers in Figures 29 and 30, respectively. The minimum detectable RF powers for the X- and L-band receivers are -65 dBm and -52 dBm, respectively.

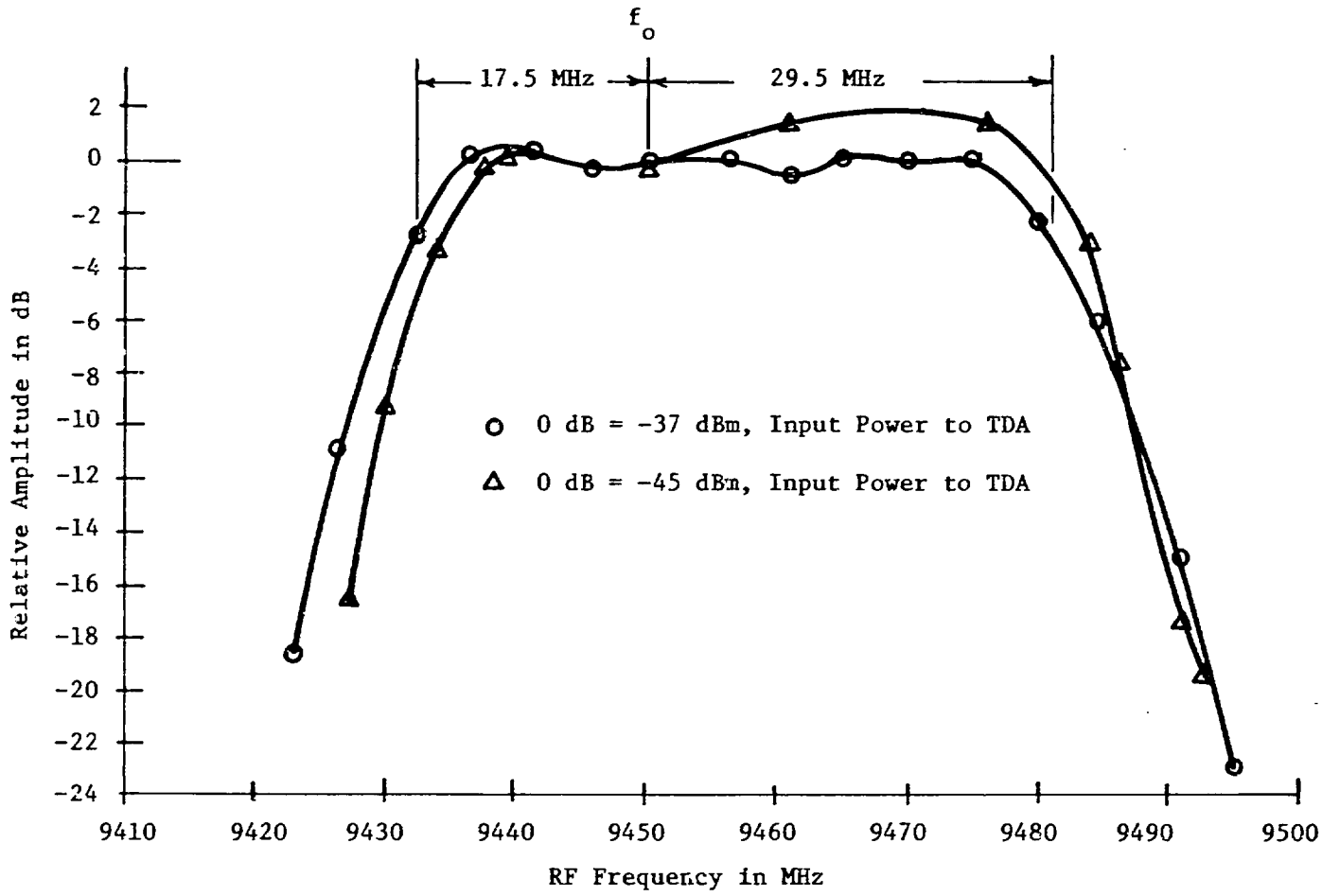

Figure 29. X-Band Incident Power Receiver Frequency Response

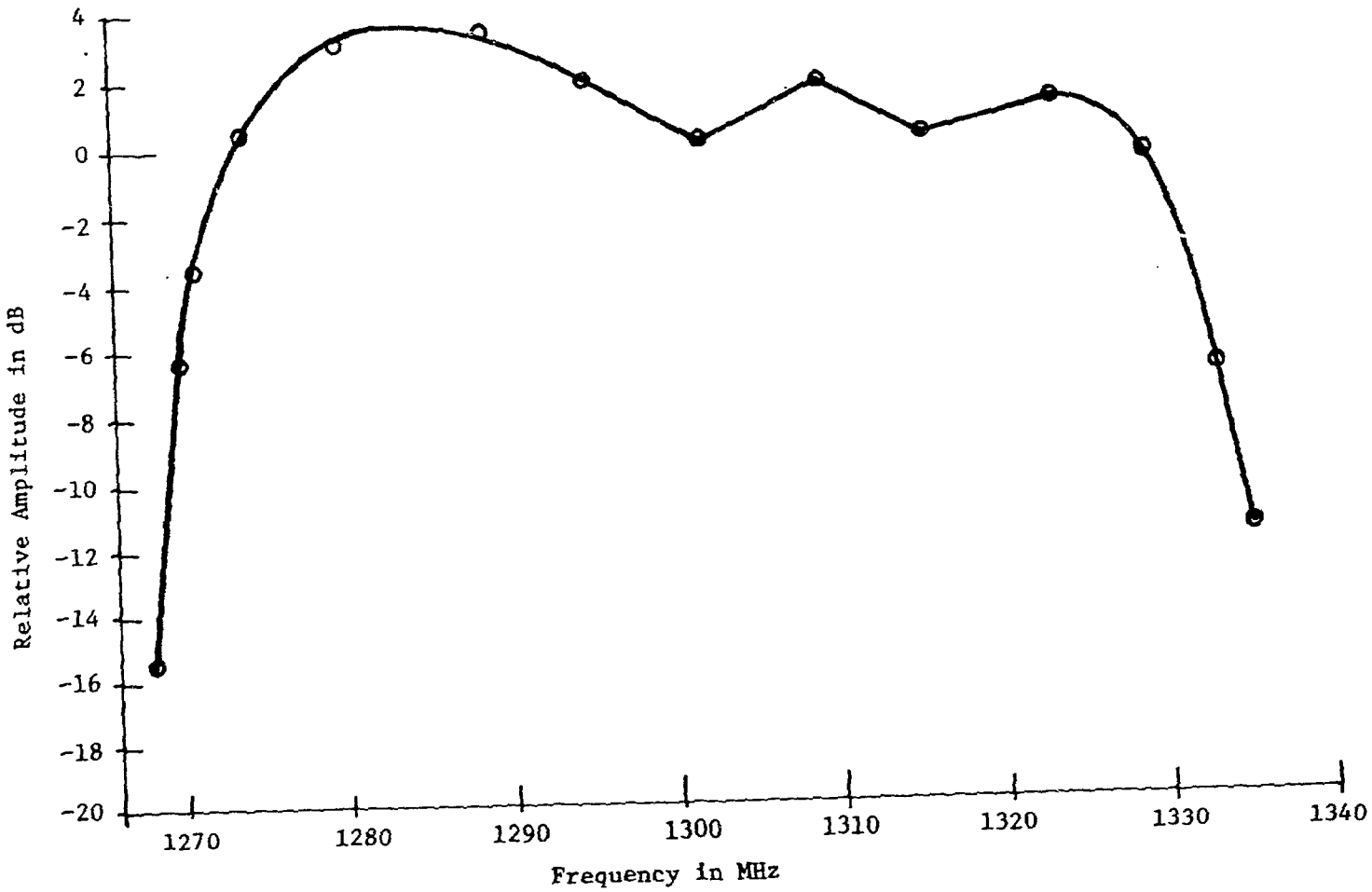

Figure 30. L-Band Incident Power Receiver Frequency Response

6

CONCLUSIONS AND RECOMMENDATIONS

Additional bistatic clutter data have been obtained for a select set of bistatic angles using coherent air-ground instrumentation developed under a previous DARPA-RADC program [1]. Two test sites were proposed for use in this data gathering program to provide bistatic scattering data for rough ground and for a forested area.

The timing of the program was such that the proposed data gathering was delayed until the winter months of 1977-1978, resulting in data being obtained from snow-covered terrain. Although bistatic data from snow-covered terrain is of great interest for bistatic systems performance analysis, difficulties in data gathering operations were encountered due to the cold weather. During the data gathering in February 1978, the extreme cold conditions resulted in an unexpected shift of the 3 cm-band frequency. Effort has been made as a part of the data analysis task and as a part of an ERIM IR&D task to correct these data. However, results obtained indicate that the uncertainty in most of this particular data set is too large for the data to be meaningful. This is discussed in Section 3.

6.1 CONCLUSIONS

The σ_o results obtained from the processed data appear to be in general agreement with other available data . A few comparisons with reported results from appropriate backscatter measurements using horizontal-horizontal polarization have been made. Results reported by Linell [4] show the average X-band σ_o value for forests to be -11 dB for low depression angles. For similar conditions, Hayes, et al. report σ_o values ranging from -14.2 to -3.6 dB. Results of Katz and Spetner [5] report average X-band σ_o values of -16 dB for $\theta_s = 80^o$ (10^o depression angle), $\overline{\sigma}_o = -11$ dB for $\theta_s = 70^o$, and

PRECEDING PAGE BLANK-NOT FILMED

$\overline{\sigma_o}$ = -10 dB for $\theta_s = 60^\circ$. Ament, et al. [6] report median L-band σ_o values of -21 dB for $\theta_s = 80^\circ$, -22 dB for $\theta_s = 70^\circ$, and -17 dB for $\theta_s = 60^\circ$. These values compare favorably with the results obtained from the March 1978 measurements of the orchard - forest scene.

The same location, site II, was used as a test site during this series of measurements and during the 1976 bistatic measurements program. A comparison of σ_o results from 1976 and 1978 obtained at 23.5 cm wavelength at site II show little variation, as shown in Figure 31. This seems to be expected; using values of dielectric constant of the snow measured during the 1978 data gathering, the depth of penetration at 23.5 cm is 2-4 meters. Scattering should then be predominantly from the snow-terrain interface and the roughness of the terrain was the same for both data measurement periods.

The utilization of the incident power receivers to provide a continuous record of illumination power level reduced the overall error in the data reported to ± 4 dB for the March data and for a portion of the February data.

6.2 RECOMMENDATIONS

Although additional quantitative measures of bistatic scattering coefficients have been provided to expand the available data base, it is believed that the requirement for bistatic scattering data still exists. In particular, all data obtained to date from two series of air-tower bistatic measurements were collected using horizontal polarization. Also, the available data base includes a limited range of bistatic angles. In addition, the air-tower coherent instrumentation developed can be used for bistatic system simulation and target measurements as well as clutter measurements.

1. The air-to-tower instrumentation provides coherent bistatic measurement capability; this system should be utilized to obtain additional calibrated clutter and target data to

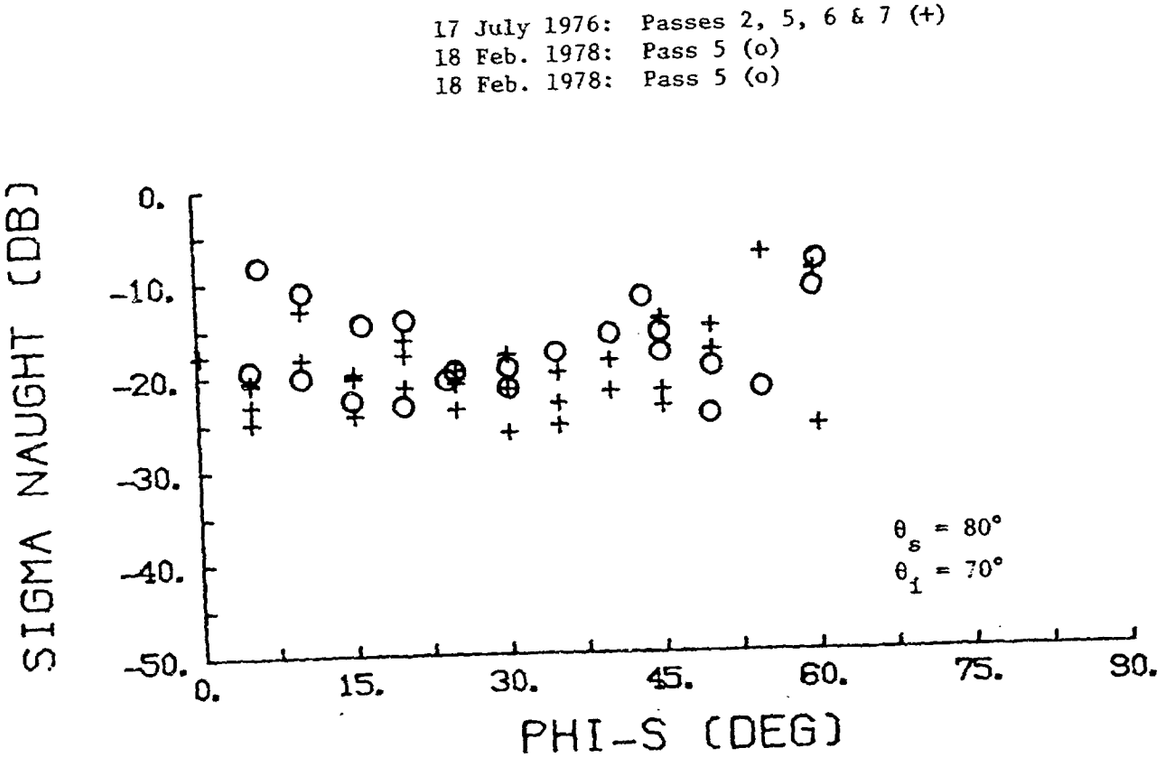

Figure 31. Comparison of 1976 and 1978 σ_o Results for 23 cm Wavelength at Site II

support bistatic system design and to verify results from bistatic system requirements. It is recommended that this capability be utilized, not only for additional clutter measurements, but to obtain target RCS measurements in a controlled bistatic clutter environment. Since the system does operate coherently, Doppler information from moving targets can be obtained to provide information for bistatic MTI system design.

2. A study of the aerial photograph of site III shows the ordered pattern of the orchard; the trees are not randomly distributed as would be expected in a natural forest. Preliminary consideration of the σ_o results obtained indicates that the values are related to the orientation of the look angles and orchard tree pattern. It is recommended that this relationship be studied to determine this relationship. These results would be of great value for application to general clutter modeling.

3. A series of data gathering flights should be conducted, using the existing instrumentation to obtain vertical polarization bistatic scattering coefficients. Since all of the measurement instrumentation and data reduction systems are available, this could be accomplished with a minimum cost. These data gathering flights should be conducted during early Spring and again in late Fall. The test sites should include a rough, bare field under very dry conditions and again, when very wet conditions exist. Water content, in addition to other ground conditions, should be measured.

REFERENCES

1. Bistatic Clutter Data Measurements Program, Final Technical Report, No. RADC-TR-77-389, ERIM, Ann Arbor, Nov 77 (A049037)

2. W. Peake and T. Oliver, The Response of Terrestrial Surfaces at Microwave Frequencies, Report No. AFAL-TR-70-301, Electroscience Laboratory, Ohio State University, Columbus, May 1971.

3. S. Evans, "Dielectric Properties of Ice and Snow: A Review," J. Glaciology, Vol. 5, 1965, pp. 773-792.

4. T. Linell, "An Experimental Investigation of the Amplitude Distribution of Radar Terrain Returns," 6th Conference of the Swedish National Committee on Scientific Radio, March 13, 1963.

5. I. Katz and L. Spetner, "Polarization and Depression Angle Dependence of Radar Terrain Return," Journal of Res. NBS, Vol. 64D, No. 5, September 1960.

6. W. Ament, F. MacDonald, and R. Shewbridge, "Radar Terrain Reflections for Several Polarizations and Frequencies," Trans. 1959 Symposium on Radar Return, Part 2, Univ. of New Mexico, Albuquerque, May 1959.

APPENDIX A
MEASUREMENT DATA

This appendix contains Figures A-1 through A-146, all of which provide plots of cross section σ_o vs. azimuth angle φ_s. In each figure, the upper graph displays all the data for the particular combination of parameters; in the lower graph, the data are averaged over 5^o intervals. Pertinent measurement parameters include frequency, polarization, as well as incidence and scattering angles (θ_i and θ_s, respectively). The frequencies used were L-band (1315 MHz) and X-band (9452 MHz). The transmitted polarization was horizontal while the received polarizations were parallel (horizontal) and cross (vertical). Values for θ_i were 60, 65, 70, and 80^o; for θ_s, they were 60, 70, 80, and 84^o.

PRECEDING PAGE BLANK-NOT FILMED

L-BAND PARALLEL T3/17/78#5

CUTOFF= 0.

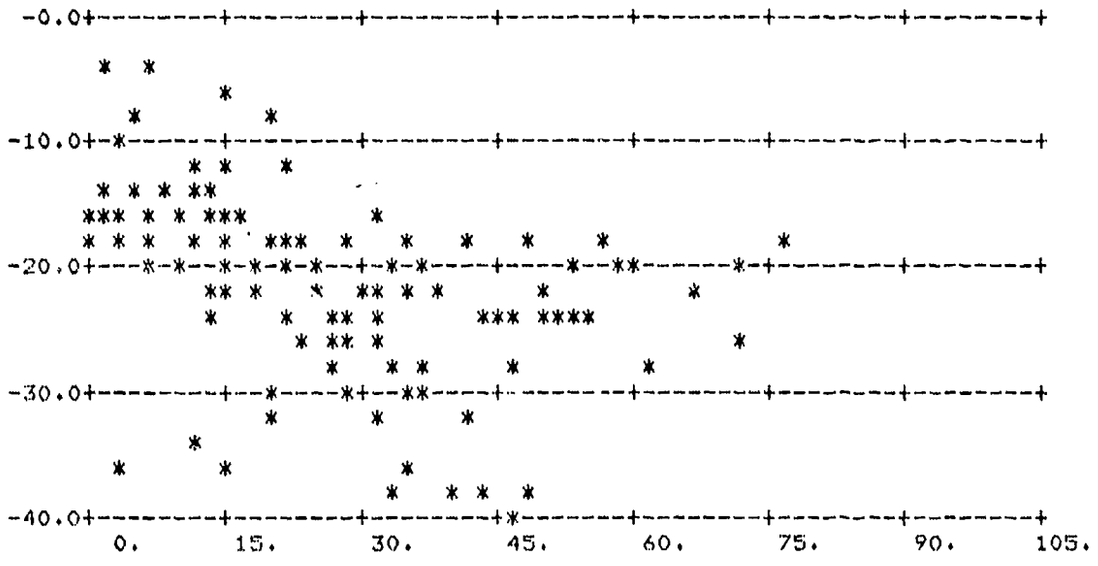

FIGURE A-1. σ_o vs ϕ_s; $\theta_s = 60°$, $\theta_i = 60°$

(Above: All Data; Below: Averages Over 5° Intervals)

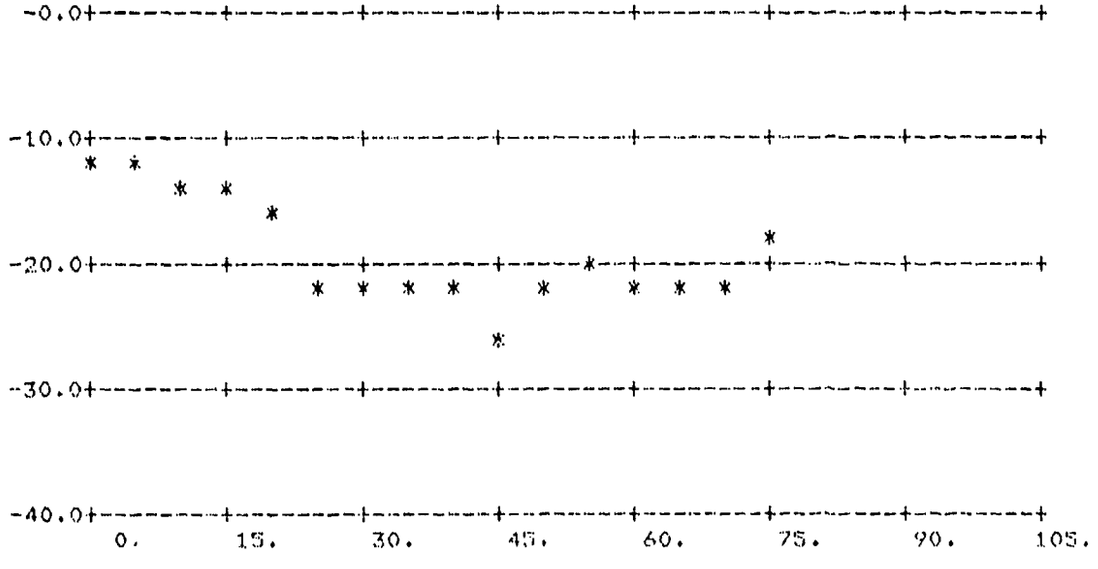

PRECEDING PAGE BLANK-NOT FILMED

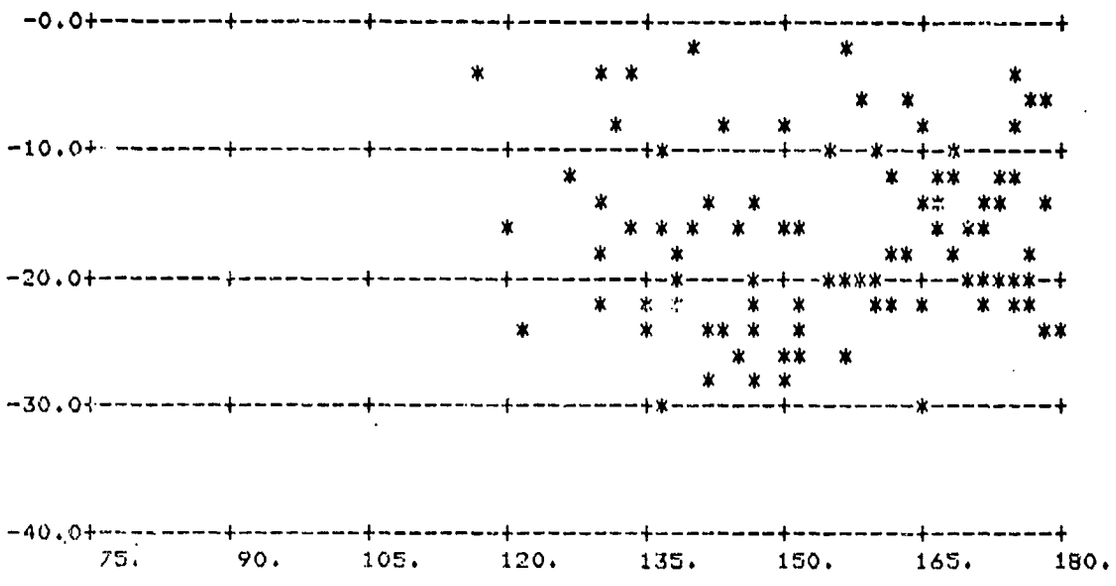

FIGURE A-2. σ_o vs ϕ_s; $\theta_s = 60°$, $\theta_i = 60°$

(Above: All Data; Below: Averages Over 5° Intervals)

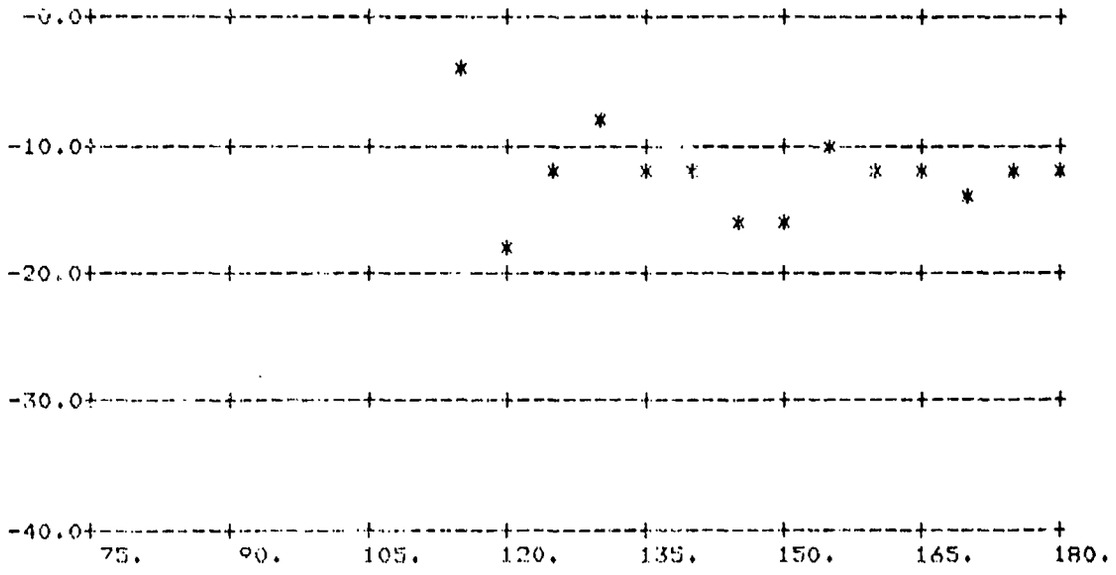

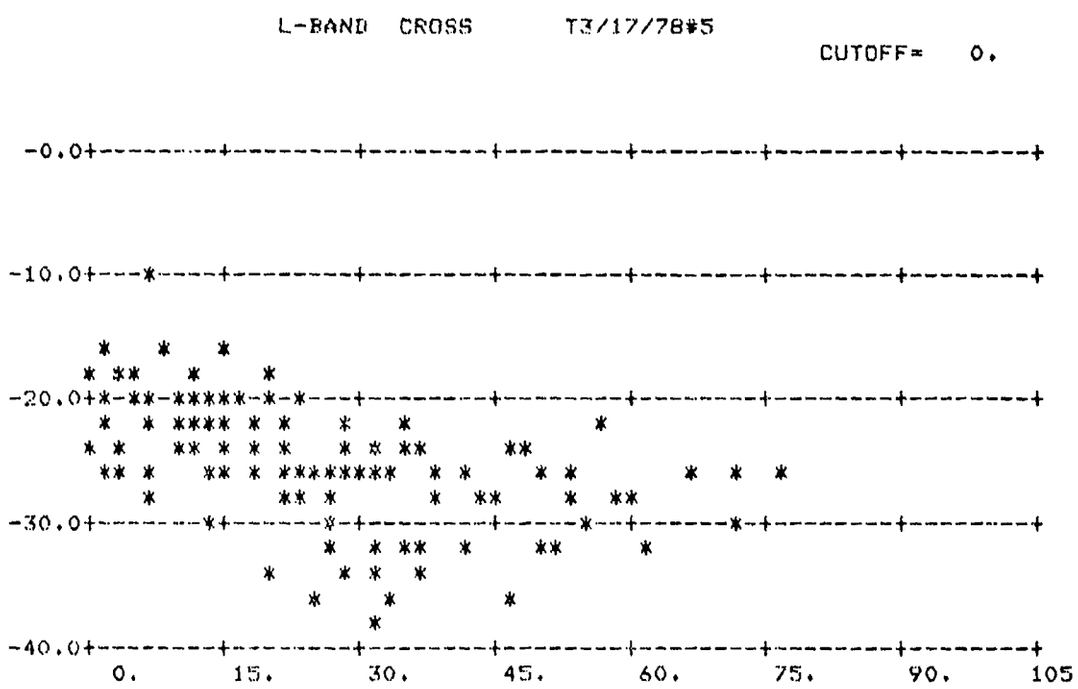

FIGURE A-3. σ_o vs ϕ_s; $\theta_s = 60°$, $\theta_i = 60°$

(Above: All Data; Below: Averages Over 5° Intervals)

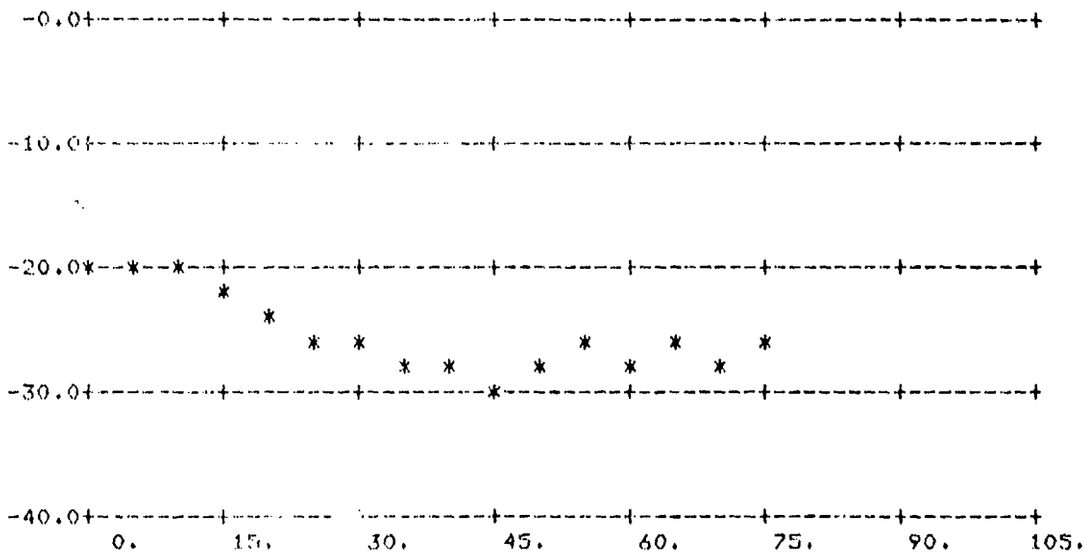

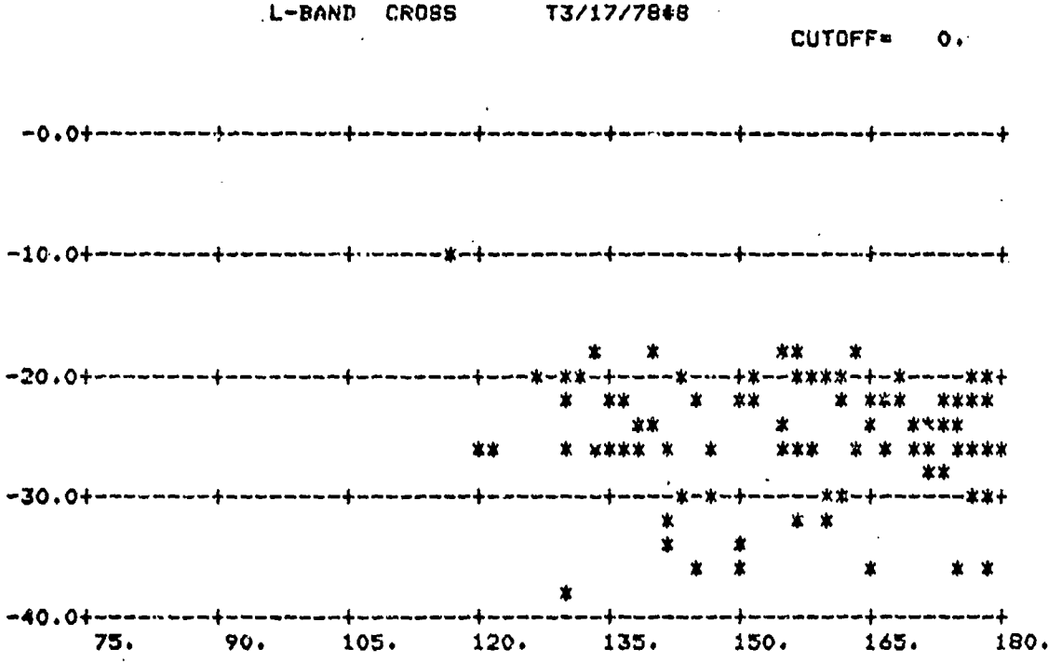

FIGURE A-4. σ_o vs ϕ_s; $\theta_s = 60°$, $\theta_i = 60°$

(Above: All Data; Below: Averages Over 3° Intervals)

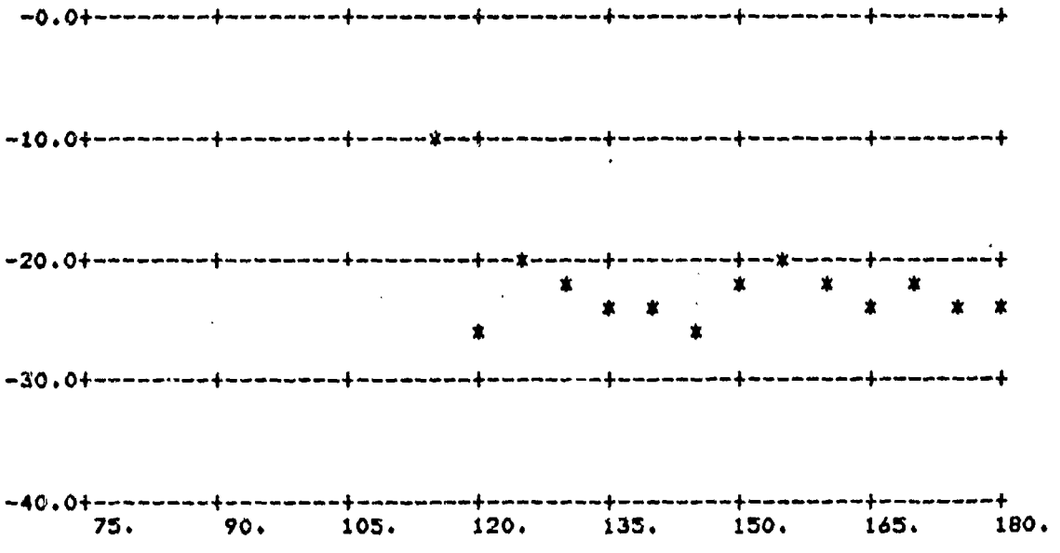

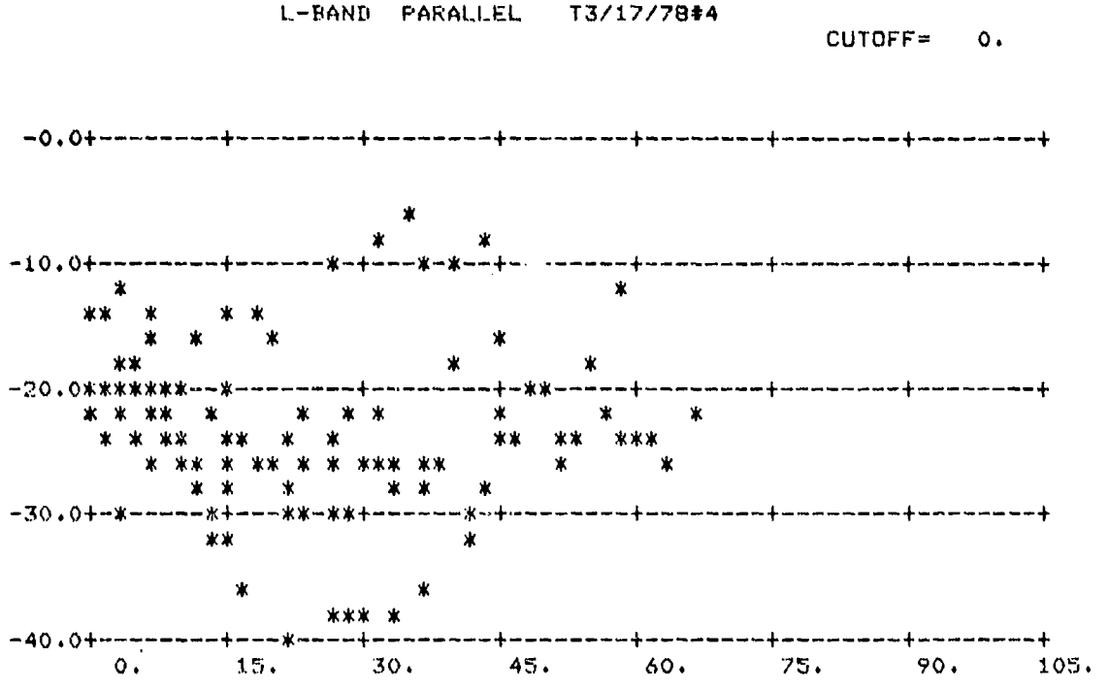

FIGURE A-5. σ_o vs ϕ_s; $\theta_s = 70°$, $\theta_i = 60°$

(Above: All Data; Below: Averages Over 5° Intervals)

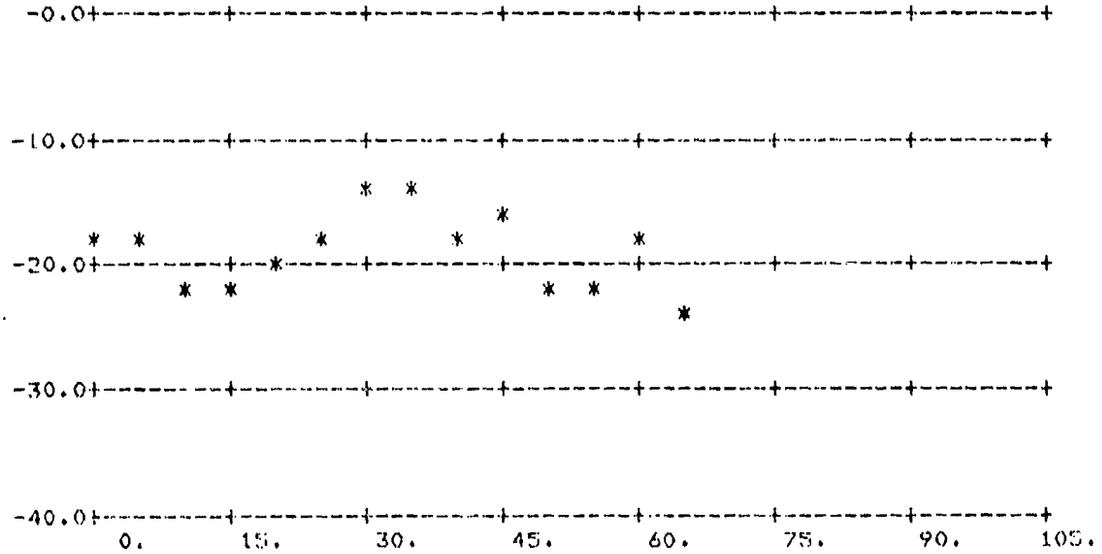

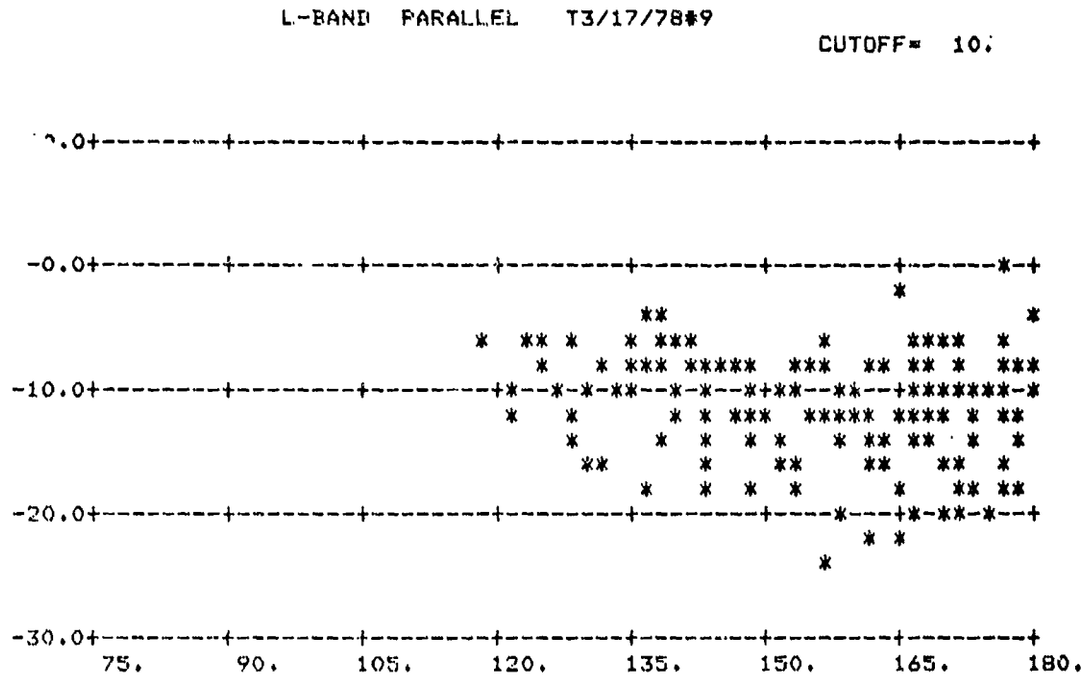

FIGURE A-6. σ_o vs ϕ_s; $\theta_s = 70°$, $\theta_i = 60°$

(Above: All Data; Below: Averages Over 5° Intervals)

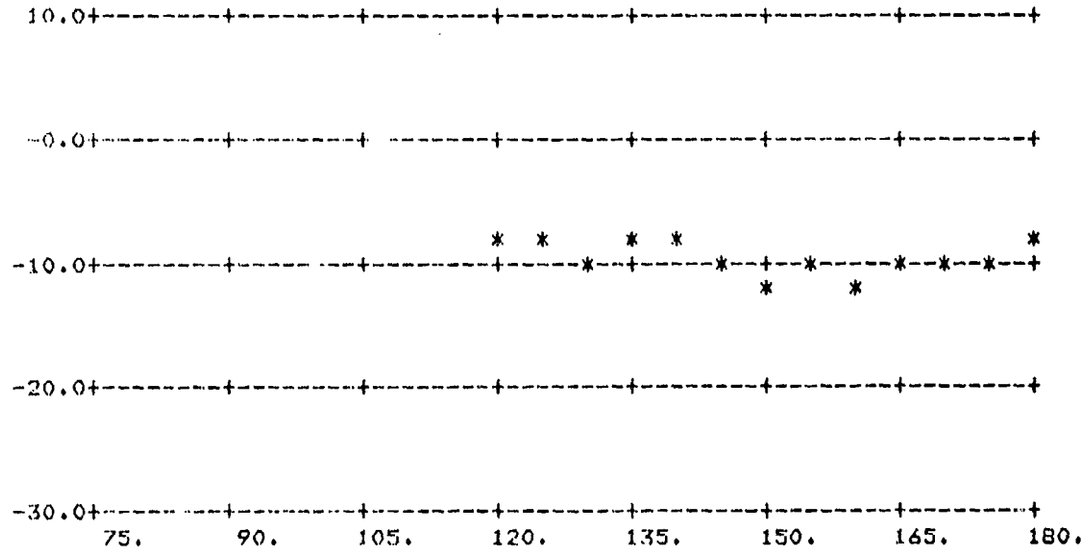

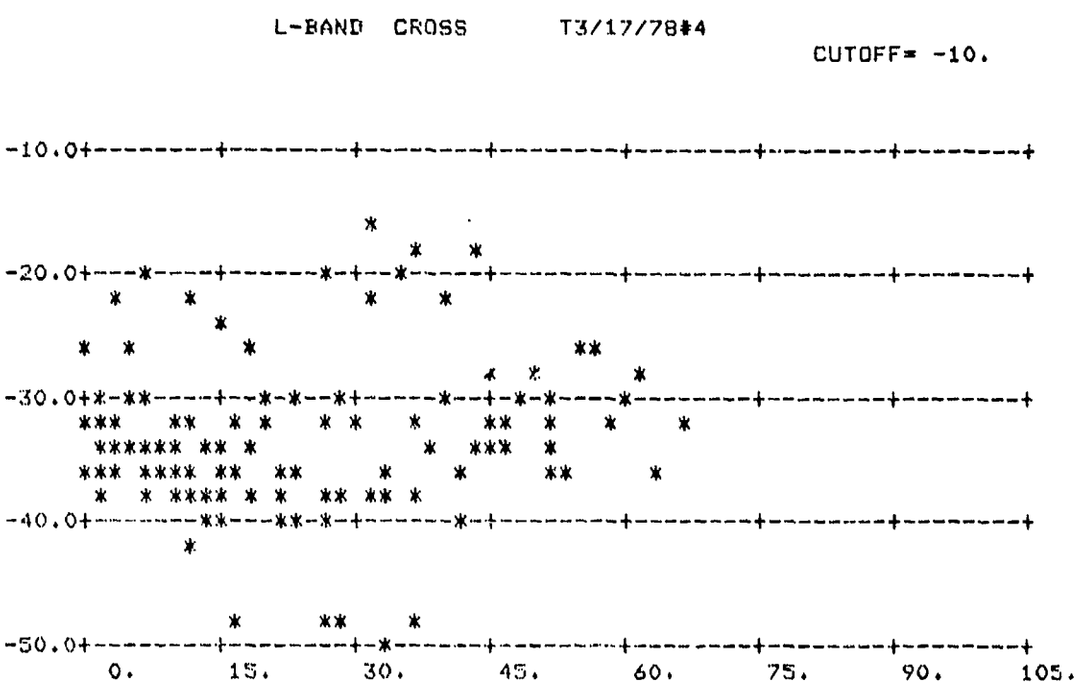

FIGURE A-7. σ_o vs ϕ_s; $\theta_s = 70°$, $\theta_i = 60°$

(Above: All Data; Below: Averages Over 5° Intervals)

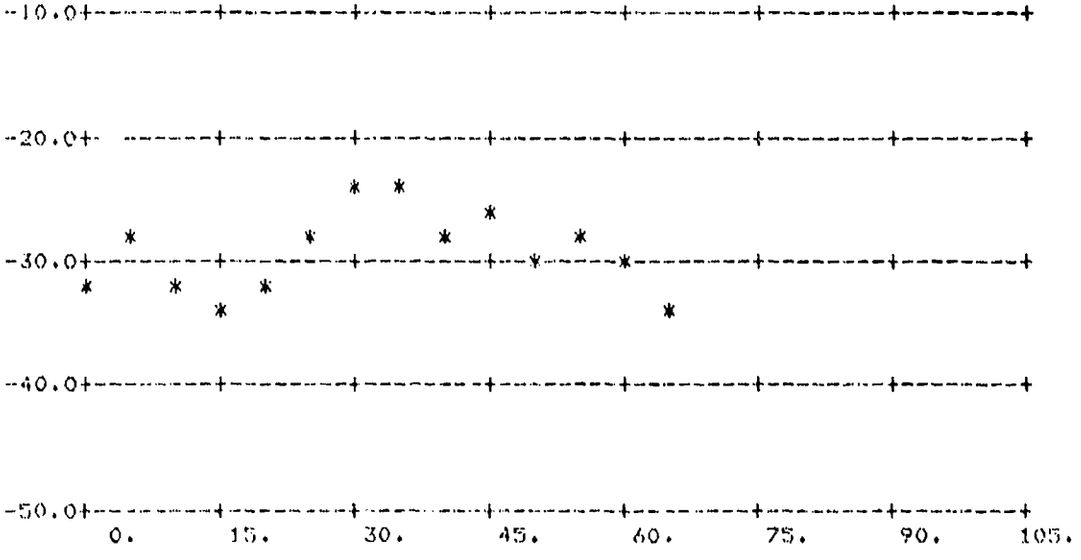

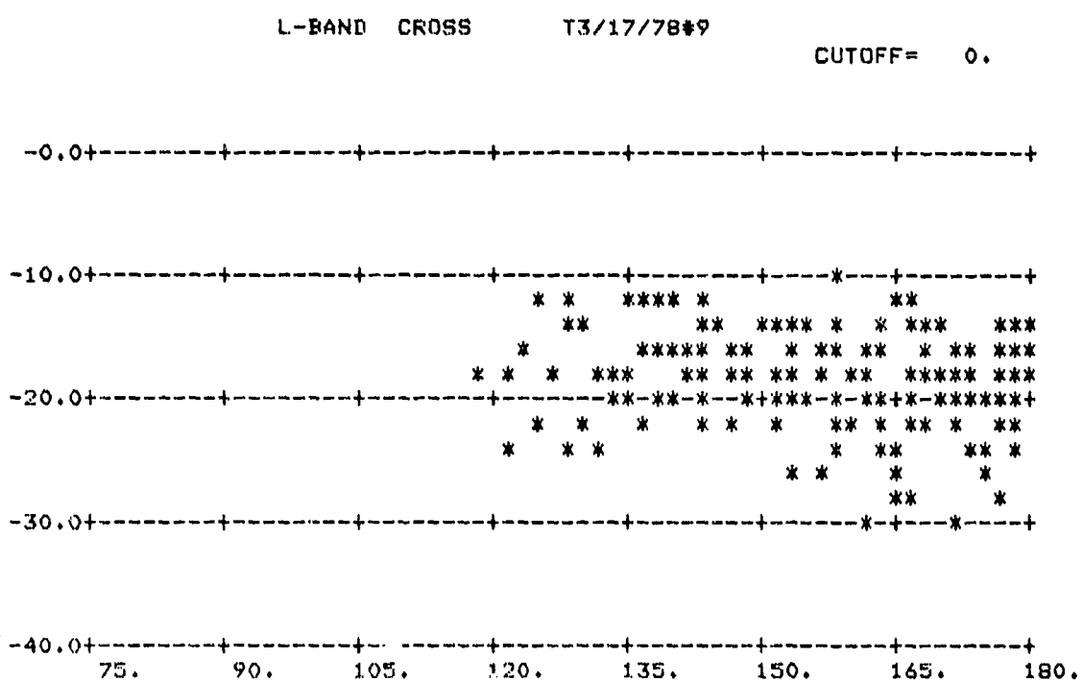

FIGURE A-8. σ_o vs ϕ_s; $\vartheta_s = 70°$, $\theta_i = 60°$

(Above: All Data; Below: Averages Over 5° Intervals)

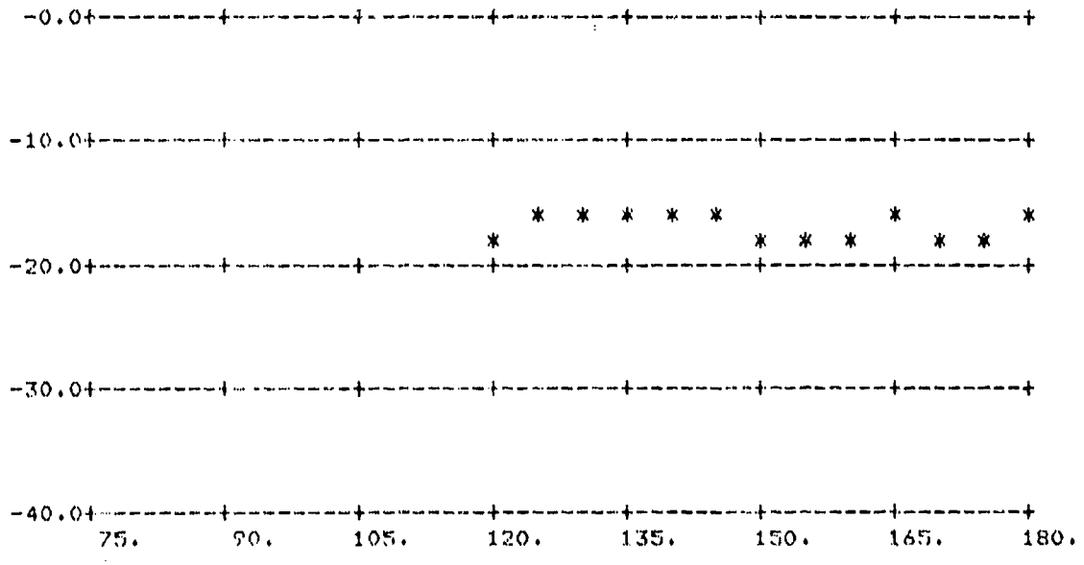

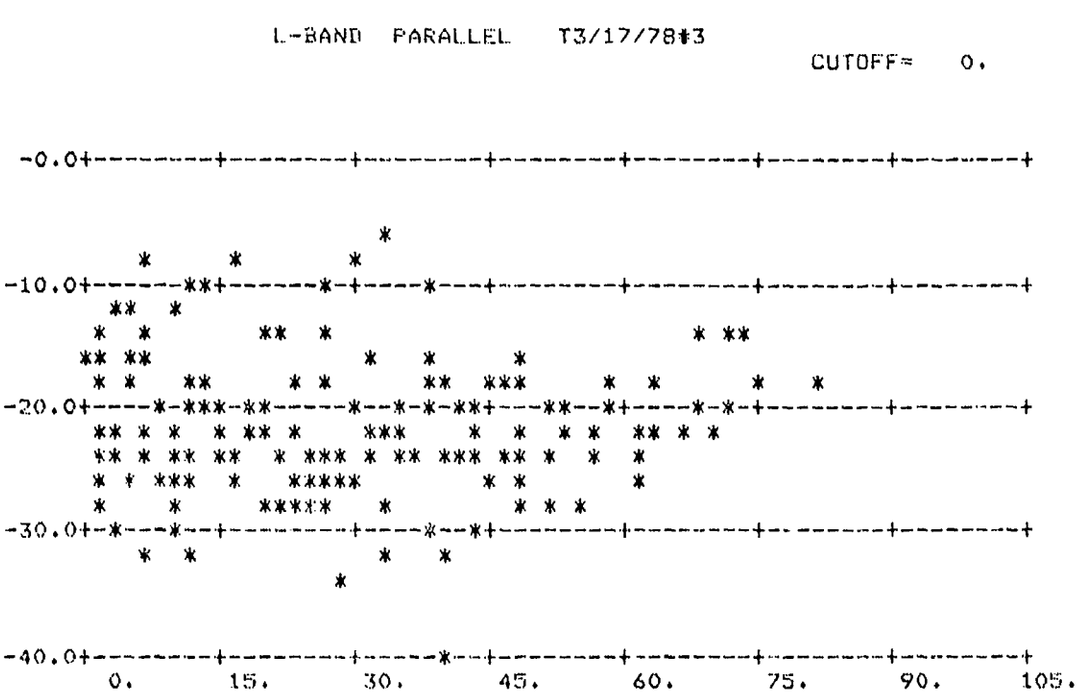

FIGURE A-9. σ_o vs ϕ_s; $\theta_s = 80°$, $\theta_i = 60°$

(Above: All Data; Below: Averages Over 5° Intervals)

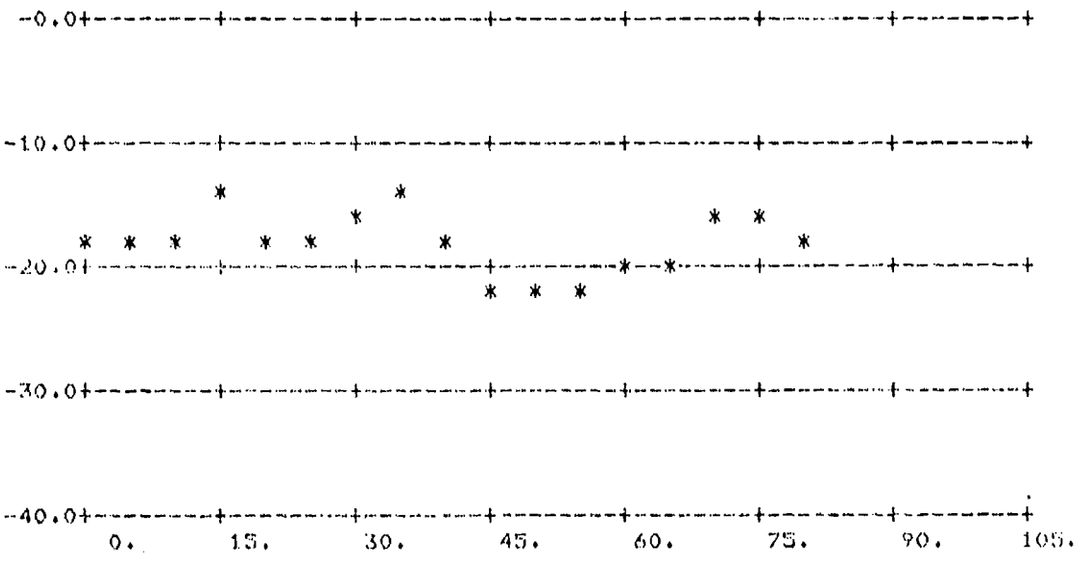

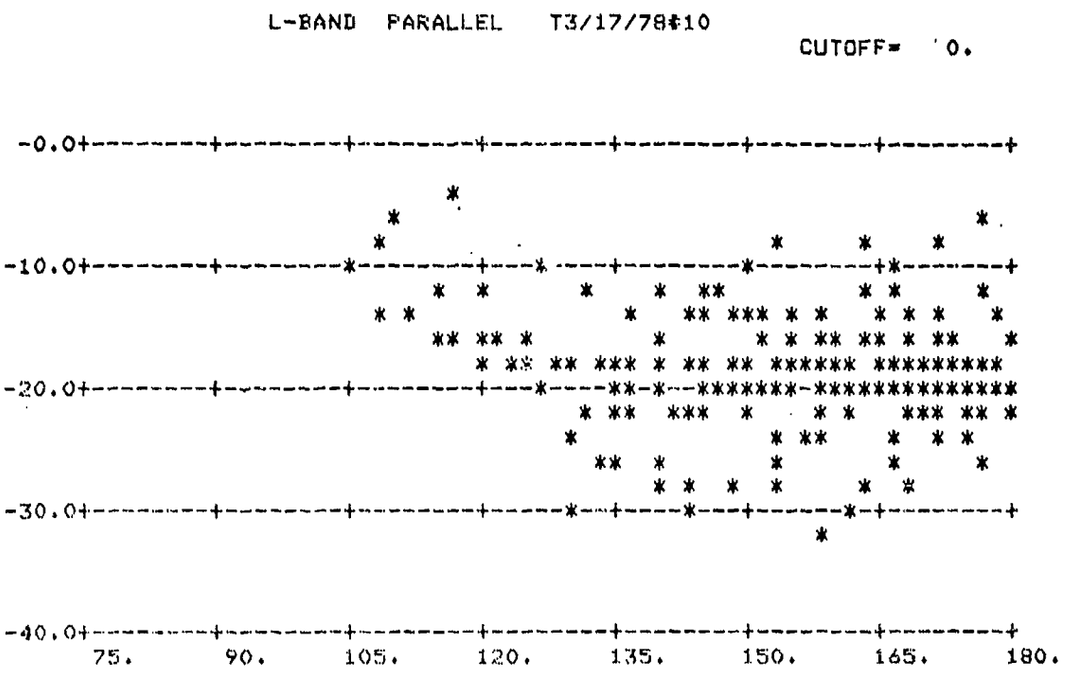

FIGURE A-10. σ_o vs ϕ_s; $\theta_s = 80°$, $\theta_i = 60°$

(Above: All Data; Below: Averages Over 5° Intervals)

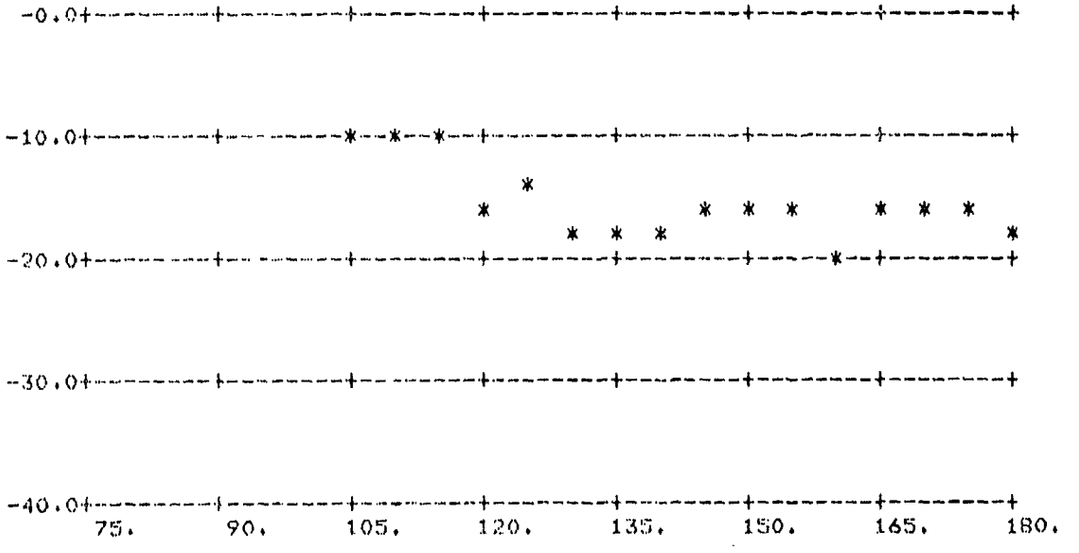

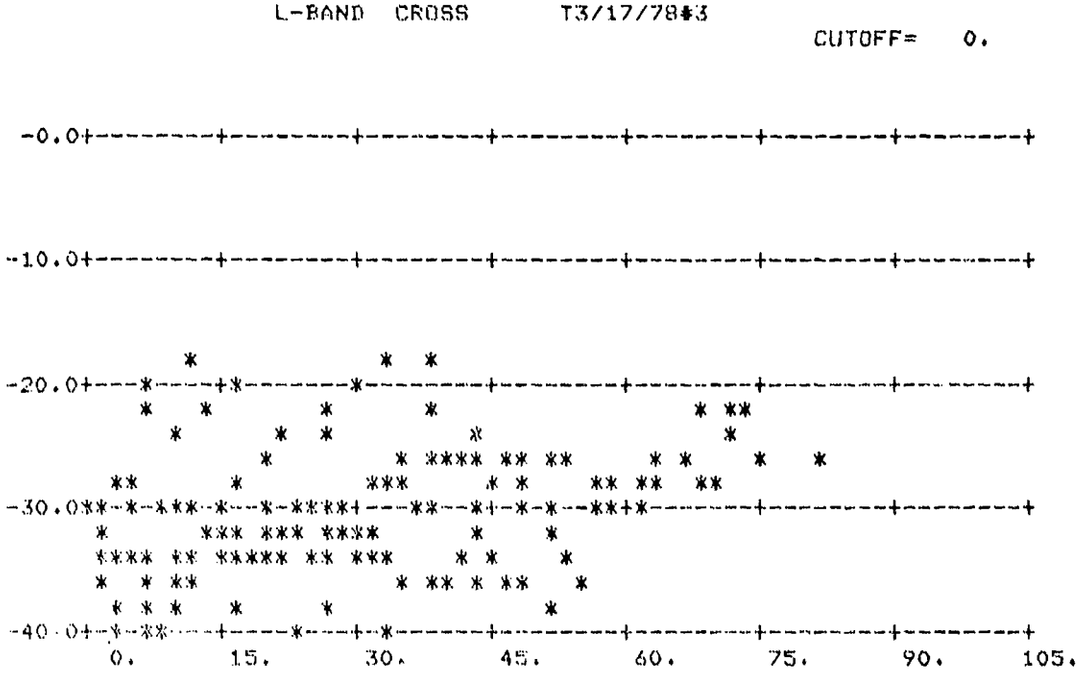

FIGURE A-11. σ_o vs ϕ_s; $\theta_s = 80°$, $\theta_i = 60°$

(Above: All Data; Below: Averages Over 5° Intervals)

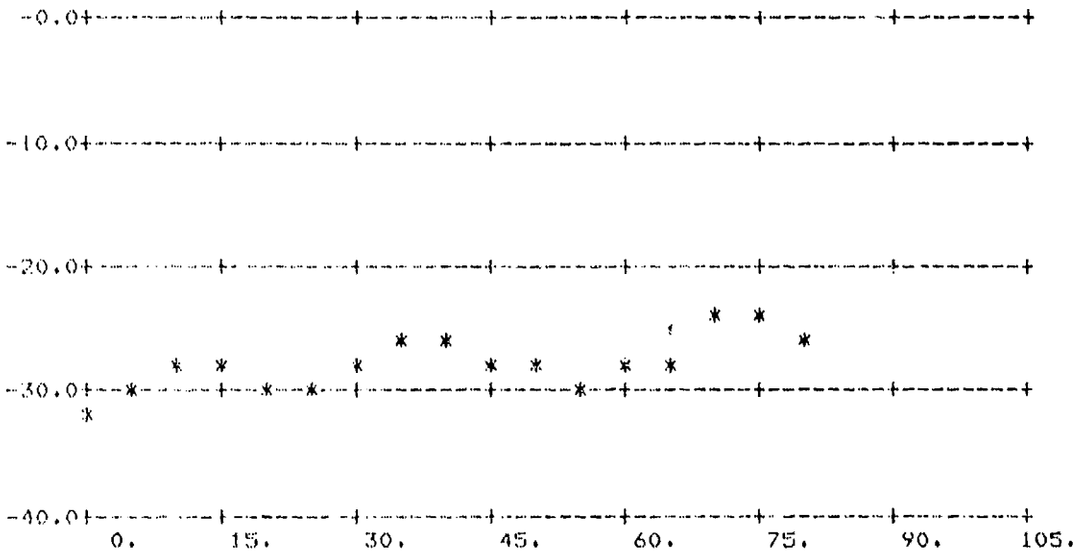

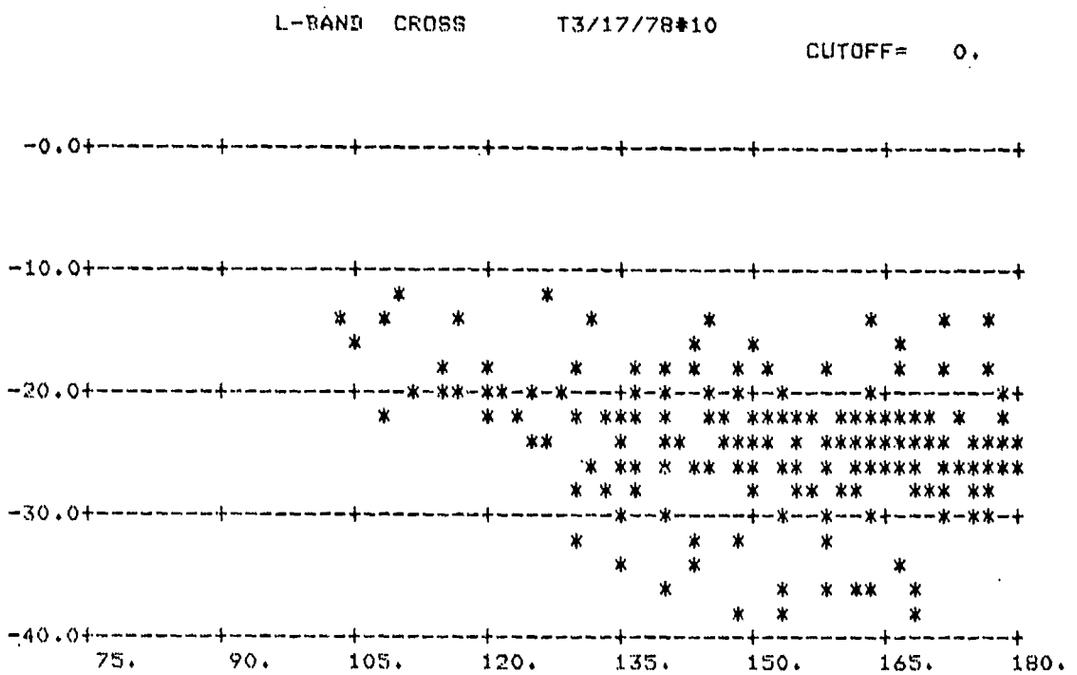

FIGURE A-12. σ_o vs ϕ_s; $\theta_s = 80°$, $\theta_i = 60°$

(Above: All Data; Below: Averages Over 5° Intervals)

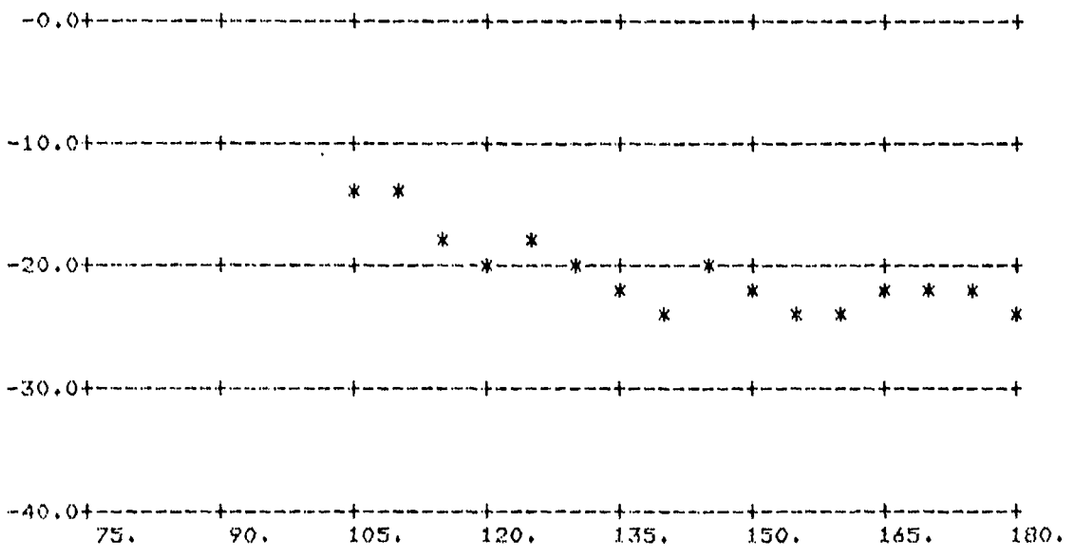

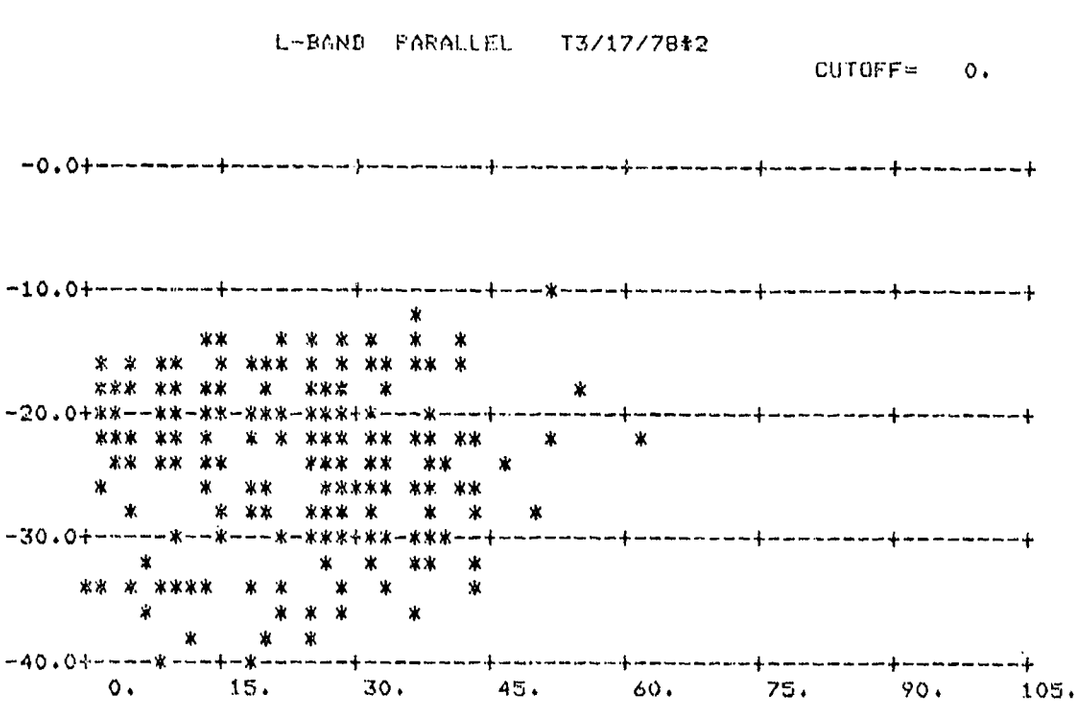

FIGURE A-13. σ_o vs ϕ_s; $\theta_s = 84°$, $\theta_i = 60°$

(Above: All Data; Below: Averages Over 5° Intervals)

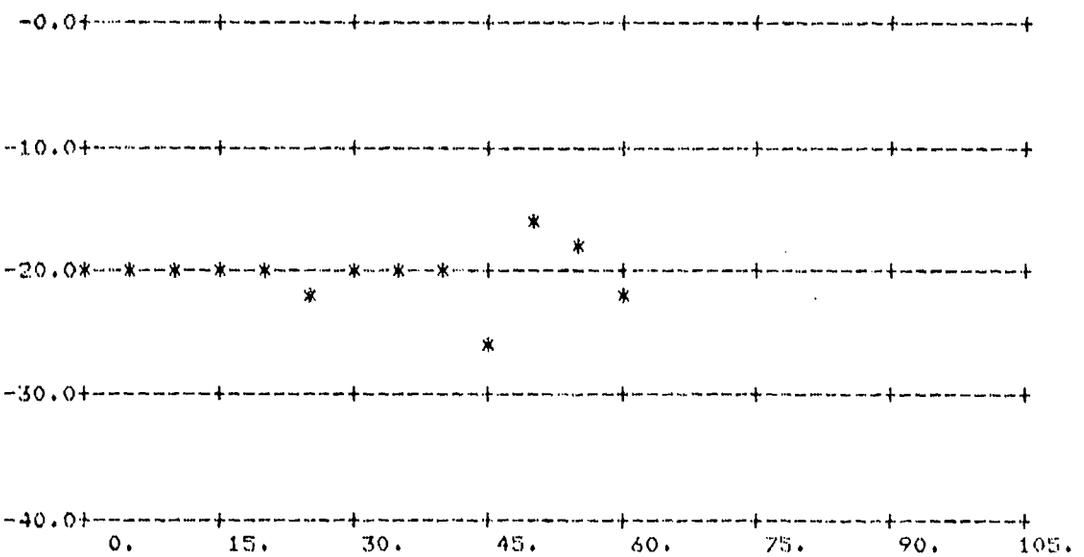

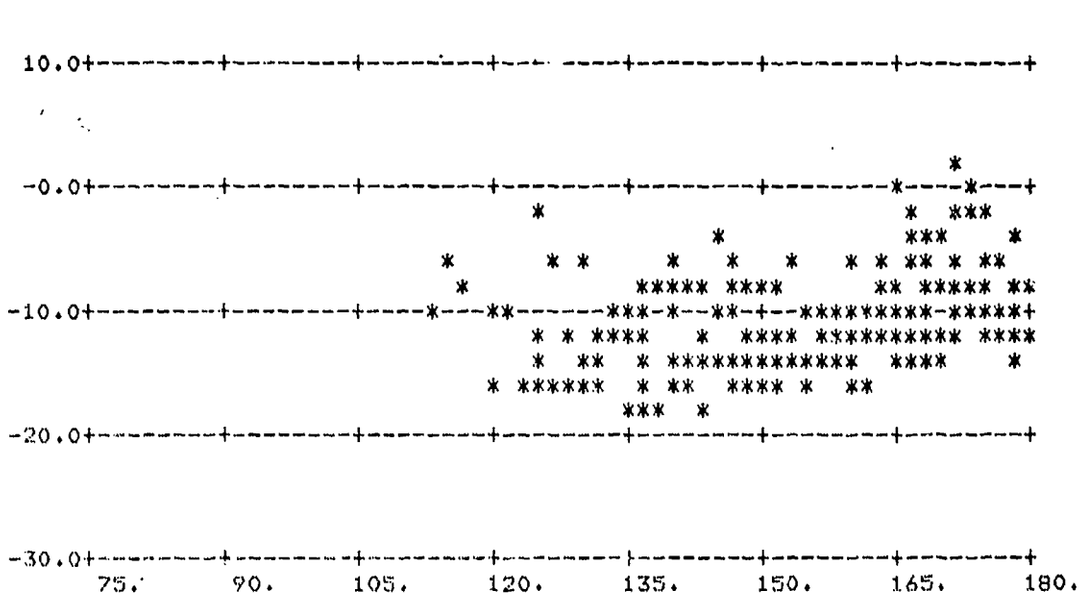

FIGURE A-14. σ_o vs ϕ_s; $\theta_s = 84°$, $\theta_i = 60°$

(Above: All Data; Below: Averages Over 5° Intervals)

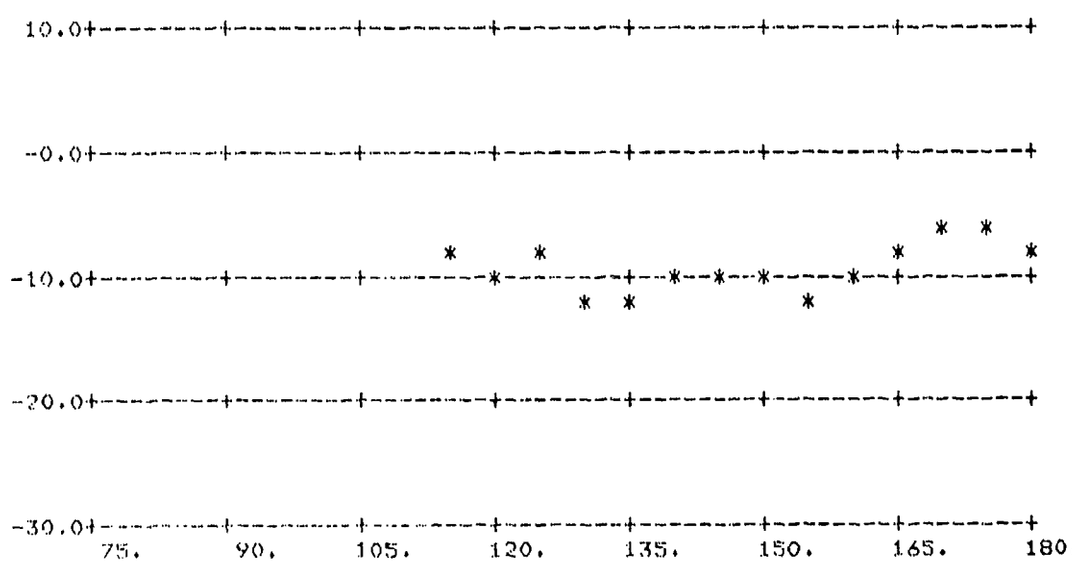

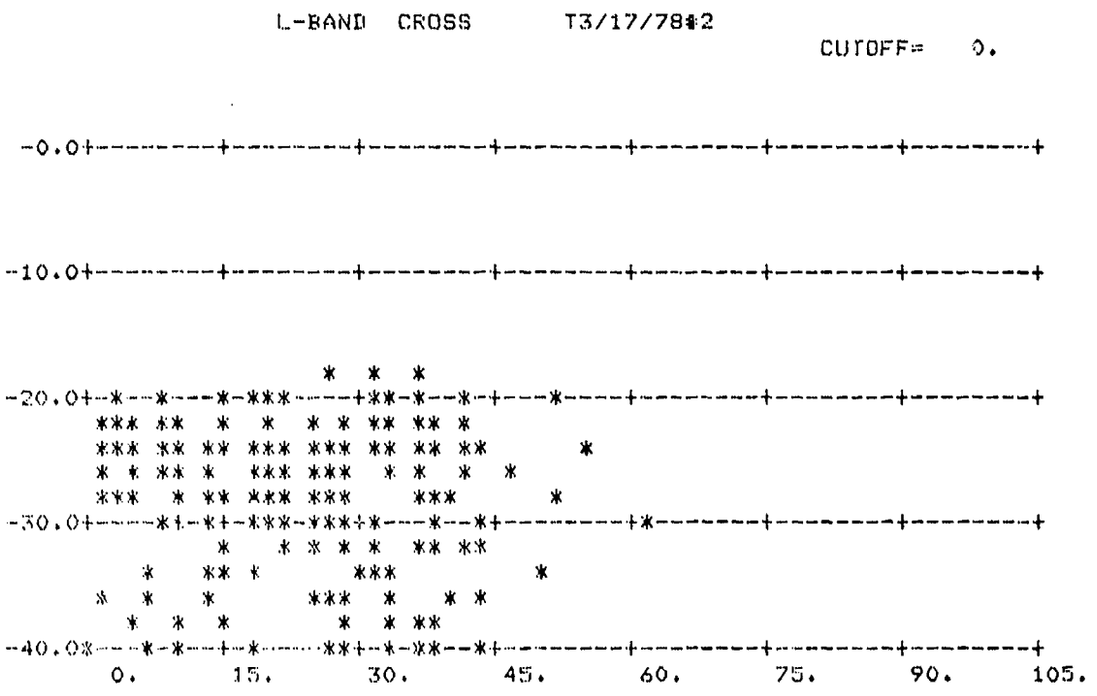

FIGURE A-15. σ_o vs ϕ_s; $\theta_s = 84°$, $\theta_i = 60°$

(Above: All Data; Below: Averages Over 5° Intervals)

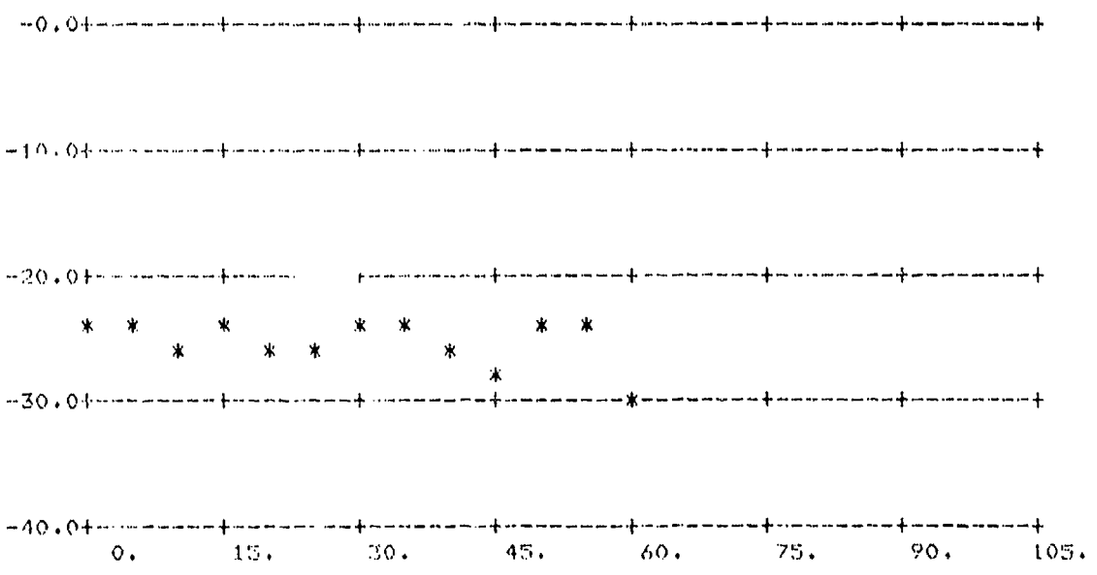

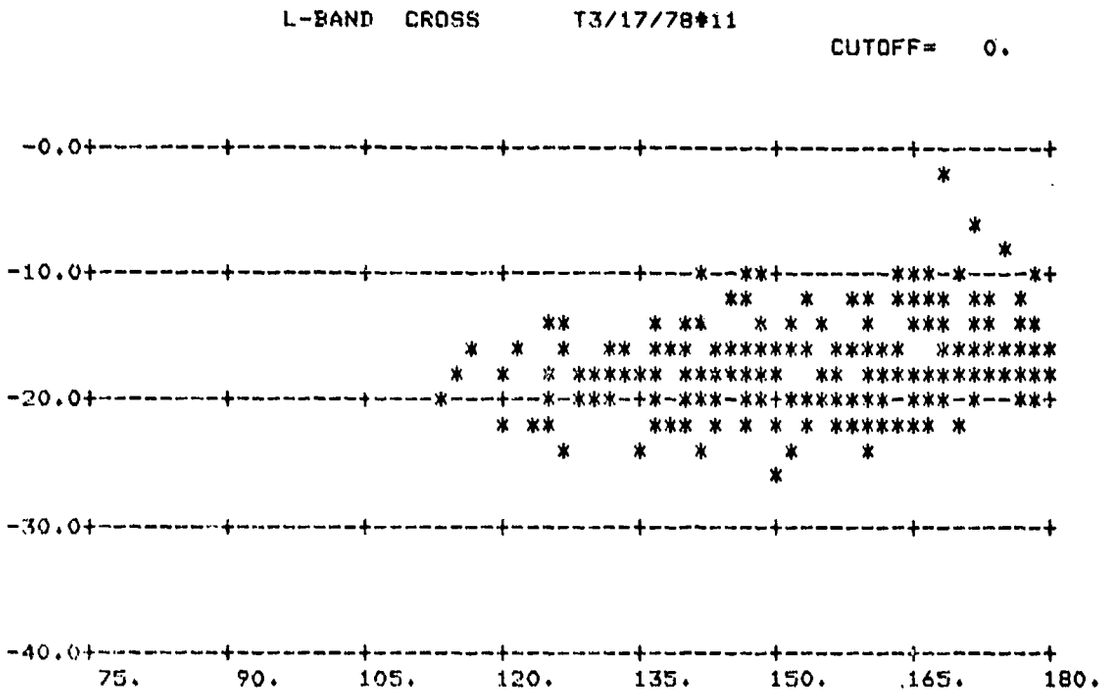

FIGURE A-16. σ_o vs ϕ_s; $\theta_s = 84°$, $\theta_i = 60°$

(Above: All Data; Below: Averages Over 5° Intervals)

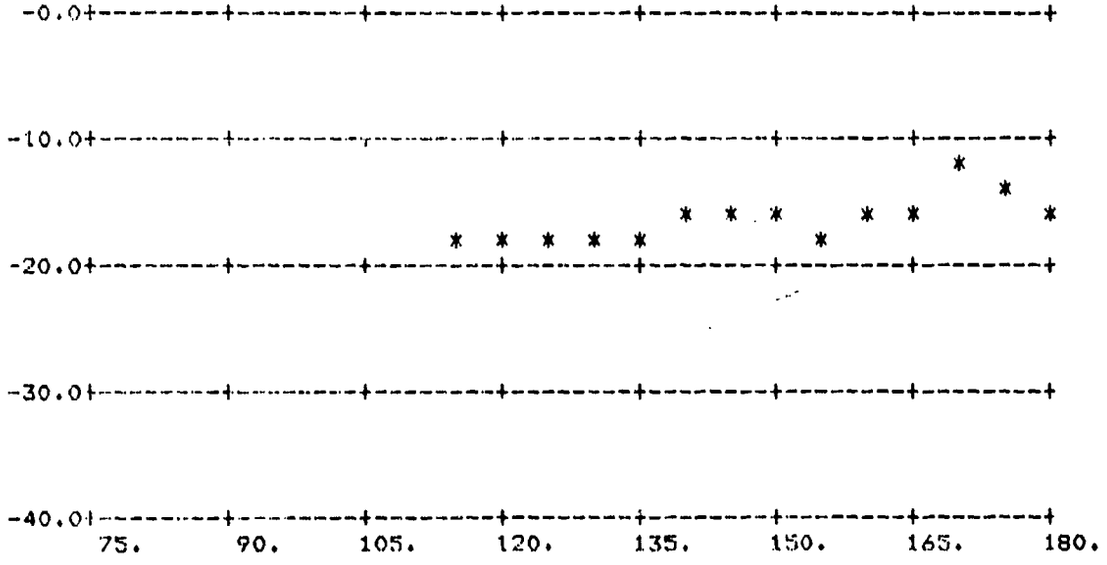

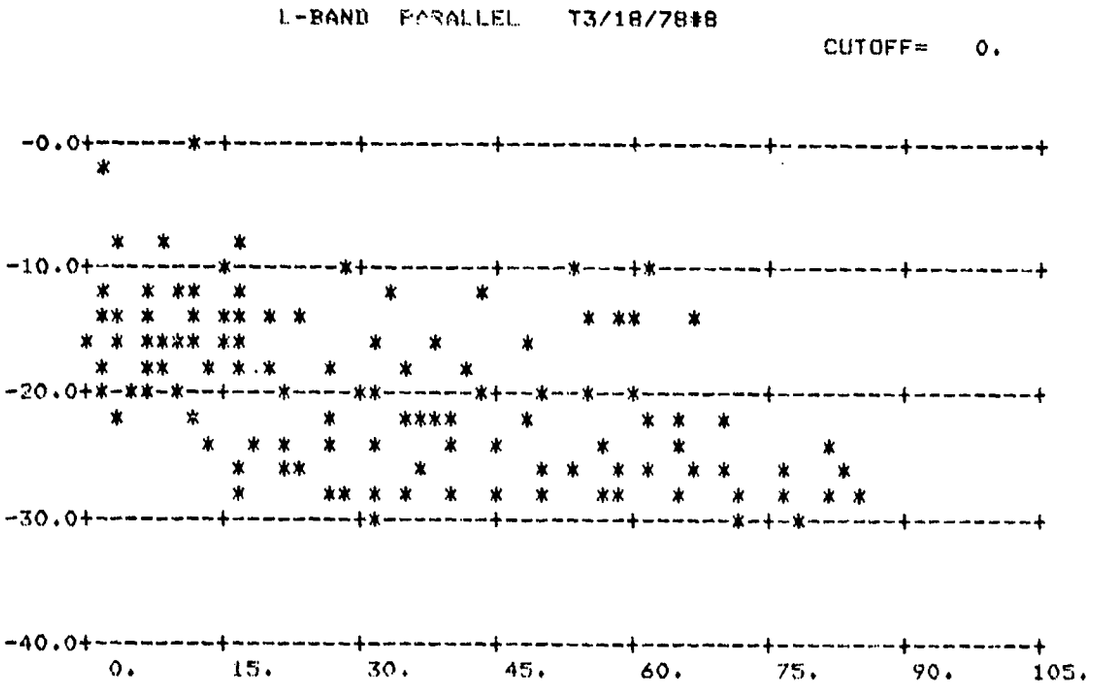

FIGURE A-17. σ_o vs ϕ_s; $\theta_s = 60°$, $\theta_i = 70°$

(Above. All Data; Below: Averages Over 5° Intervals)

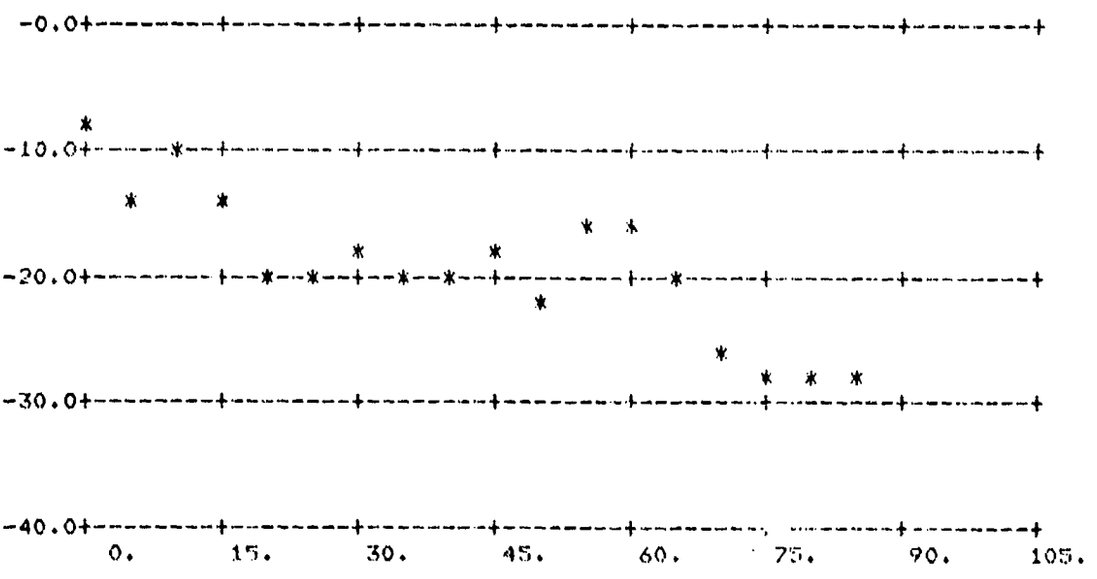

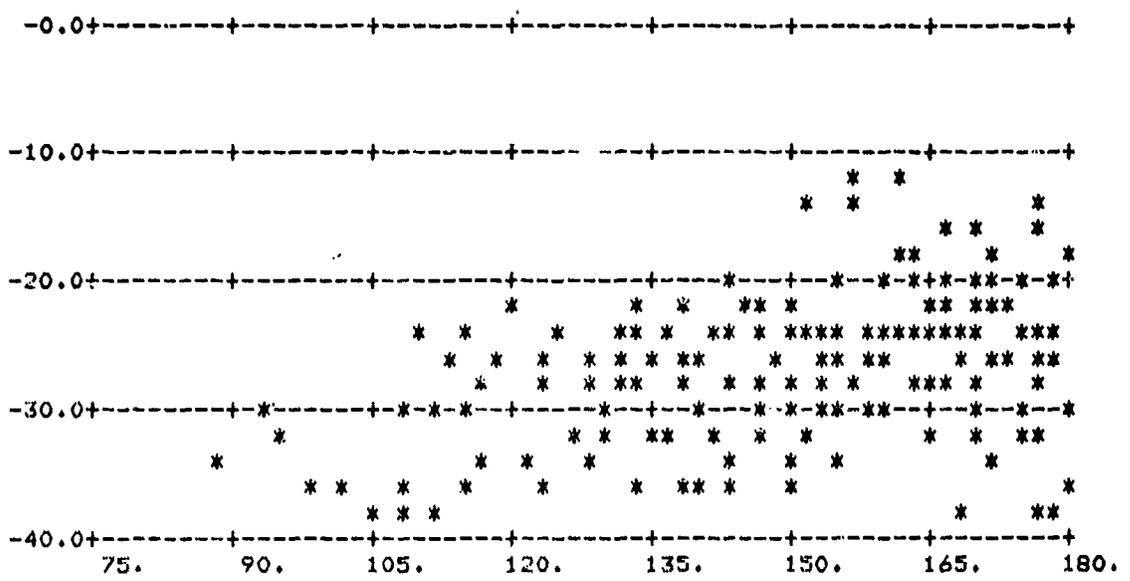

FIGURE A-18. σ_o vs ϕ_s; $\theta_s = 60°$, $\theta_i = 70°$

(Above: All Data; Below: Averages Over 5° Intervals)

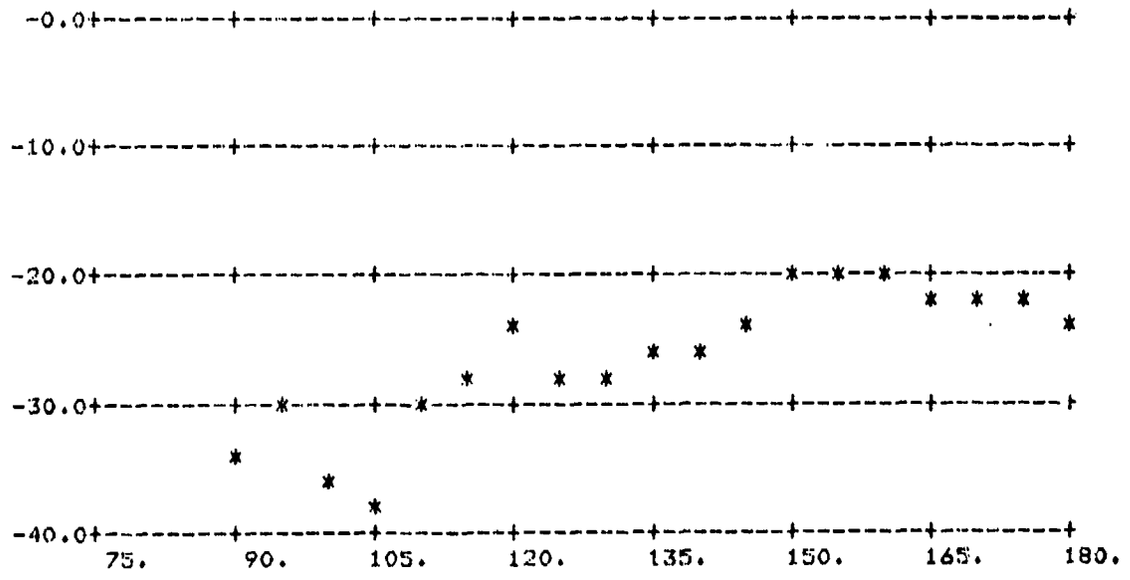

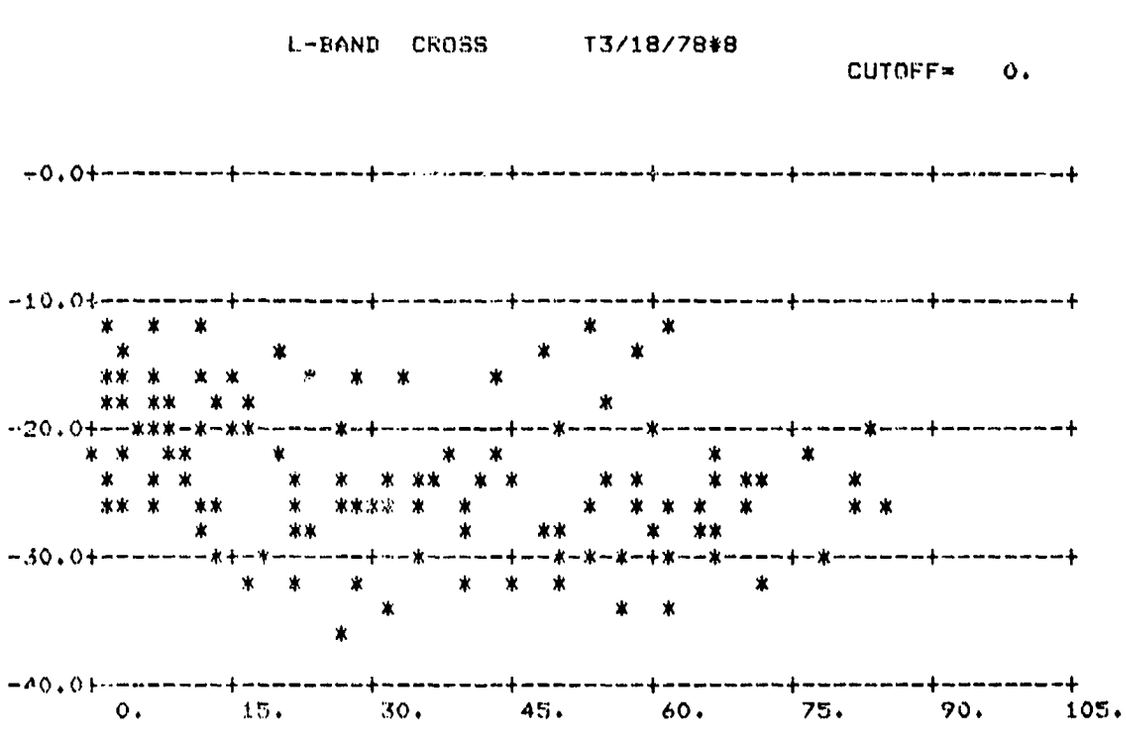

FIGURE A-19. σ_o vs ϕ_s; $\theta_s = 60°$, $\theta_i = 70°$

(Above: All Data; Below: Averages Over 5° Intervals)

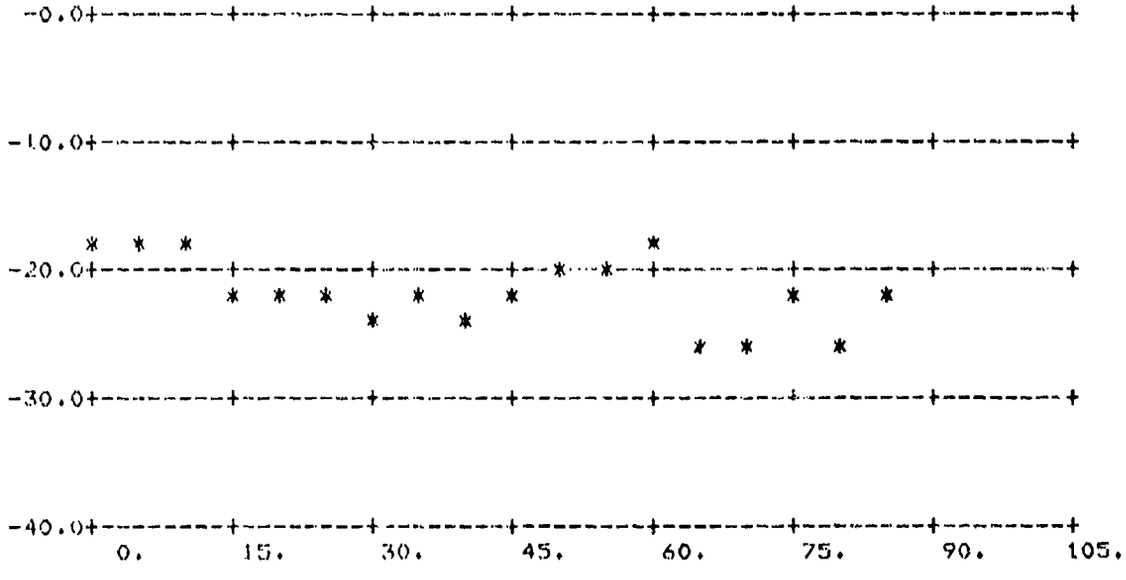

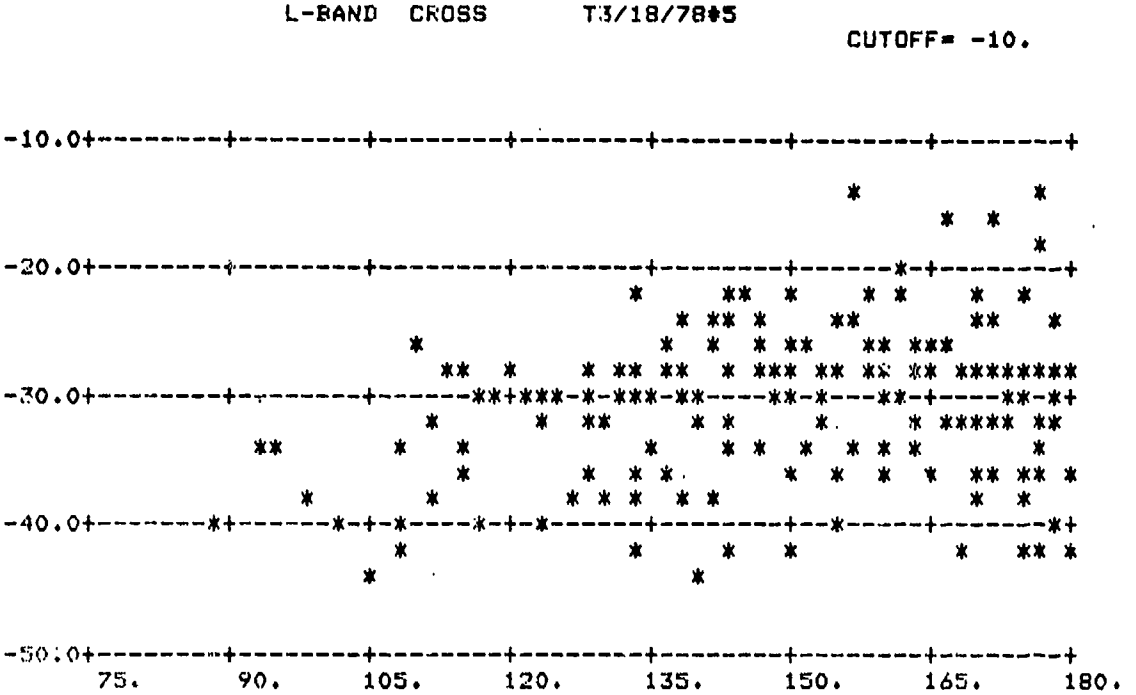

FIGURE A-20. σ_o vs ϕ_s; $\theta_s = 60°$, $\theta_i = 70°$

(Above: All Data; Below: Averages Over 5° Intervals)

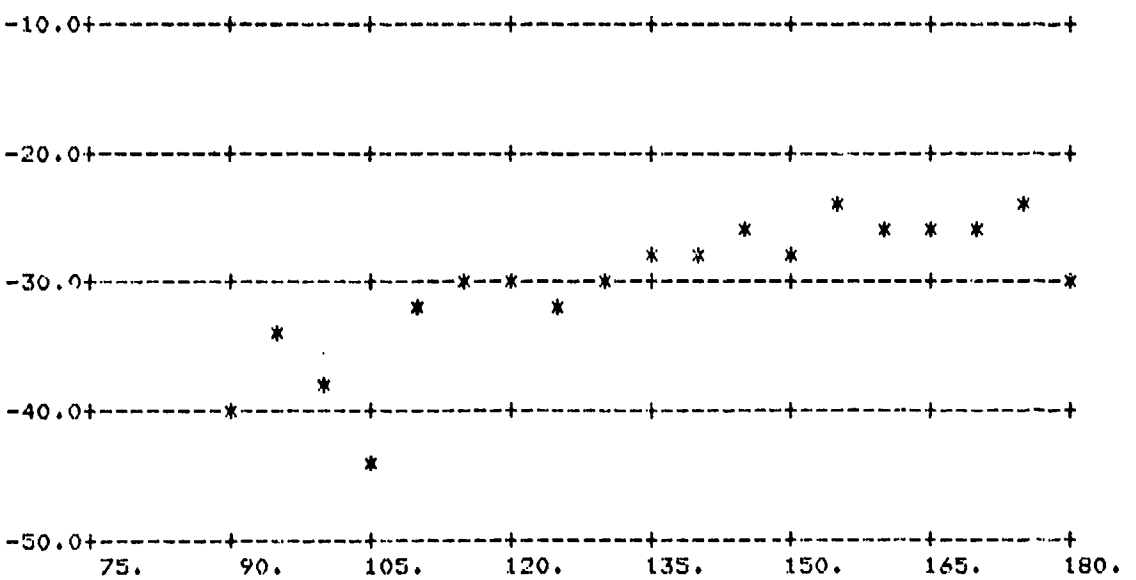

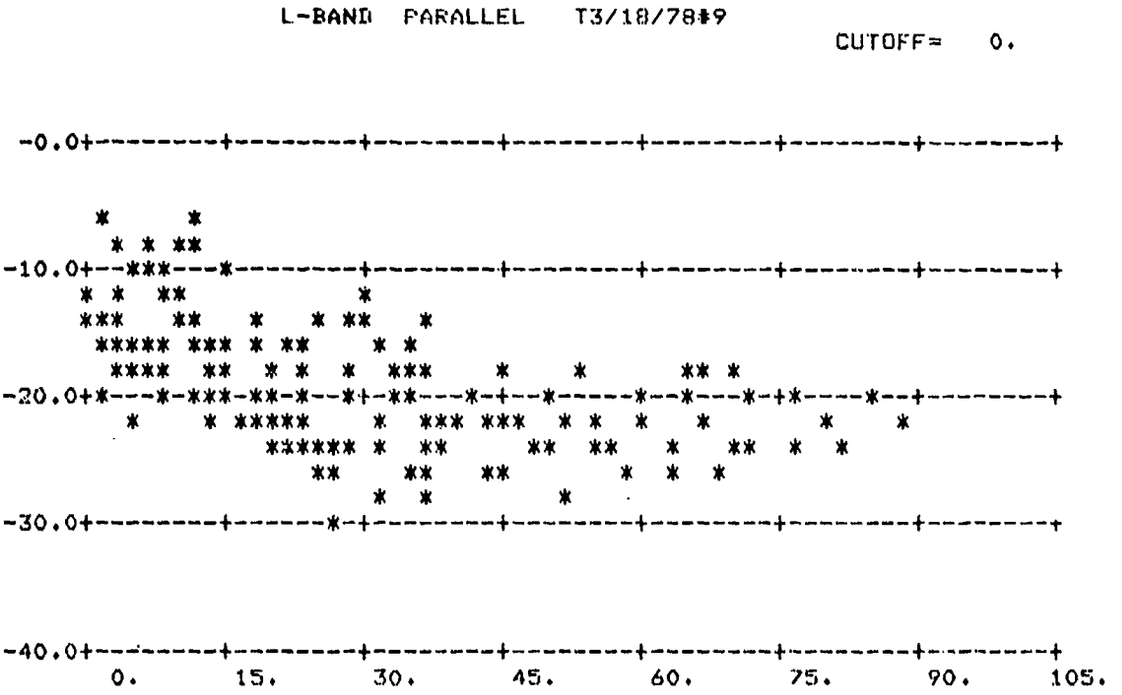

FIGURE A-21. σ_o vs ϕ_s; $\theta_s = 70°$, $\theta_i = 70°$

(Above: All Data; Below: Averages Over 5° Intervals)

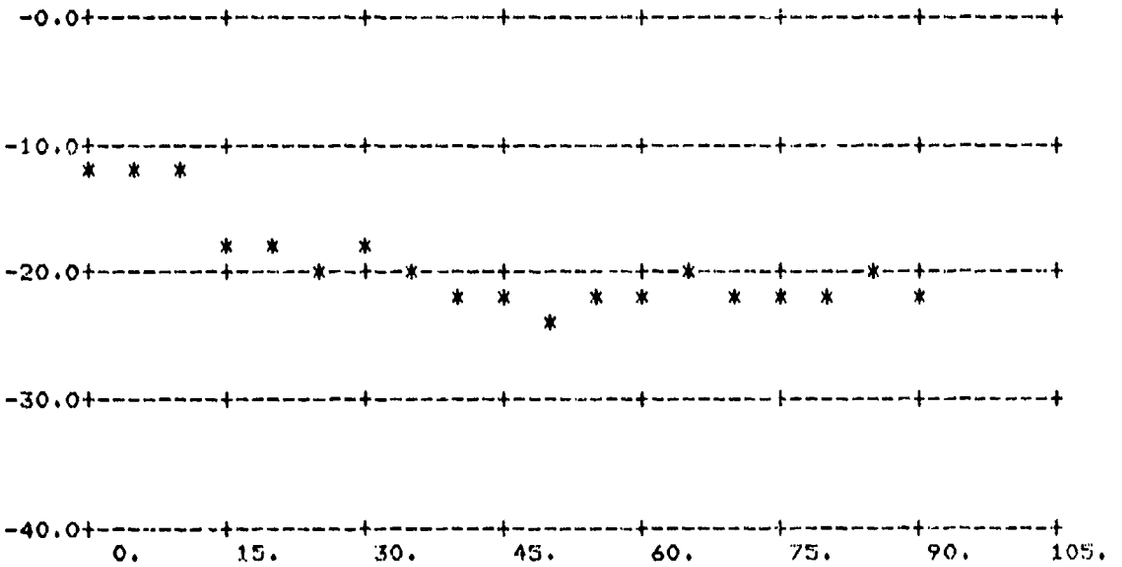

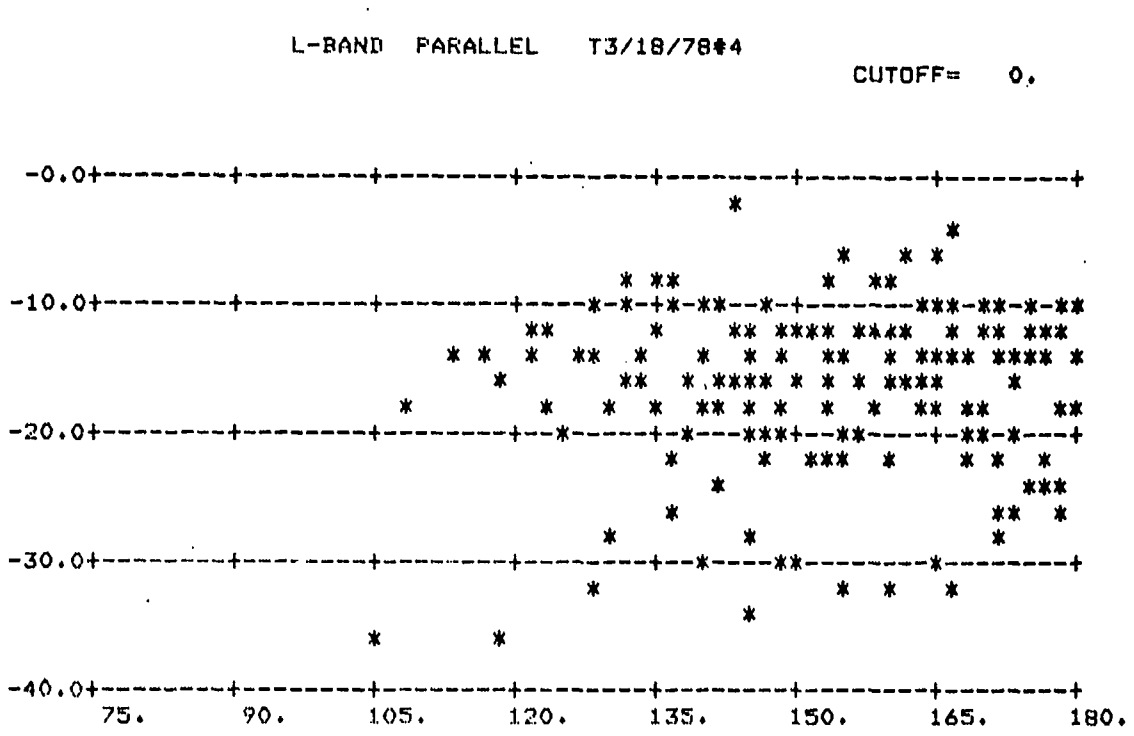

FIGURE A-22. σ_o vs ϕ_s; $\theta_s = 70°$, $\theta_i = 70°$

(Above: All Data; Below: Averages Over 5° Intervals)

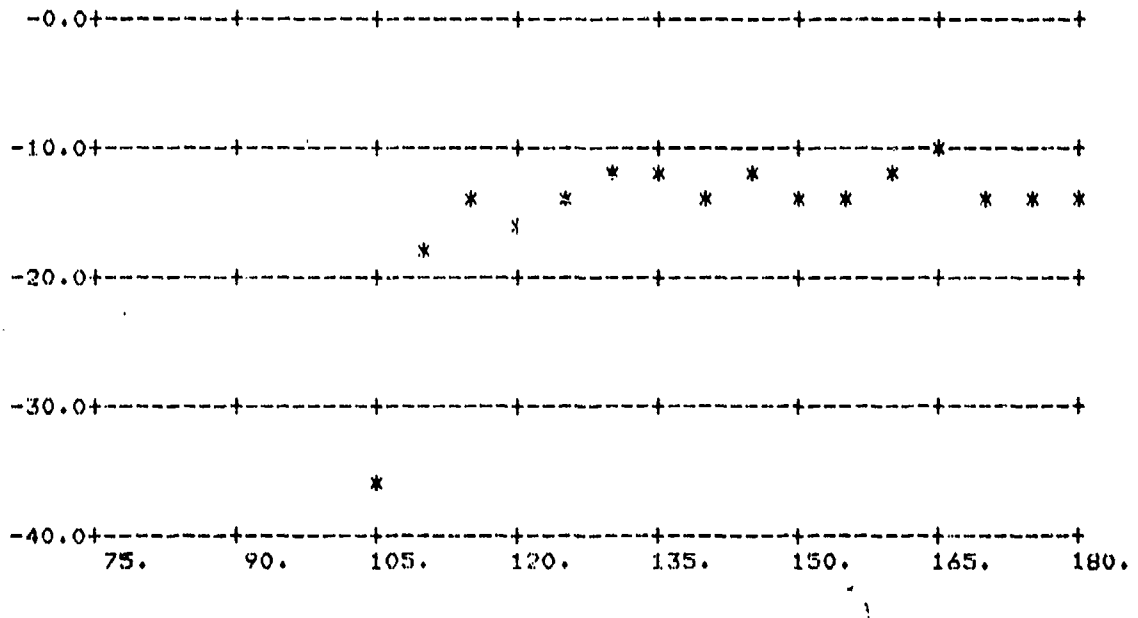

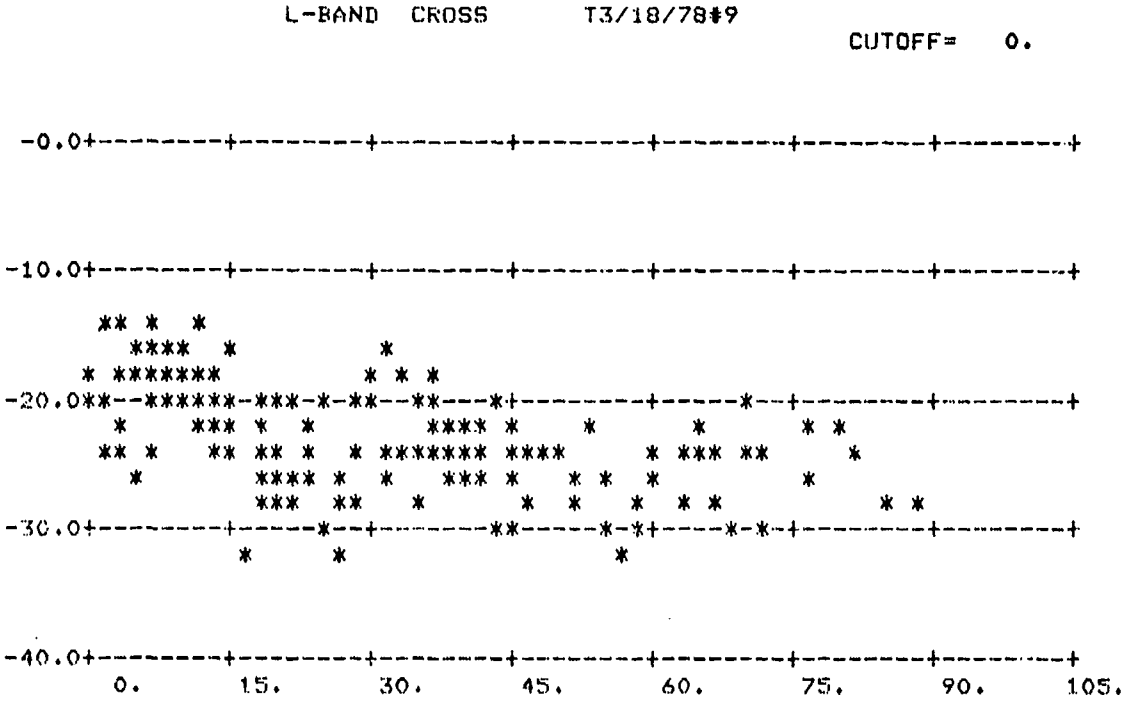

FIGURE A-23. σ_o vs ϕ_s; $\theta_s = 70°$, $\theta_i = 70°$

(Above: All Data; Below: Averages Over 5° Intervals)

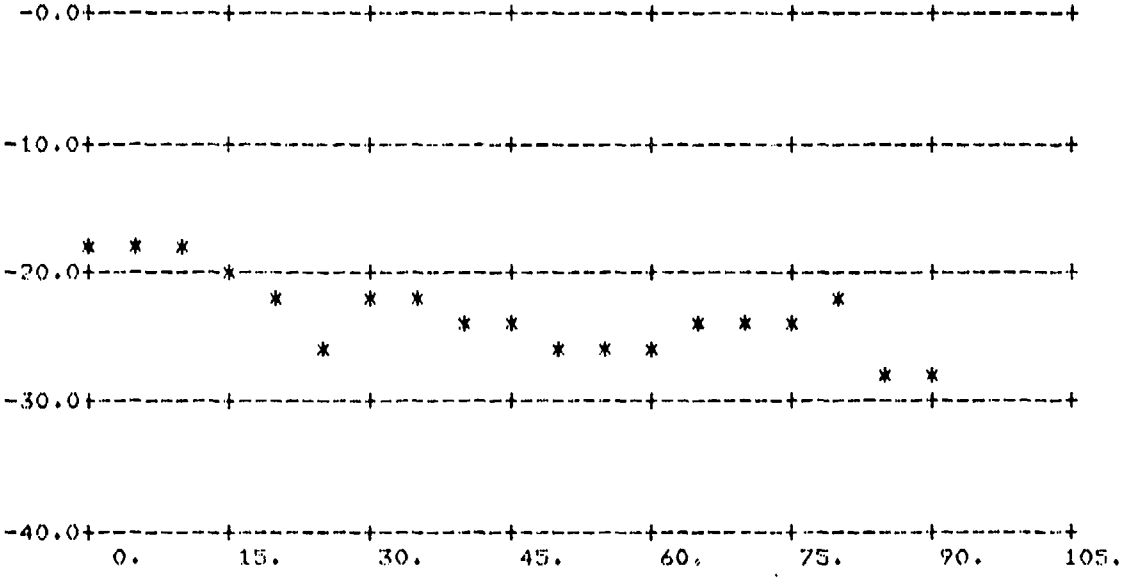

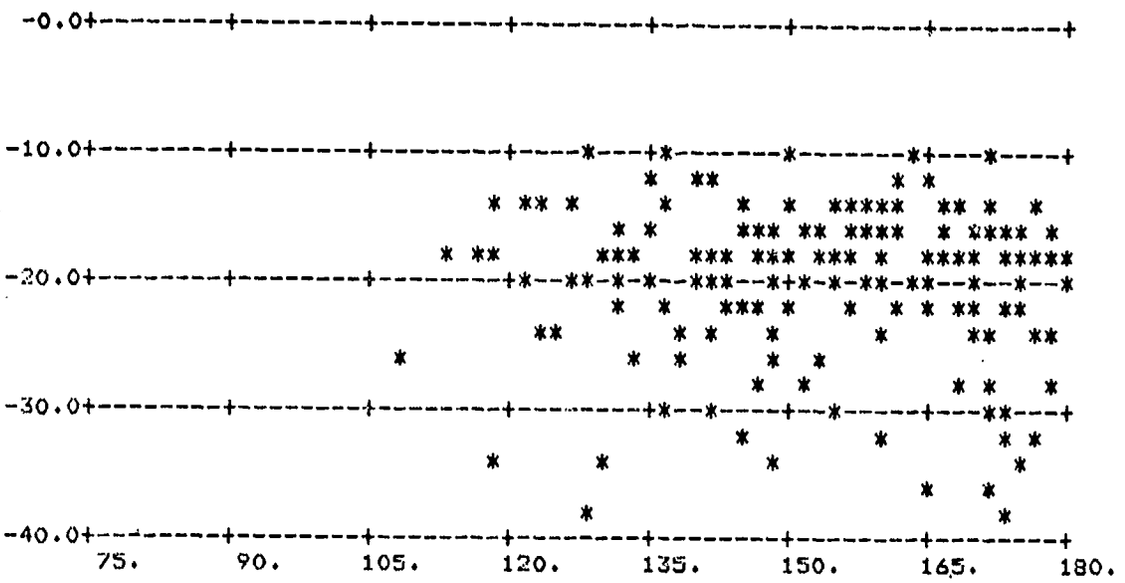

FIGURE A-24. σ_o vs ϕ_s; $\theta_s = 70°$, $\theta_i = 70°$

(Above: All Data; Below: Averages Over 5° Intervals)

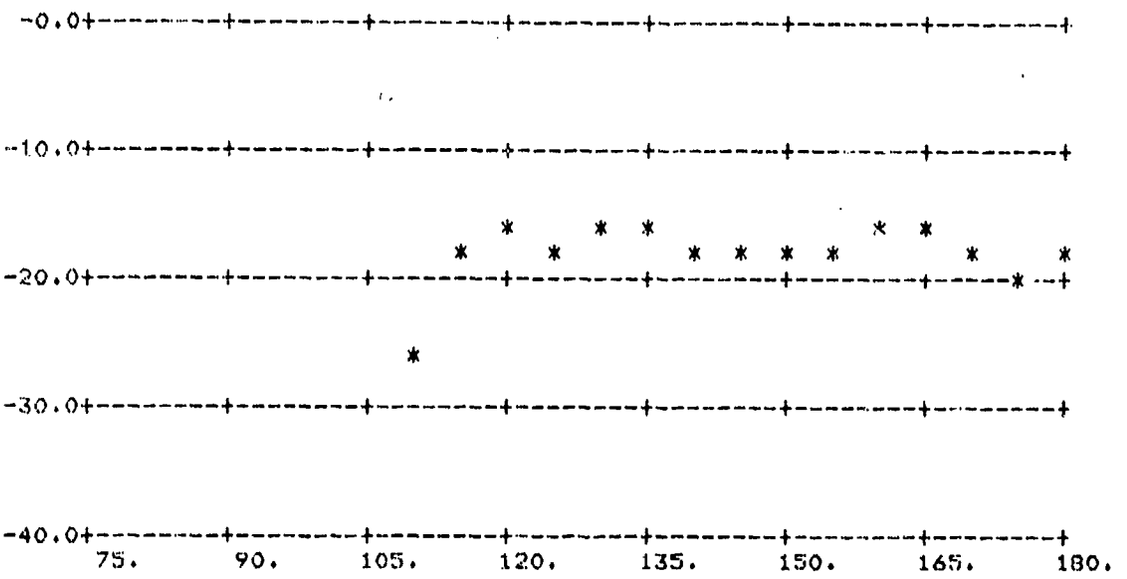

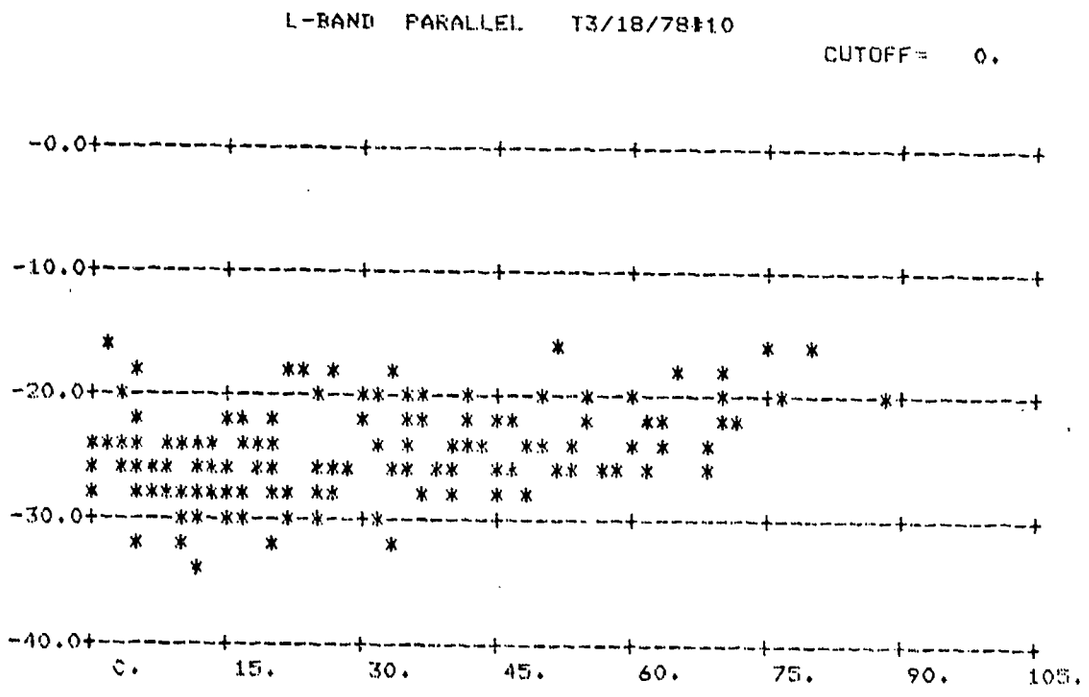

FIGURE A-25. σ_o vs ϕ_s; $\theta_s = 80°$, $\theta_i = 70°$

(Above: All Data; Below: Averages Over 5° Intervals)

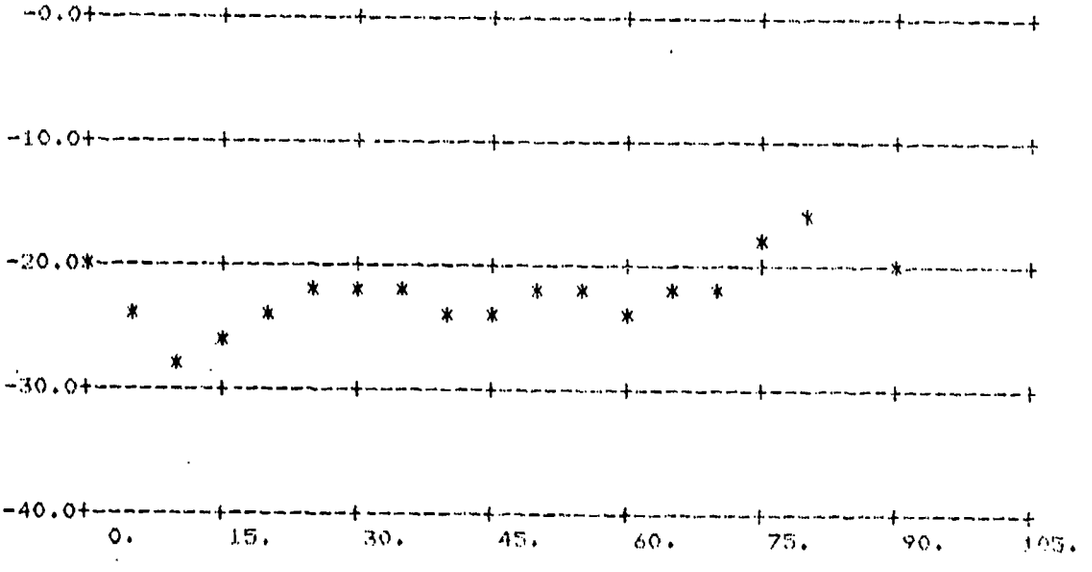

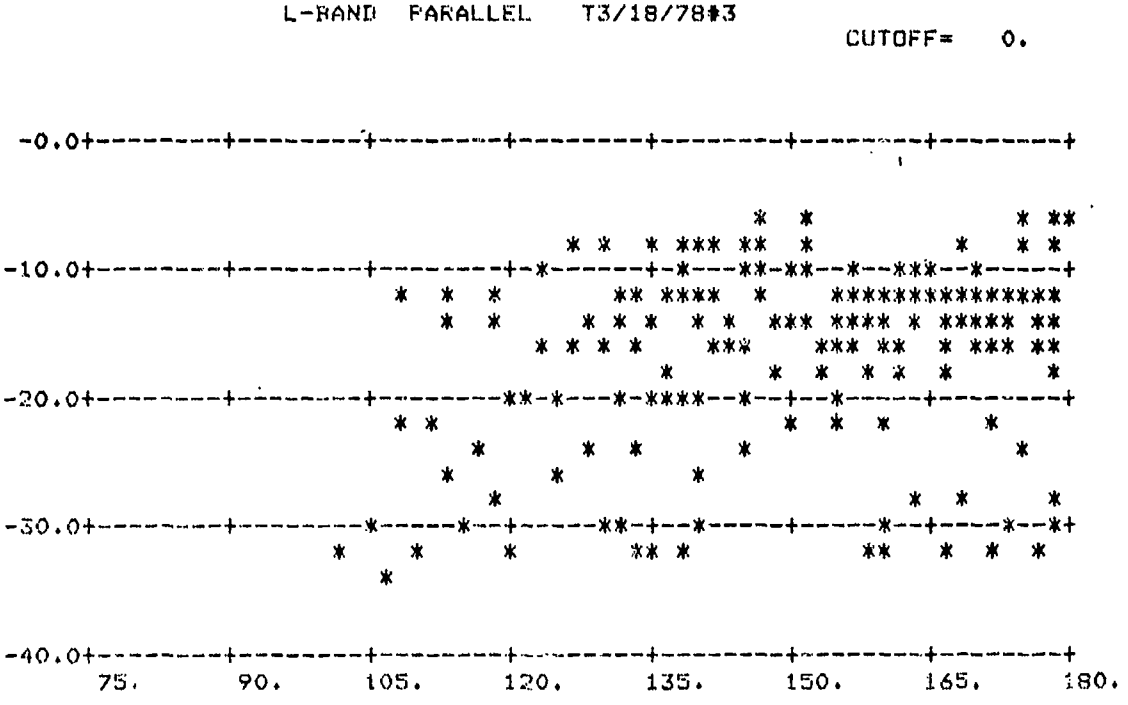

FIGURE A-26. σ_o vs ϕ_s; $\theta_s = 80°$, $\theta_i = 70°$

(Above: All Data; Below: Averages Over 5° Intervals)

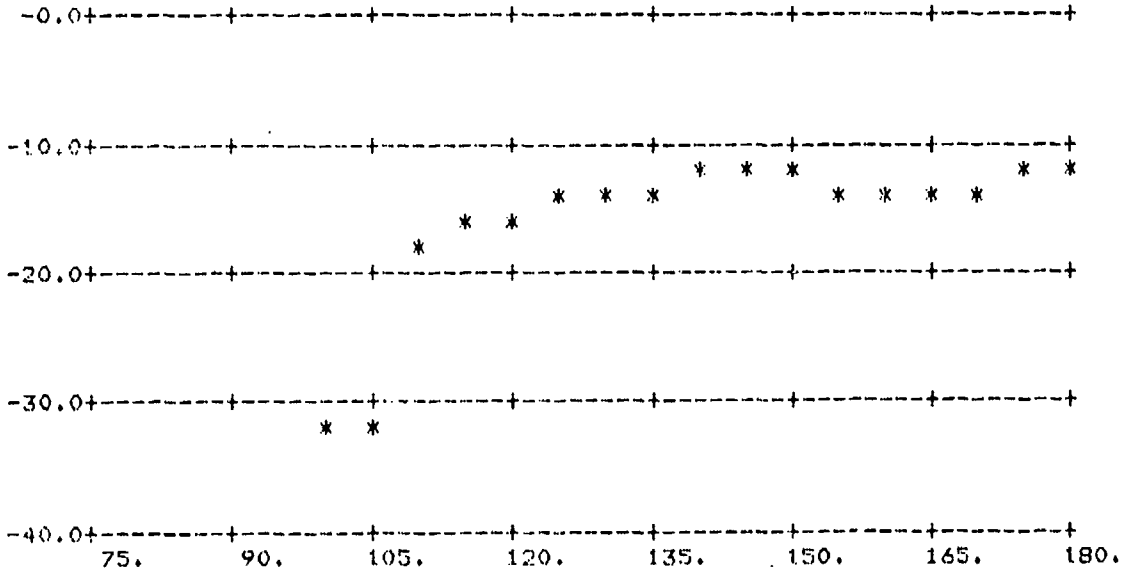

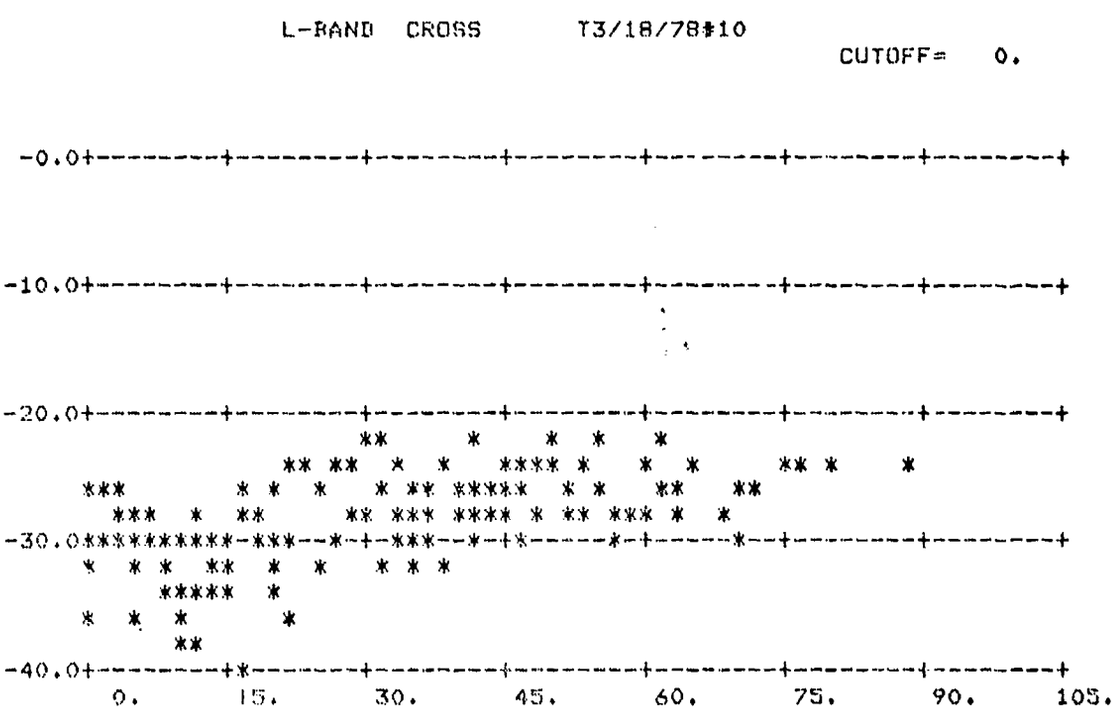

FIGURE A-27. σ_o vs ϕ_s; $\theta_s = 80°$, $\theta_i = 70°$

(Above: All Data; Below: Averages Over 5° Intervals)

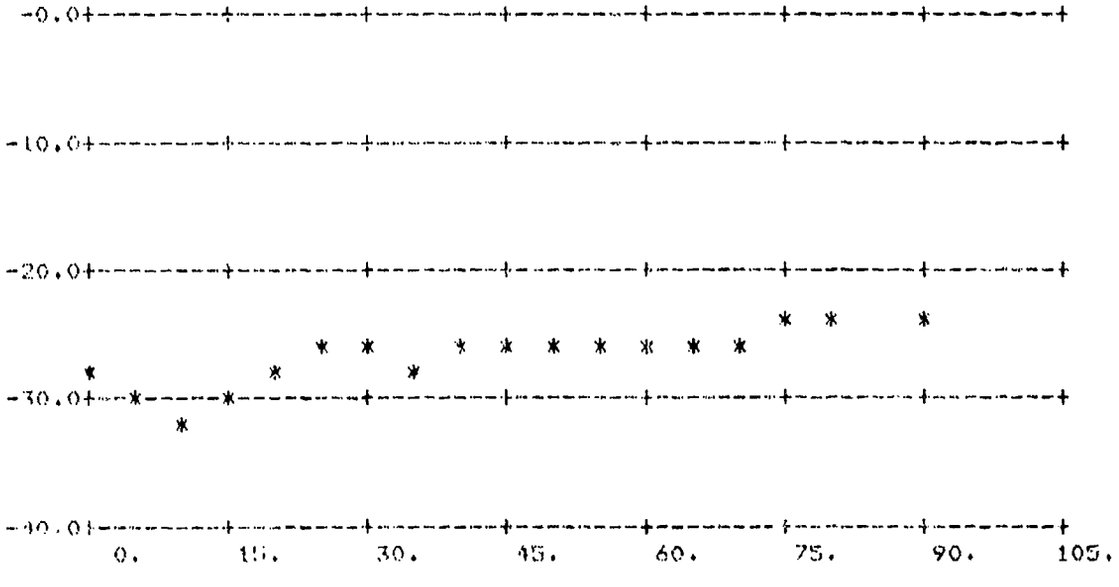

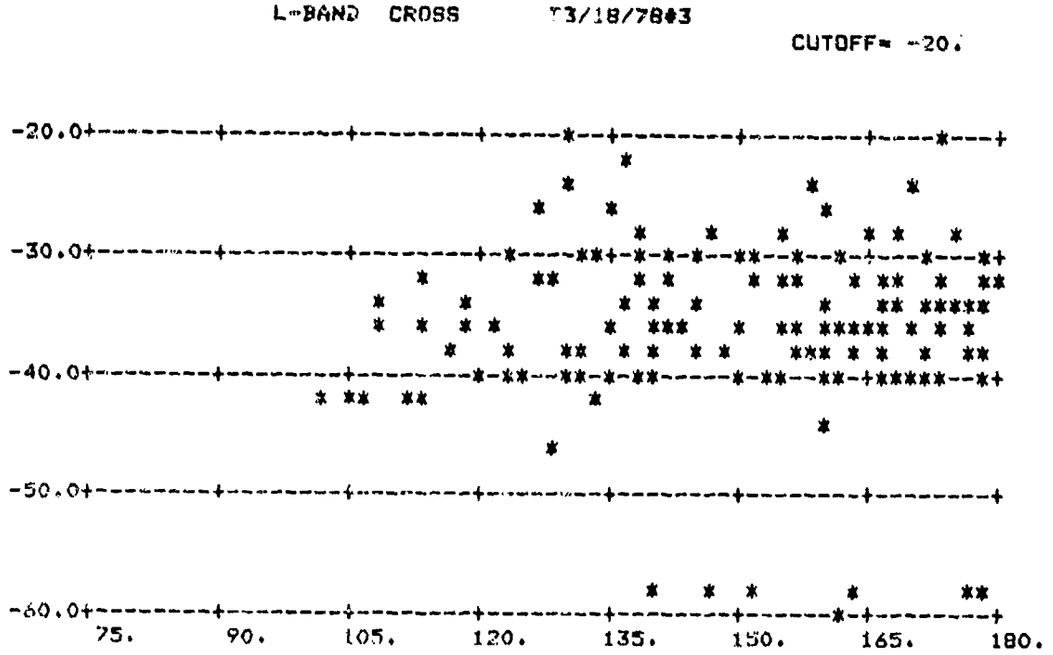

FIGURE A-28. σ_o vs ϕ_s; $\theta_s = 80°$, $\theta_i = 70°$

(Above: All Data; Below: Averages Over 5° Intervals)

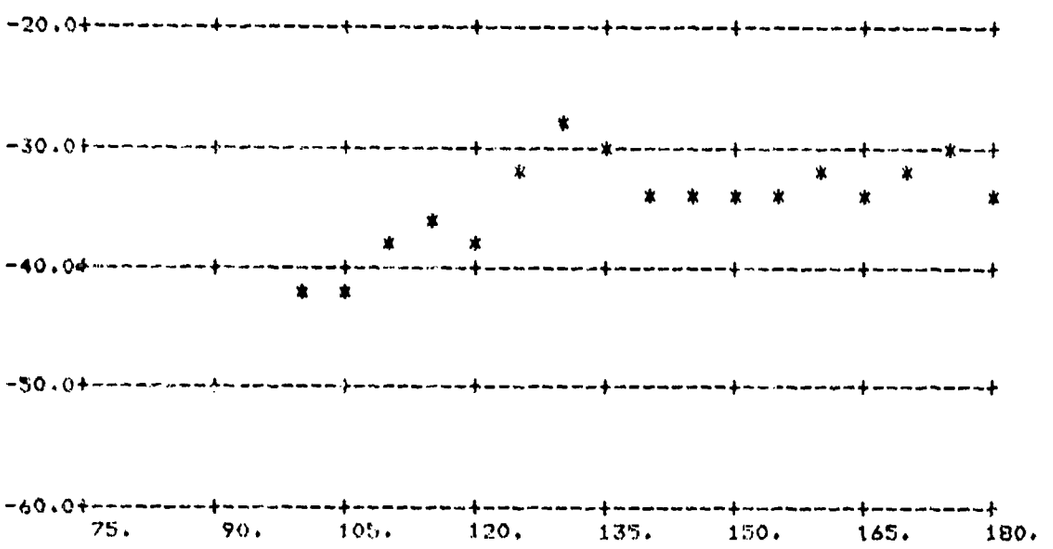

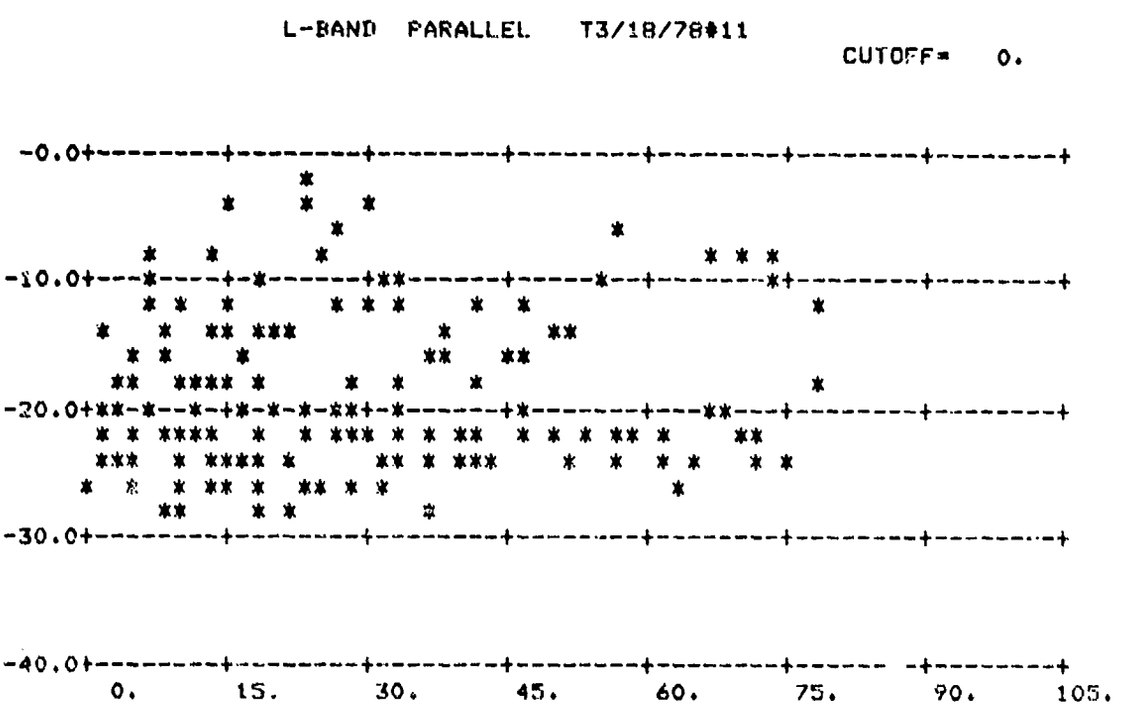

FIGURE A-29. σ_o vs ϕ_s; $\theta_s = 84°$, $\theta_i = 70°$

(Above: All Data; Below: Averages Over 5° Intervals)

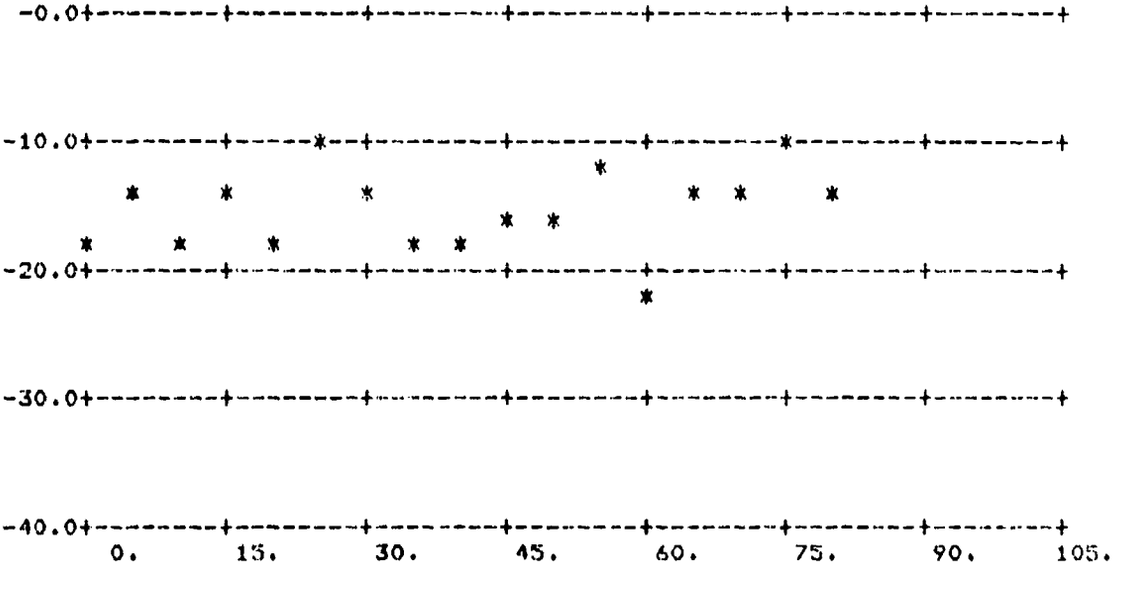

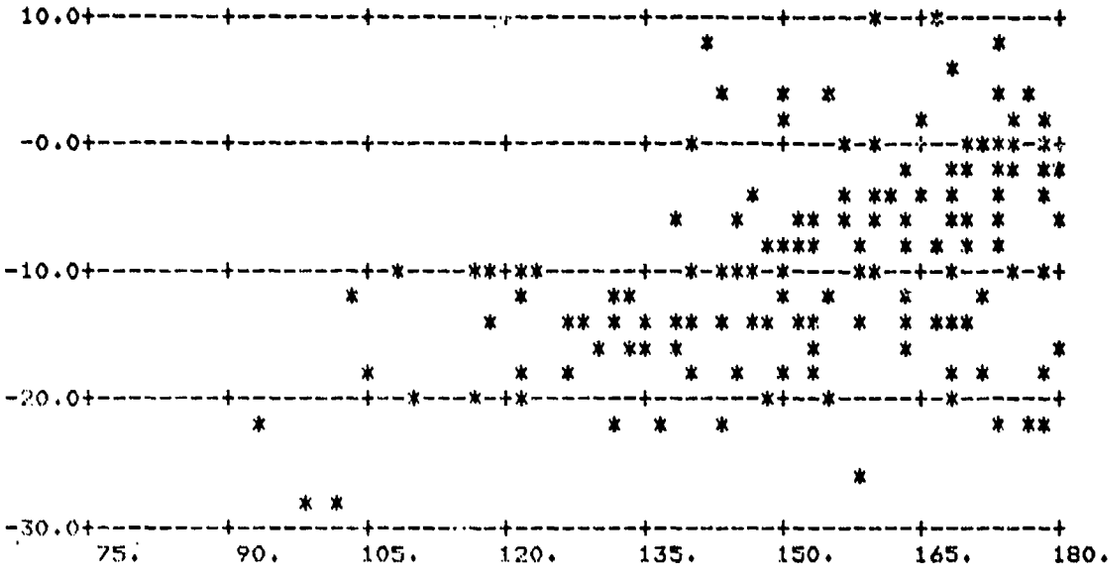

FIGURE A-30. σ_o vs ϕ_s; $\theta_s = 84°$, $\theta_i = 70°$

(Above: All Data; Below: Averages Over 5° Intervals)

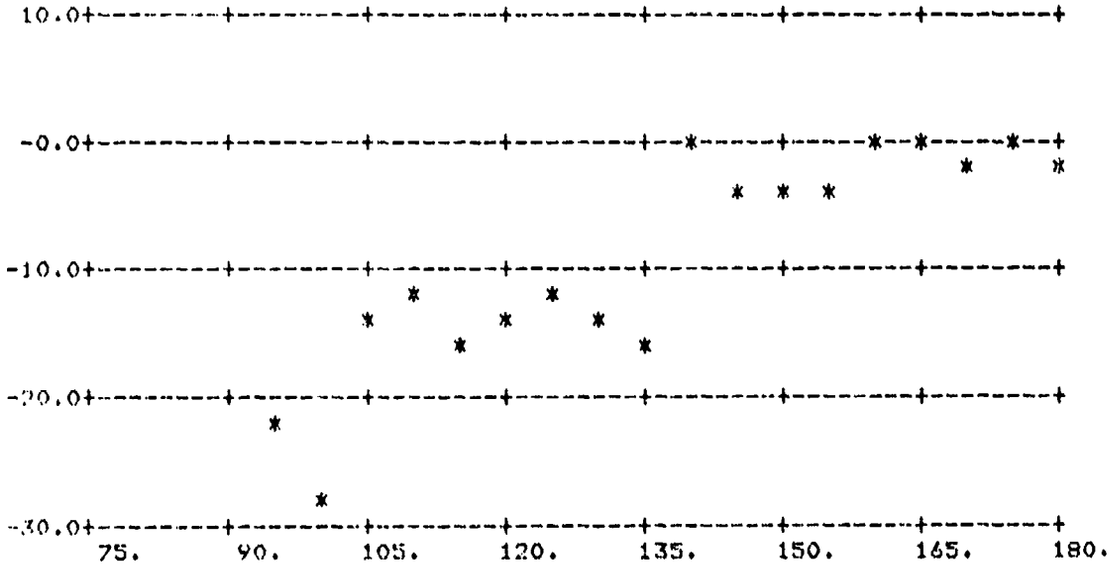

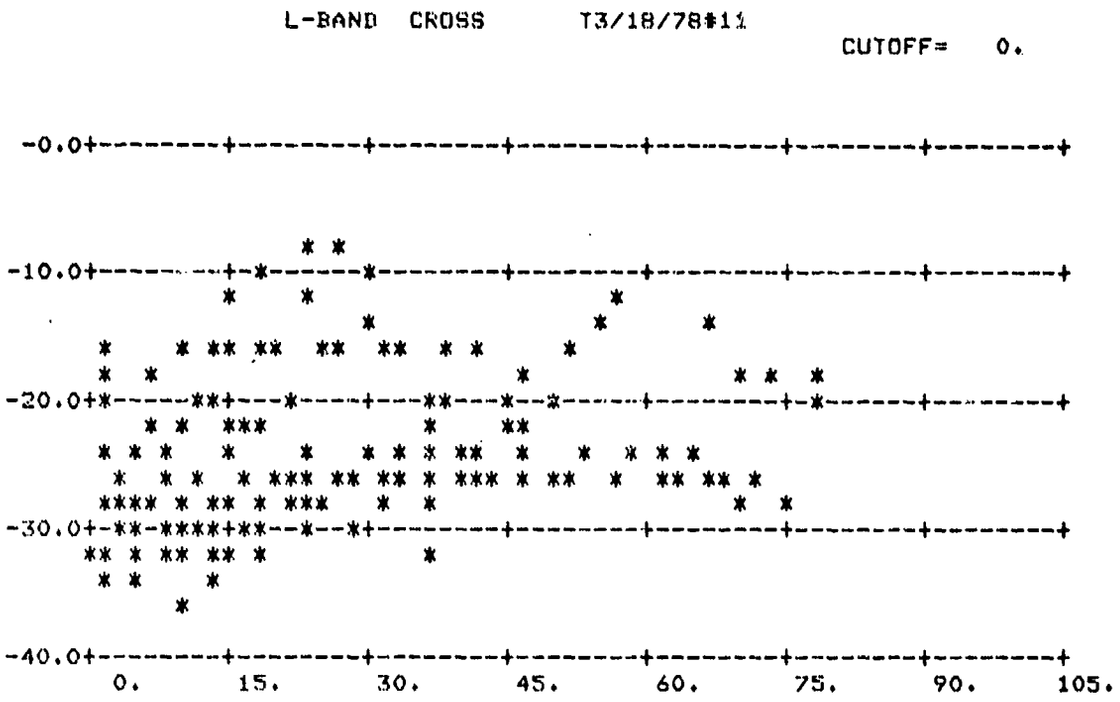

FIGURE A-31. σ_o vs ϕ_s; $\theta_s = 84°$, $\theta_i = 70°$

(Above: All Data; Below: Averages Over 5° Intervals)

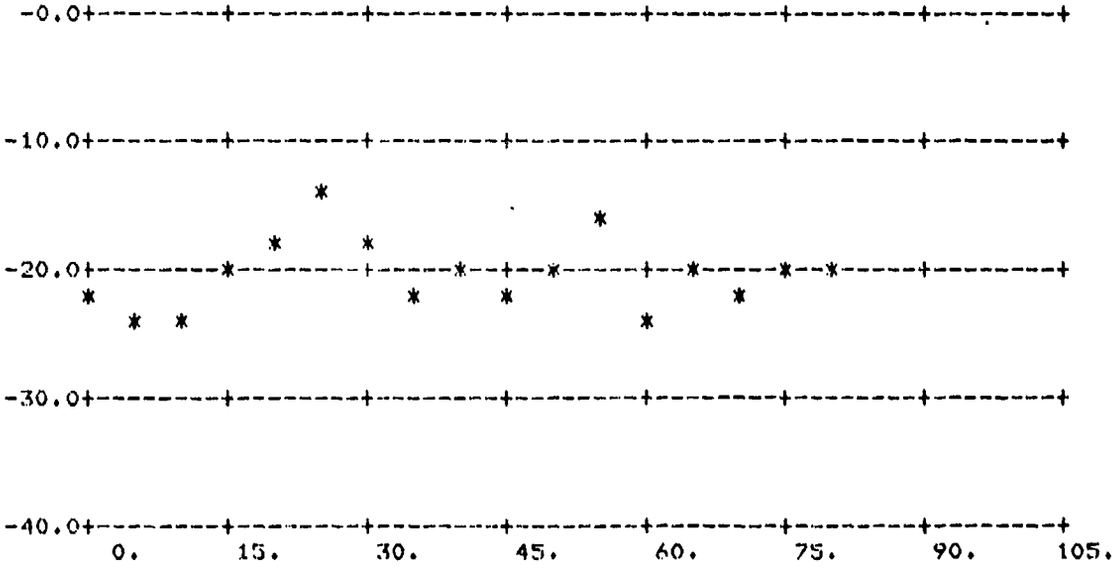

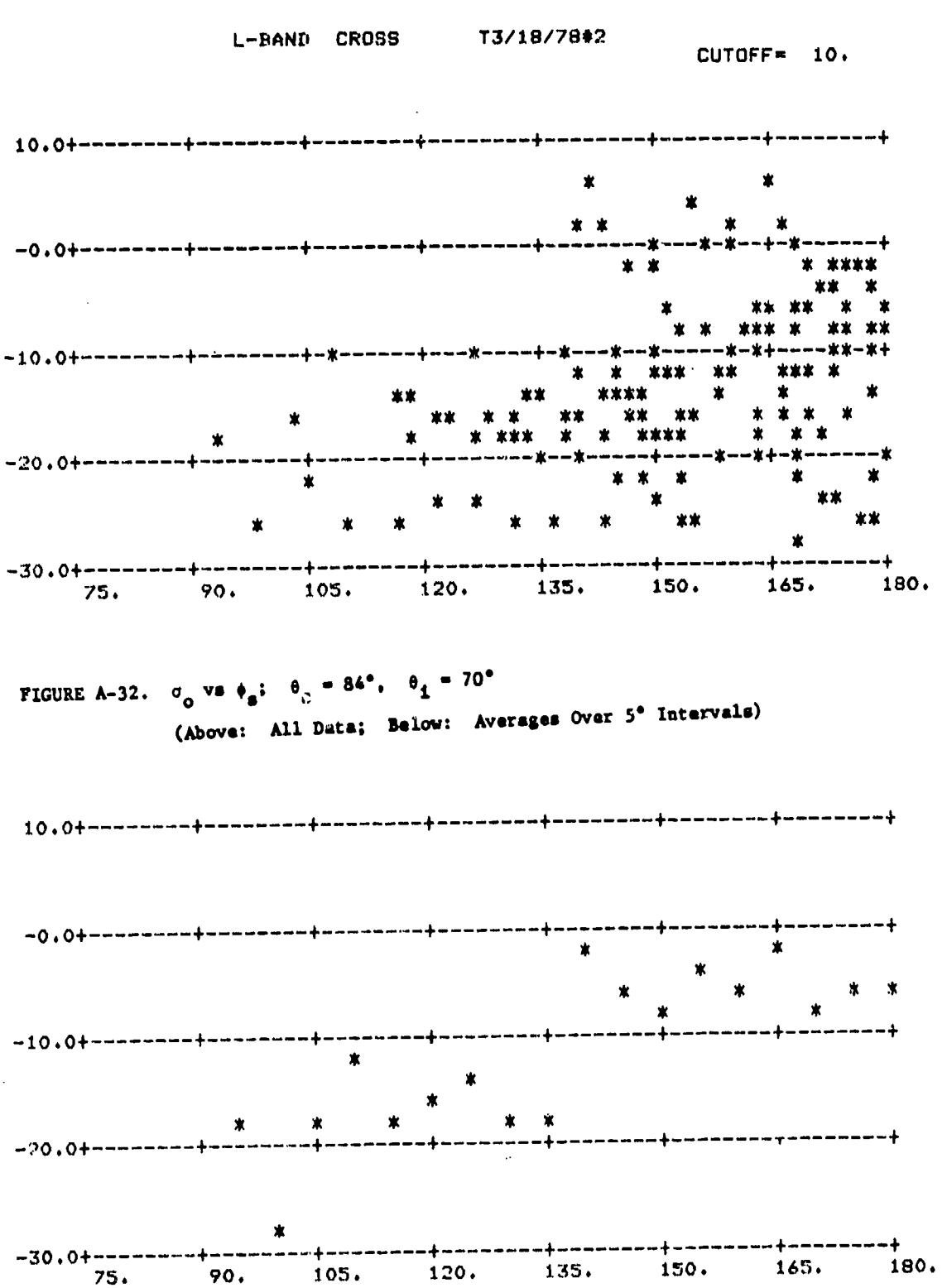

FIGURE A-32. σ_o vs ϕ_s; θ_i = 84°, θ_i = 70°
(Above: All Data; Below: Averages Over 5° Intervals)

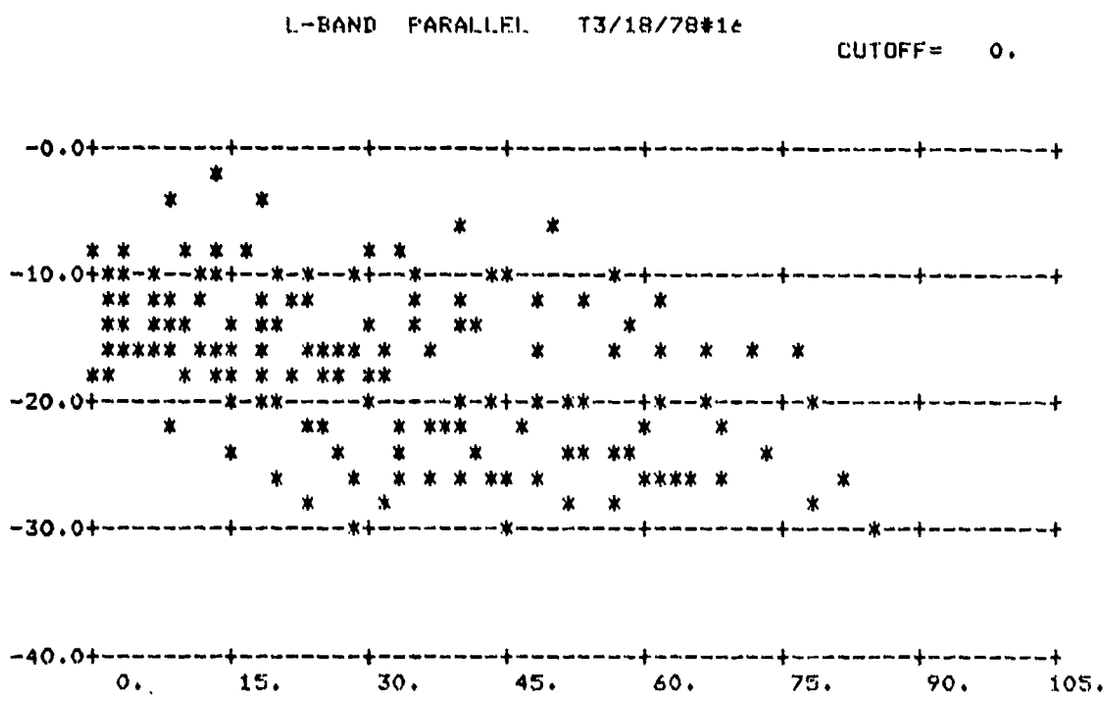

FIGURE A-33. σ_o vs ϕ_s; $\theta_s = 60°$, $\theta_i = 70°$

(Above: All Data; Below: Averages Over 5° Intervals)

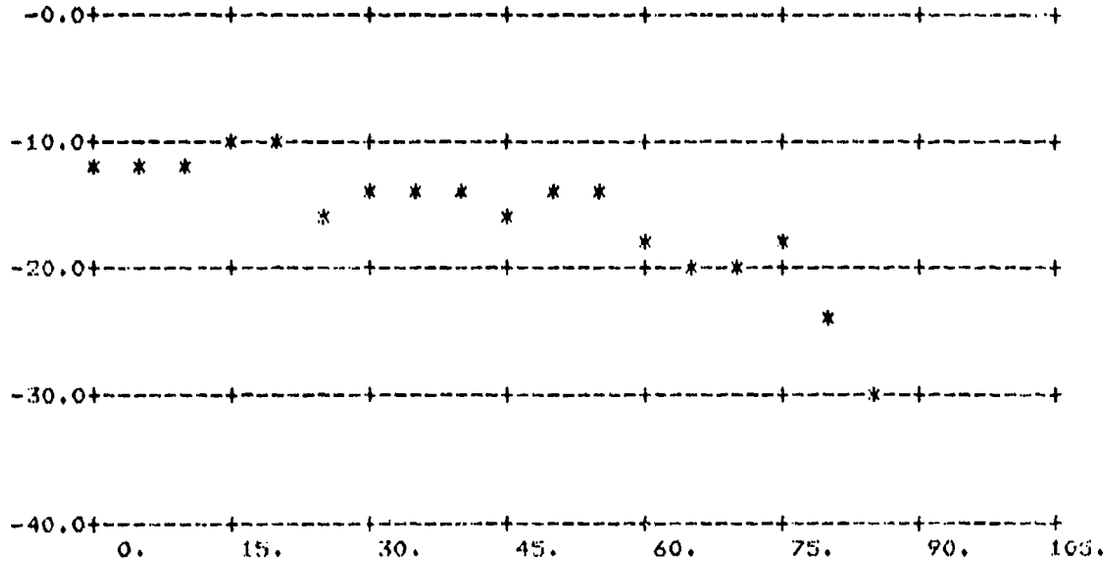

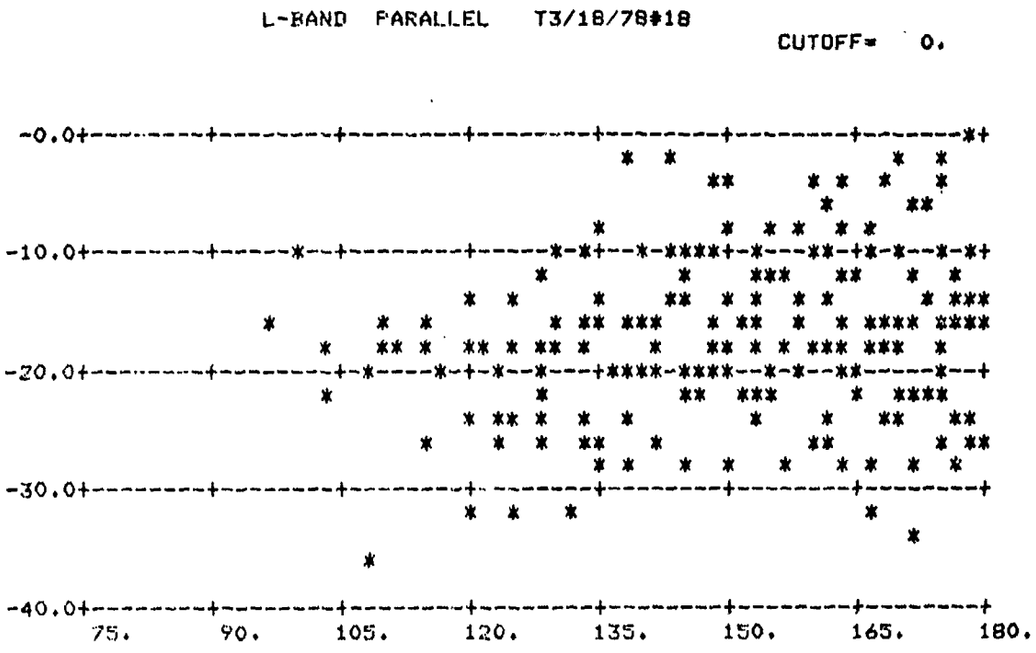

FIGURE A-34. σ_o vs ϕ_s; $\theta_s = 60°$, $\theta_i = 80°$

(Above: All Data; Below: Averages Over 5° Intervals)

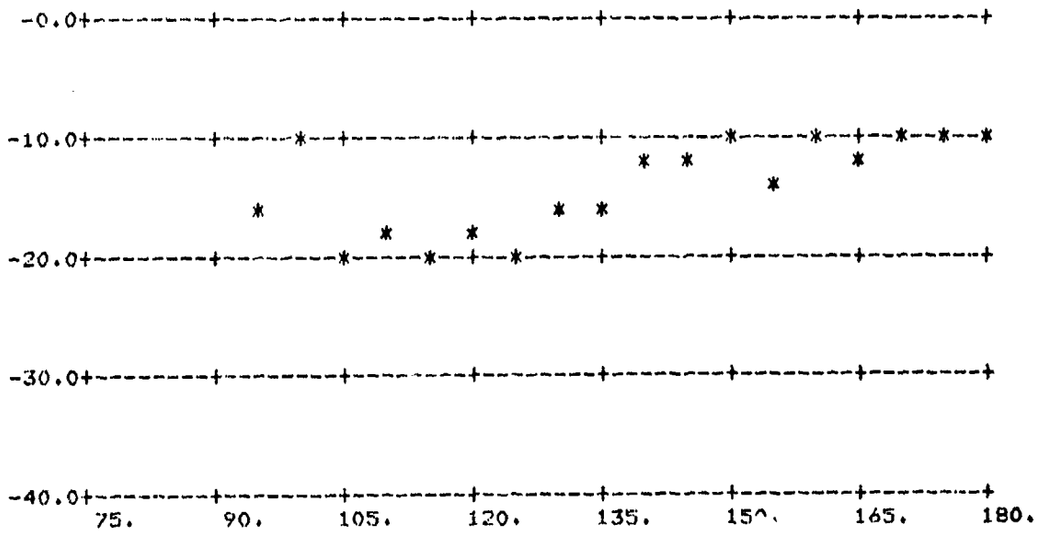

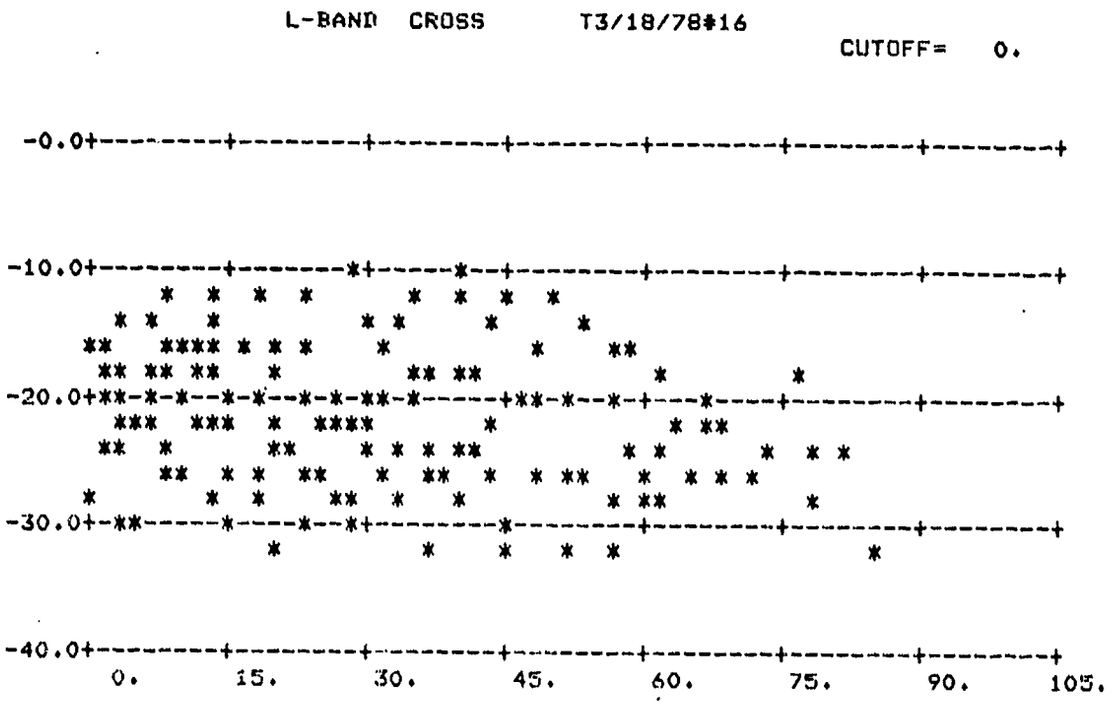

FIGURE A-35. σ_o vs ϕ_s; $\theta_s = 60°$, $\theta_i = 80°$

(Above: All Data; Below: Averages Over 5° Intervals)

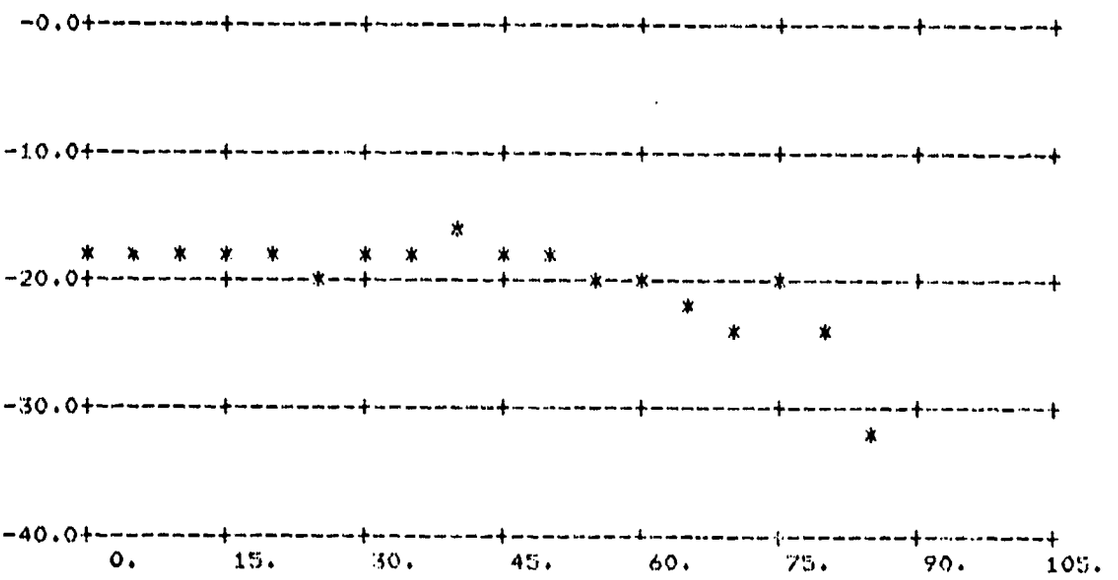

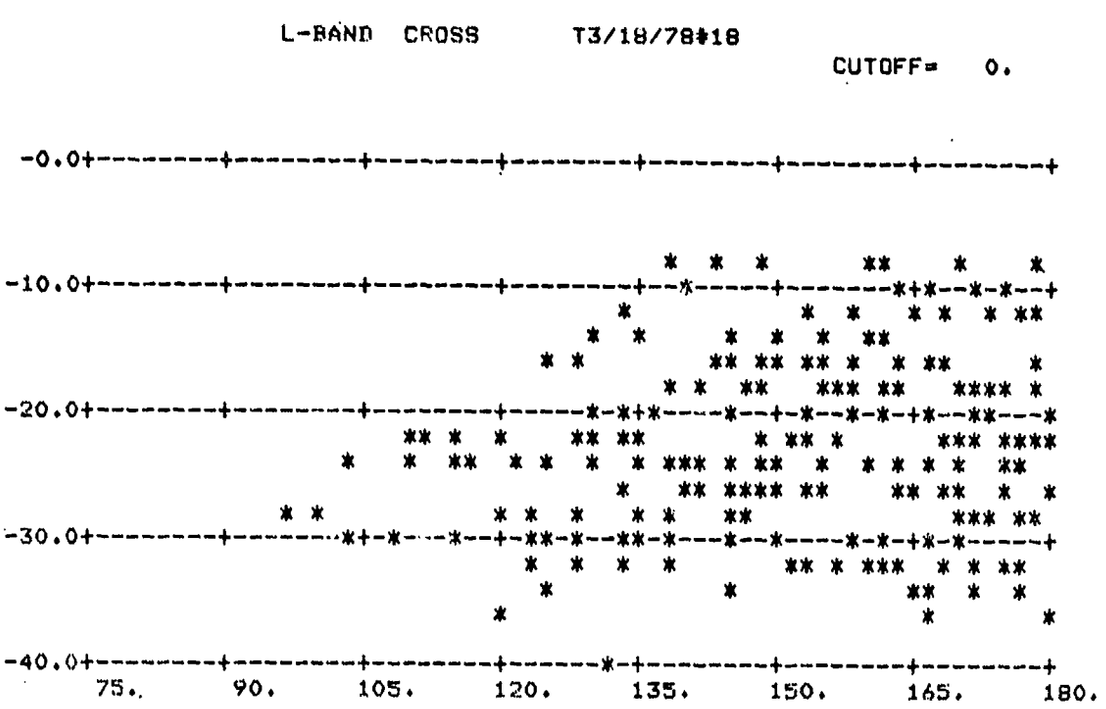

FIGURE A-36. σ_o vs ϕ_s; $\theta_s = 60°$, $\theta_i = 80°$

(Above: All Data; Below: Averages Over 5° Intervals)

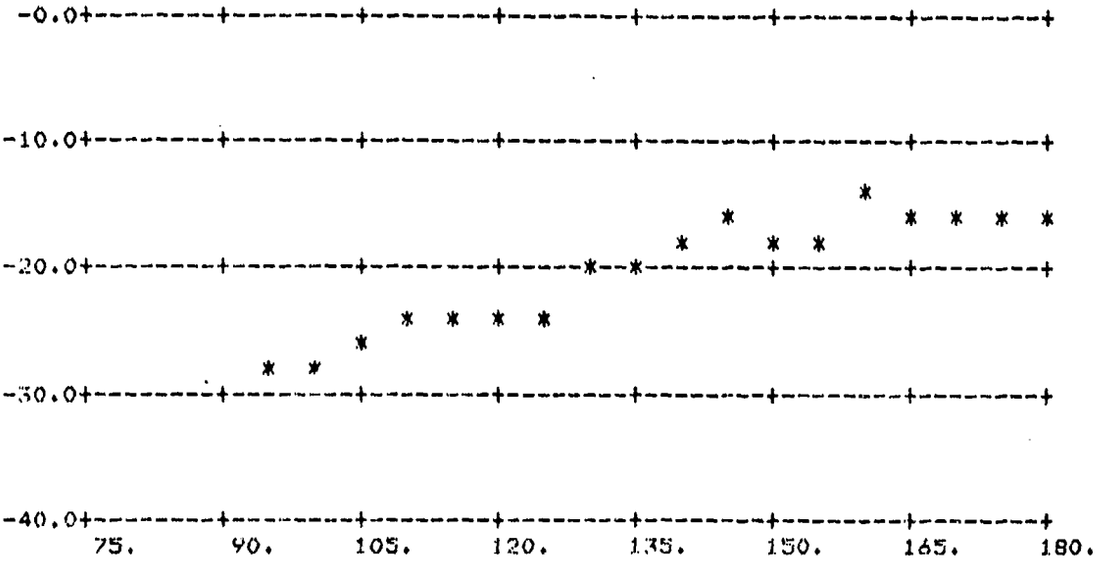

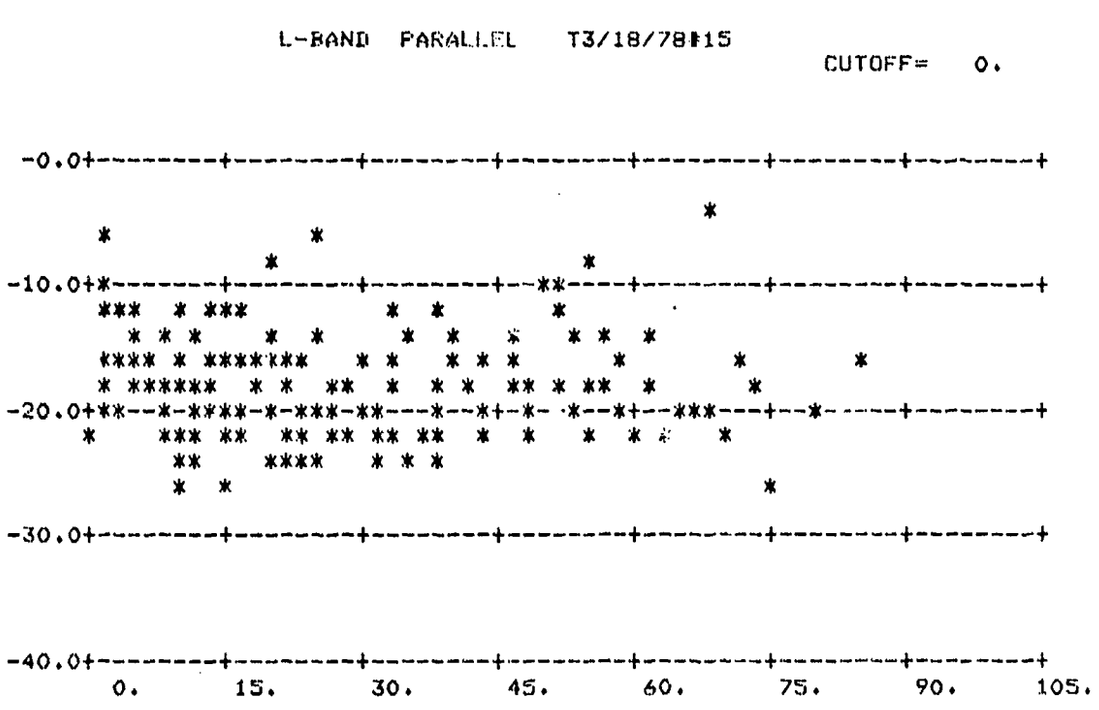

FIGURE A-37. σ_o vs ϕ_s; $\theta_s = 70°$, $\theta_i = 80°$

(Above: All Data; Below: Averages Over 5° Intervals)

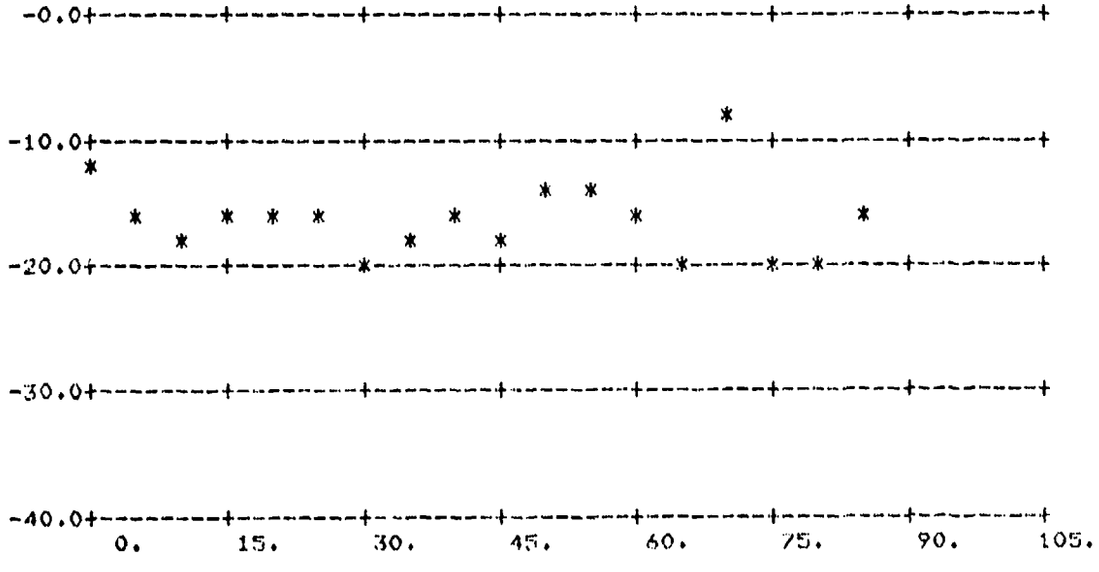

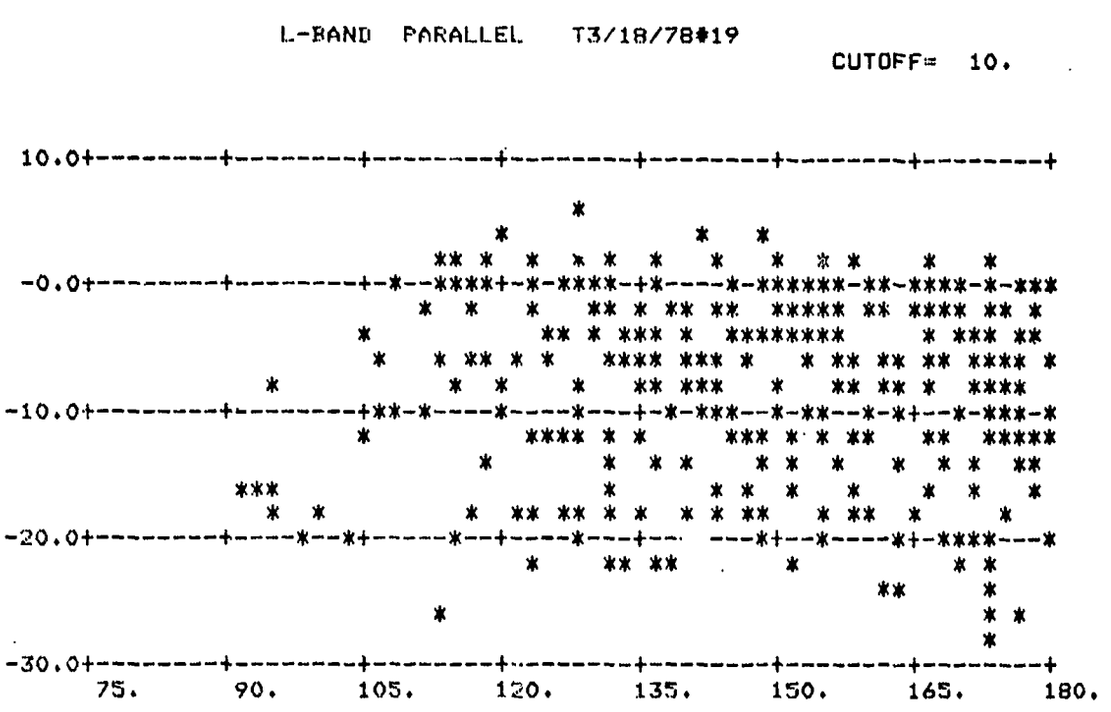

FIGURE A-38. σ_o vs ϕ_s; $\theta_s = 70°$, $\theta_i = 80°$

(Above: All Data; Below: Averages Over 5° Intervals)

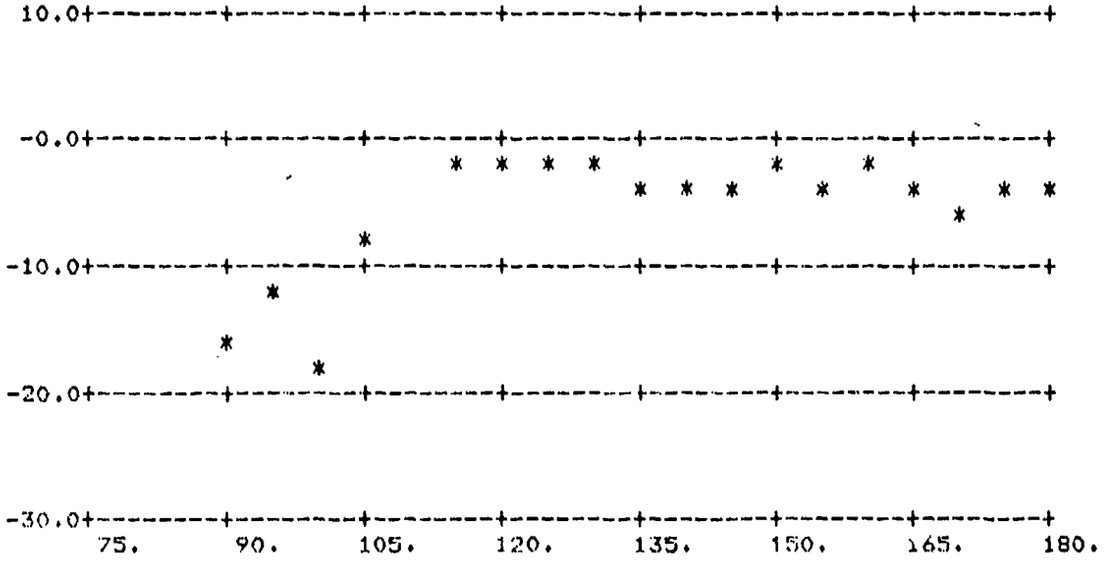

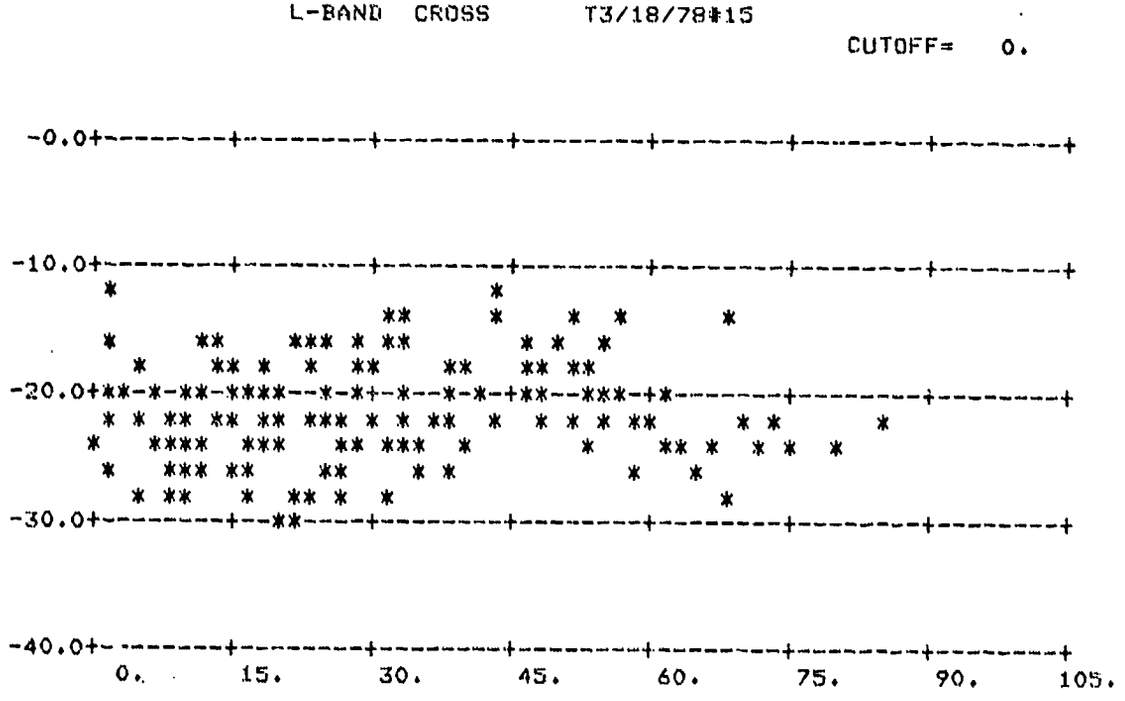

FIGURE A-39. σ_o vs ϕ_s; $\theta_s = 70°$, $\theta_i = 80°$

(Above: All Data; Below: Averages Over 5° Intervals)

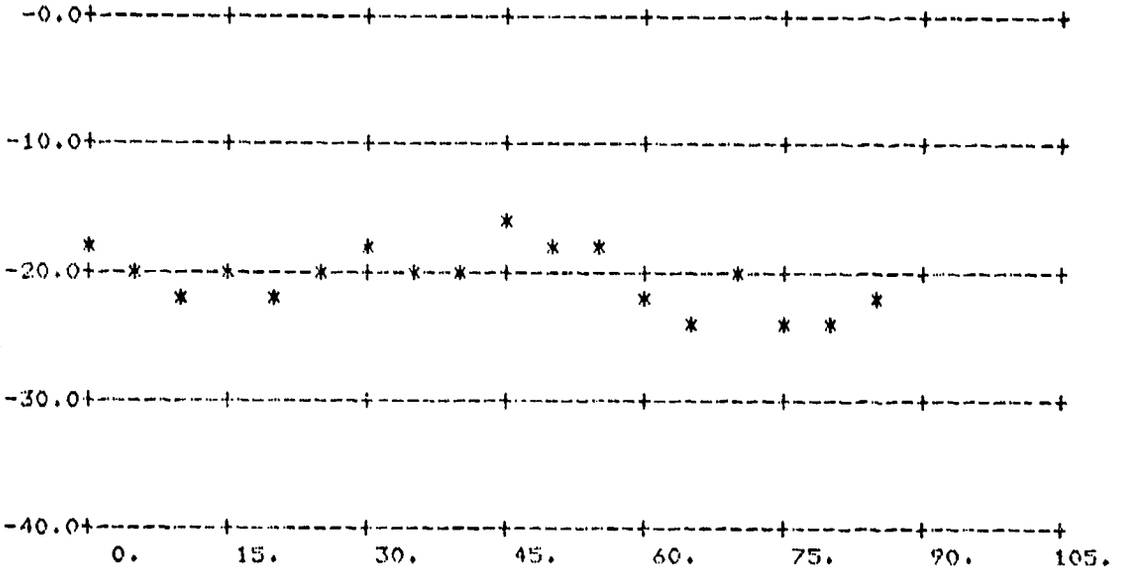

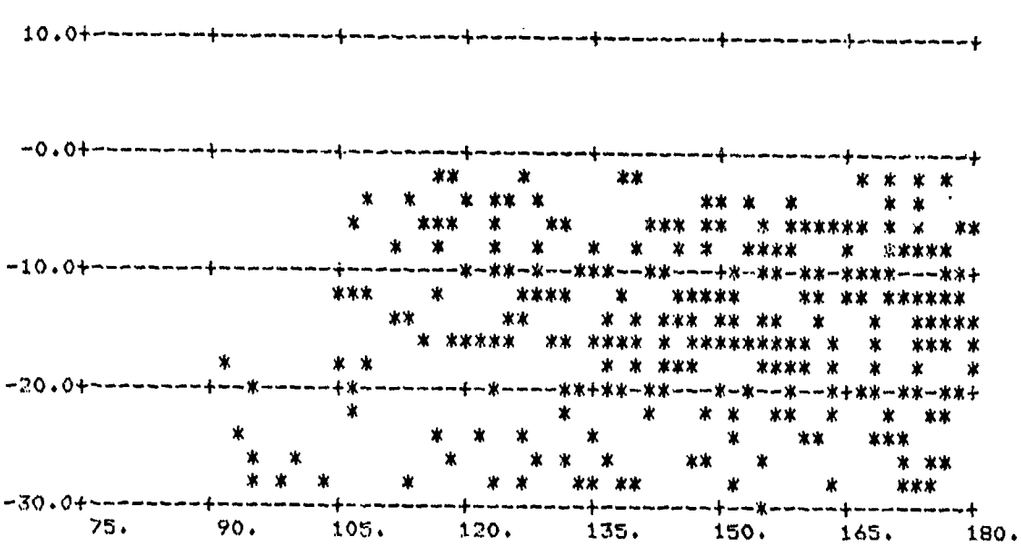

FIGURE A-40. σ_o vs ϕ_s; $\theta_s = 70°$, $\theta_i = 80°$

(Above: All Data; Below: Averages Over 5° Intervals)

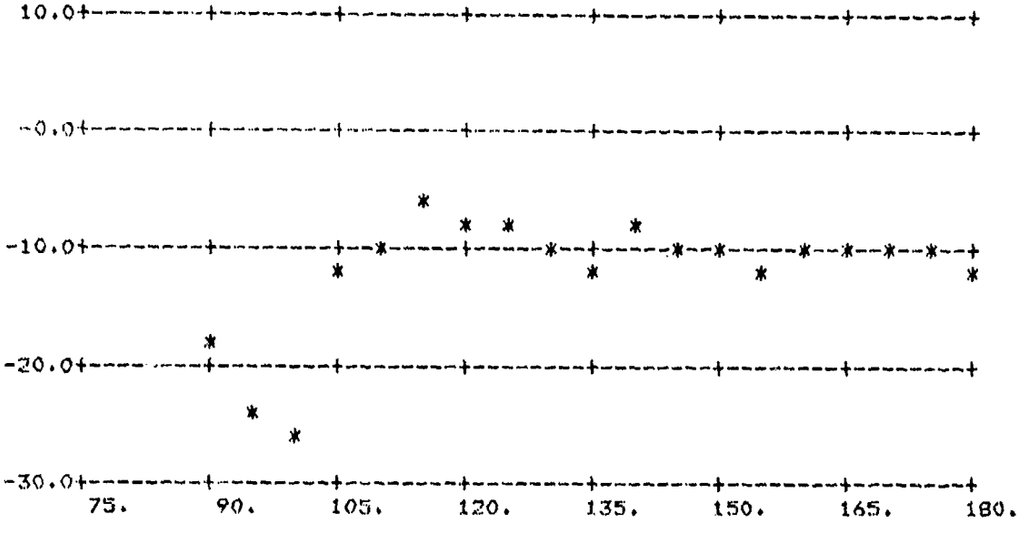

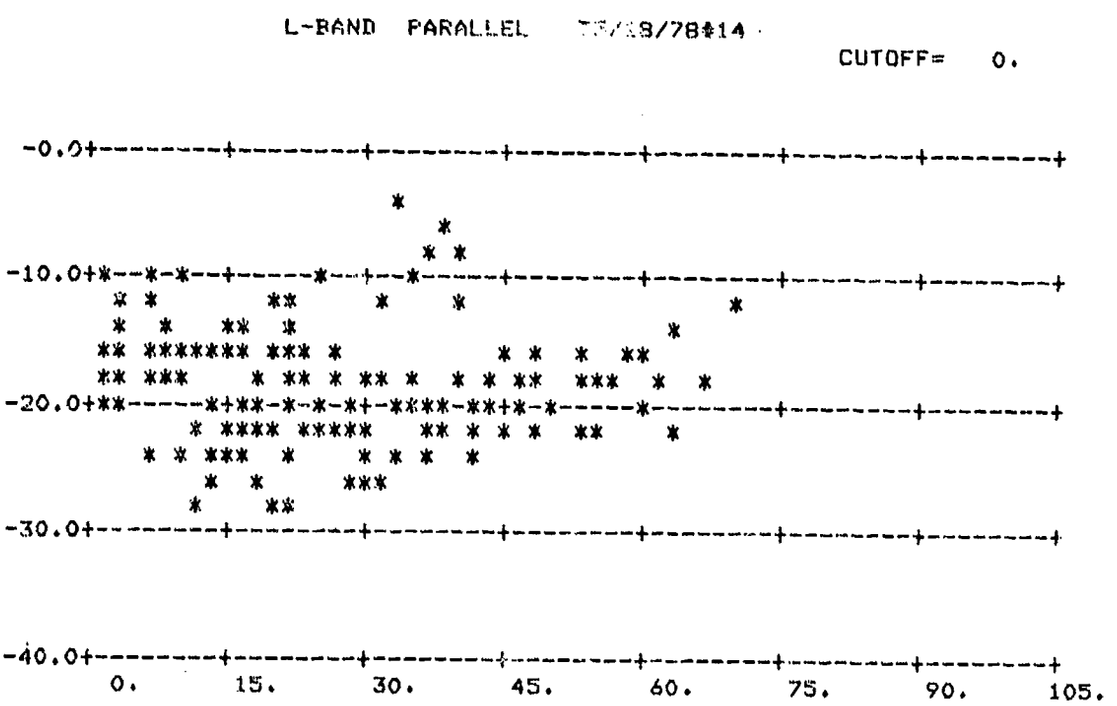

FIGURE A-41. σ_o vs ϕ_s; $\theta_s = 80°$, $\theta_i = 80°$

(Above: All Data; Below: Averages Over 5° Intervals)

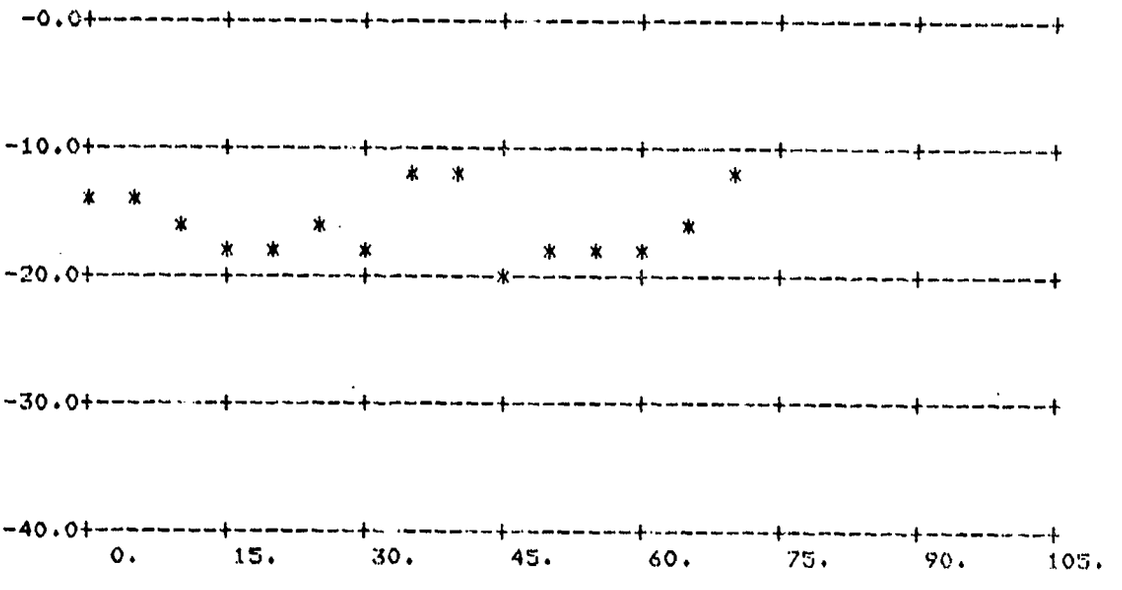

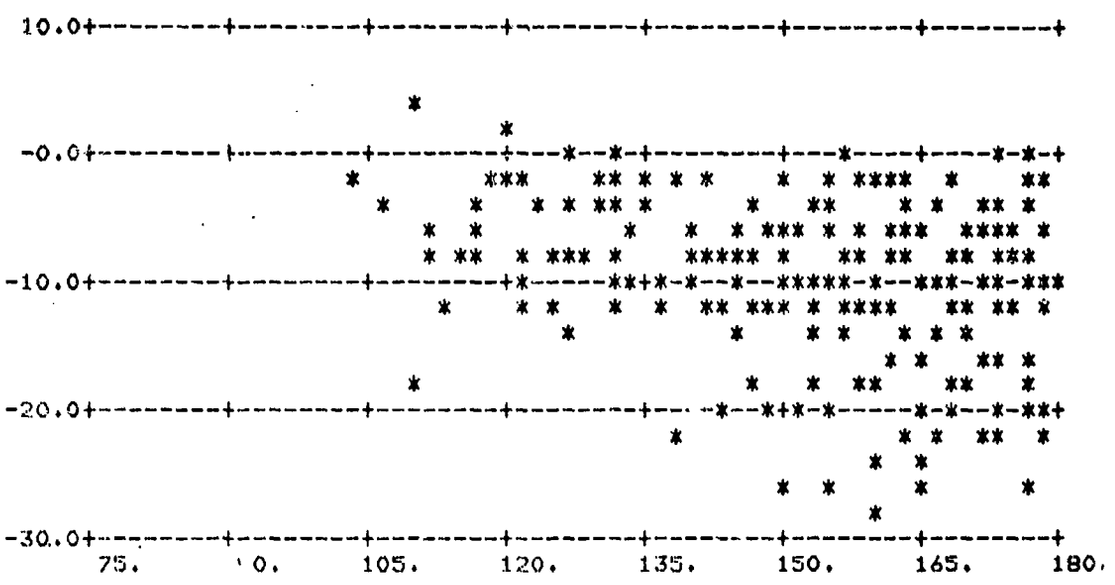

FIGURE A-42. σ_o vs ϕ_s; $\theta_s = 80°$, $\theta_i = 80°$

(Above: All Data; Below: Averages Over 5° Intervals)

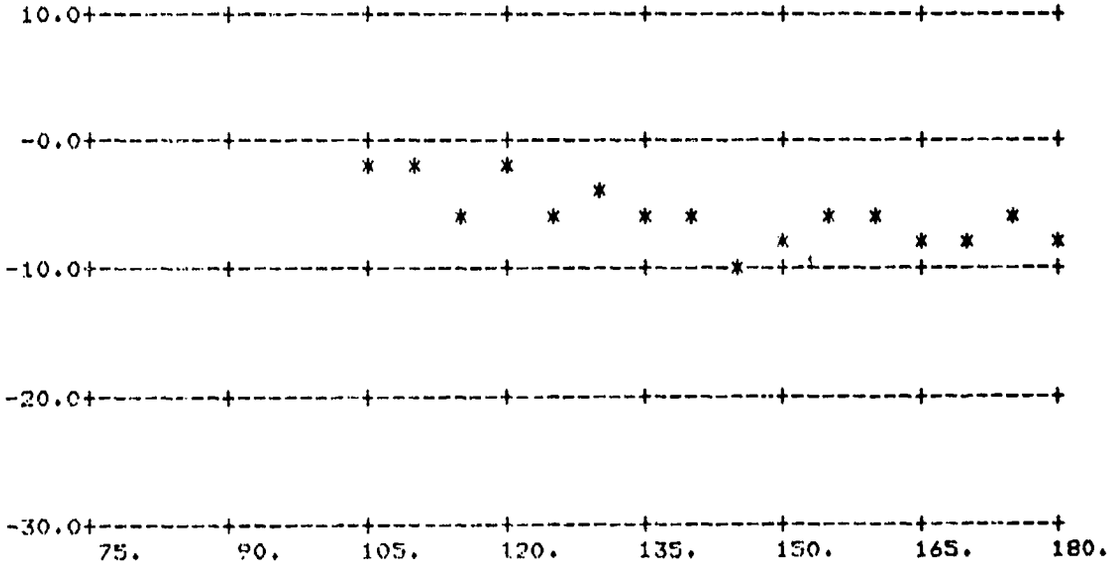

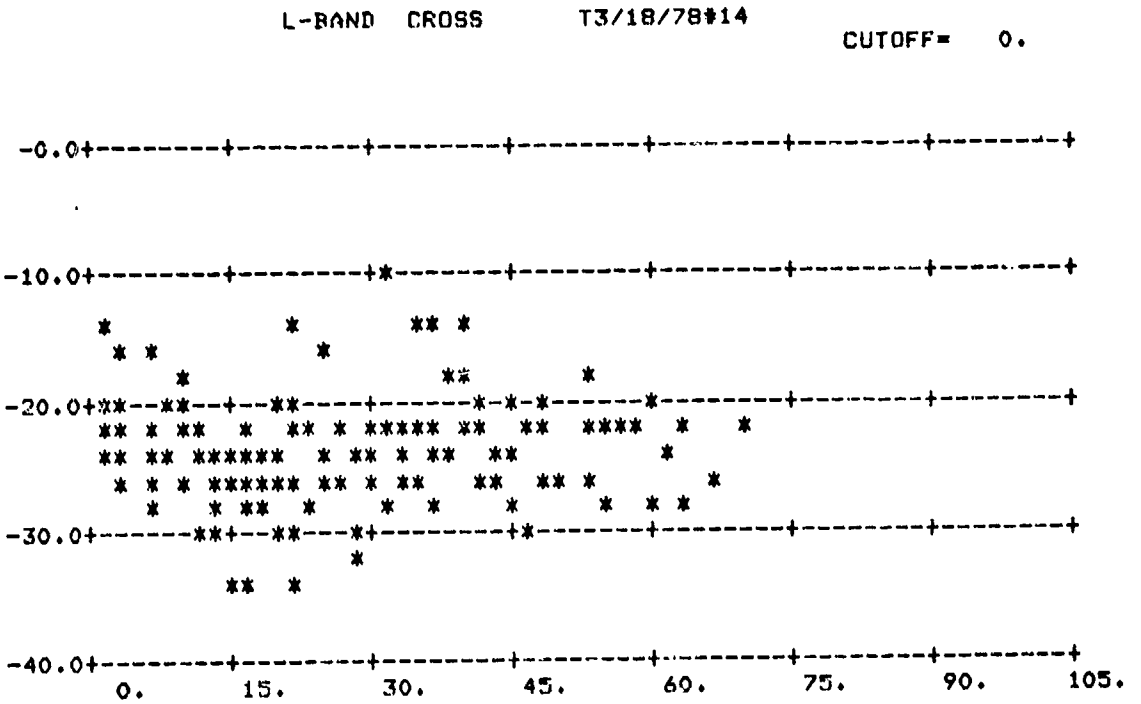

FIGURE A-43. σ_o vs ϕ_s; $\theta_s = 80°$, $\theta_i = 80°$

(Above: All Data; Below: Averages Over 5° Intervals)

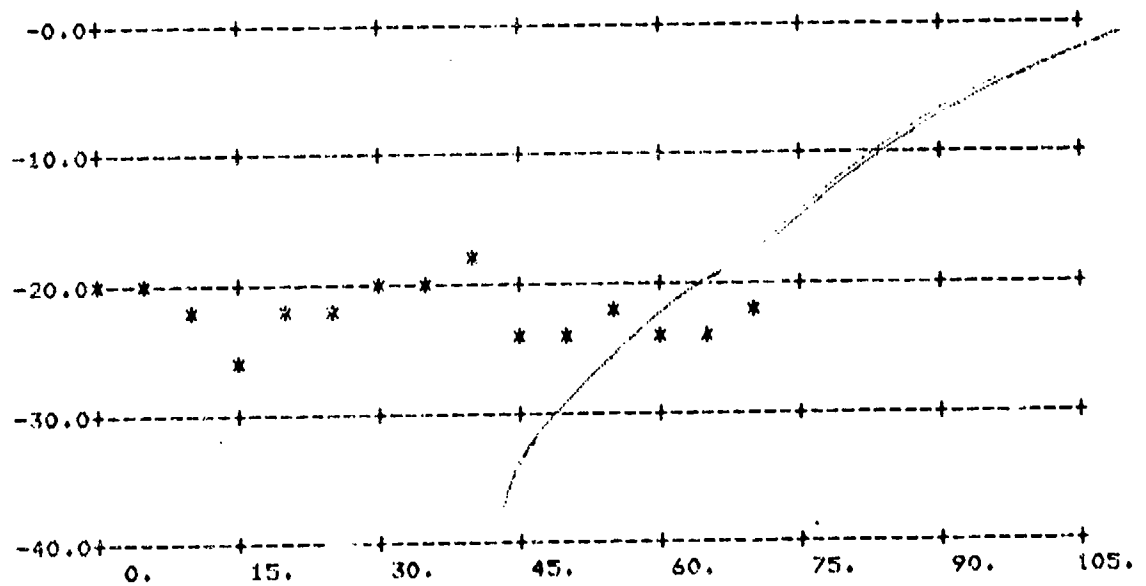

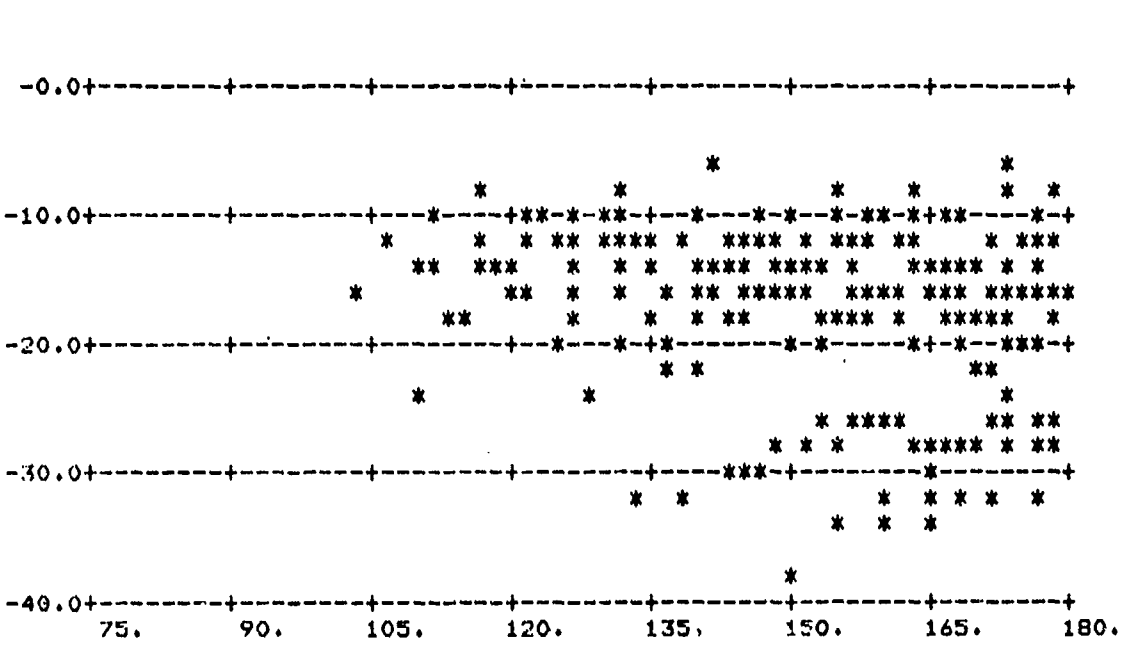

FIGURE A-44. σ_o vs ϕ_s; $\theta_s = 80°$, $\theta_i = 80°$

(Above: All Data; Below: Averages Over 5° Intervals)

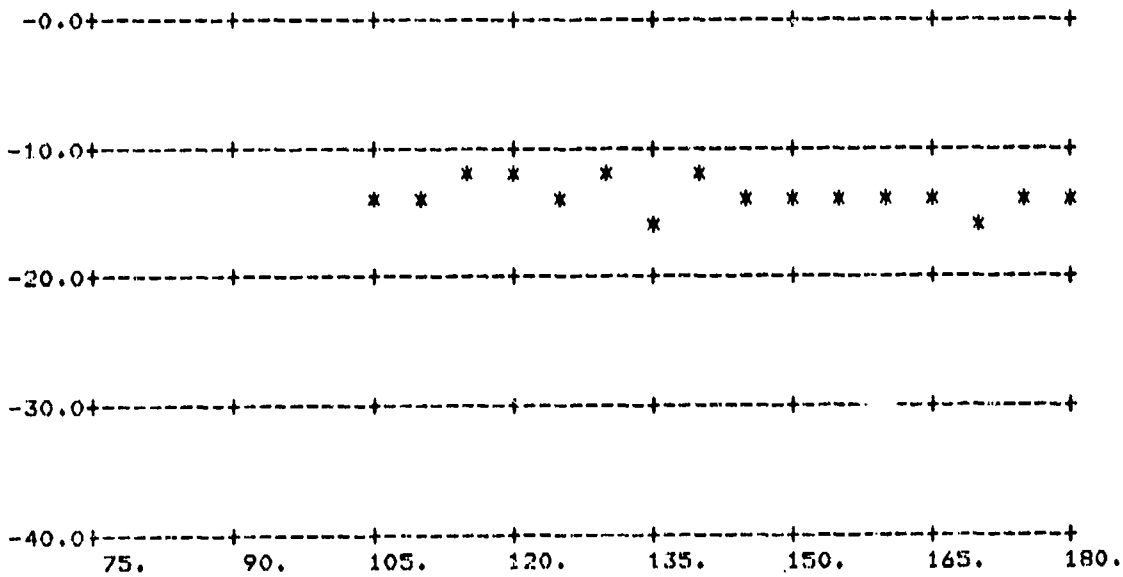

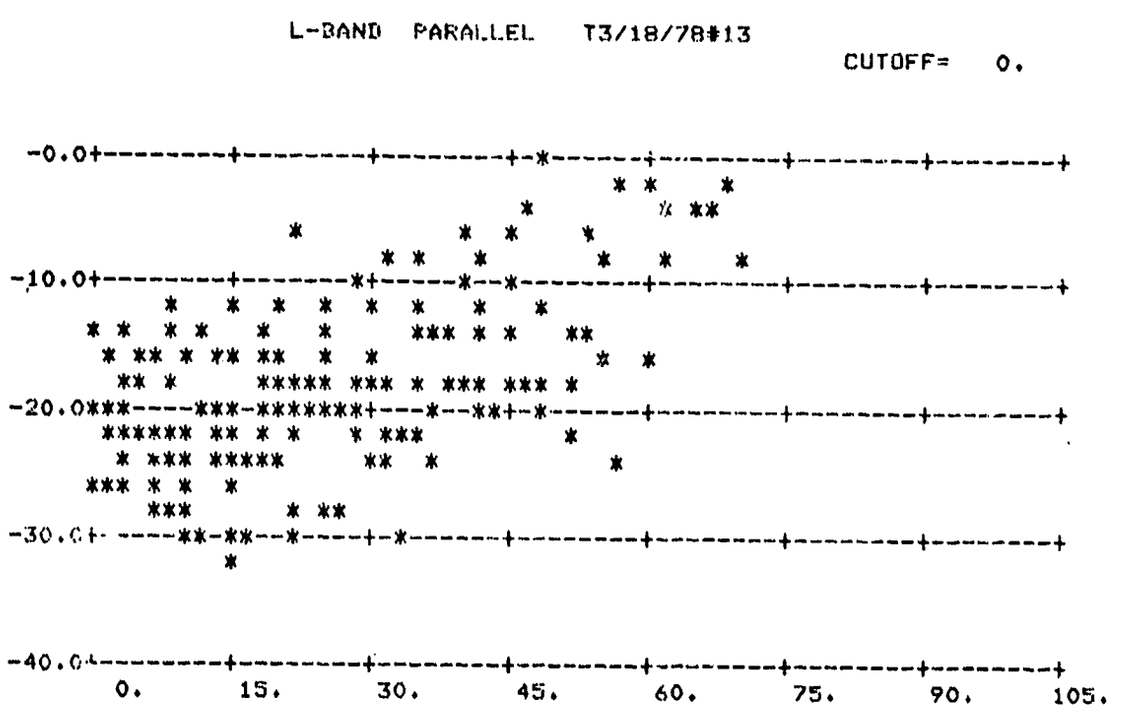

FIGURE A-45. σ_o vs ϕ_s; $\theta_s = 84°$, $\theta_i = 80°$

(Above: All Data; Below: Averages Over 5° Intervals)

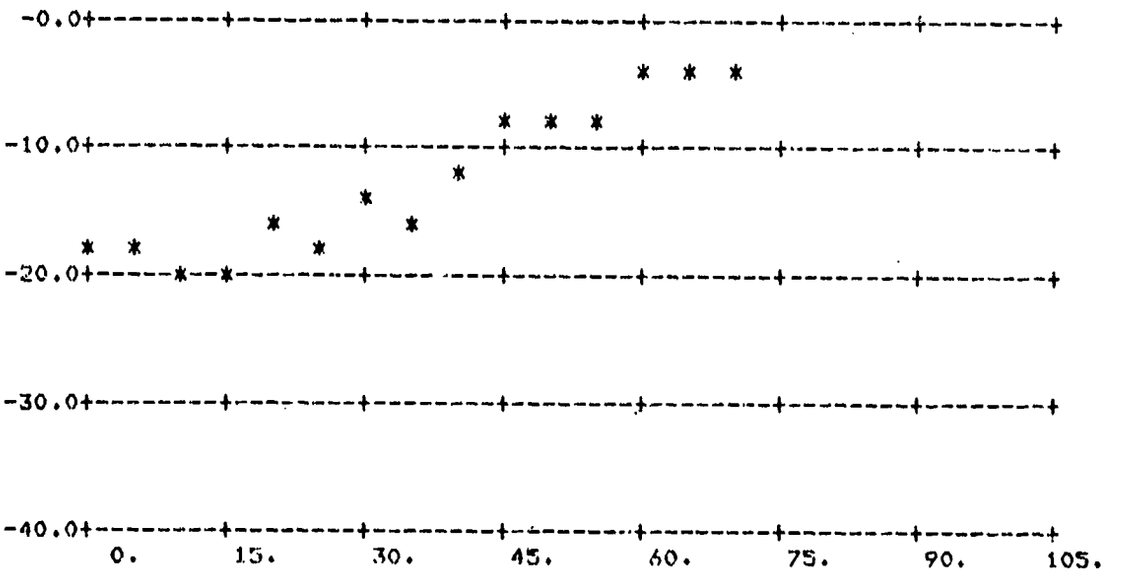

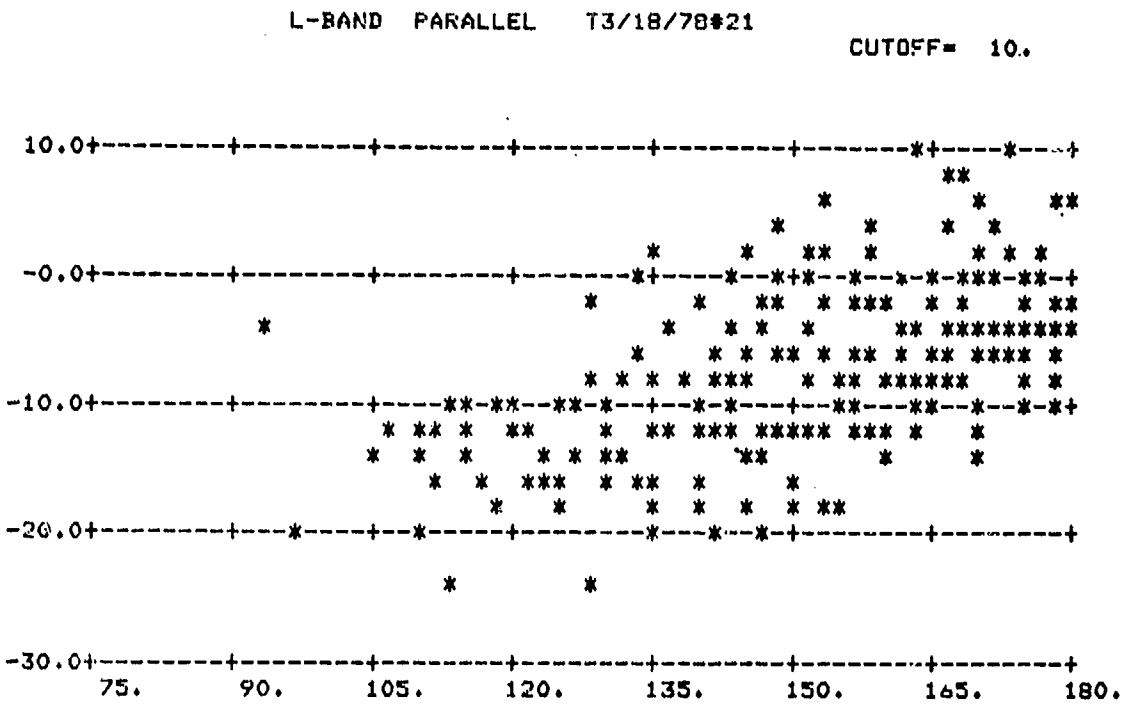

FIGURE A-46. σ_o vs ϕ_s; $\theta_s = 84°$, $\theta_i = 80°$

(Above: All Data; Below: Averages Over 5° Intervals)

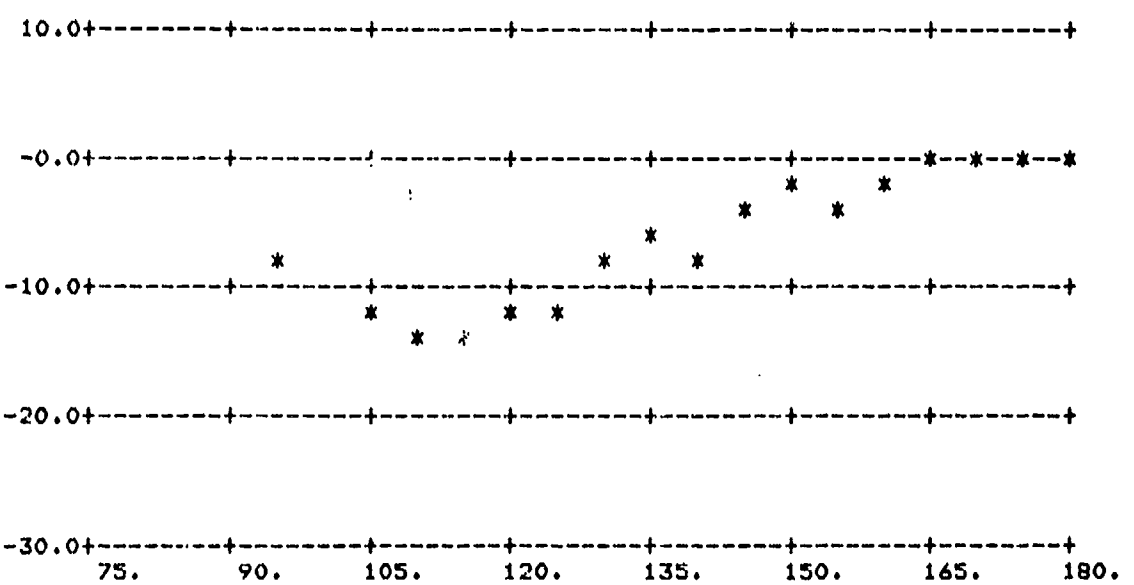

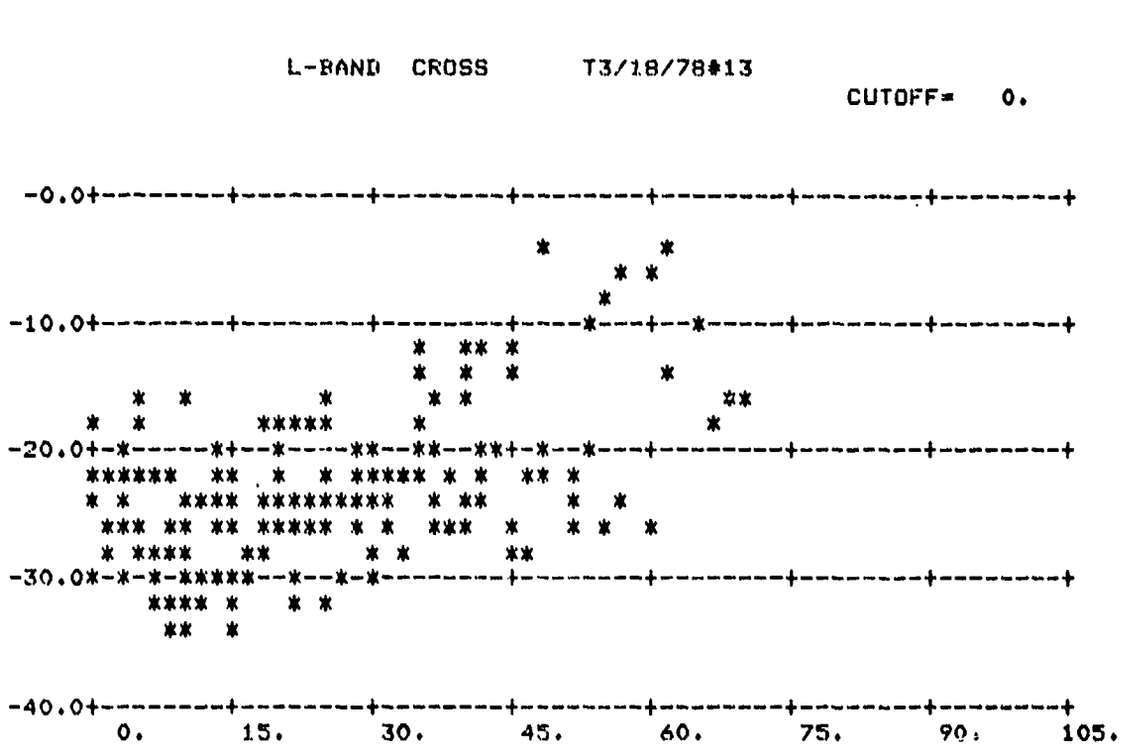

FIGURE A-47. σ_o vs ϕ_s; $\theta_s = 84°$, $\theta_i = 80°$

(Above: All Data; Below: Averages Over 5° Intervals)

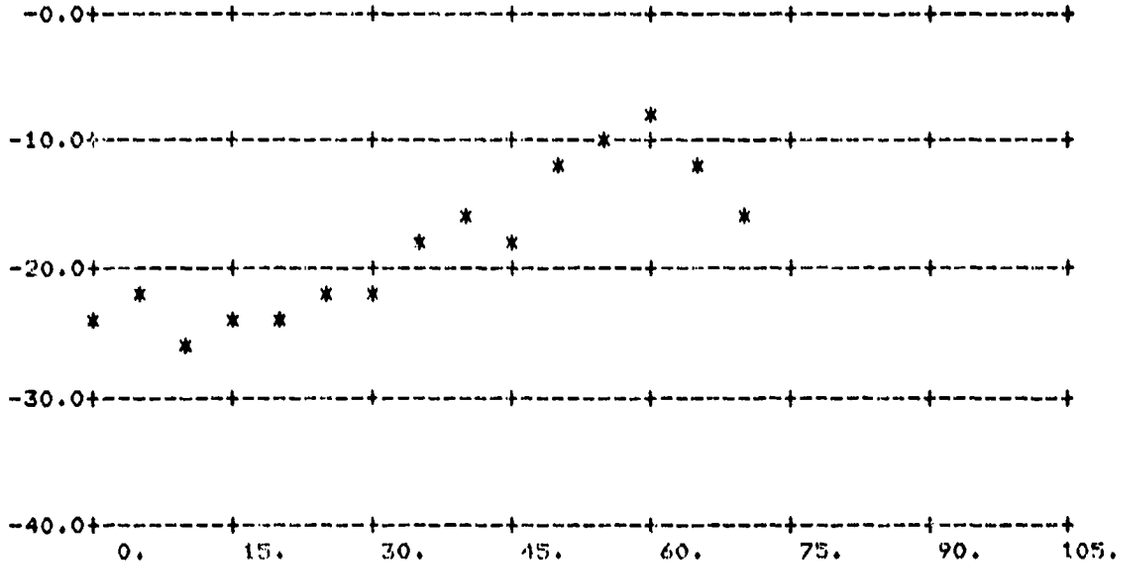

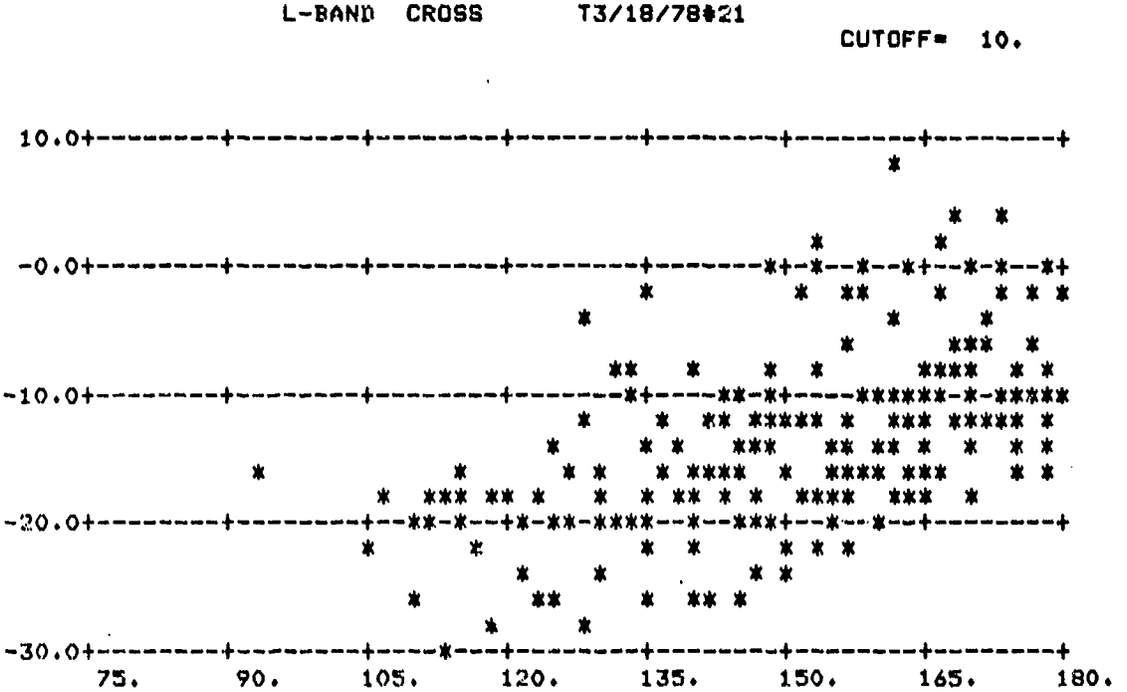

FIGURE A-48. σ_o vs ϕ_s; $\theta_s = 84°$, $\theta_i = 80°$

(Above: All Data; Below: Averages Over 5° Intervals)

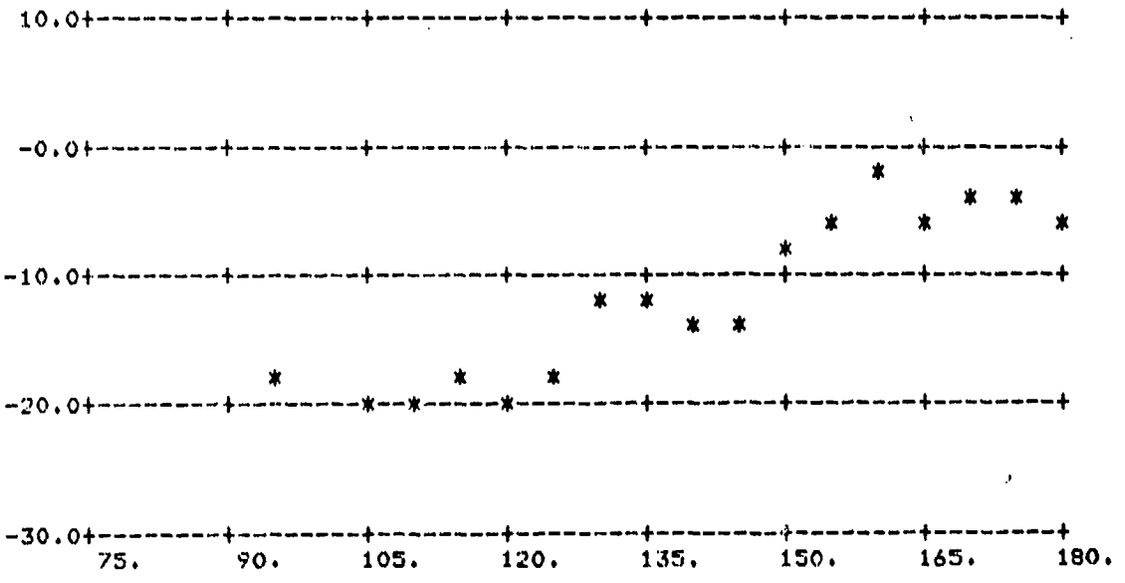

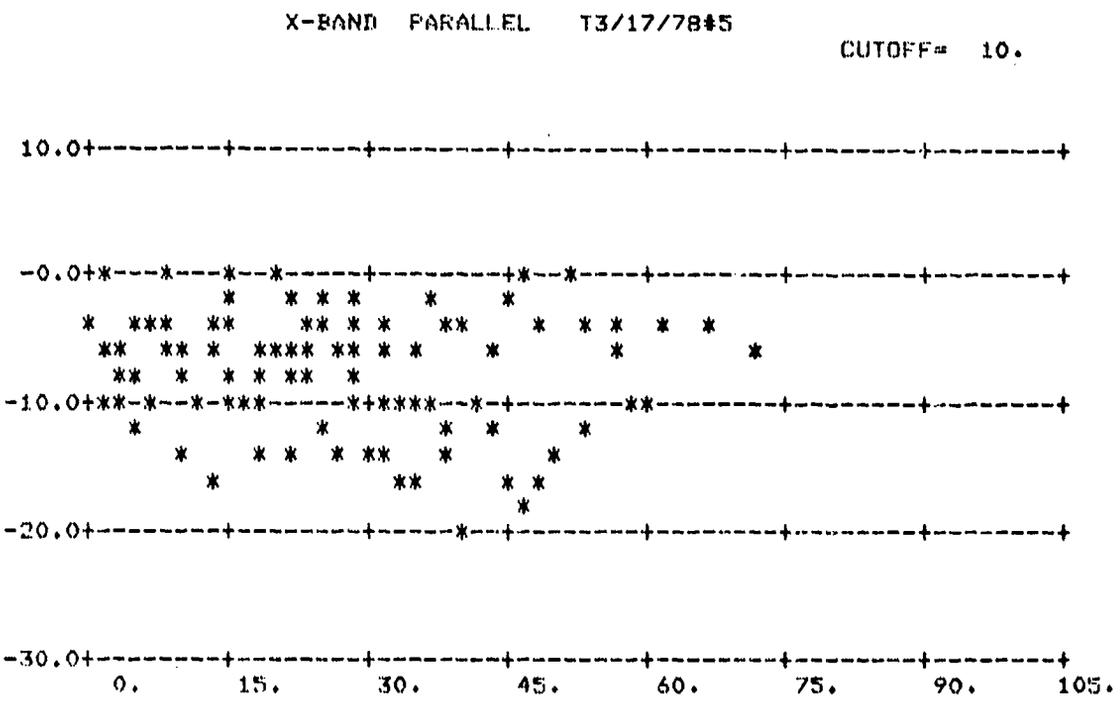

FIGURE A-49. σ_o vs ϕ_s; $\theta_s = 60°$, $\theta_i = 60°$

(Above: All Data; Below: Averages Over 5° Intervals)

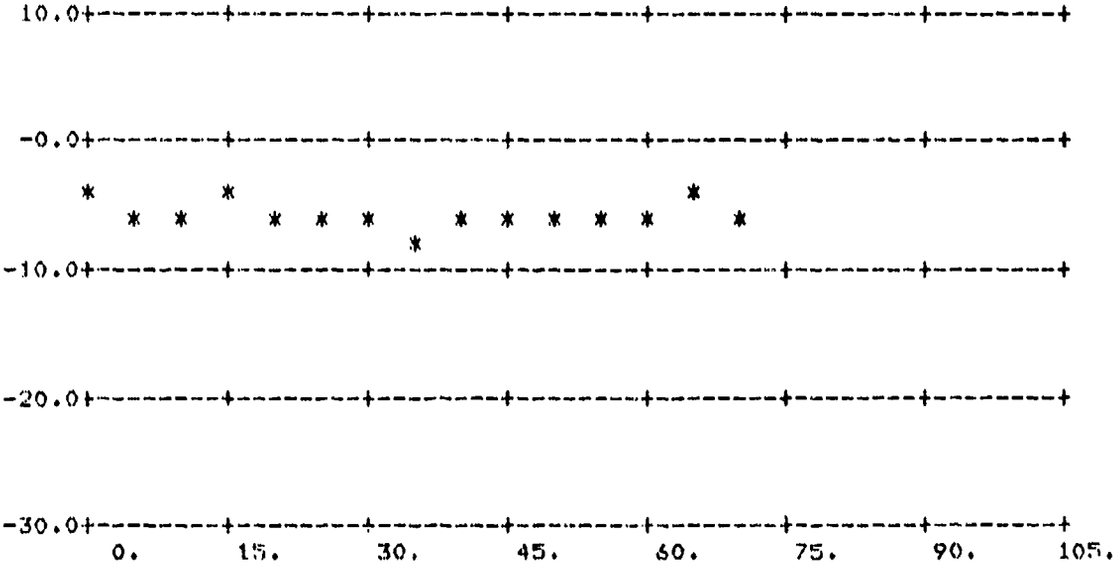

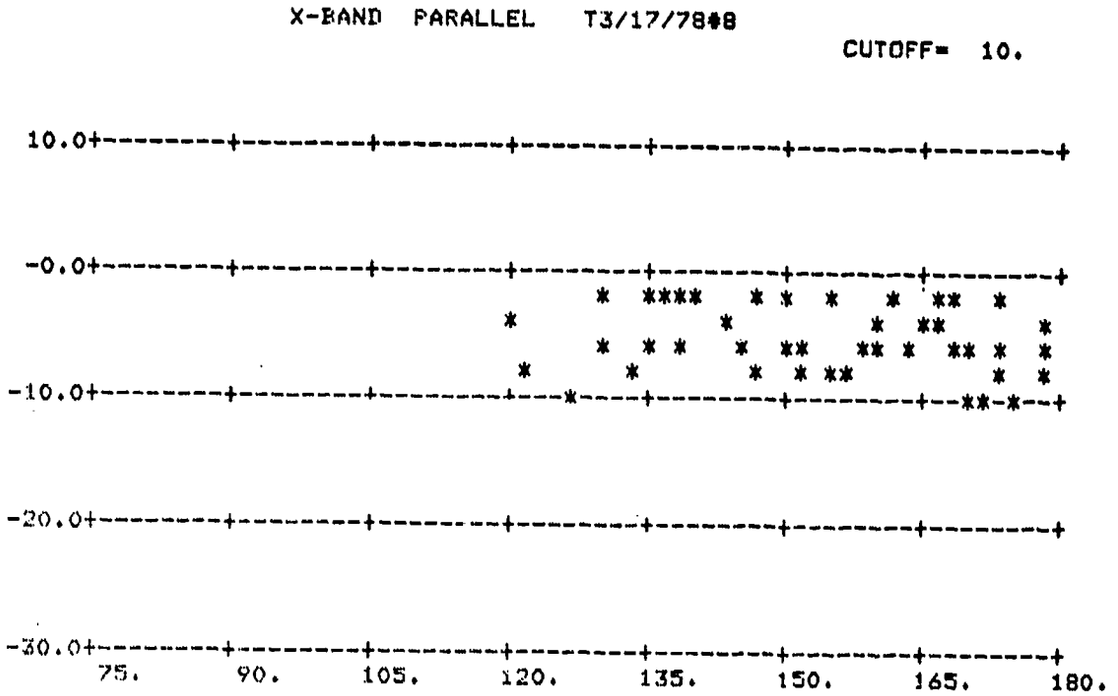

FIGURE A-50. σ_o vs ϕ_s; $\theta_s = 60°$, $\theta_i = 60°$

(Above: All Data; Below: Averages Over 5° Intervals)

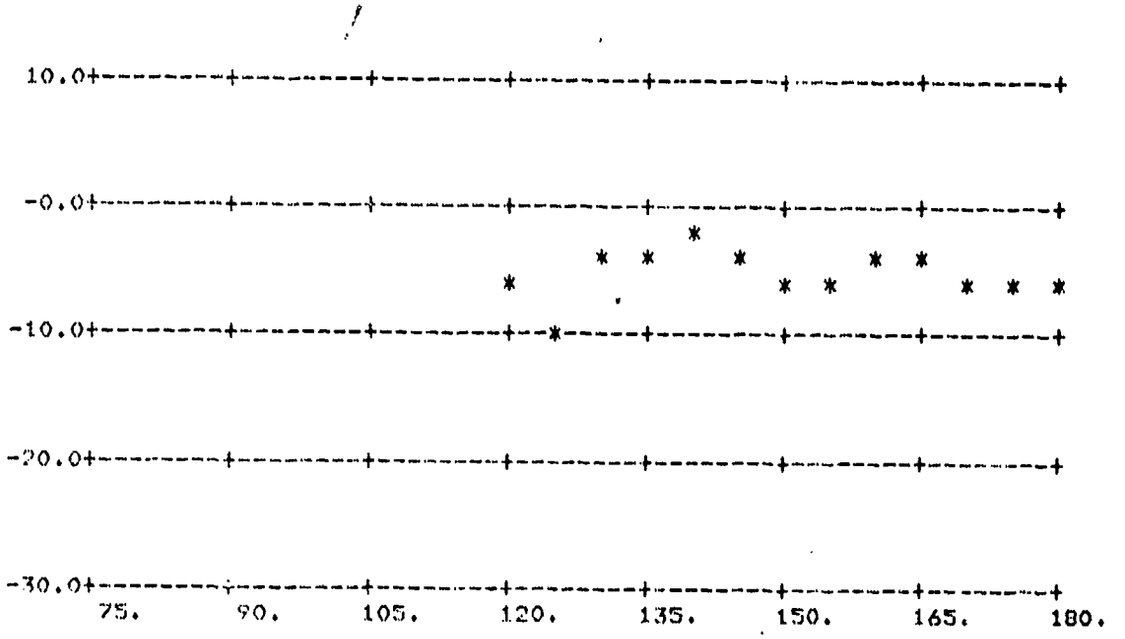

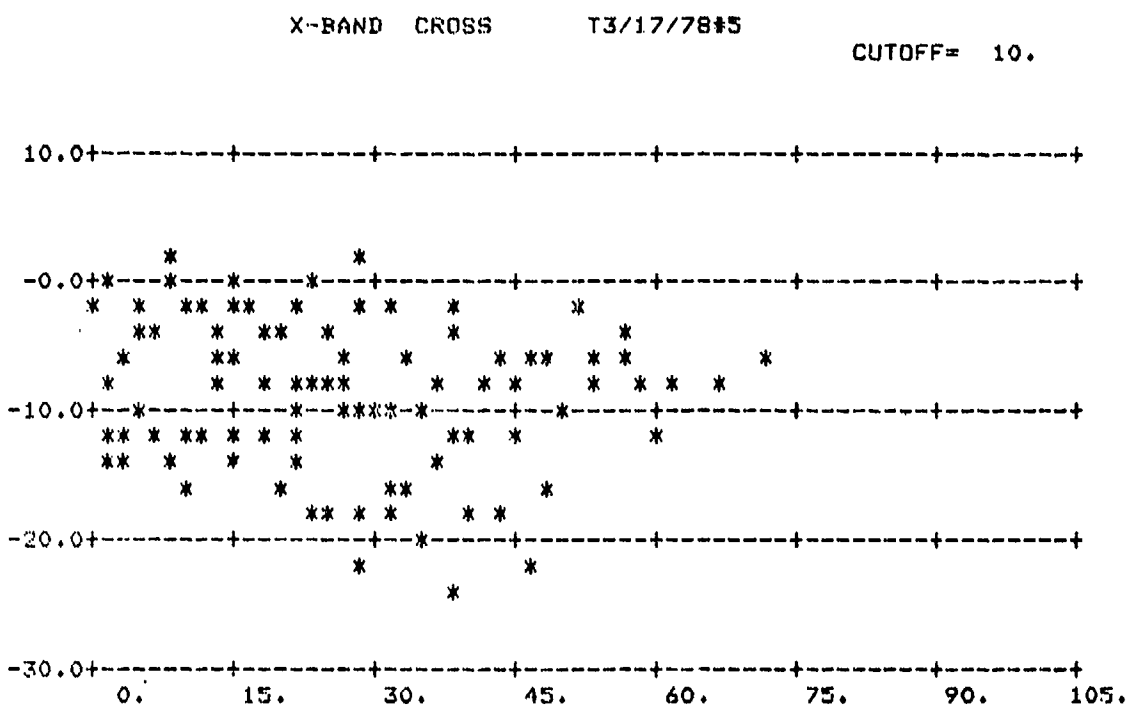

FIGURE A-51. σ_o vs ϕ_s; $\theta_s = 60°$, $\theta_i = 60°$

(Above: All Data; Below: Averages Over 5° Intervals)

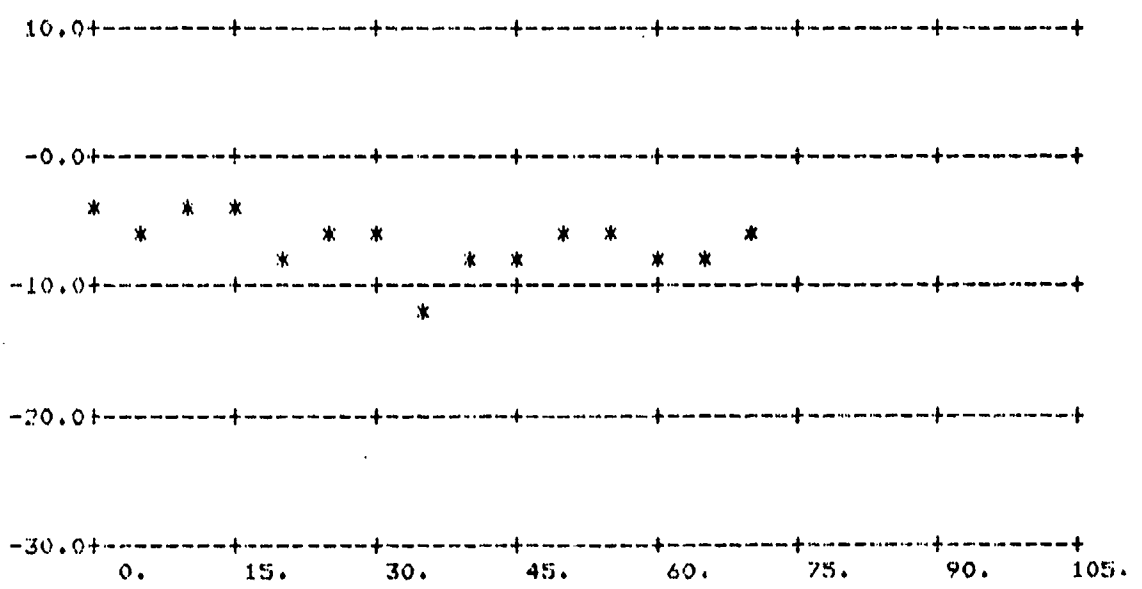

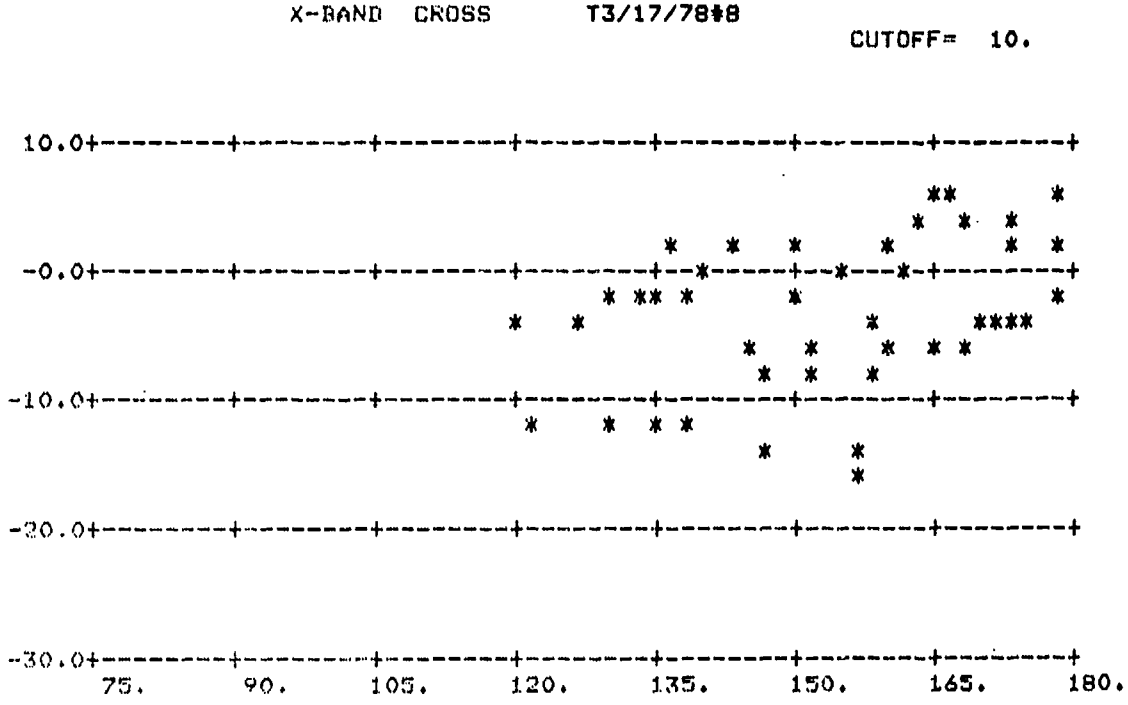

FIGURE A-52. σ_o vs ϕ_s; $\theta_s = 60°$, $\theta_i = 60°$

(Above: All Data; Below: Averages Over 5° Intervals)

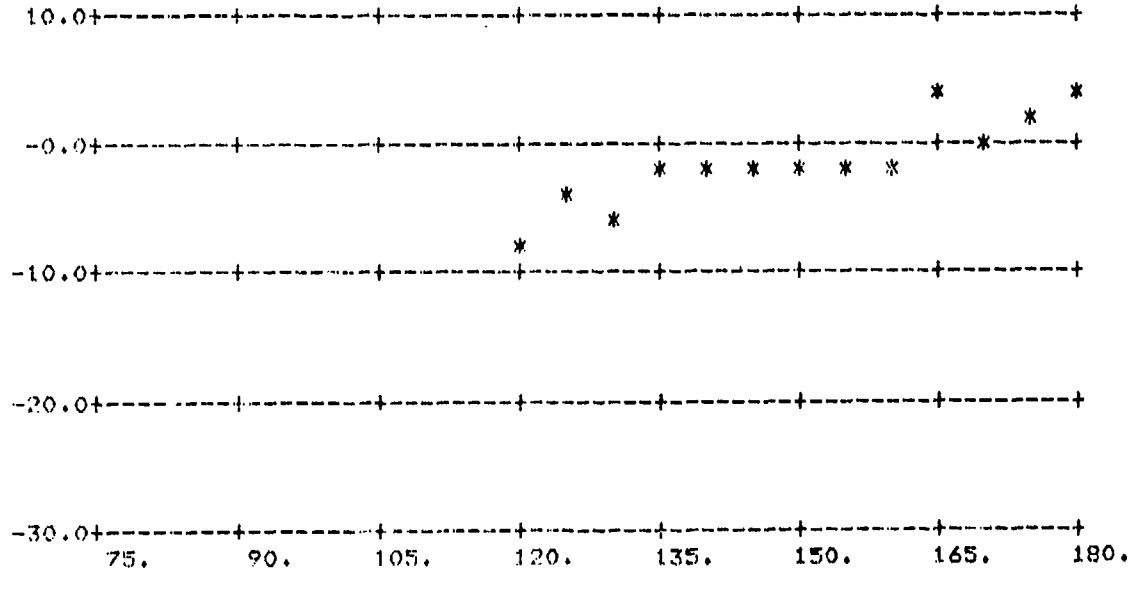

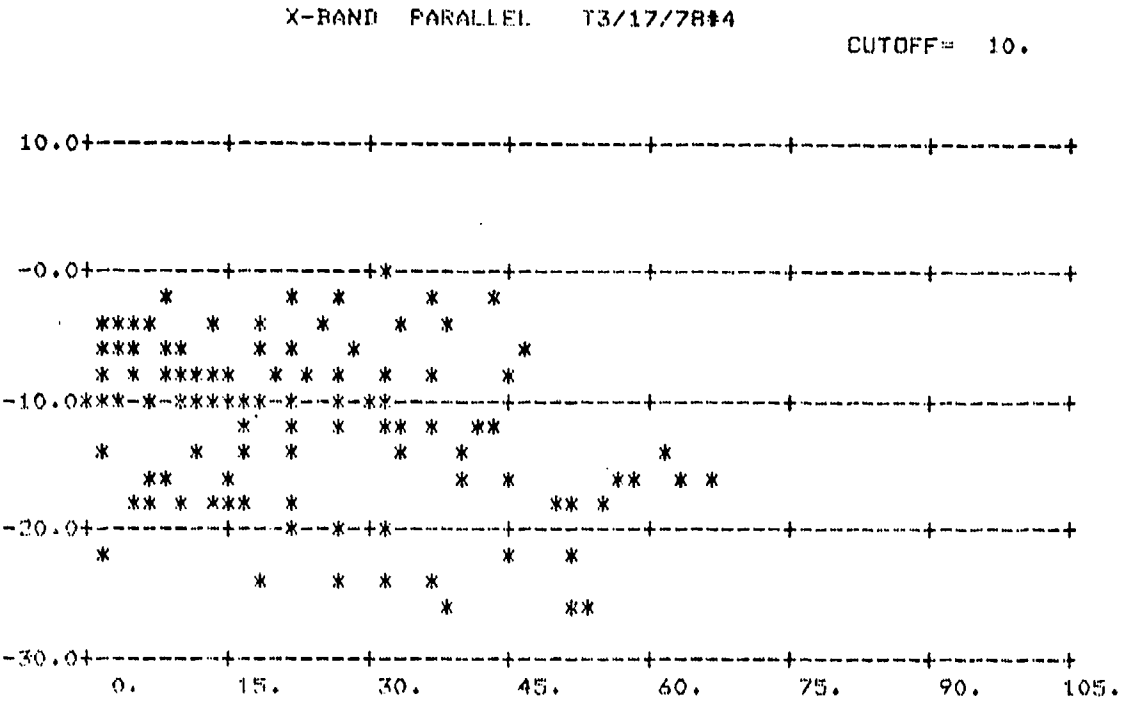

FIGURE A-53. σ_o vs ϕ_s ; $\theta_s = 70°$, $\theta_i = 60°$

(Above: All Data; Below: Averages Over 5° Intervals)

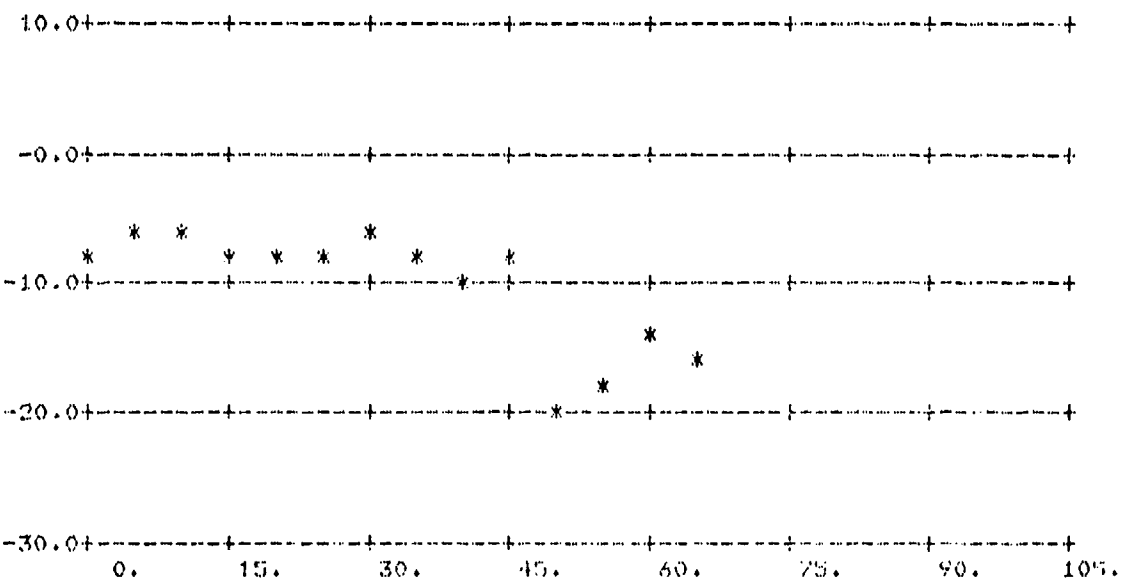

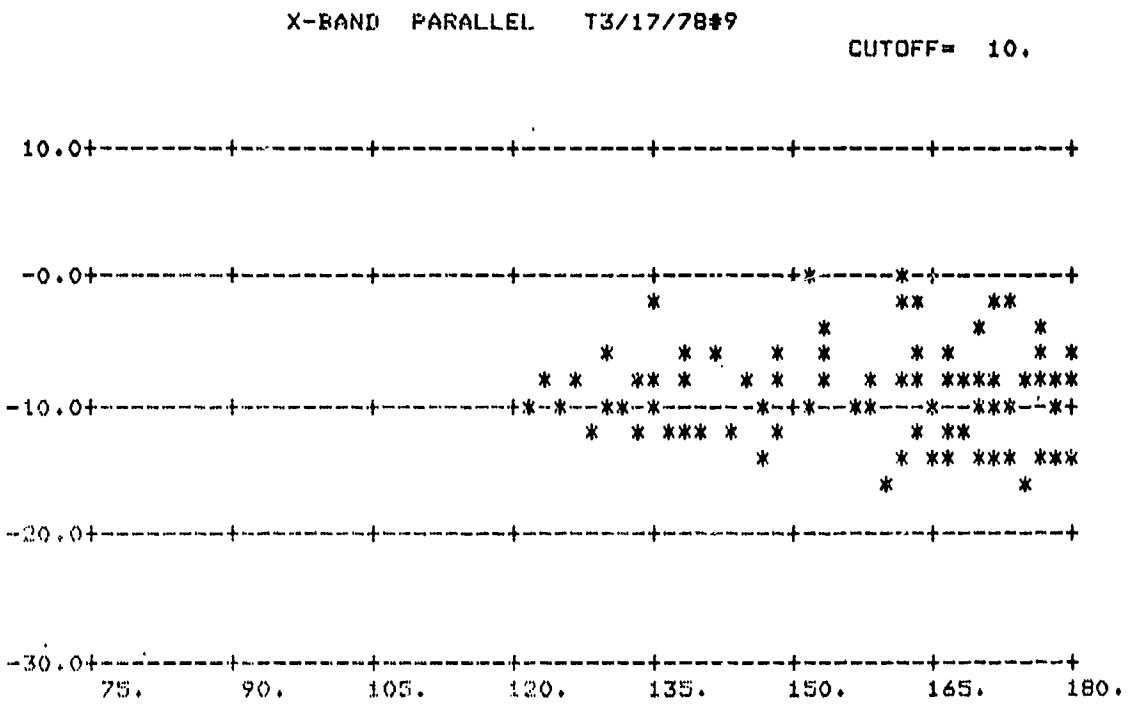

FIGURE A-54. σ_o vs ϕ_s; $\theta_s = 70°$, $\theta_i = 60°$

(Above: All Data; Below: Averages Over 5° Intervals)

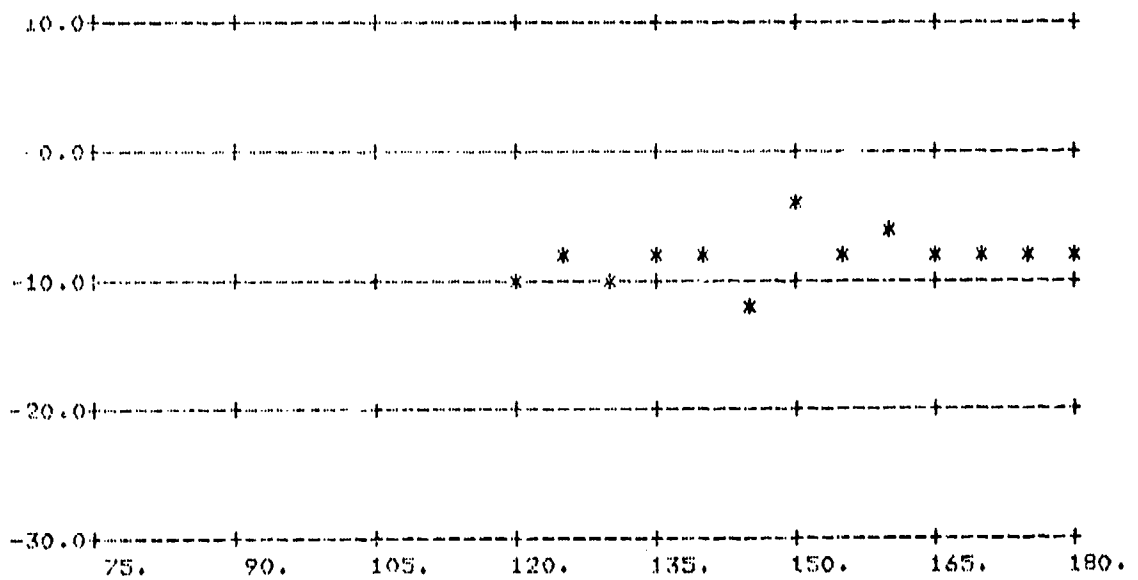

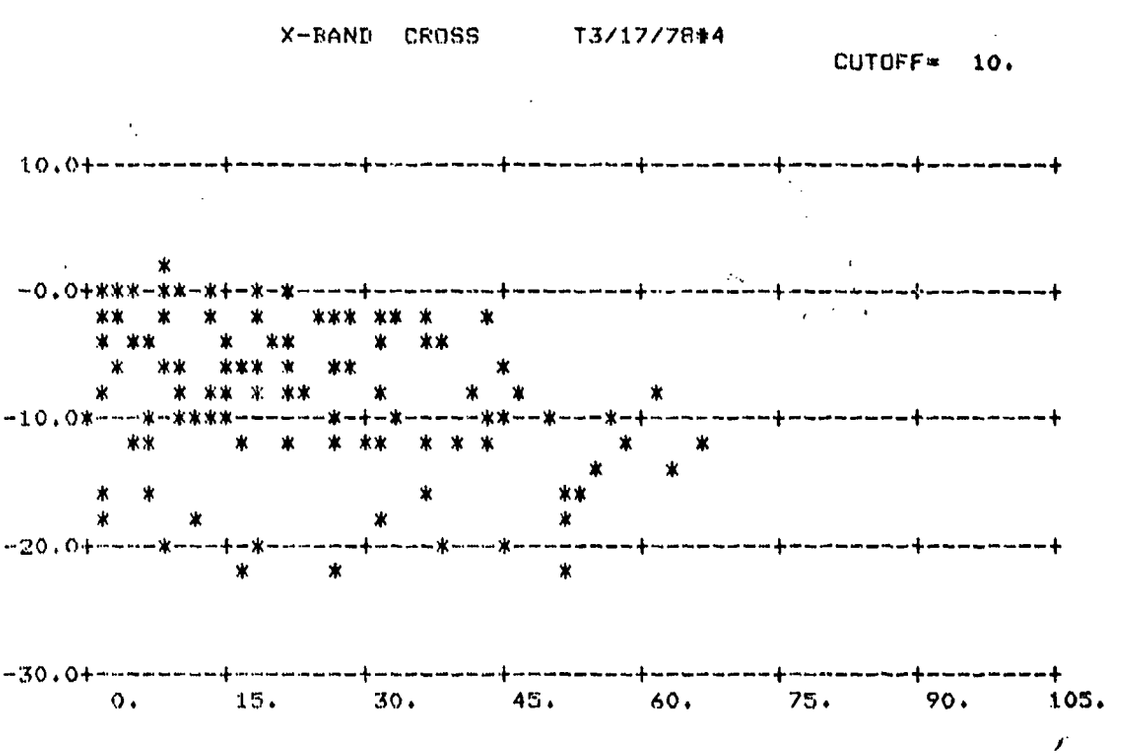

FIGURE A-55. σ_o vs ϕ_s; $\theta_s = 70°$, $\theta_i = 60°$

(Above: All Data; Below: Averages Over 5° Intervals)

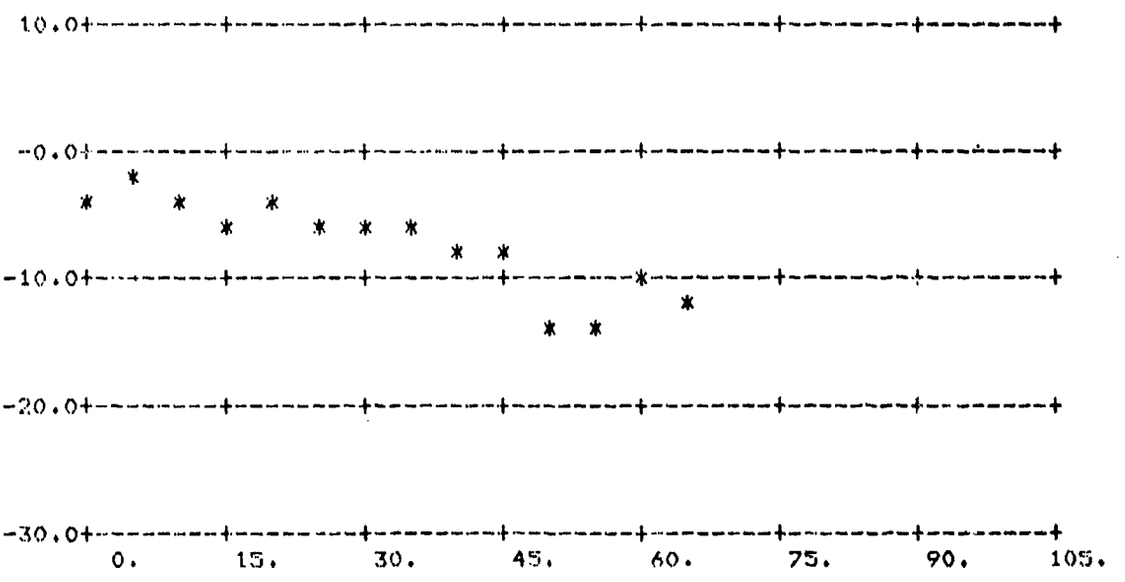

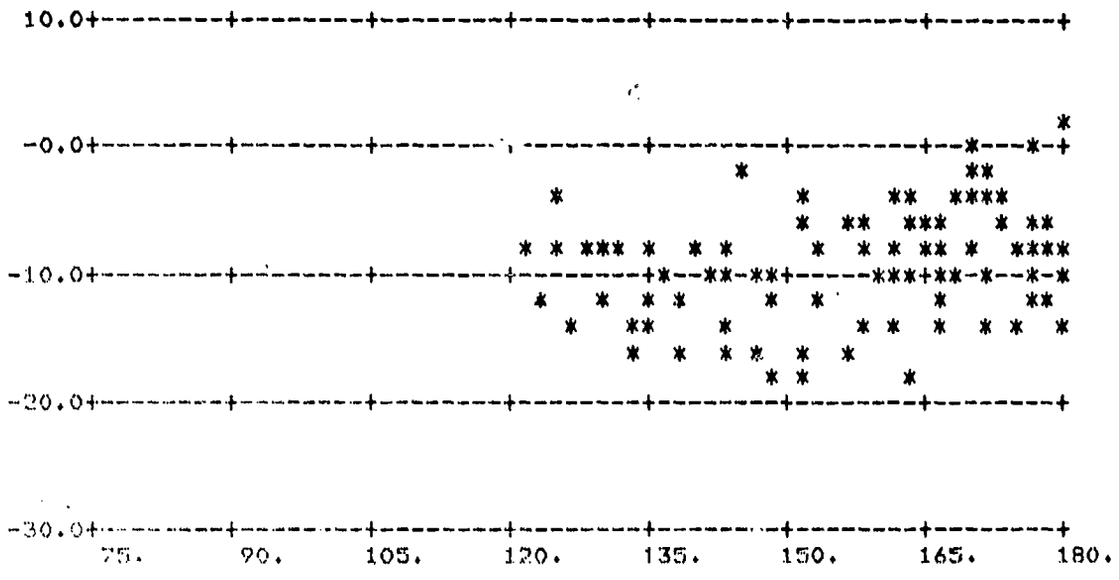

FIGURE A-56. σ_o vs ϕ_s; $\theta_s = 70°$, $\theta_i = 60°$

(Above: All Data; Below: Averages Over 5° Intervals)

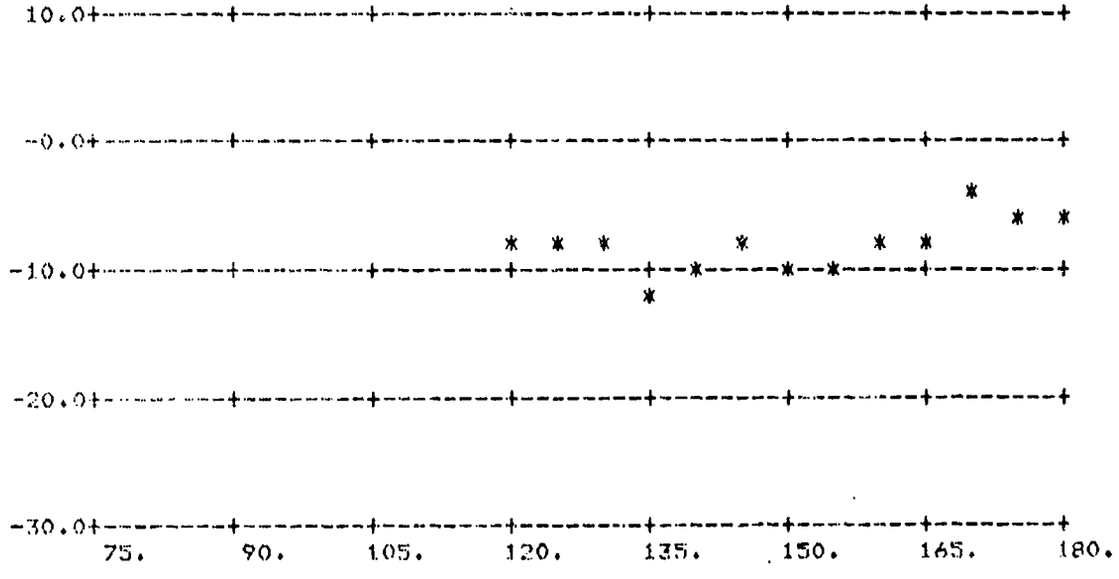

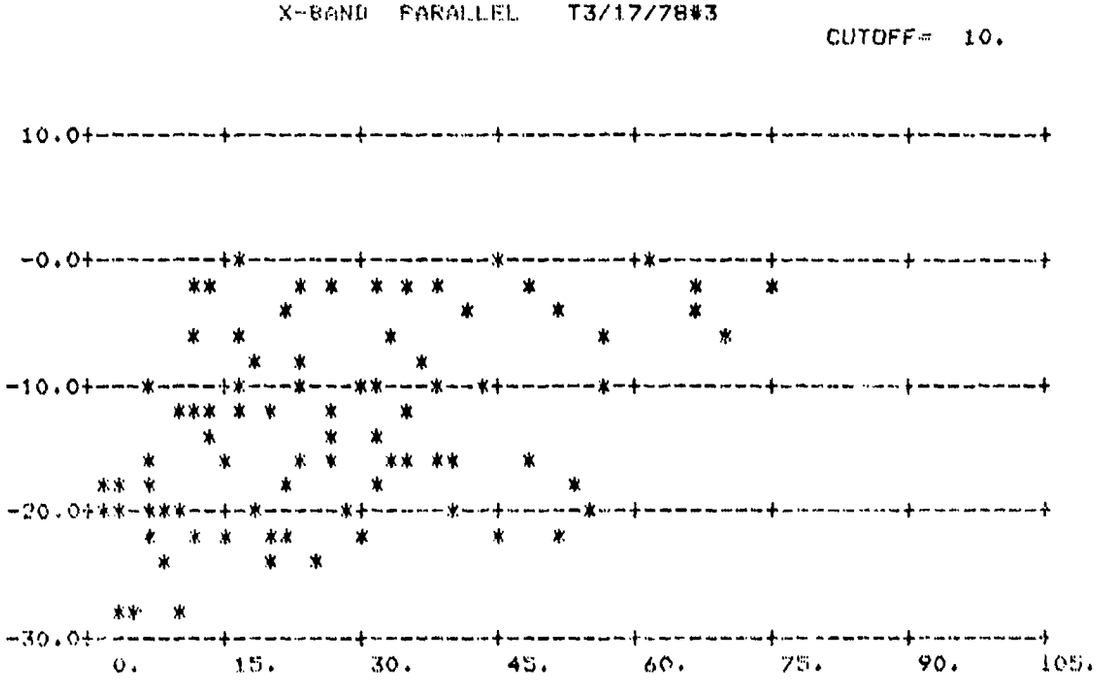

FIGURE A-57. σ_o vs ϕ_s; $\theta_s = 80°$, $\theta_i = 60°$

(Above: All Data; Below: Averages Over 5° Intervals)

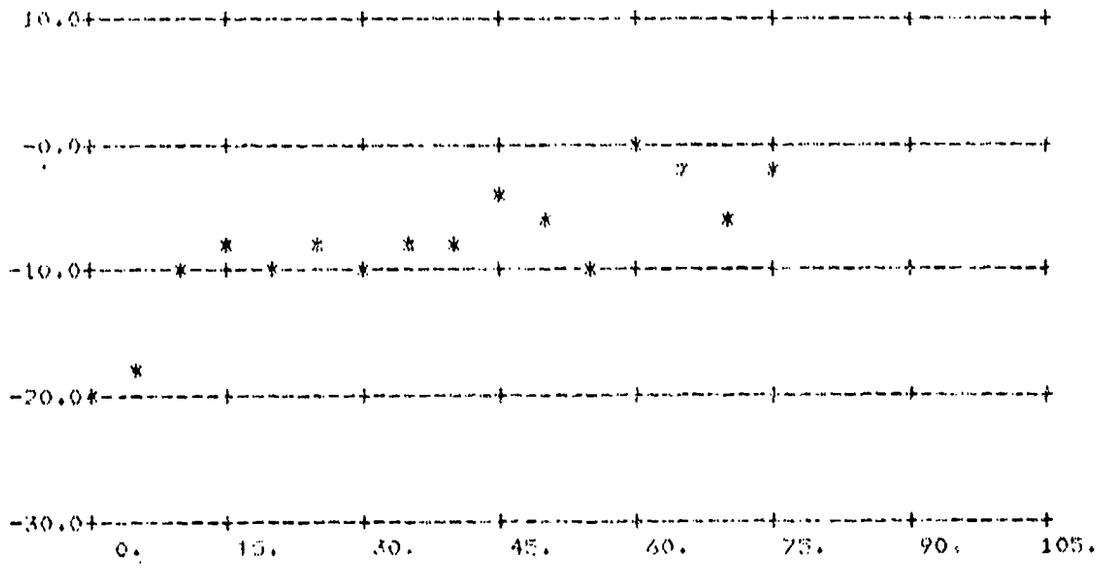

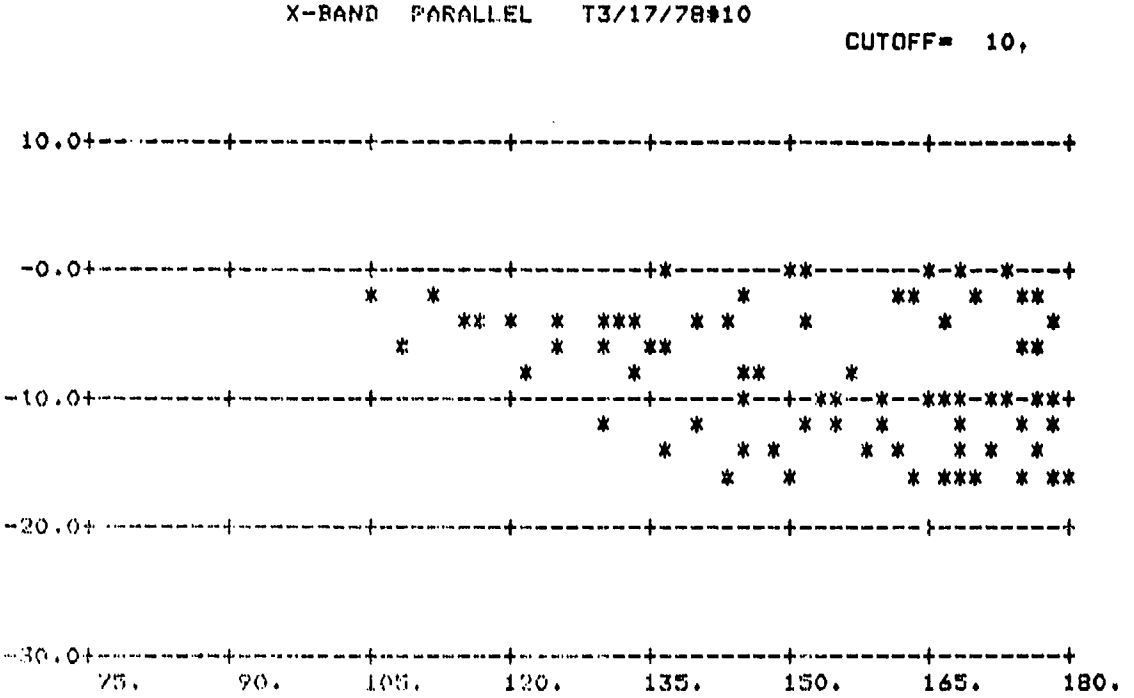

FIGURE A-58. σ_o vs ϕ_s; $\theta_s = 80°$, $\theta_i = 60°$

(Above: All Data; Below: Averages Over 5° Intervals)

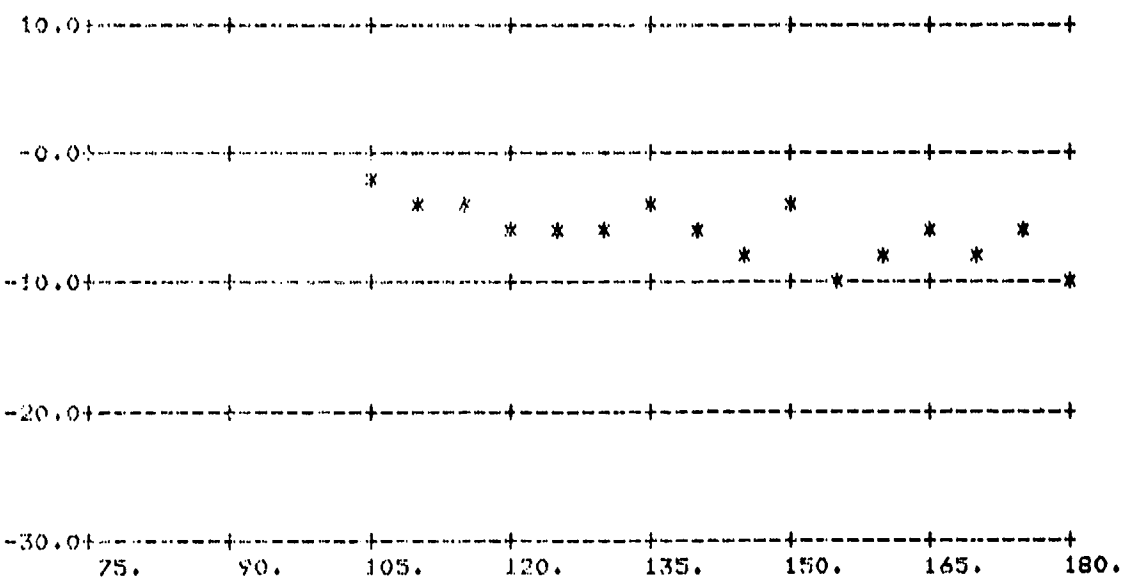

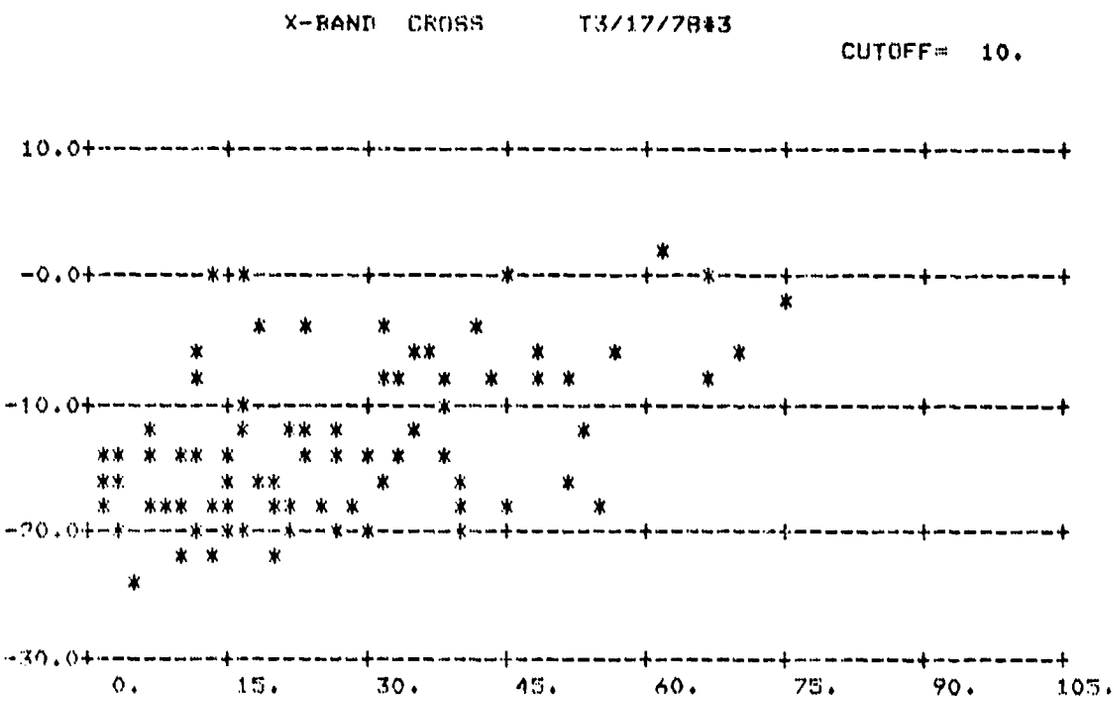

FIGURE A-59. σ_o vs ϕ_s; $\theta_s = 80°$, $\theta_i = 60°$

(Above: All Data; Below: Averages Over 5° Intervals)

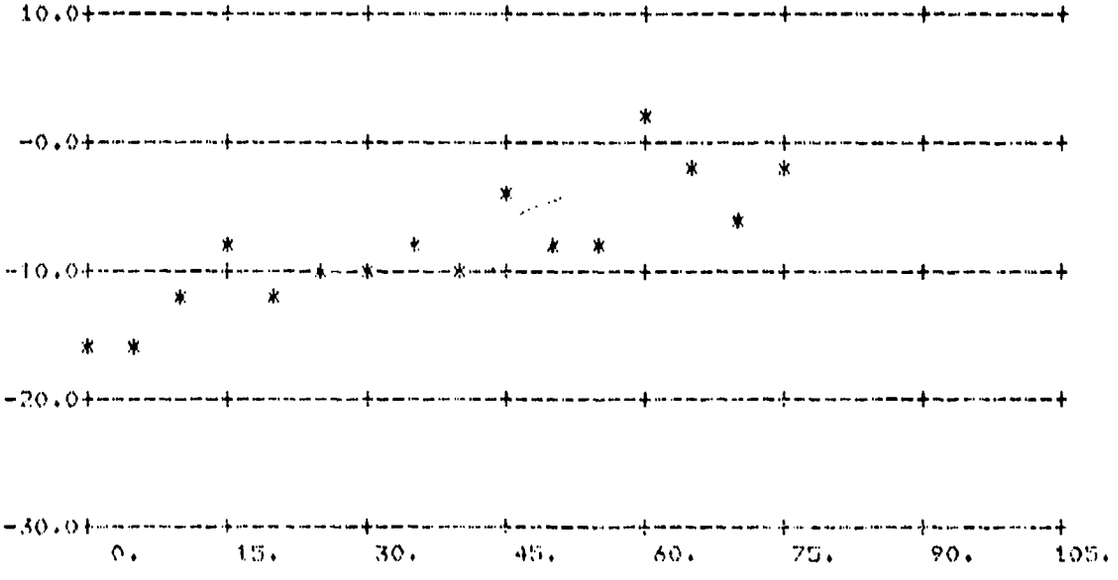

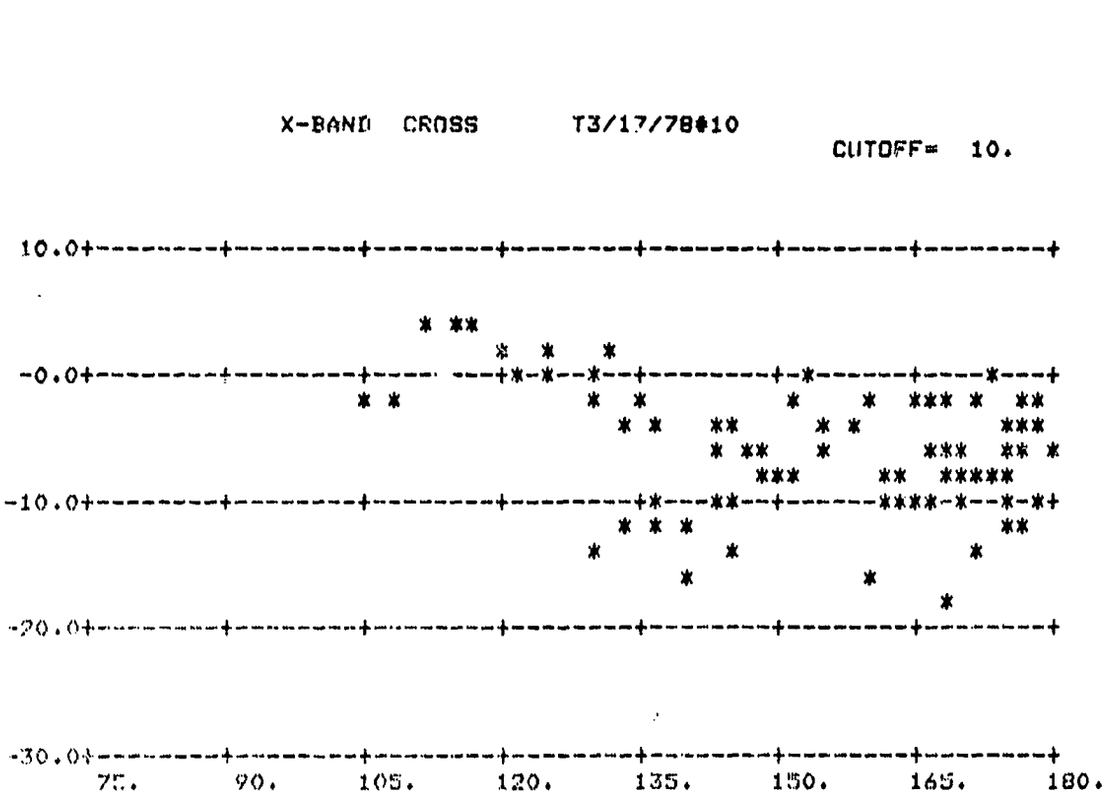

FIGURE A-60. σ_o vs ϕ_s; $\theta_s = 80°$, $\theta_i = 60°$

(Above: All Data; Below: Averages Over 5° Intervals)

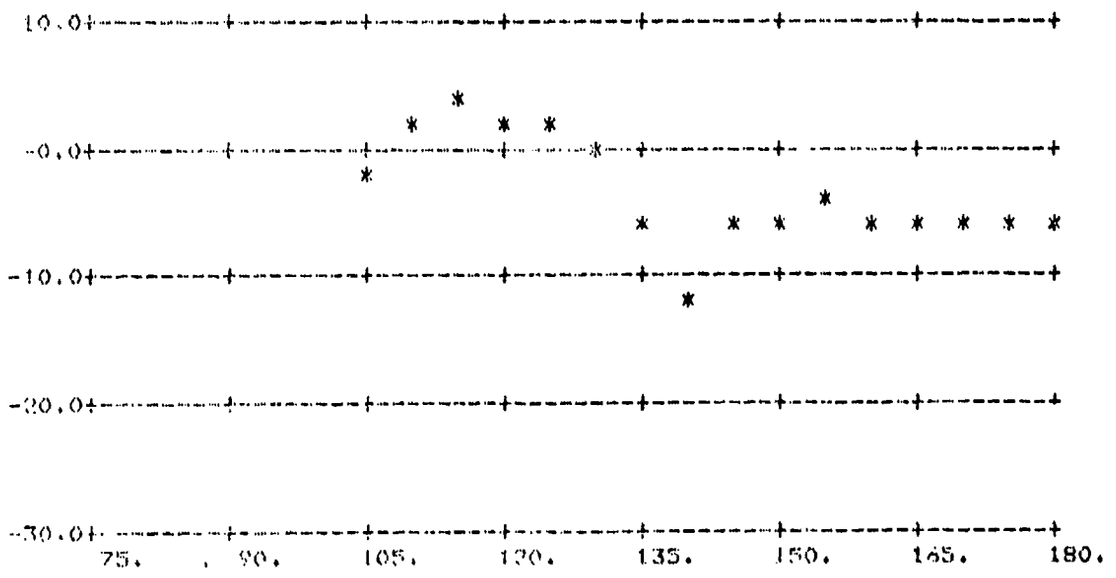

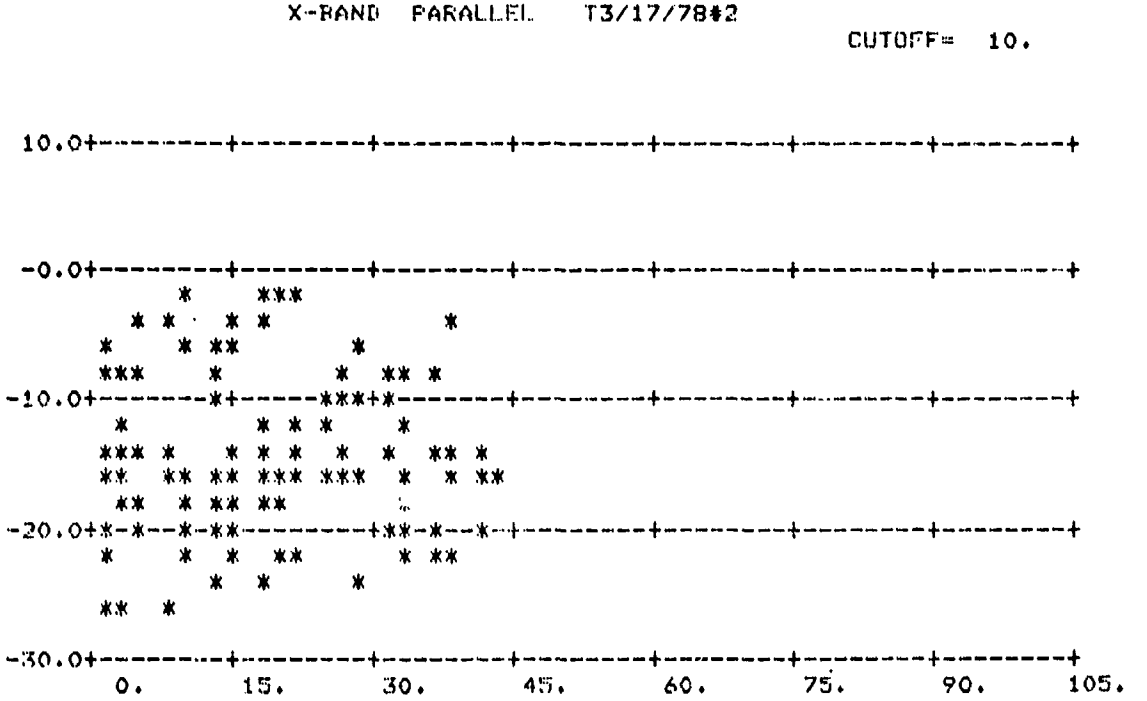

FIGURE A-61. σ_o vs ϕ_s; $\theta_s = 84°$, $\theta_i = 60°$

(Above: All Data; Below: Averages Over 5° Intervals)

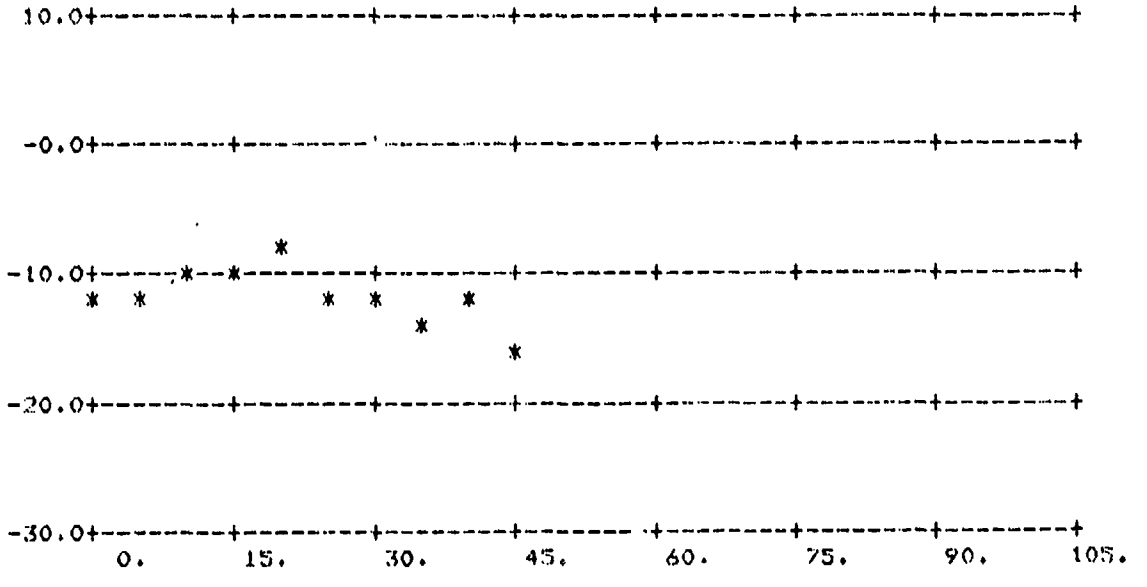

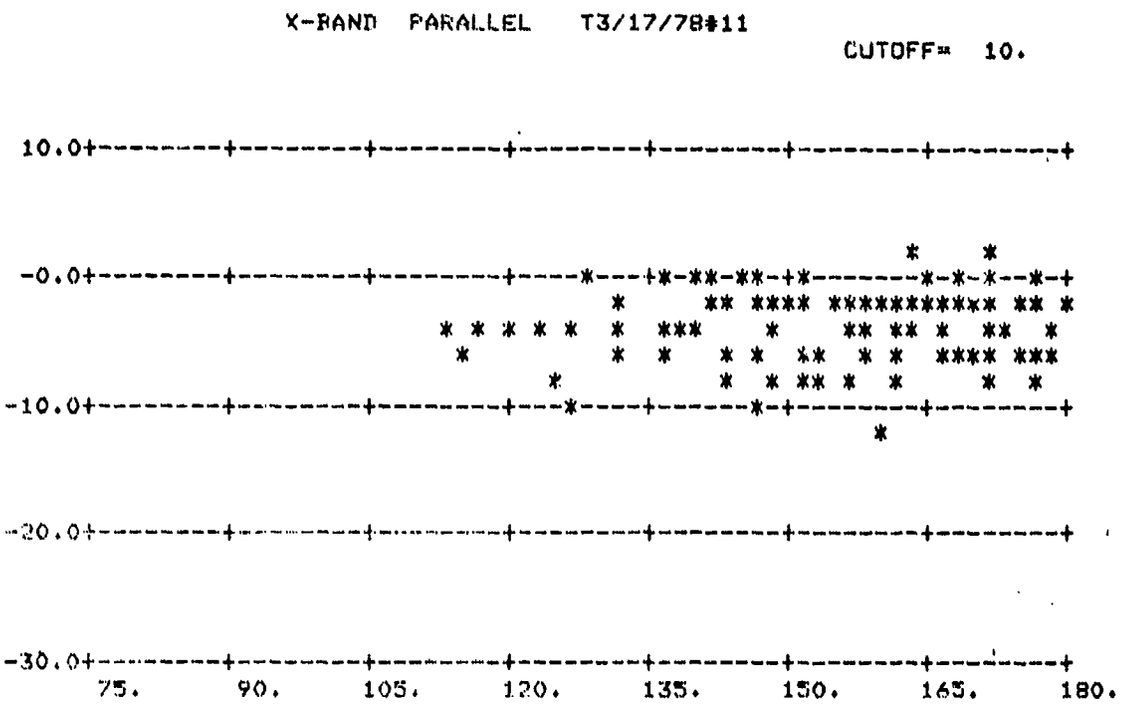

FIGURE A-62. σ_o vs ϕ_s; $\theta_s = 84°$, $\theta_i = 60°$

(Above: All Data; Below: Averages Over 5° Intervals)

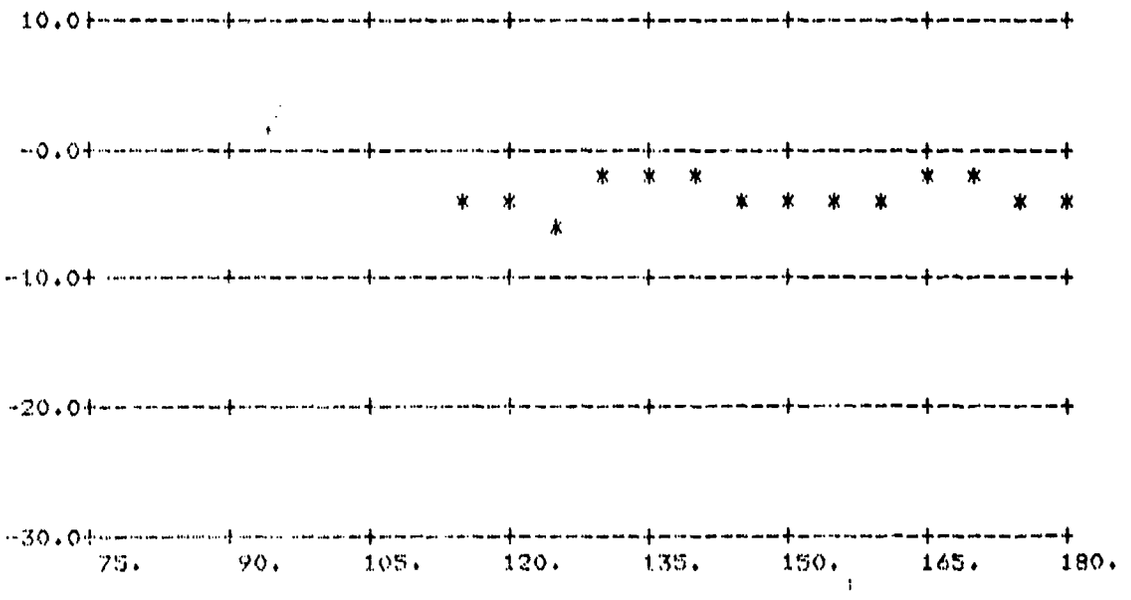

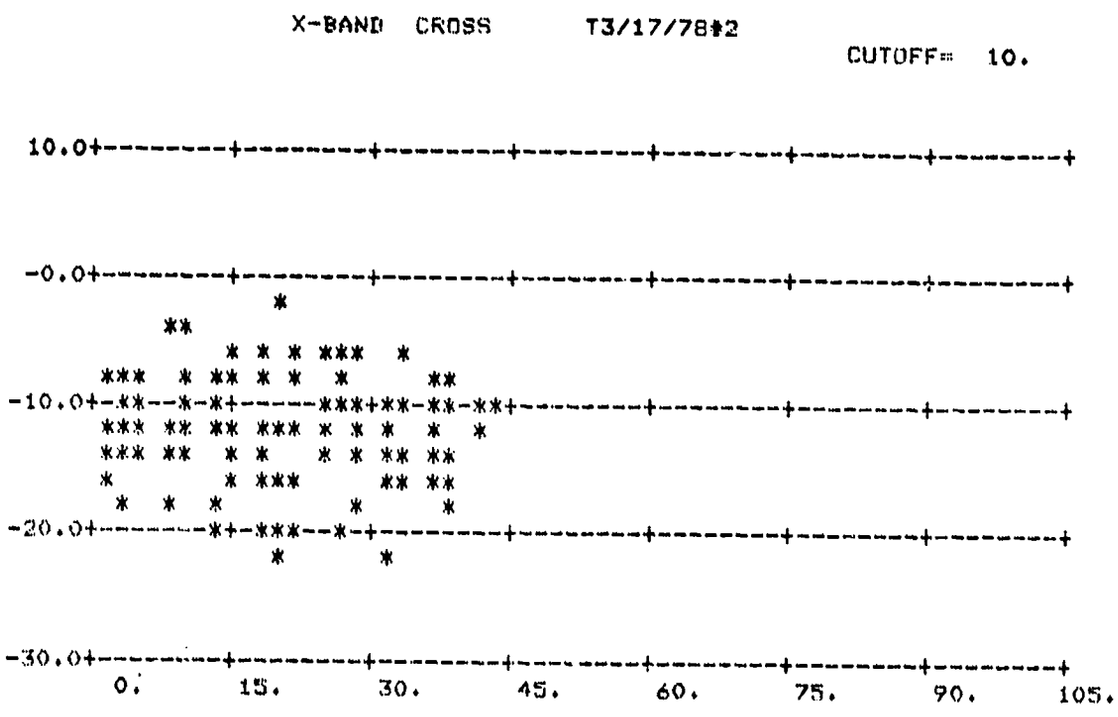

FIGURE A-63. σ_o vs ϕ_s; $\theta_s = 84°$, $\theta_i = 60°$

(Above: All Data; Below: Averages Over 5° Intervals)

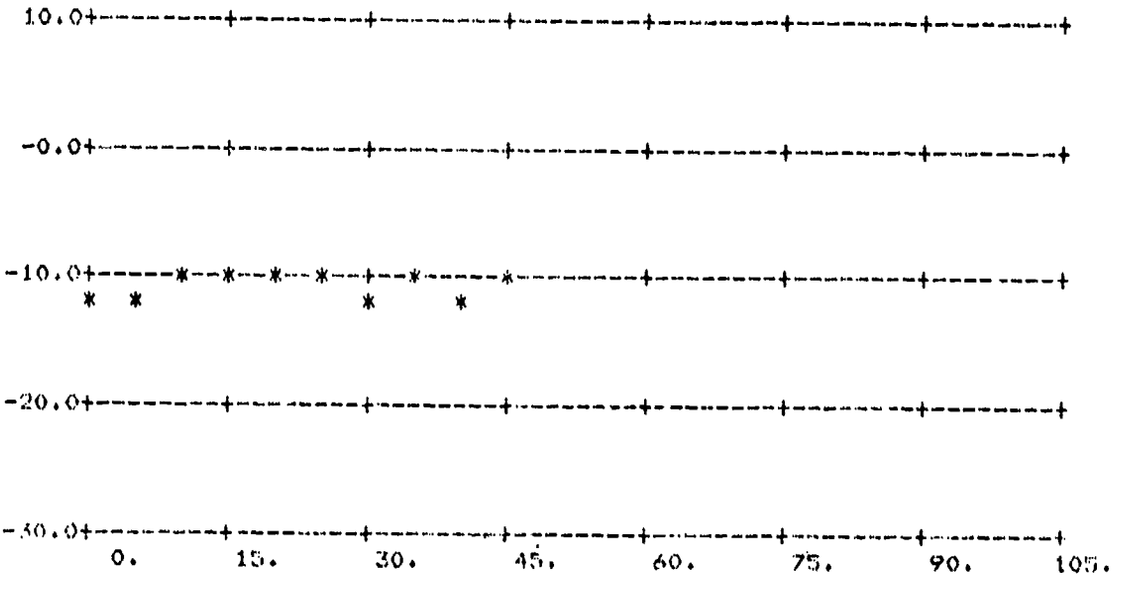

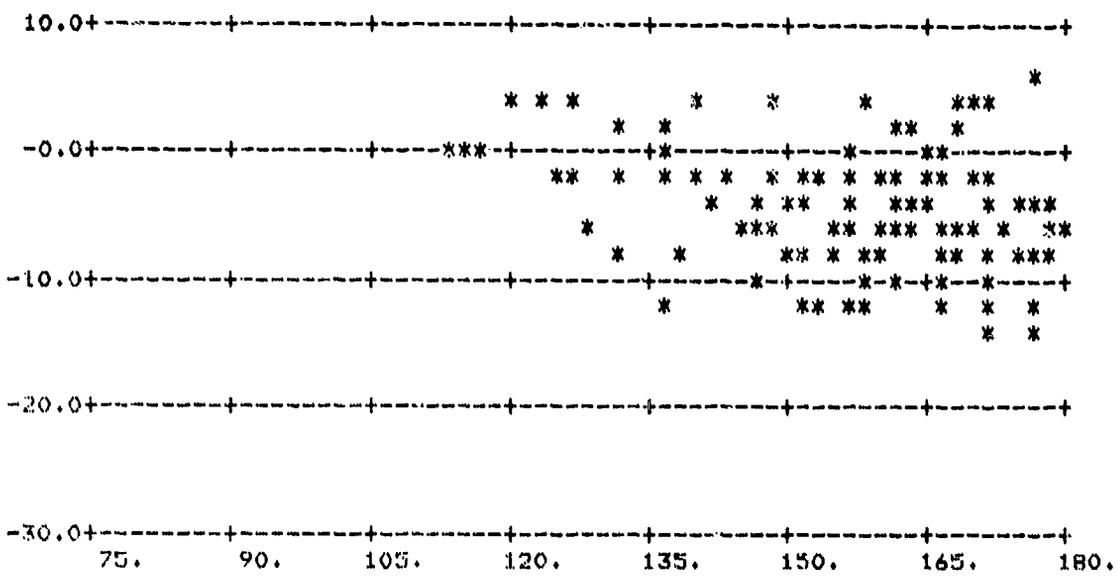

FIGURE A-64. σ_o vs ϕ_s; $\theta_s = 84°$, $\theta_i = 60°$

(Above: All Data; Below: Averages Over 5° Intervals)

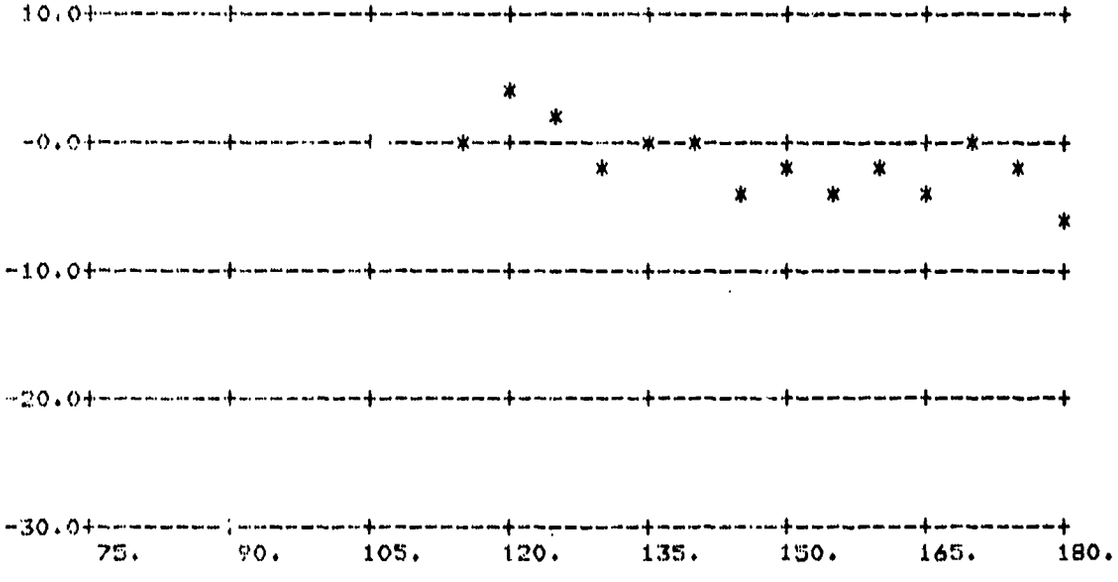

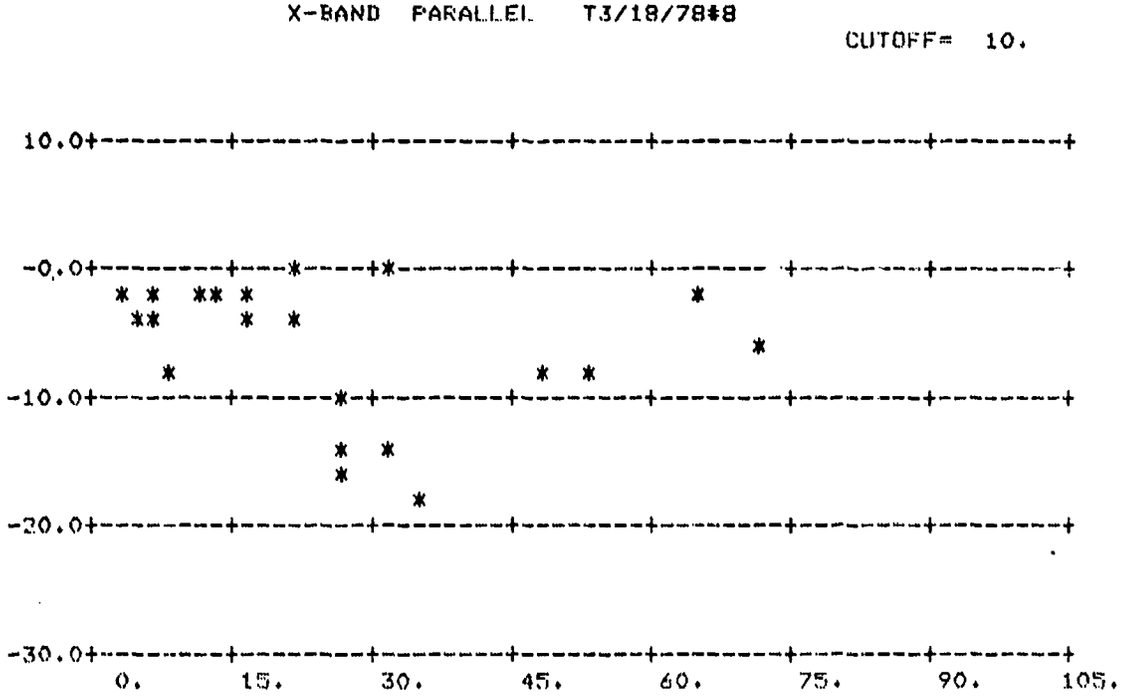

FIGURE A-65. σ_o vs ϕ_s; $\theta_s = 60°$, $\theta_i = 70°$

(Above: All Data; Below: Averages Over 5° Intervals)

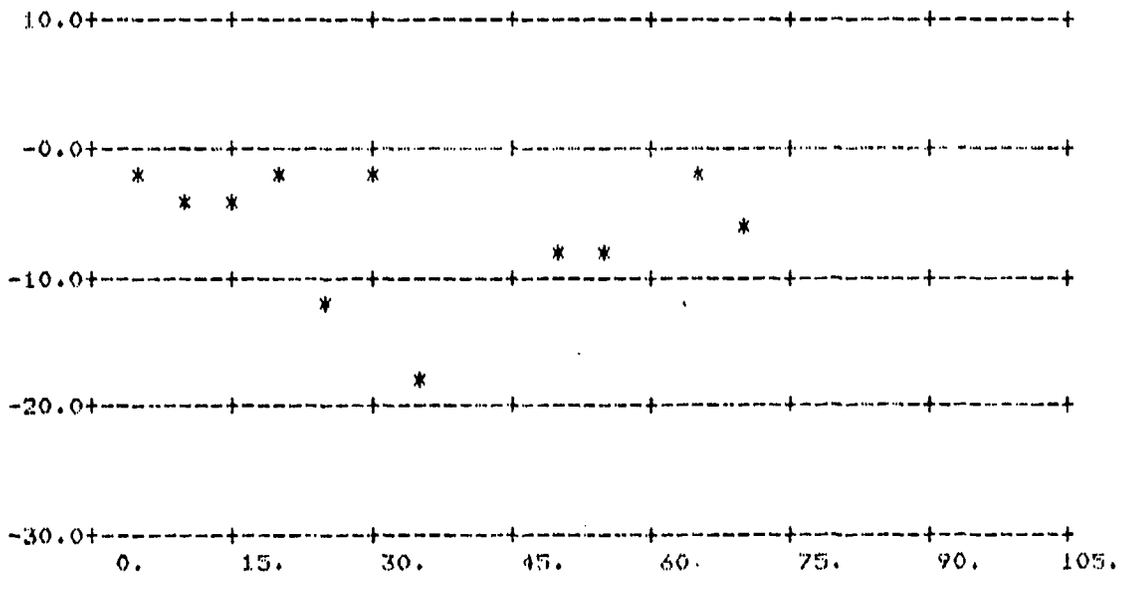

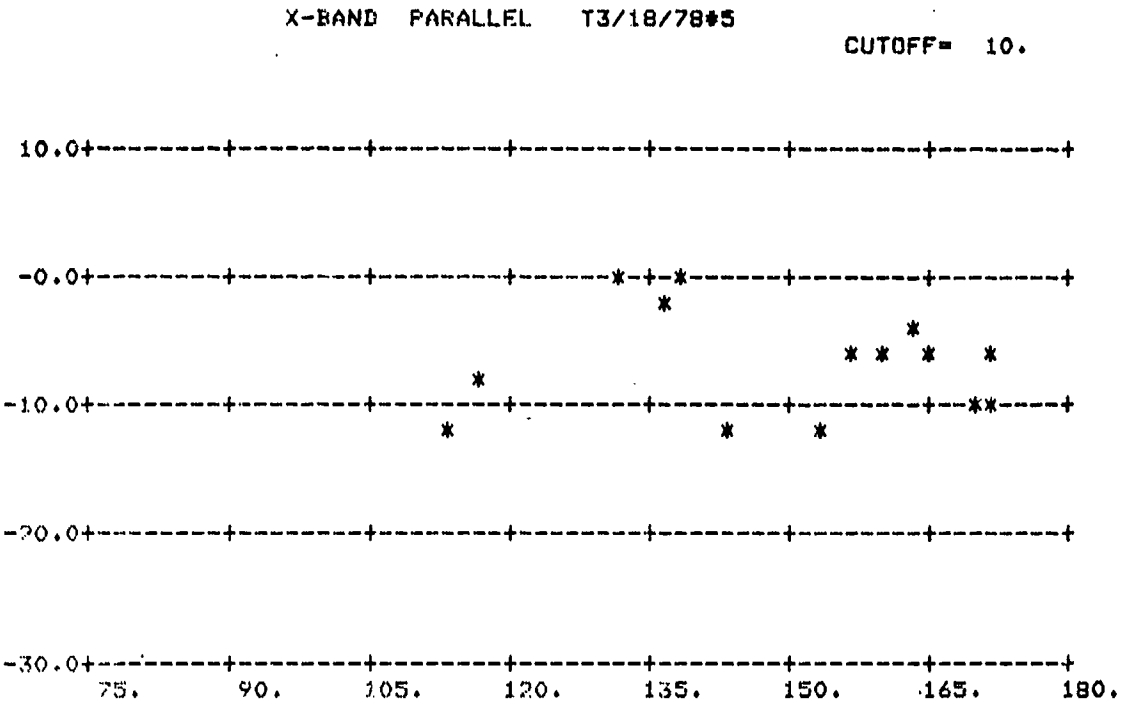

FIGURE A-66. σ_o vs ϕ_s; $\theta_s = 60°$, $\theta_i = 70°$

(Above: All Data; Below: Averages Over 5° Intervals)

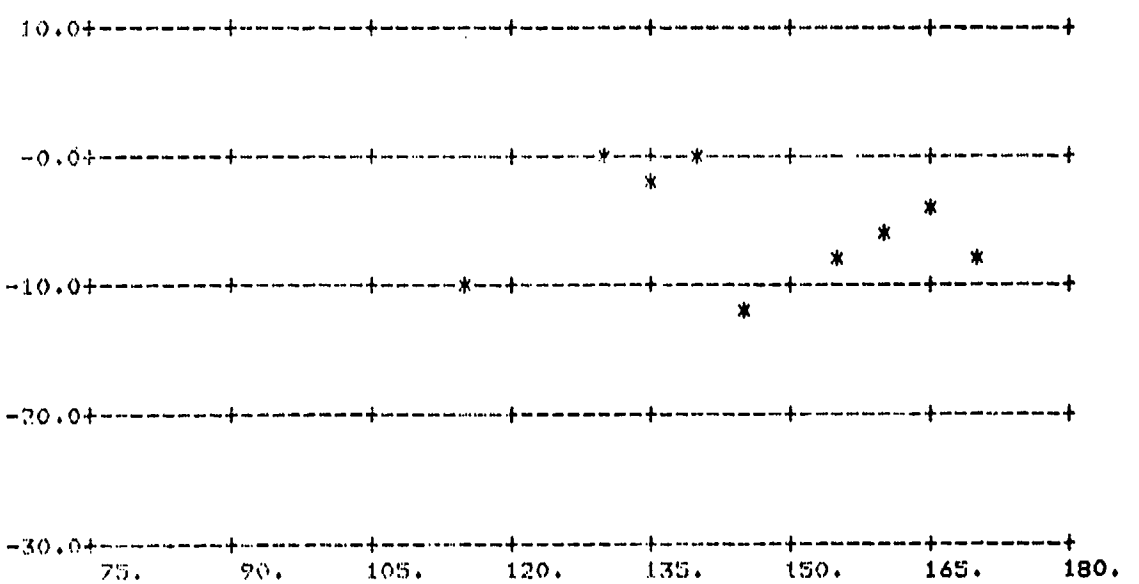

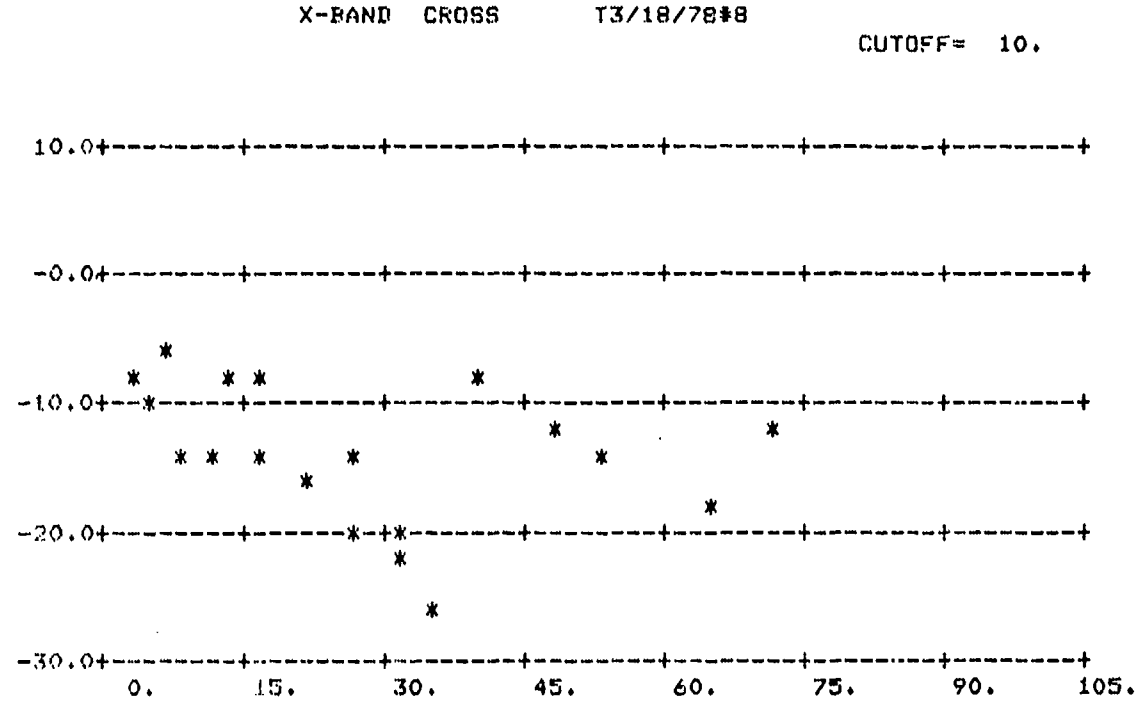

FIGURE A-67. σ_o vs ϕ_s; $\theta_s = 60°$, $\theta_i = 70°$

(Above: All Data; Below: Averages Over 5° Intervals)

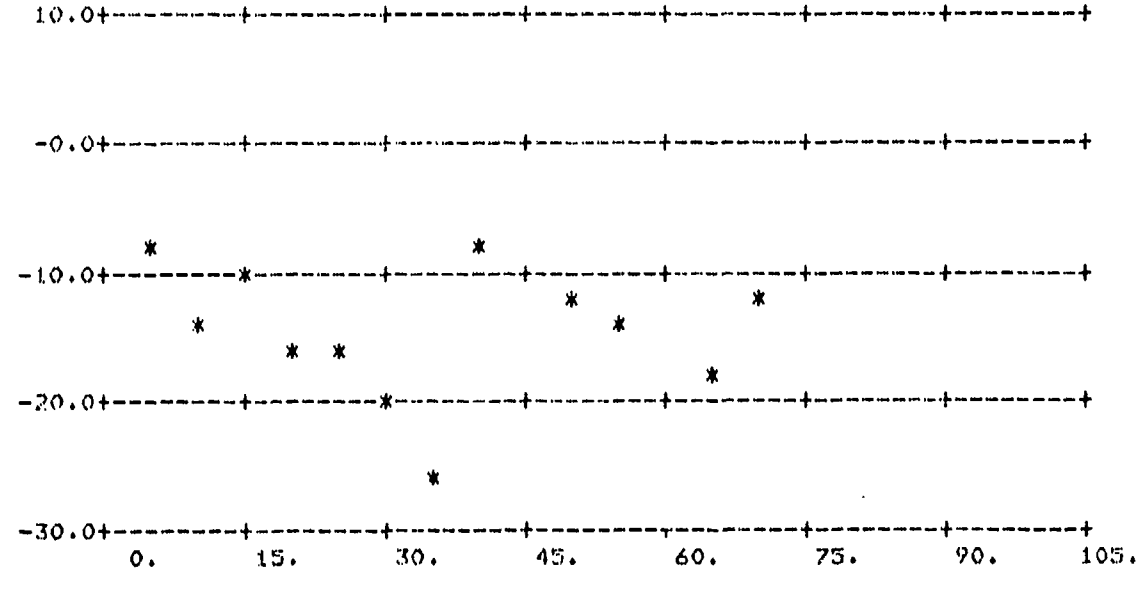

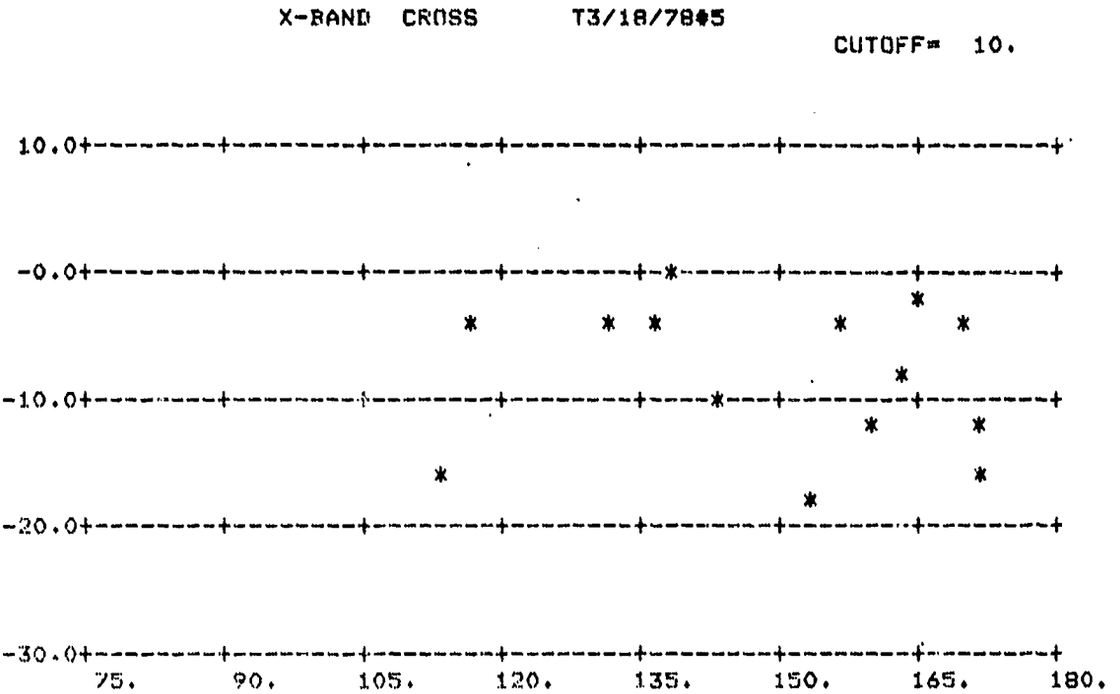

FIGURE A-68. σ_o vs ϕ_s; $\theta_s = 60°$, $\theta_i = 70°$
(Above: All Data; Below: Averages Over 5° Intervals)

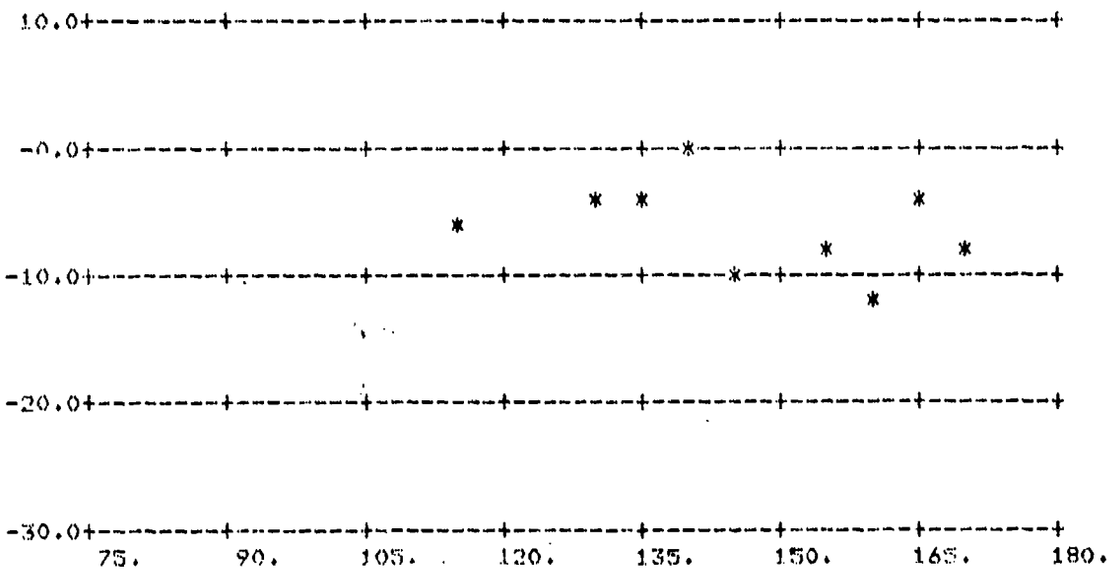

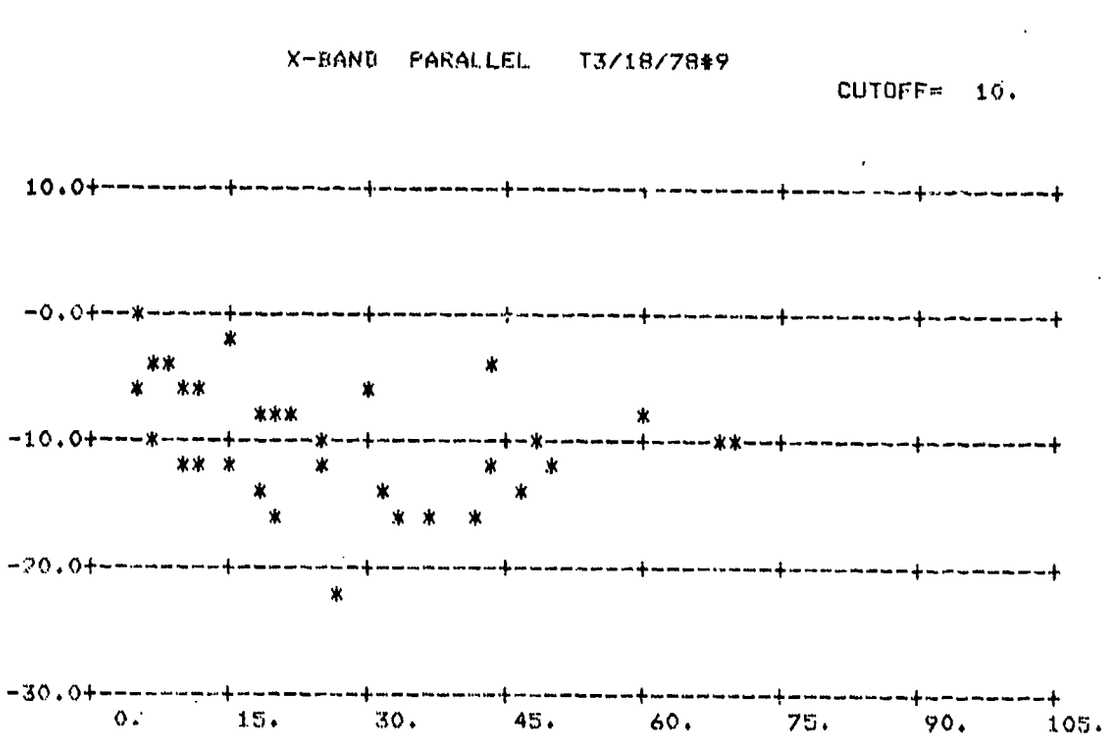

FIGURE A-69. σ_o vs ϕ_s; $\theta_s = 70°$, $\theta_i = 70°$

(Above: All Data; Below: Averages Over 5° Intervals)

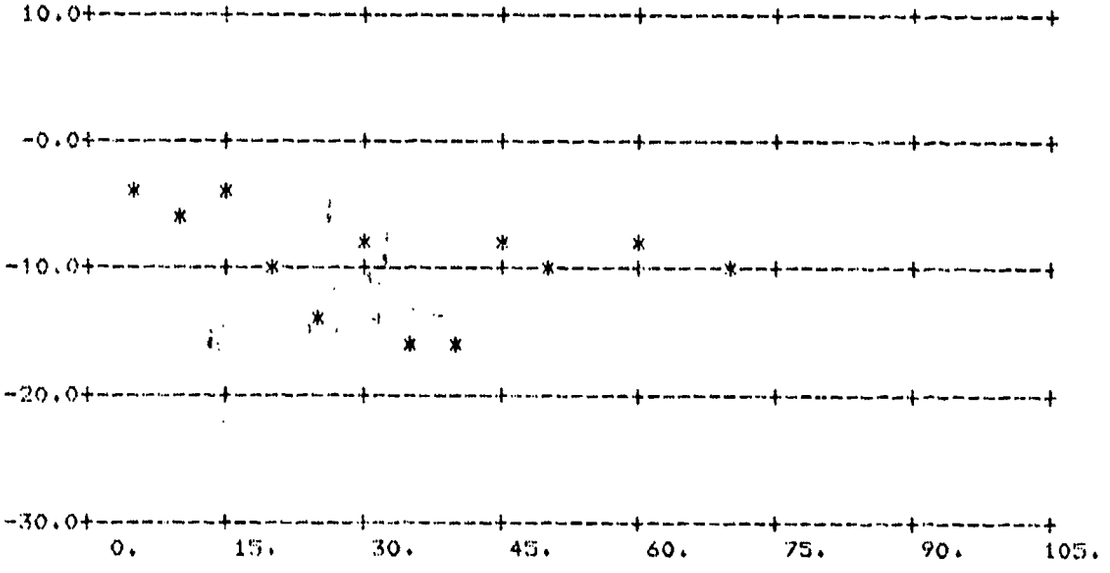

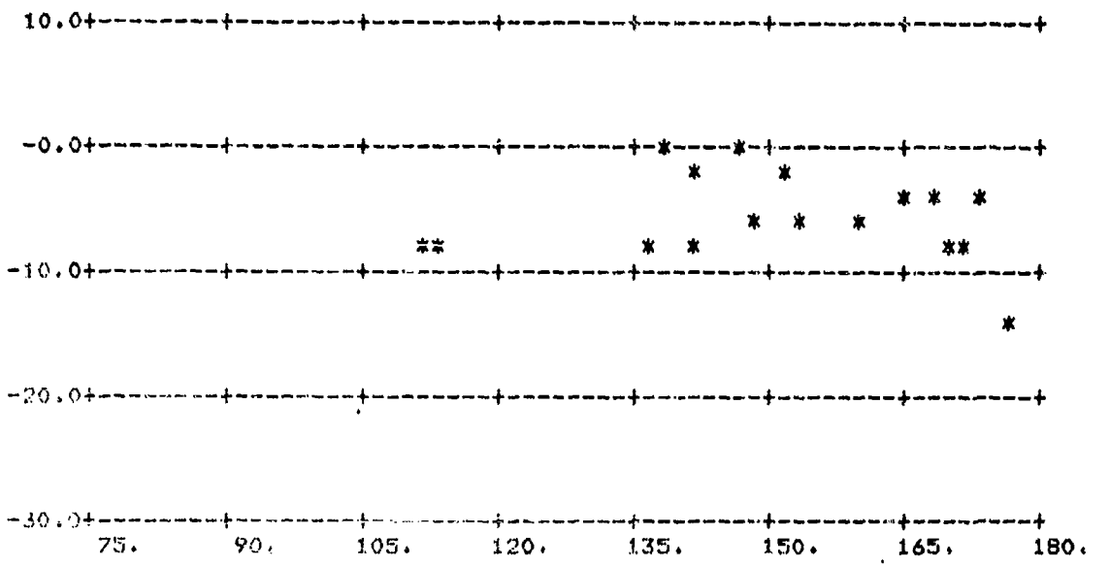

FIGURE A-70. σ_o vs ϕ_s; $\theta_s = 70°$, $\theta_i = 70°$

(Above: All Data; Below: Averages Over 5° Intervals)

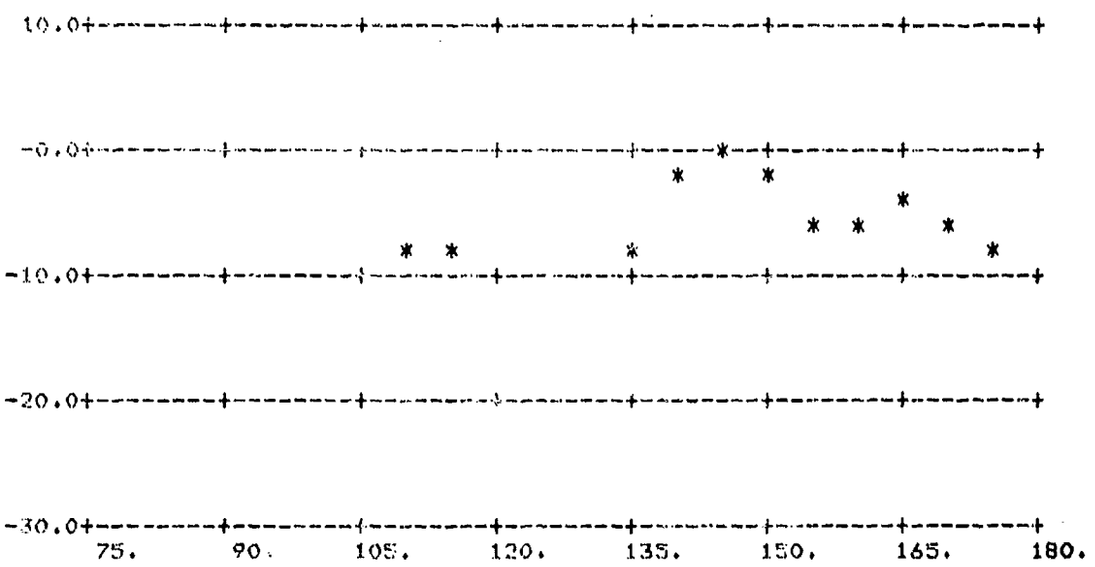

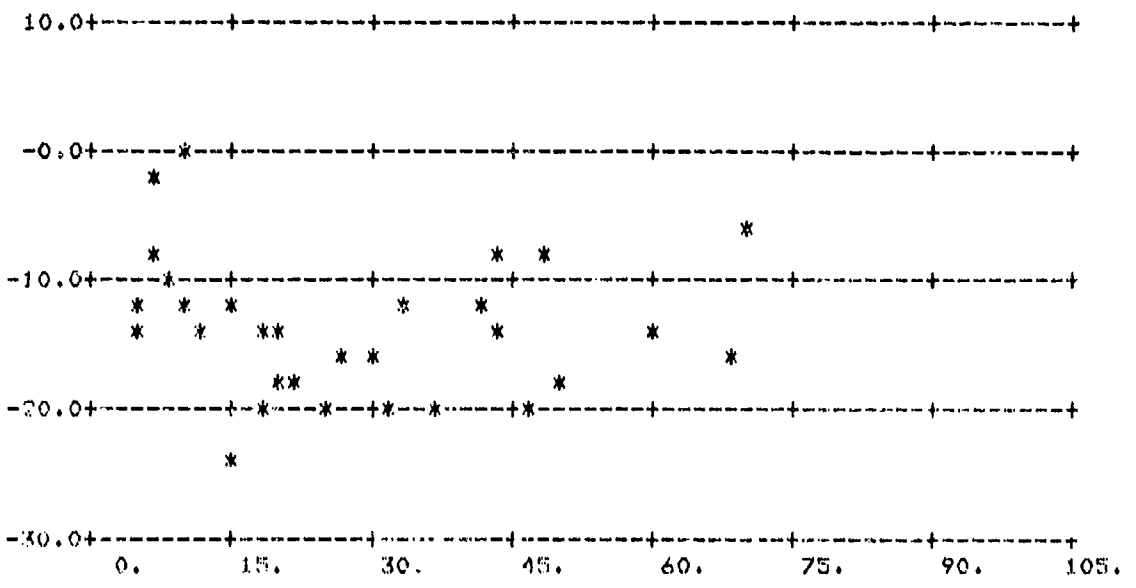

FIGURE A-71. σ_o vs ϕ_s; $\theta_s = 70°$, $\theta_i = 70°$

(Above: All Data; Below: Averages Over 5° Intervals)

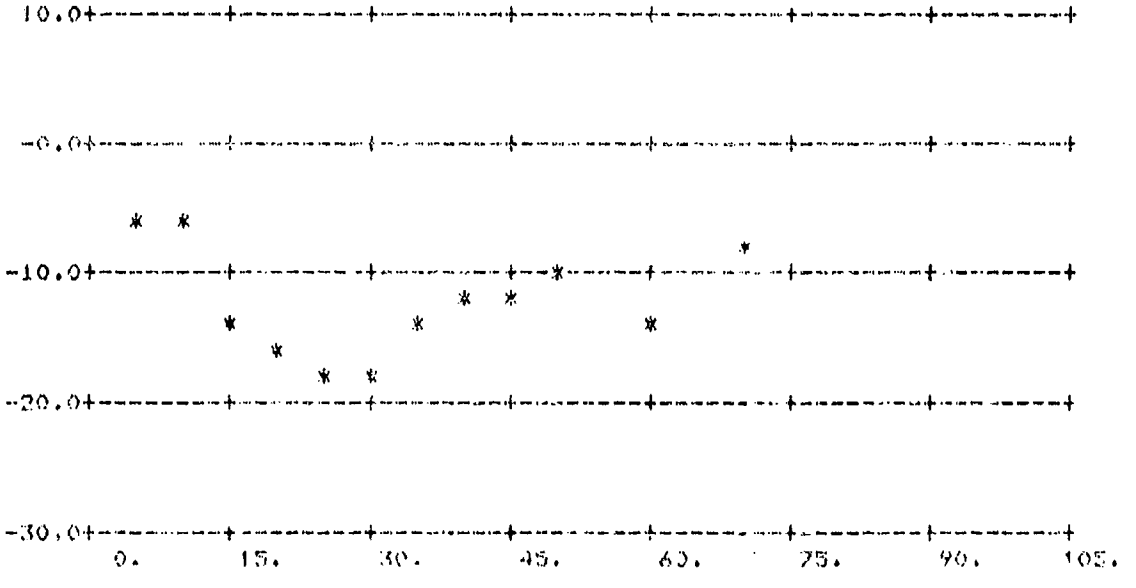

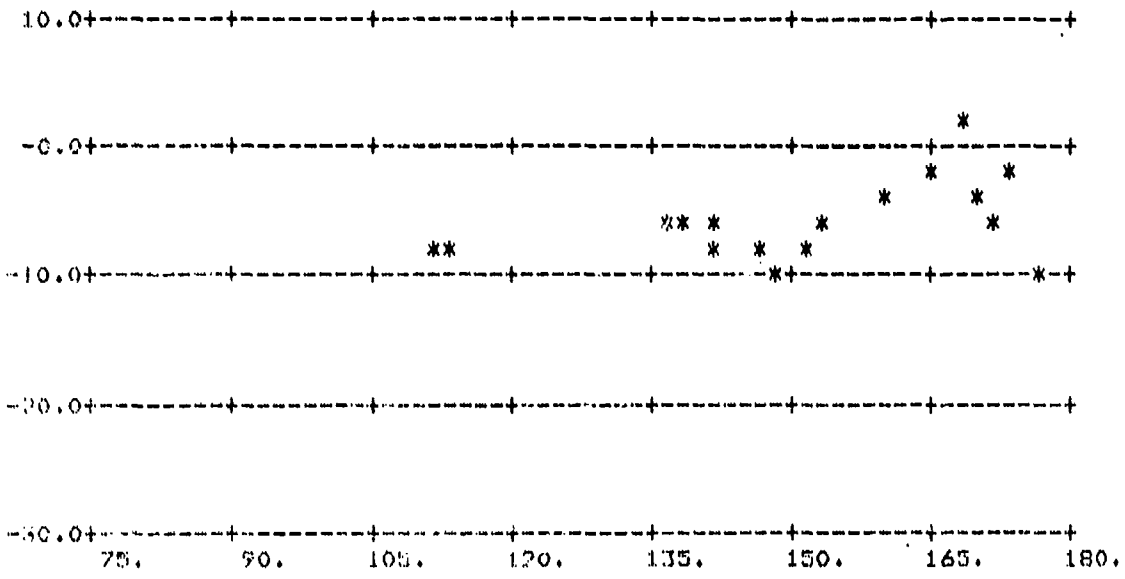

FIGURE A-72. σ_o vs ϕ_s; $\theta_s = 70°$, $\theta_i = 70°$
(Above: All Data; Below: Averages Over 5° Intervals)

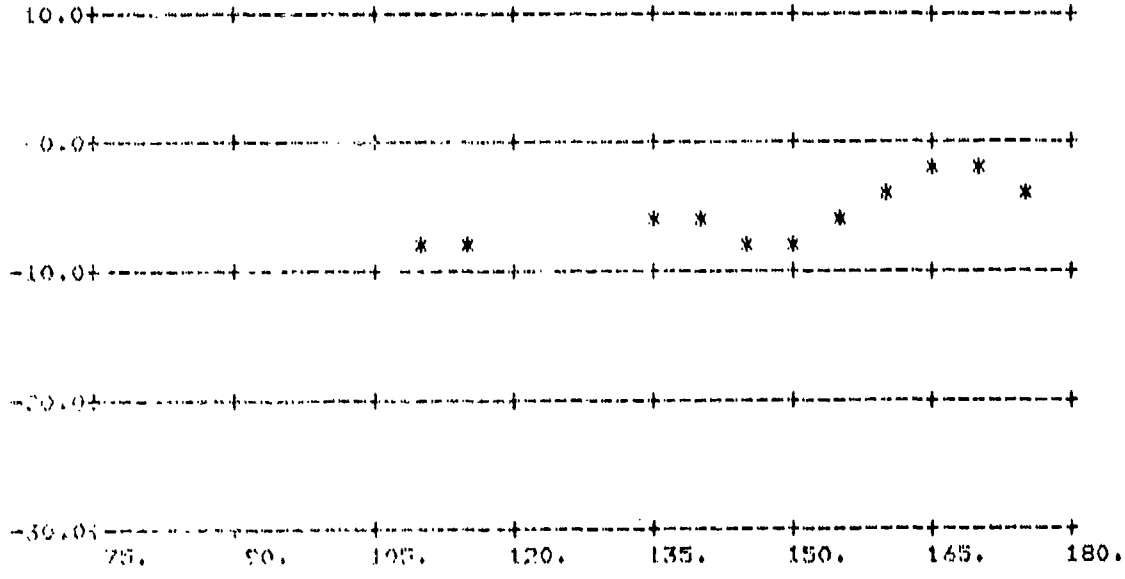

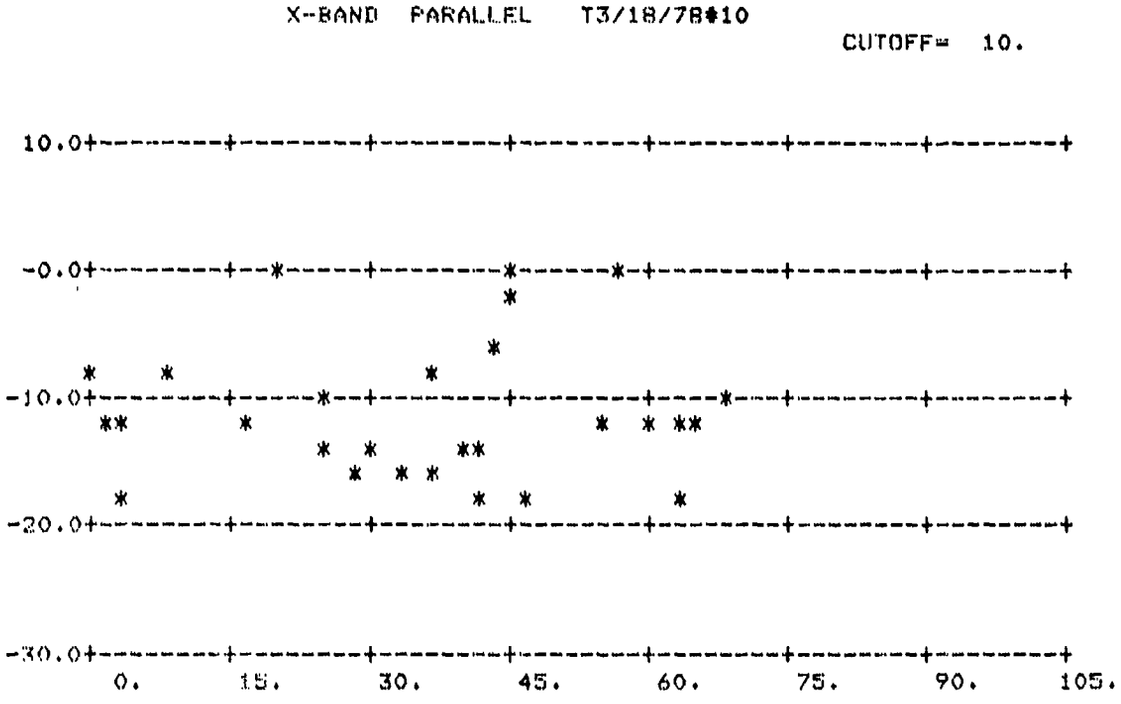

FIGURE A-73. σ_o vs ϕ_s; $\theta_s = 80°$, $\theta_i = 70°$

(Above: All Data; Below: Averages Over 5° Intervals)

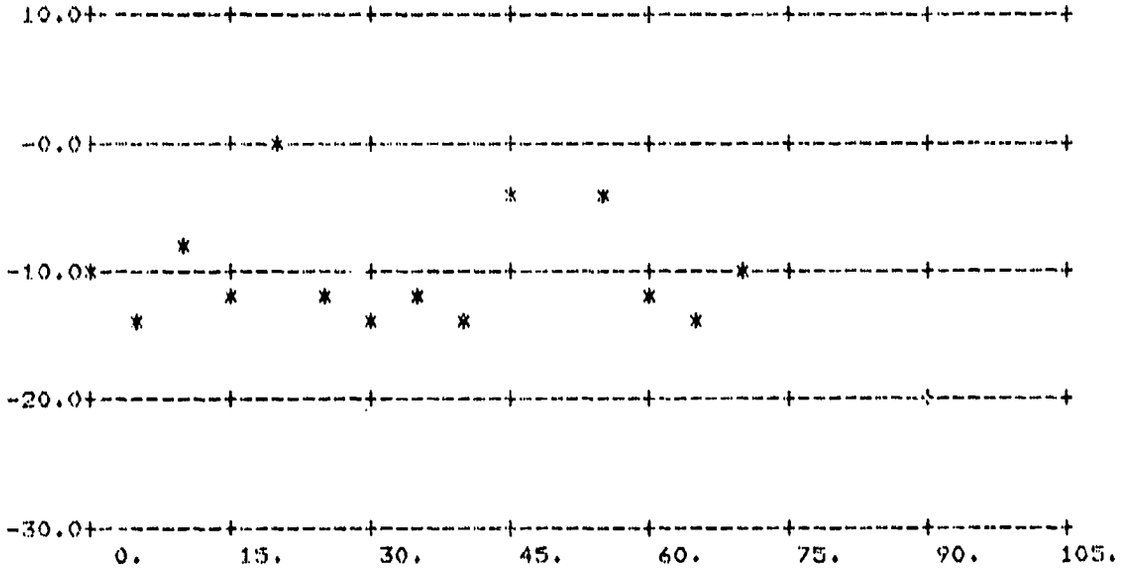

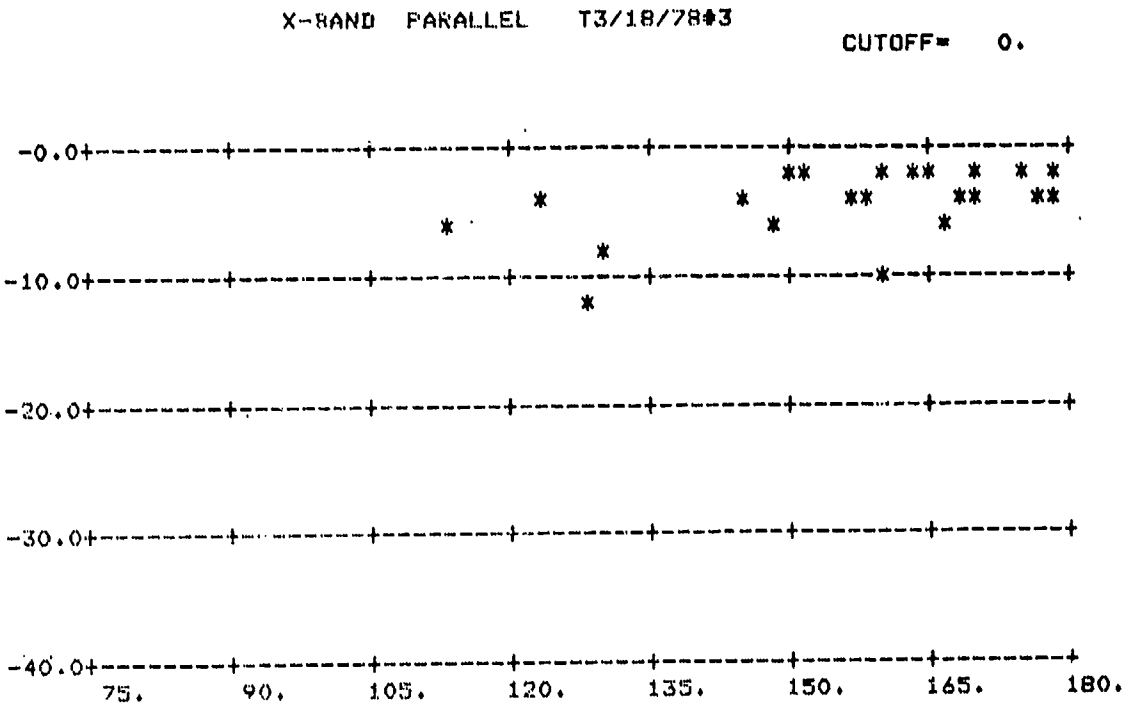

FIGURE A-74. σ_o vs ϕ_s; $\theta_s = 80°$, $\theta_i = 70°$

(Above: All Data; Below: Averages Over 5° Intervals)

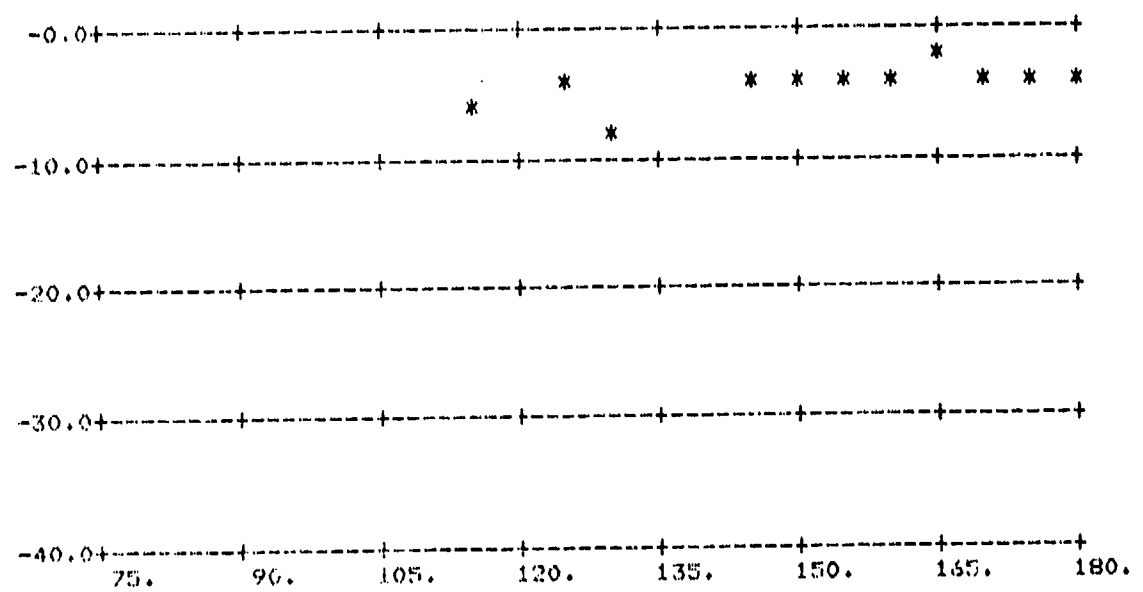

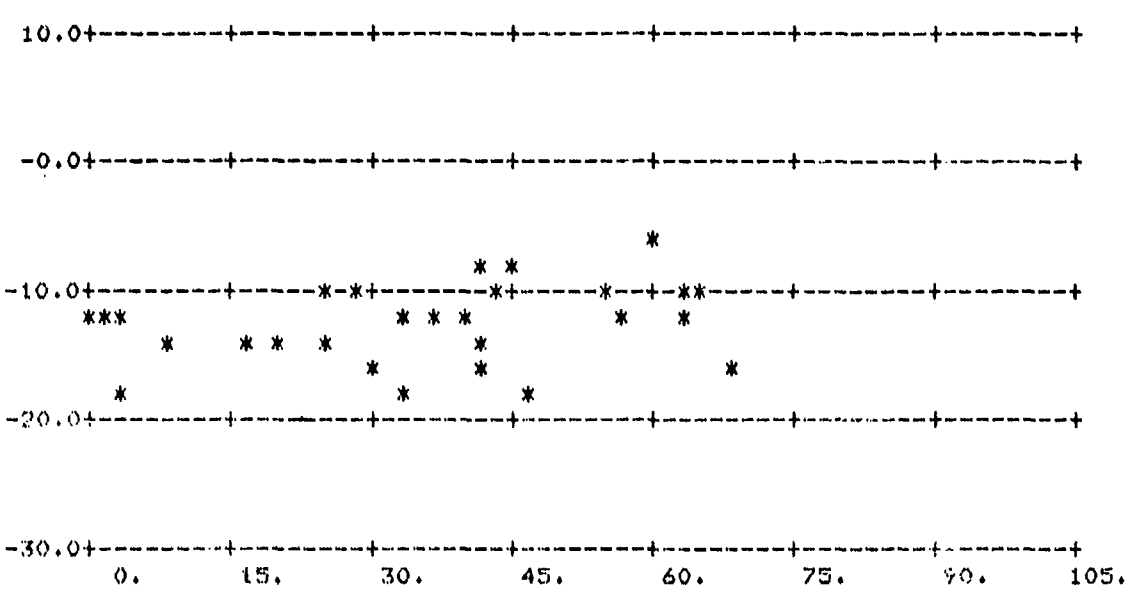

FIGURE A-75. σ_o vs ϕ_s; $\theta_s = 80°$, $\theta_i = 70°$

(Above: All Data; Below: Averages Over 5° Intervals)

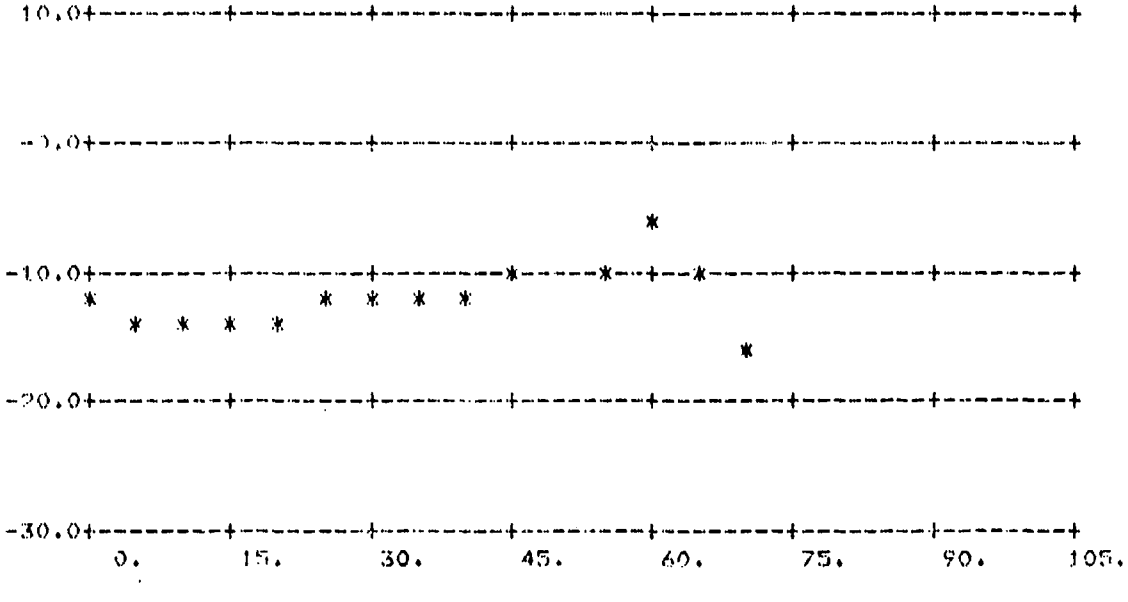

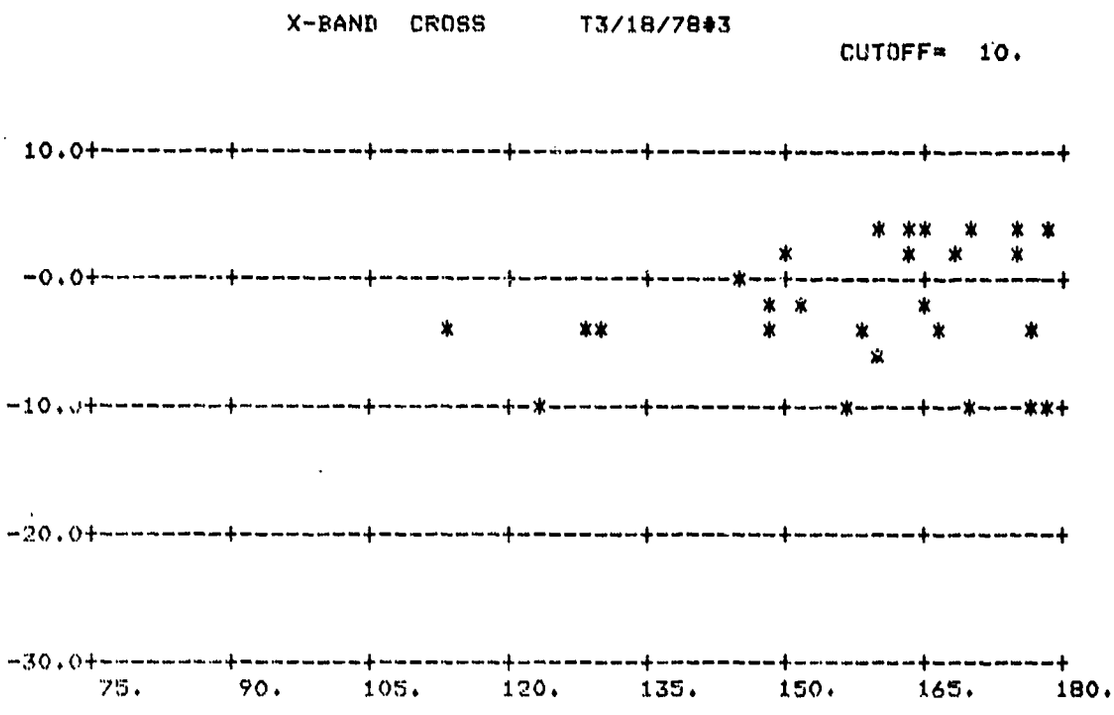

FIGURE A-76. σ_o vs ϕ_s; $\theta_s = 80°$, $\theta_i = 70°$

(Above: All Data; Below: Averages Over 5° Intervals)

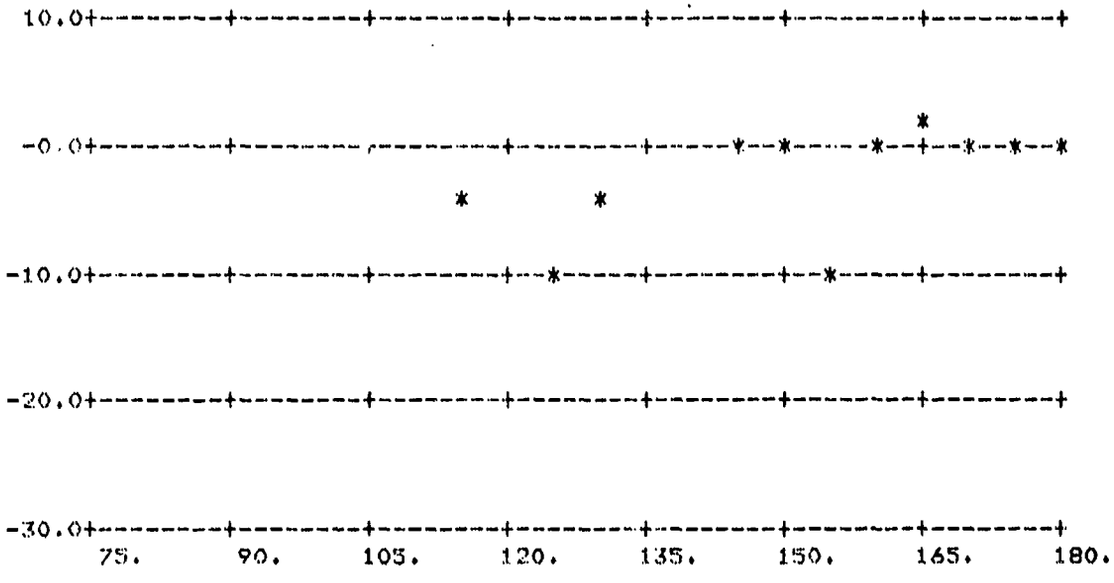

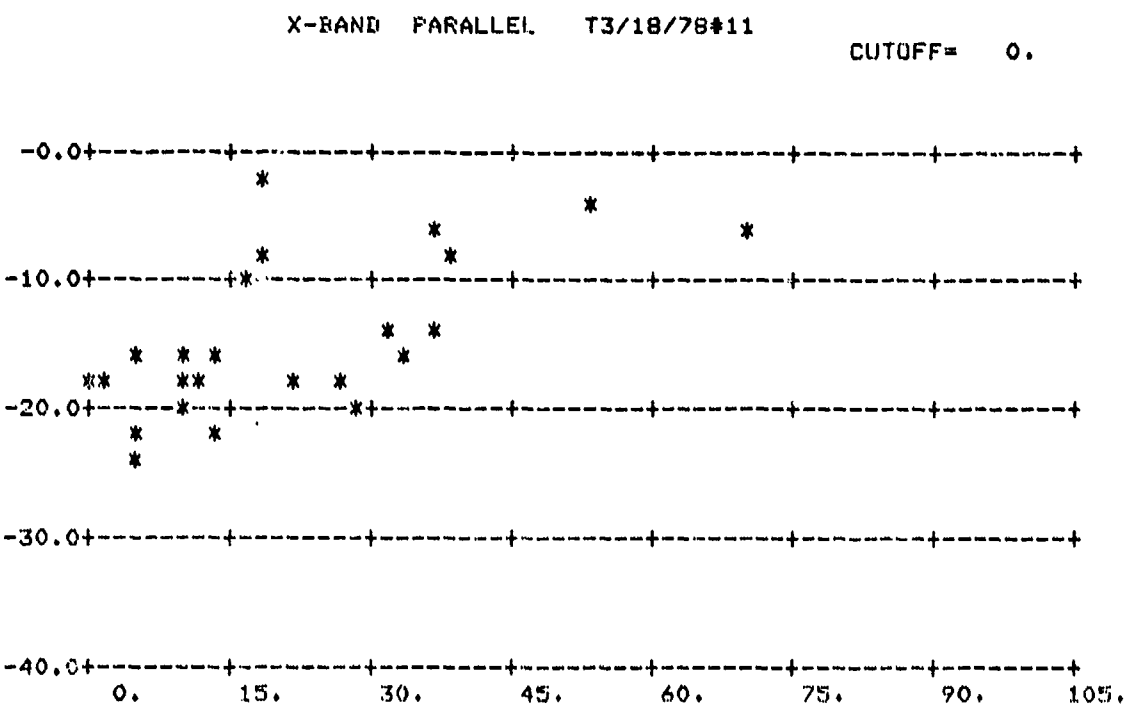

FIGURE A-77. σ_o vs ϕ_s; $\theta_s = 84°$, $\theta_i = 70°$

(Above: All Data; Below: Averages Over 5° Intervals)

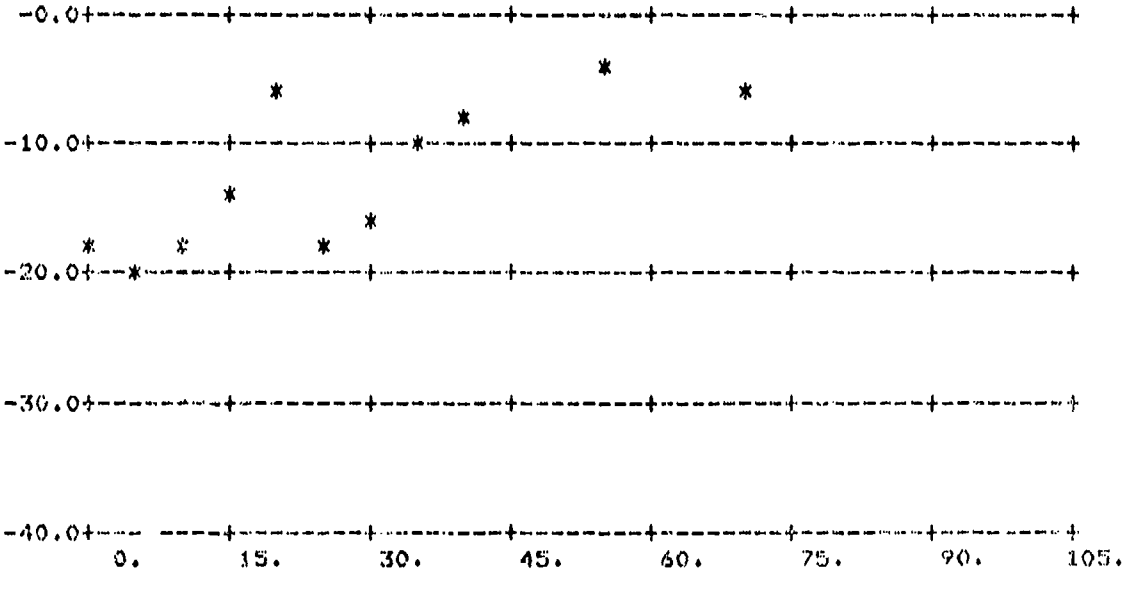

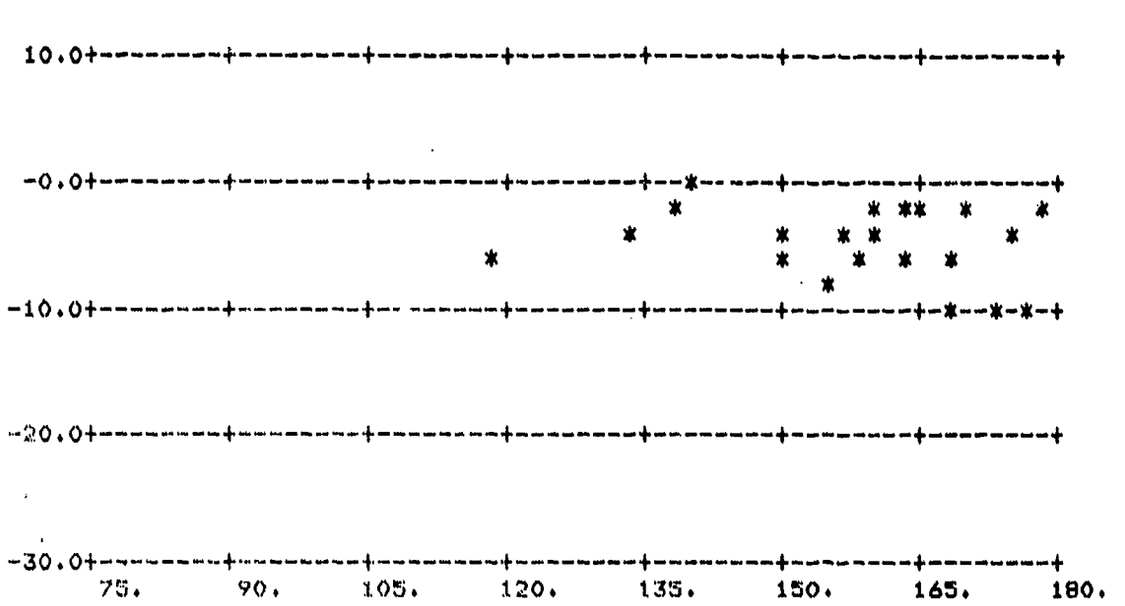

FIGURE A-78. σ_o vs ϕ_s; $\theta_s = 84°$, $\theta_i = 70°$

(Above: All Data; Below: Averages Over 5° Intervals)

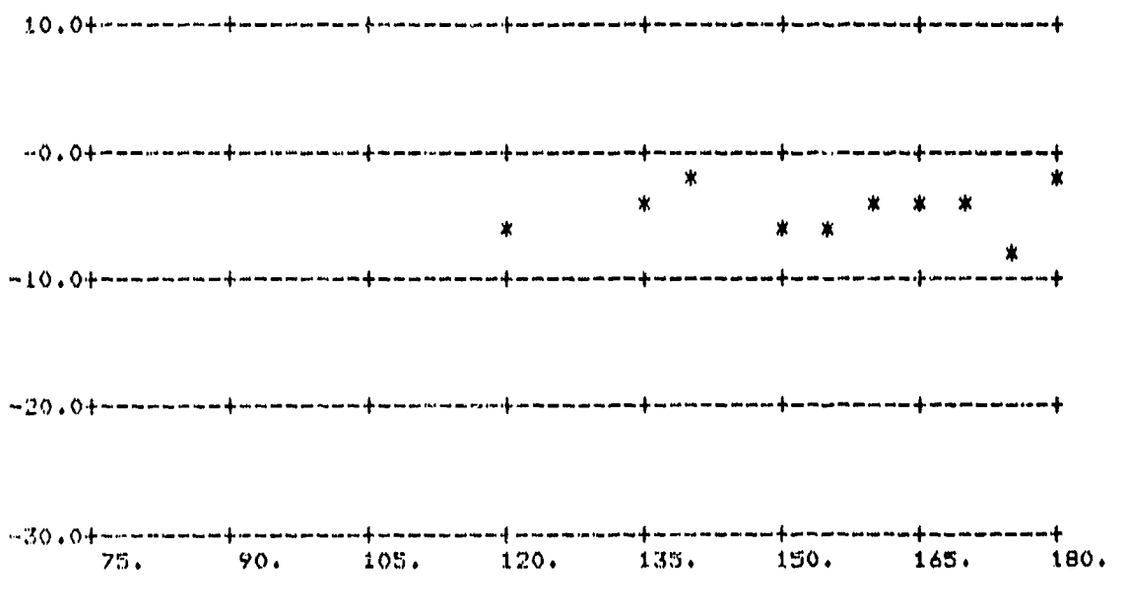

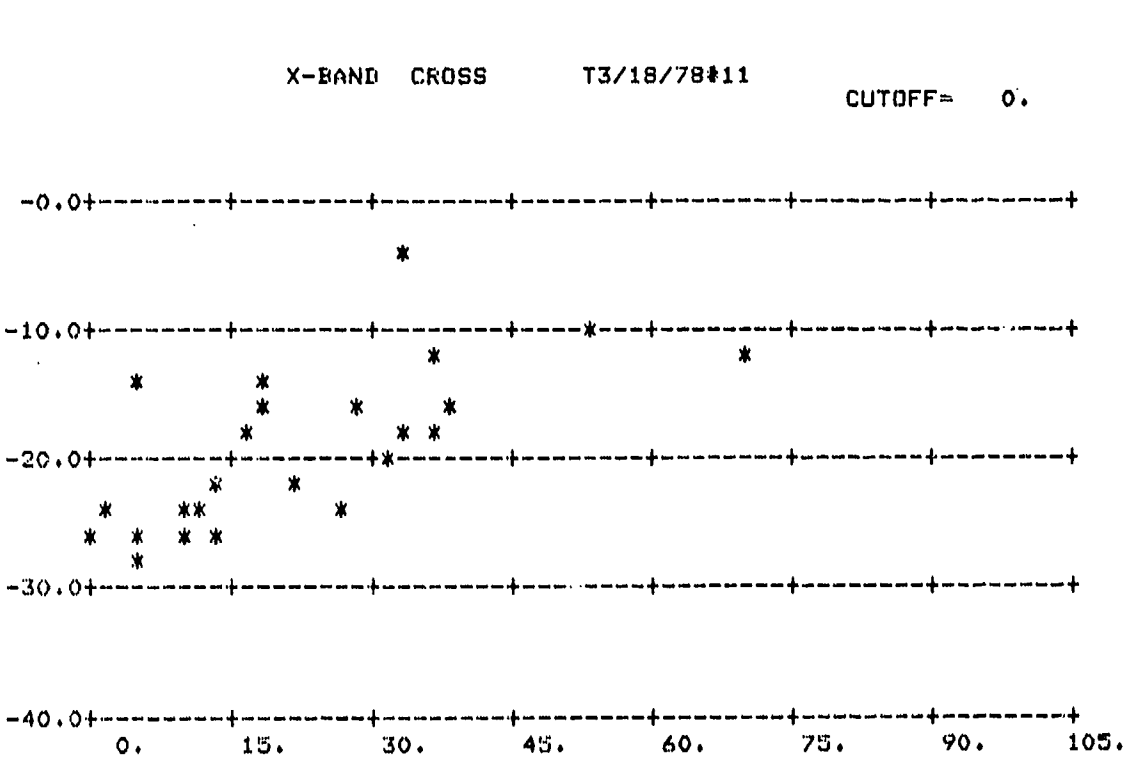

FIGURE A-79. σ_o vs ϕ_s; $\theta_s = 84°$, $\theta_i = 70°$

(Above: All Data; Below: Averages Over 5° Intervals)

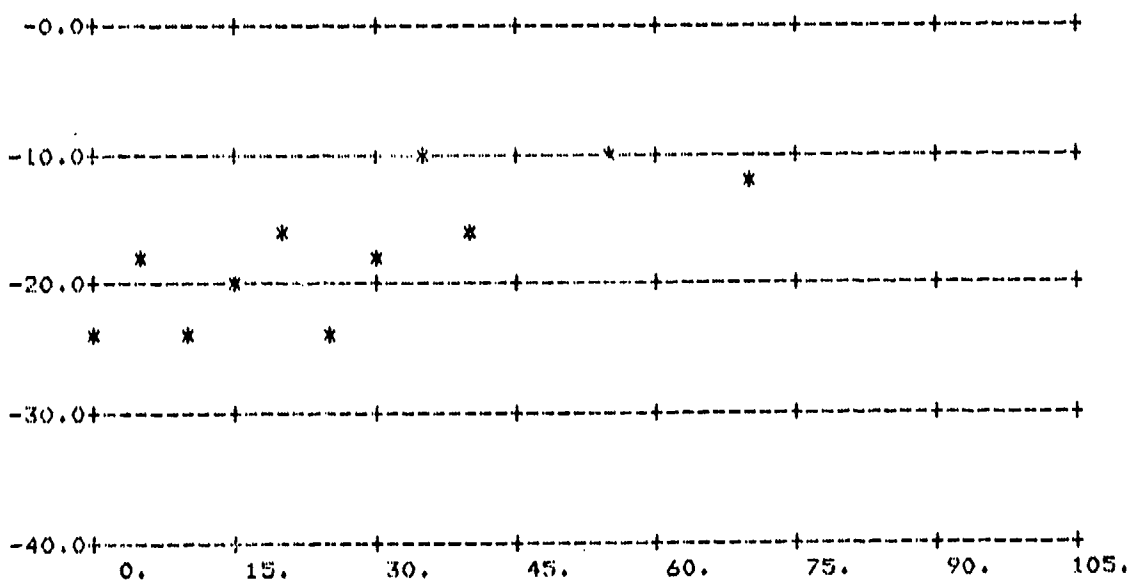

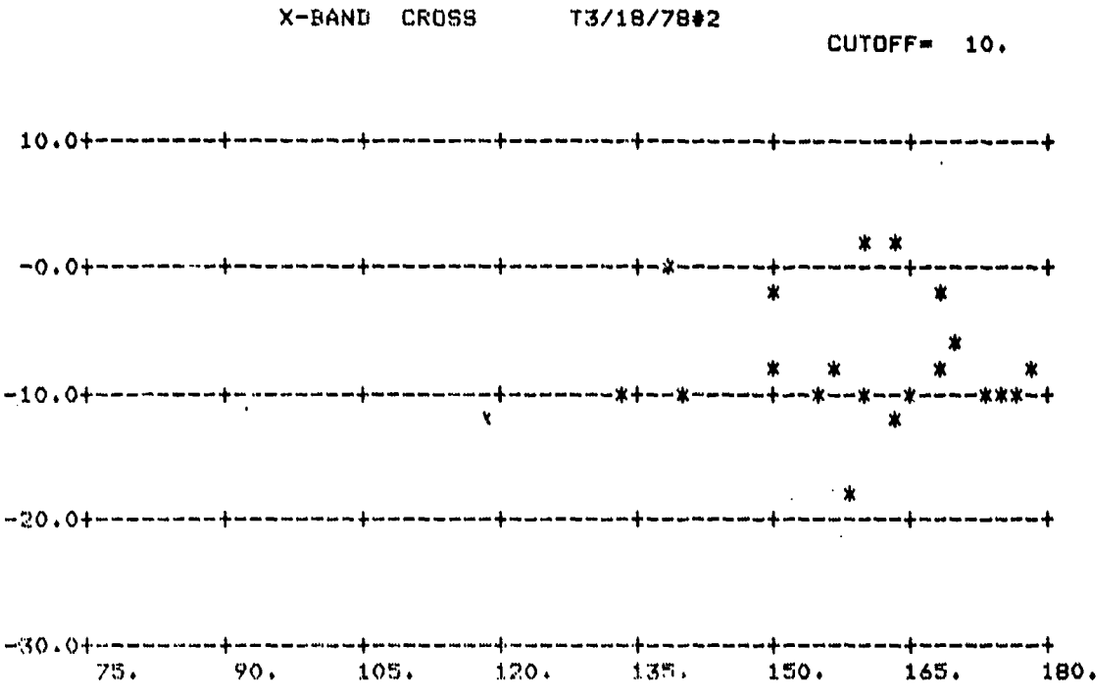

FIGURE A-80. σ_o vs ϕ_s; $\theta_s = 84°$, $\theta_i = 70°$

(Above: All Data; Below: Averages Over 5° Intervals)

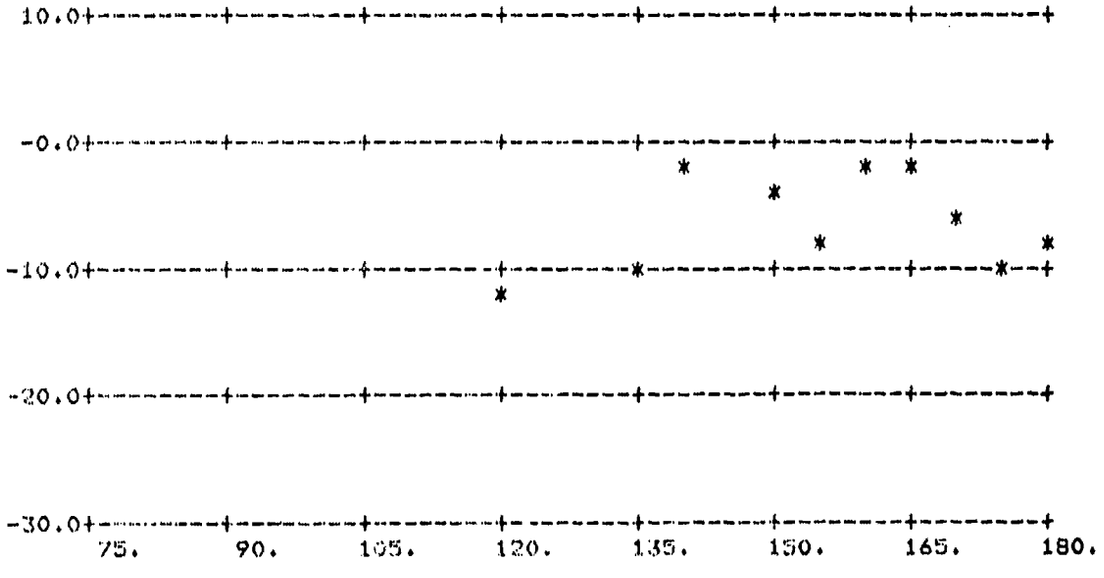

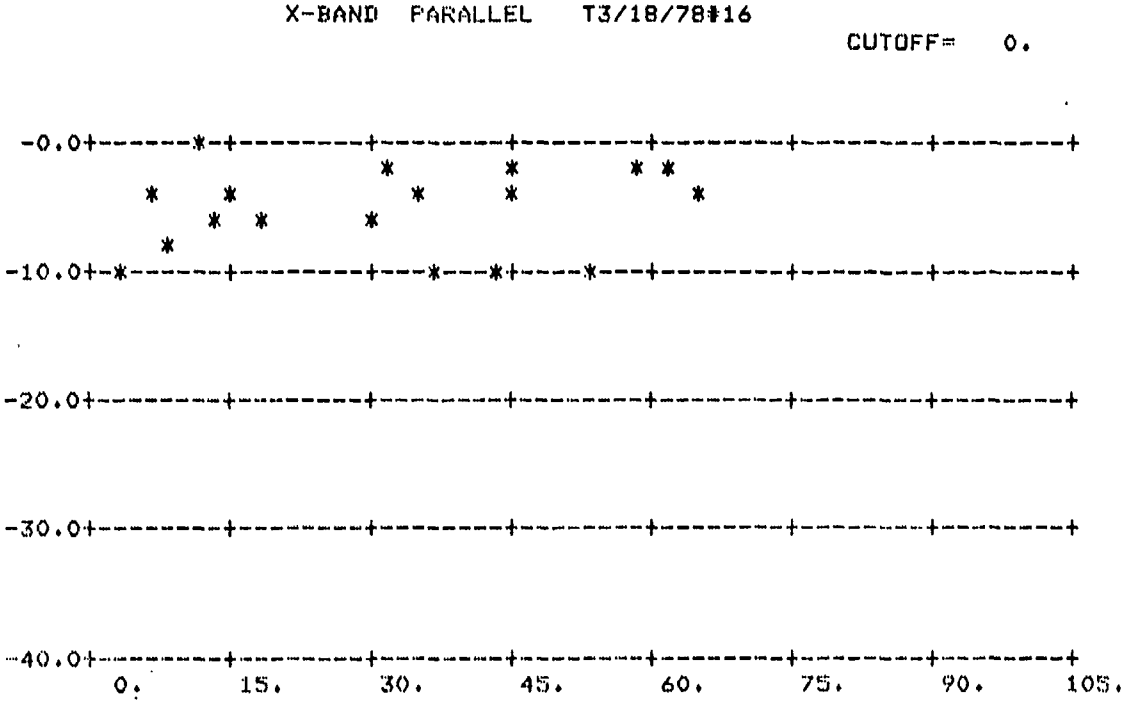

FIGURE A-81. σ_o vs ϕ_s; $\theta_s = 60°$, $\theta_i = 80°$

(Above: All Data; Below: Averages Over 5° Intervals)

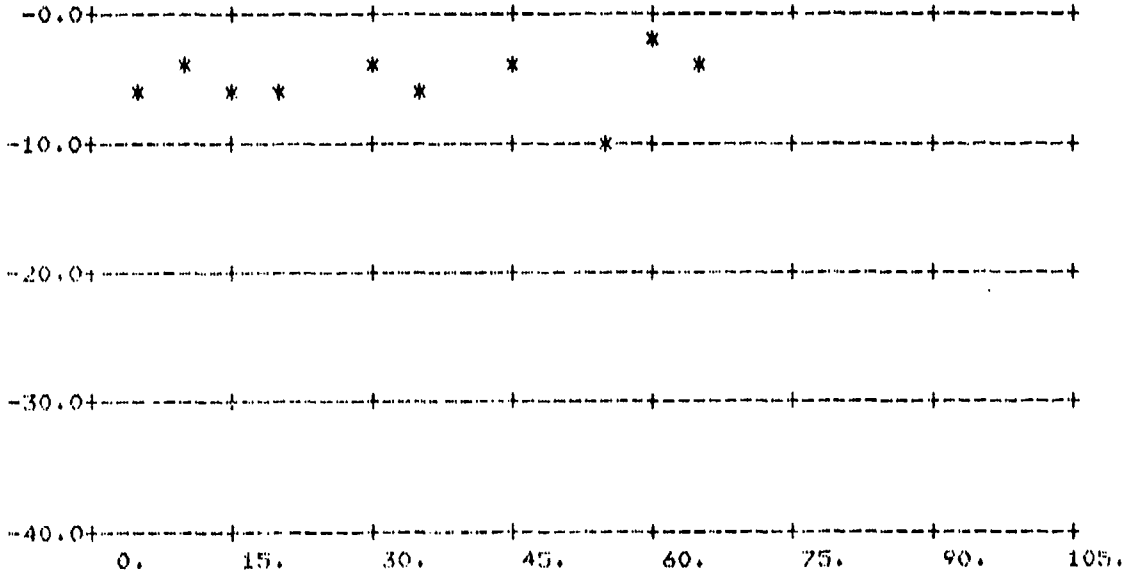

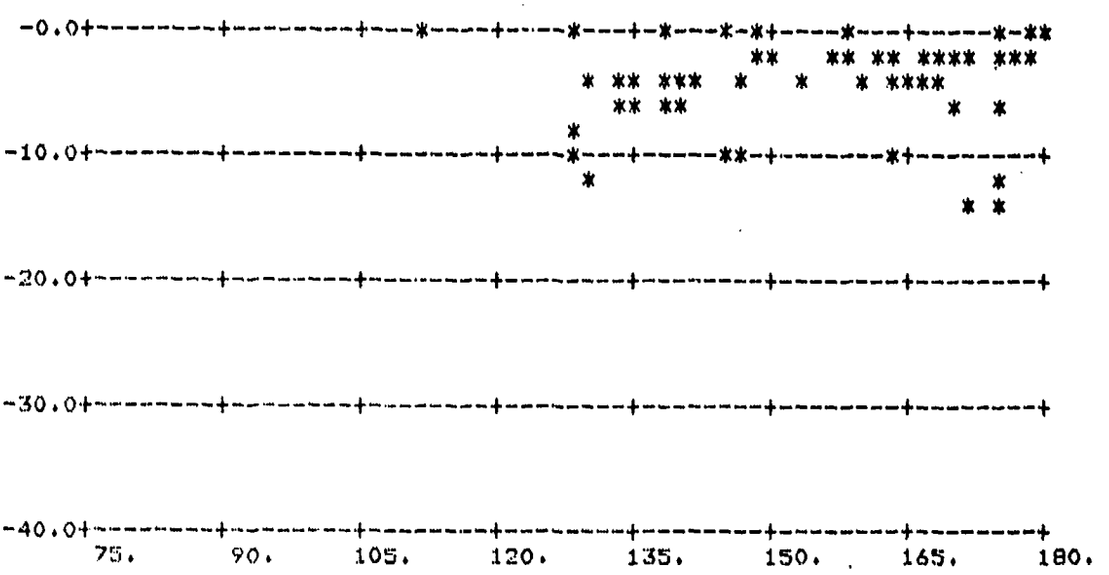

FIGURE A-82. σ_o vs ϕ_s; $\theta_s = 60°$, $\theta_i = 80°$

(Above: All Data; Below: Averages Over 5° Intervals)

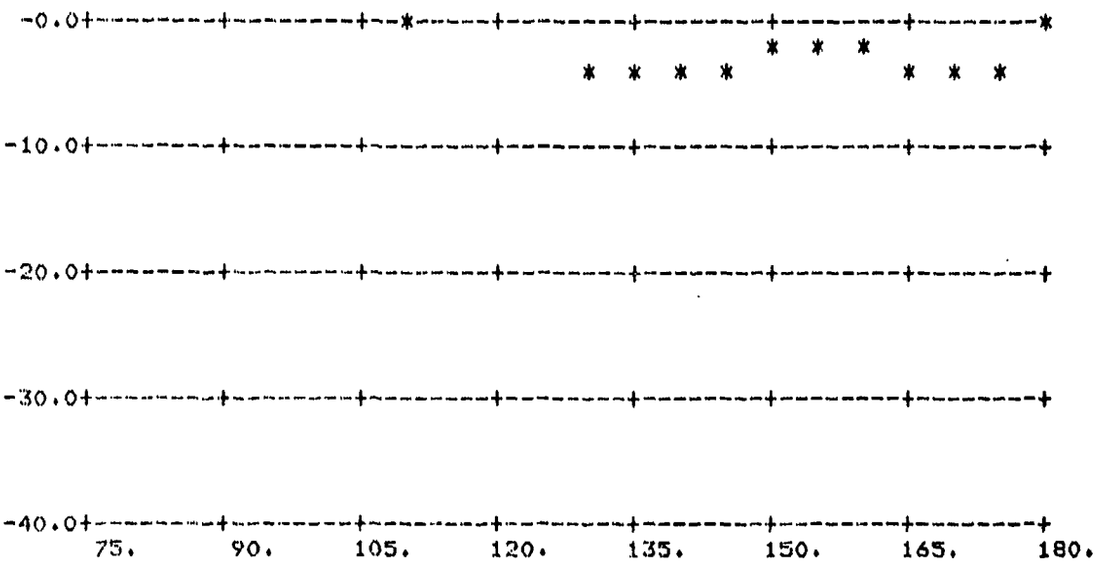

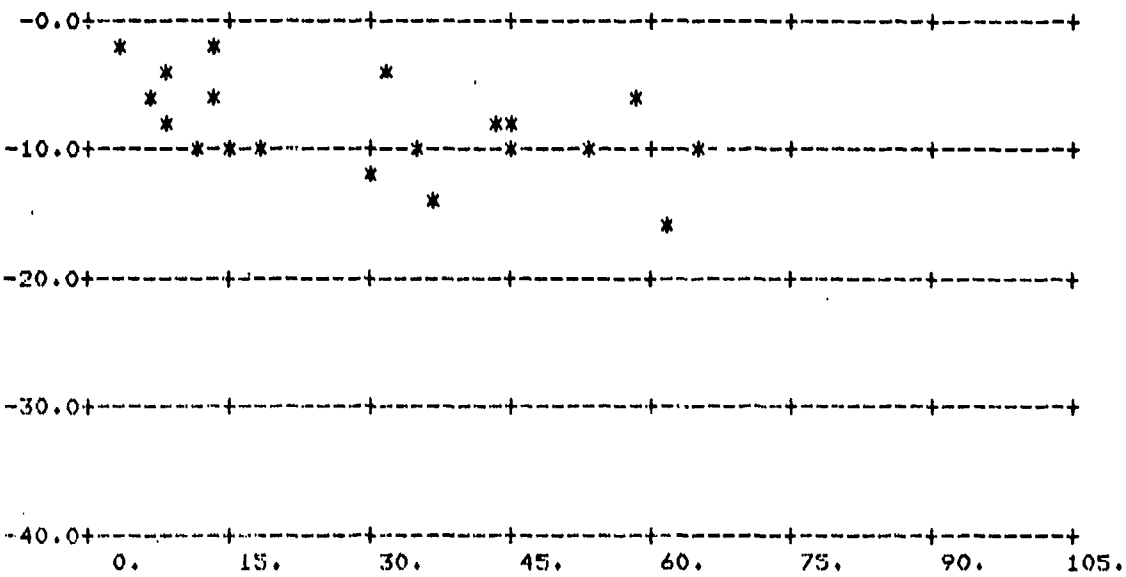

FIGURE A-83. σ_o vs ϕ_s; $\theta_s = 60°$, $\theta_i = 80°$

(Above: All Data; Below: Averages Over 5° Intervals)

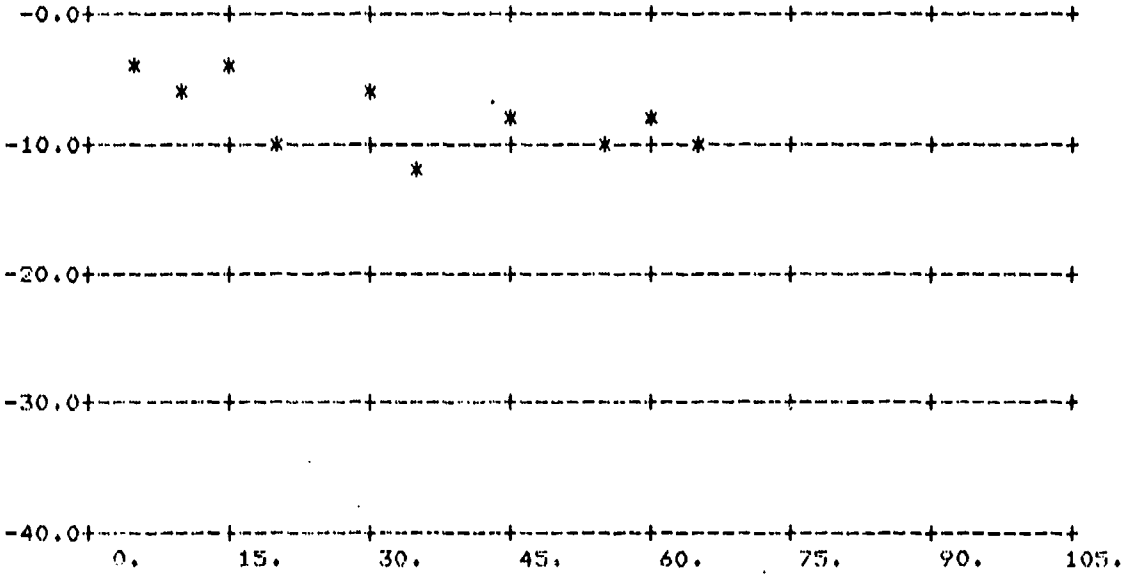

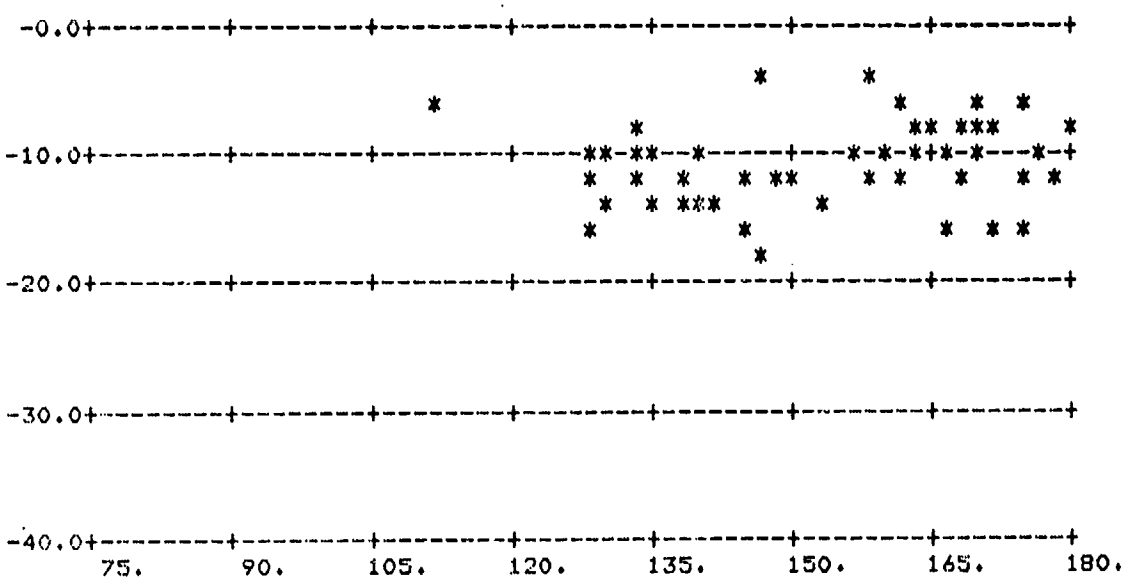

FIGURE A-84. σ_o vs ϕ_s; $\theta_n = 60°$, $\theta_i = 80°$

(Above: All Data; Below: Averages Over 5° Intervals)

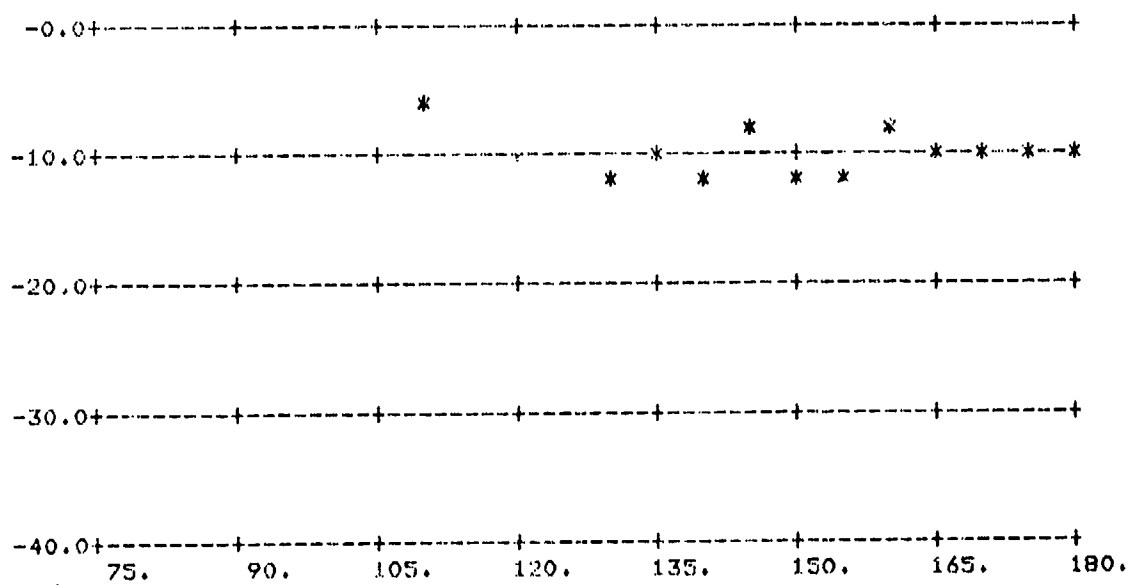

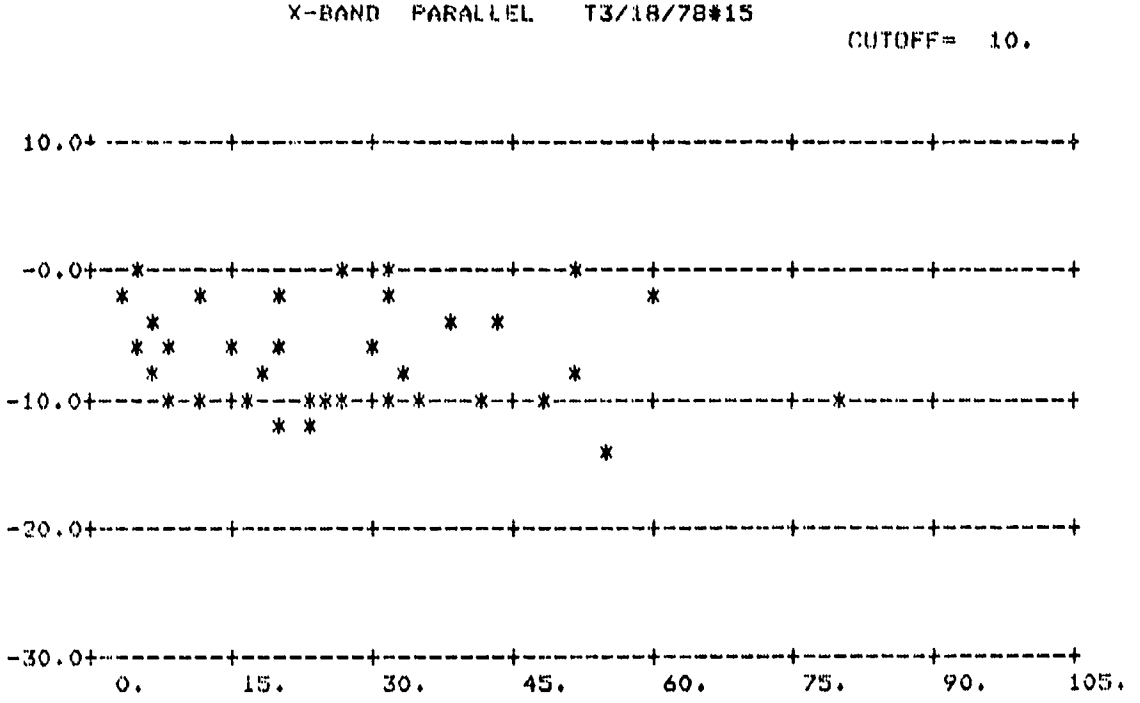

FIGURE A-85. σ_o vs ϕ_s; $\theta_s = 70°$, $\theta_i = 80°$

(Above: All Data; Below: Averages Over 5° Intervals)

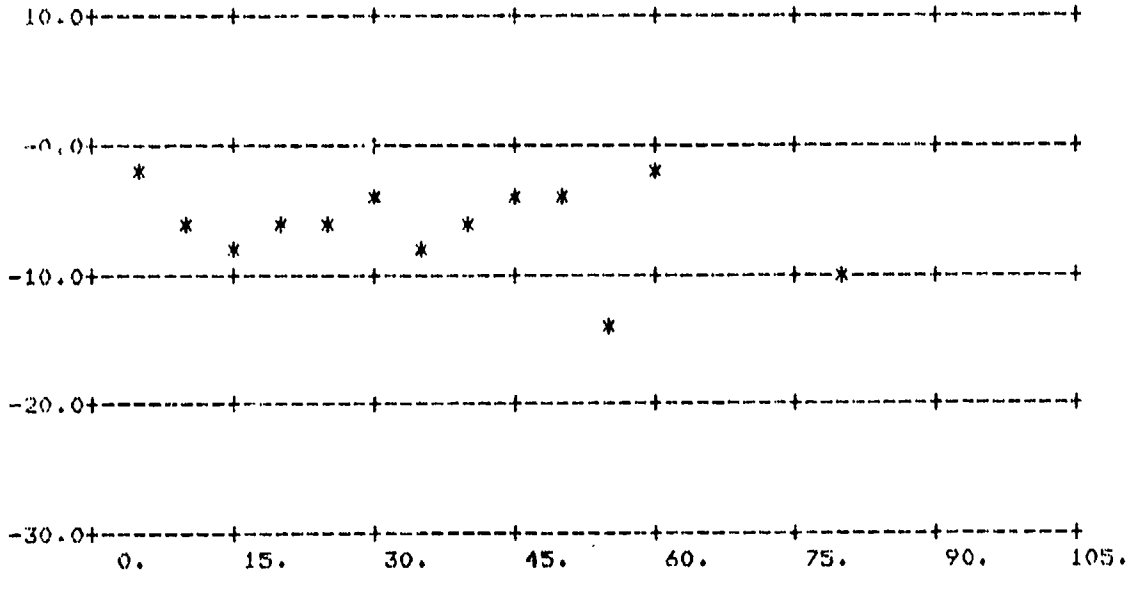

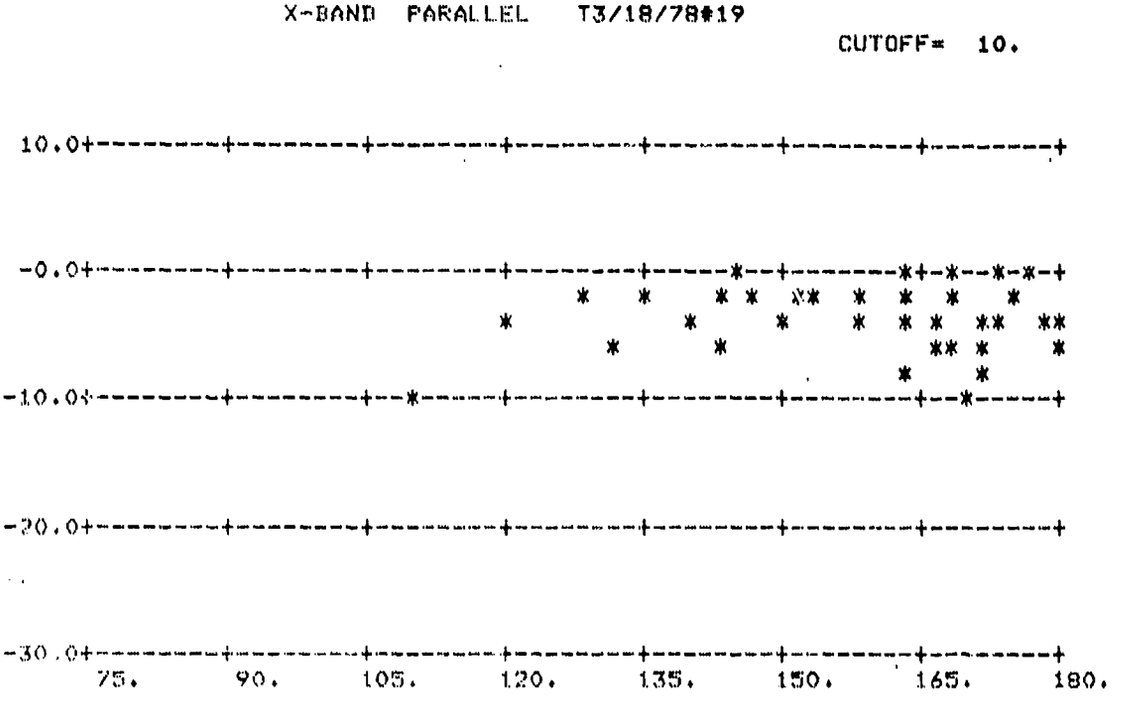

FIGURE A-86. σ_o vs ϕ_s; $\theta_s = 70°$, $\theta_i = 80°$

(Above: All Data; Below: Averages Over 5° Intervals)

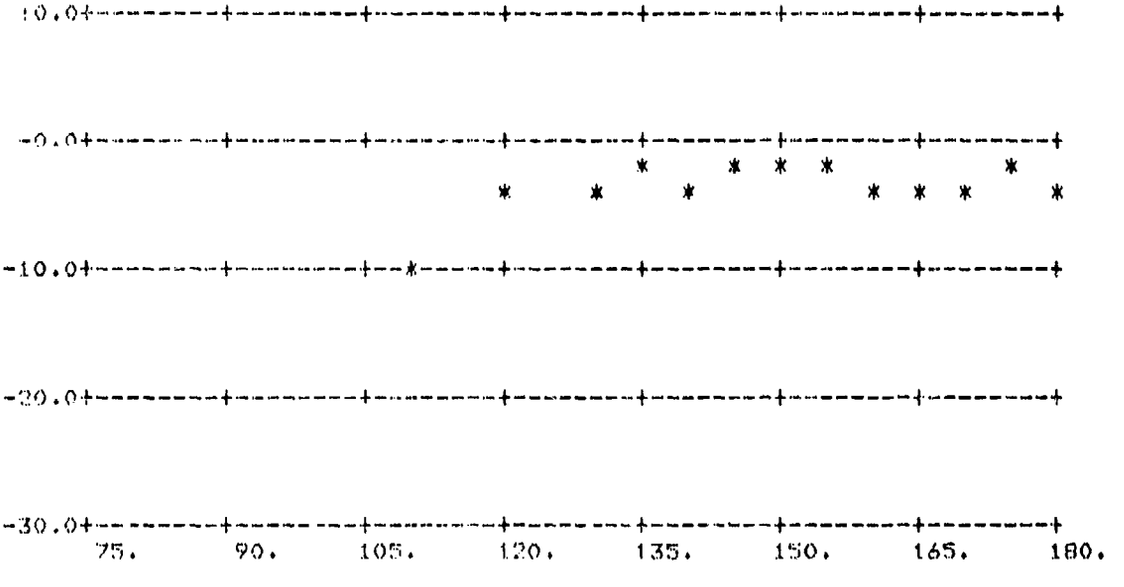

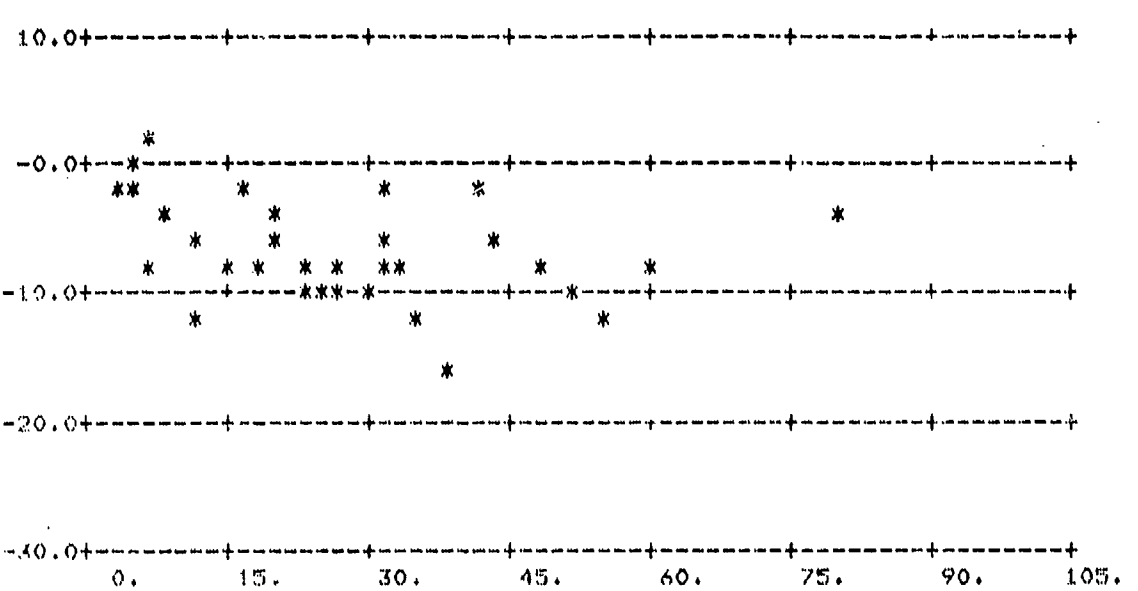

FIGURE A-87. σ_o vs ϕ_s; $\theta_s = 70°$, $\theta_i = 80°$

(Above: All Data; Below: Averages Over 5° Intervals)

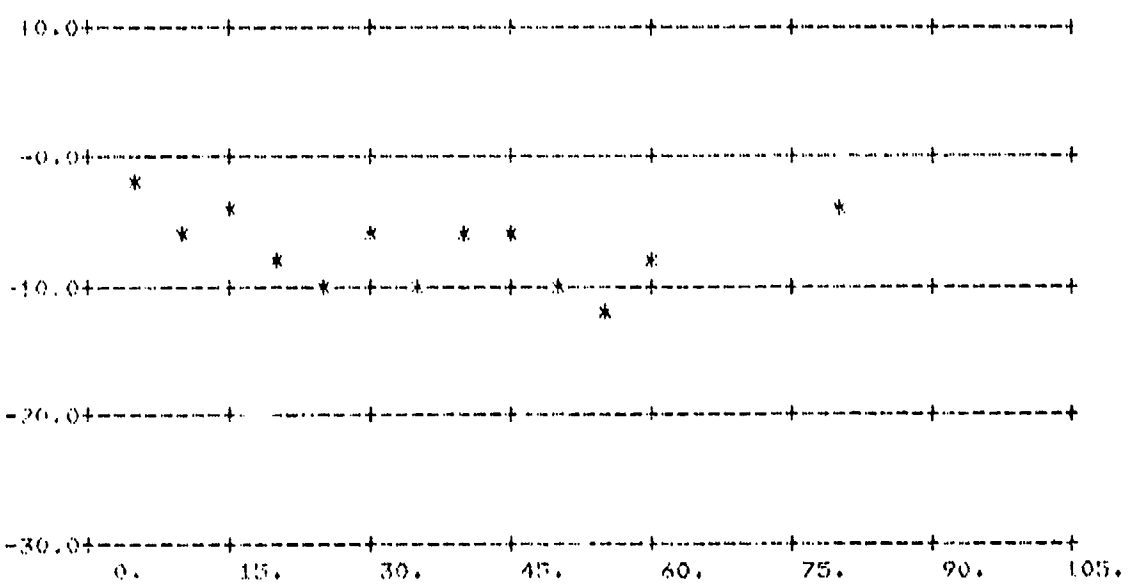

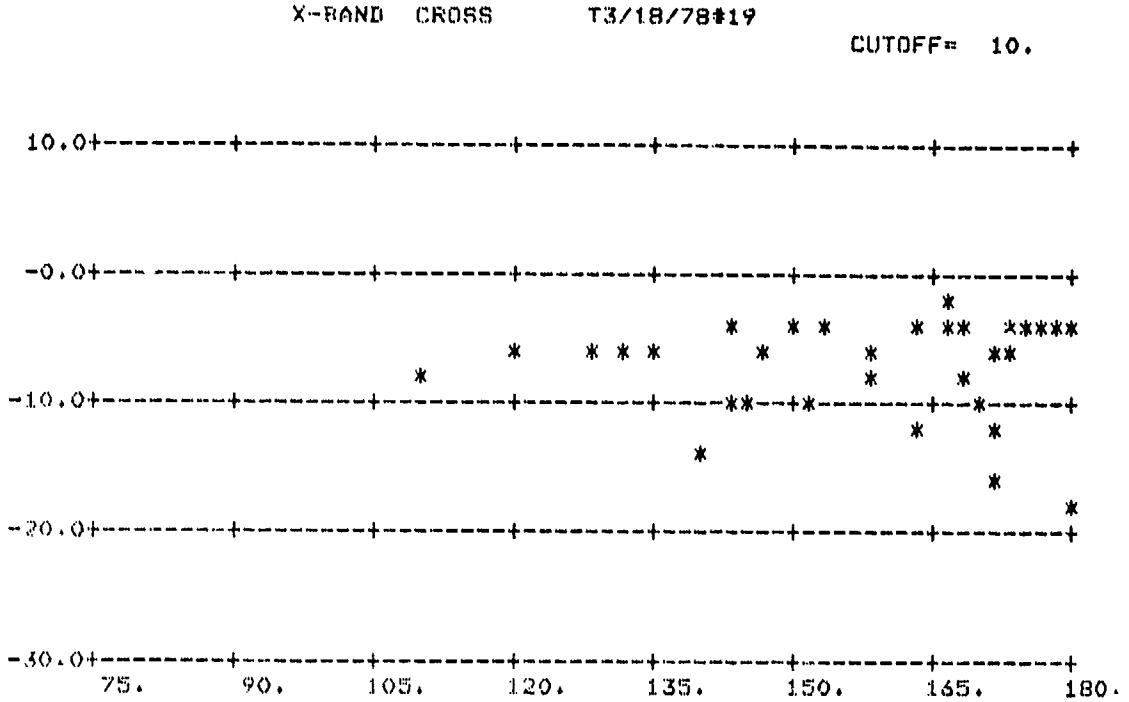

FIGURE A-88. σ_o vs ϕ_s; $\theta_s = 70°$, $\theta_i = 80°$

(Above: All Data; Below: Averages Over 5° Intervals)

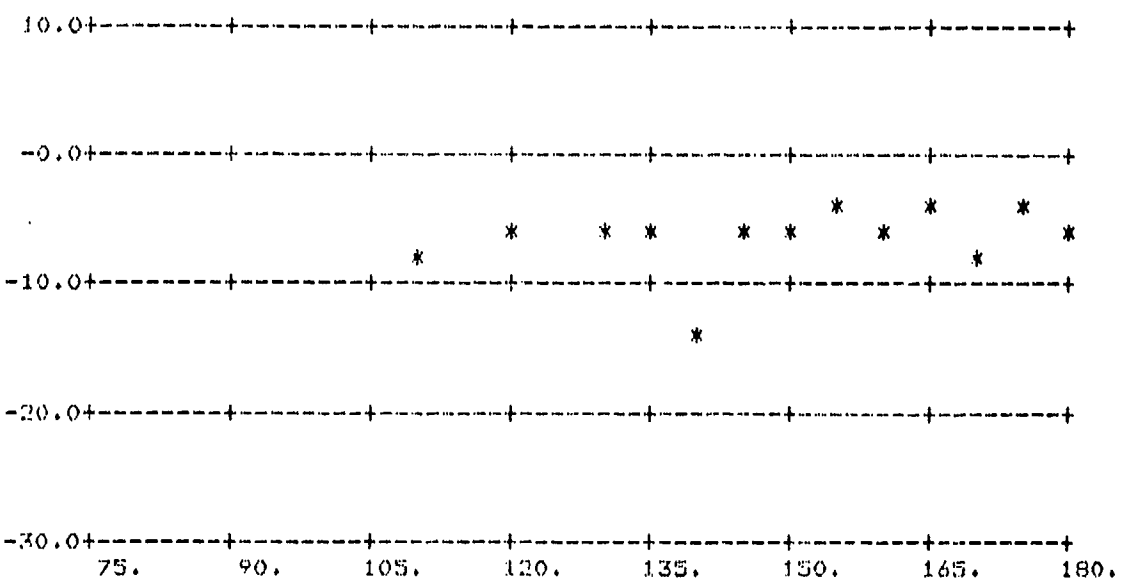

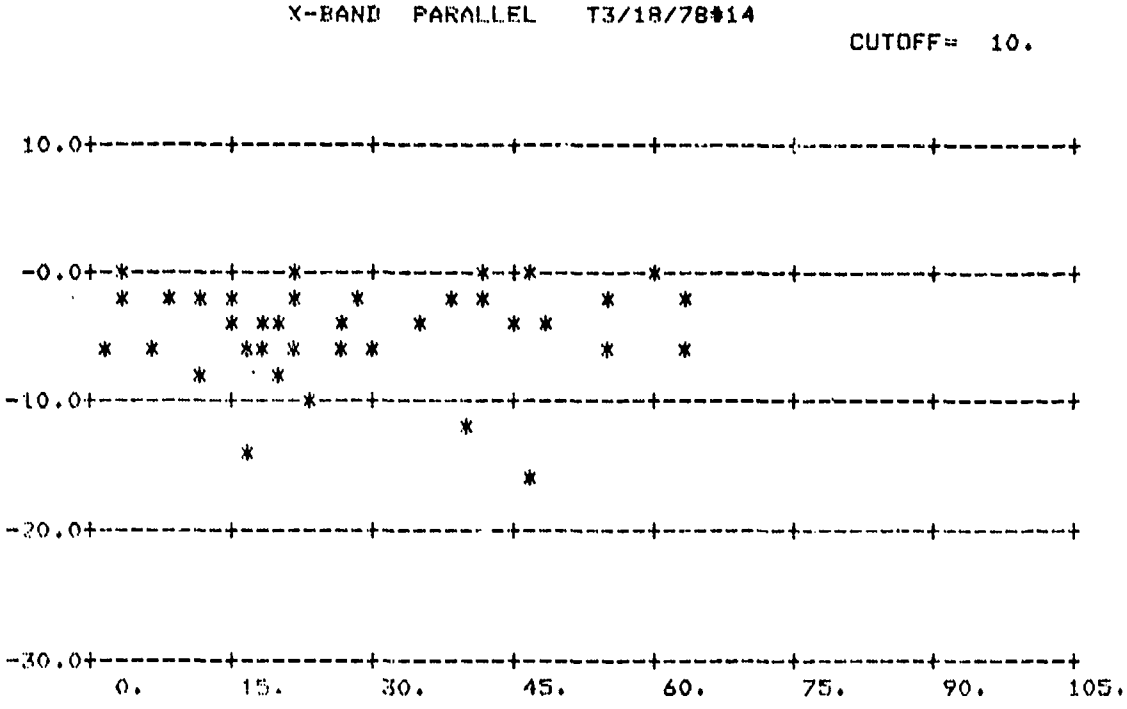

FIGURE A-89. σ_o vs ϕ_s; $\theta_s = 80°$, $\theta_i = 80°$

(Above: All Data; Below: Averages Over 5° Intervals)

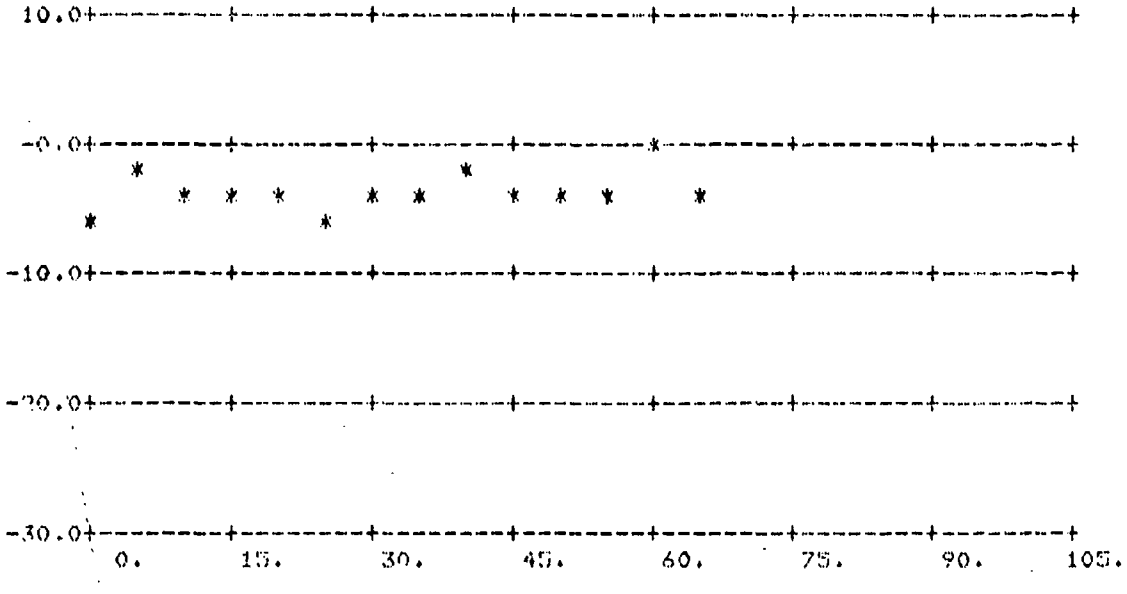

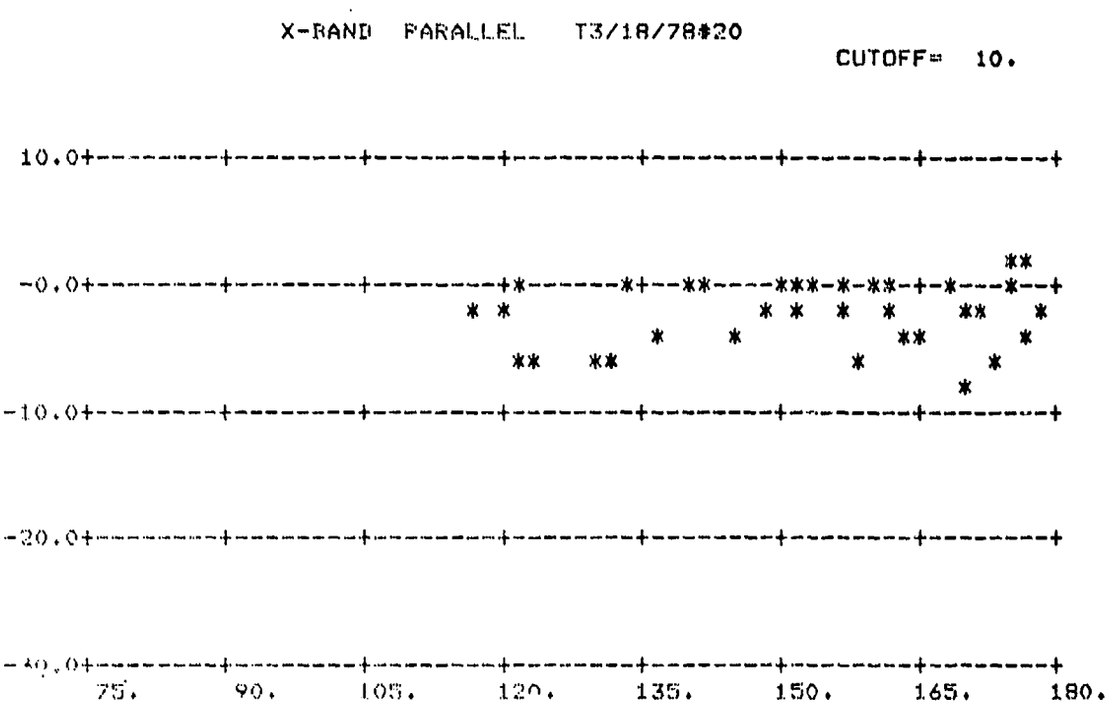

FIGURE A-90. σ_o vs ϕ_s; $\theta_s = 80°$, $\theta_i = 80°$

(Above: All Data; Below: Averages Over 5° Intervals)

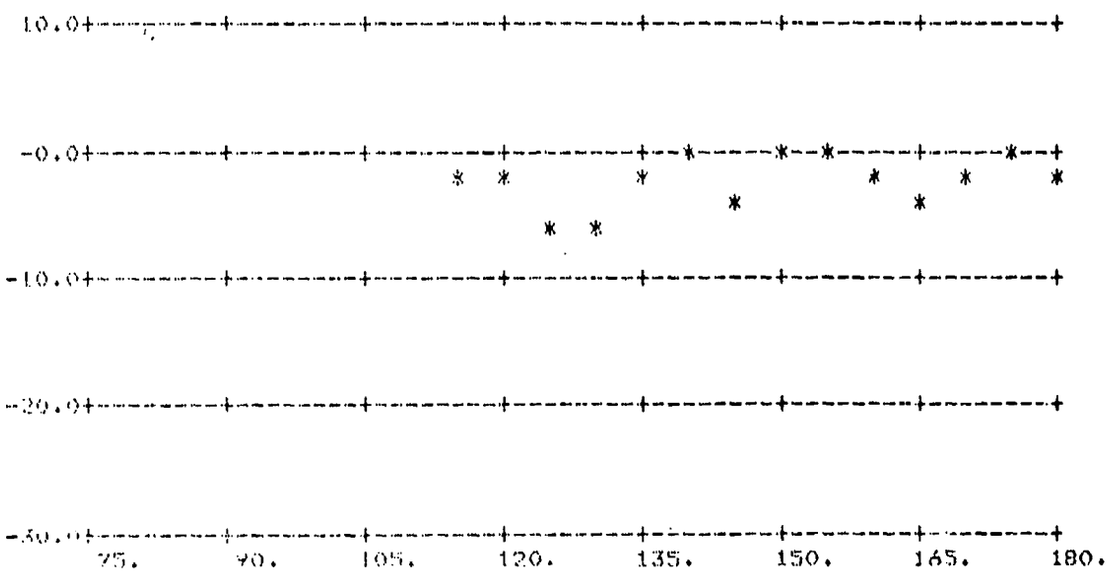

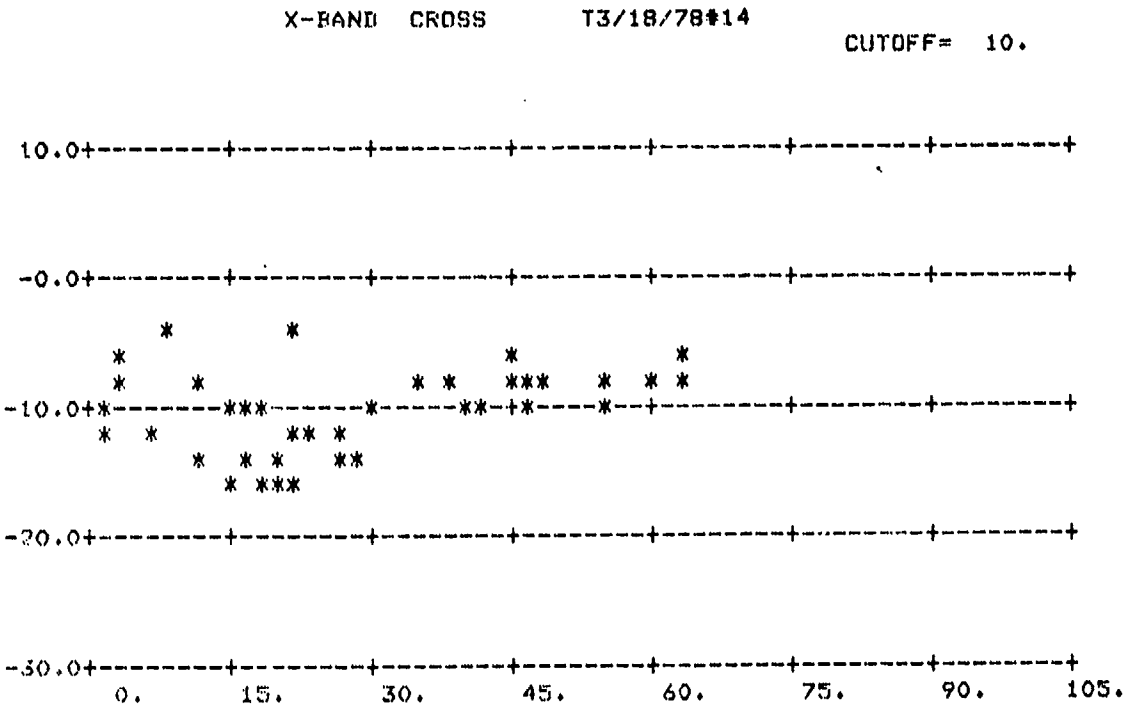

FIGURE A-91. σ_o vs ϕ_s; $\theta_s = 80°$, $\theta_i = 80°$

(Above: All Data; Below: Averages Over 5° Intervals)

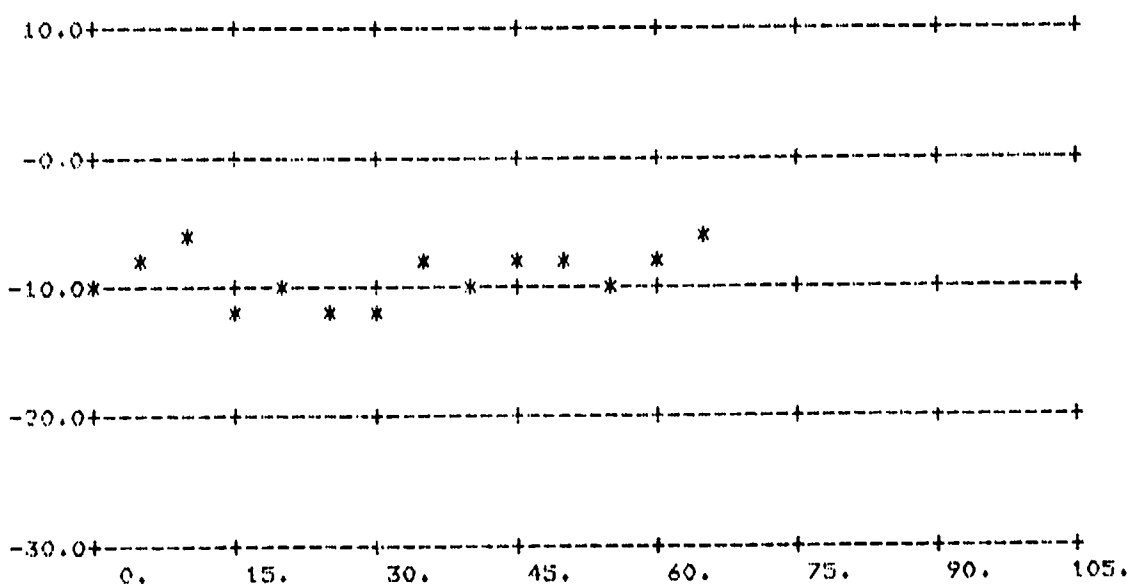

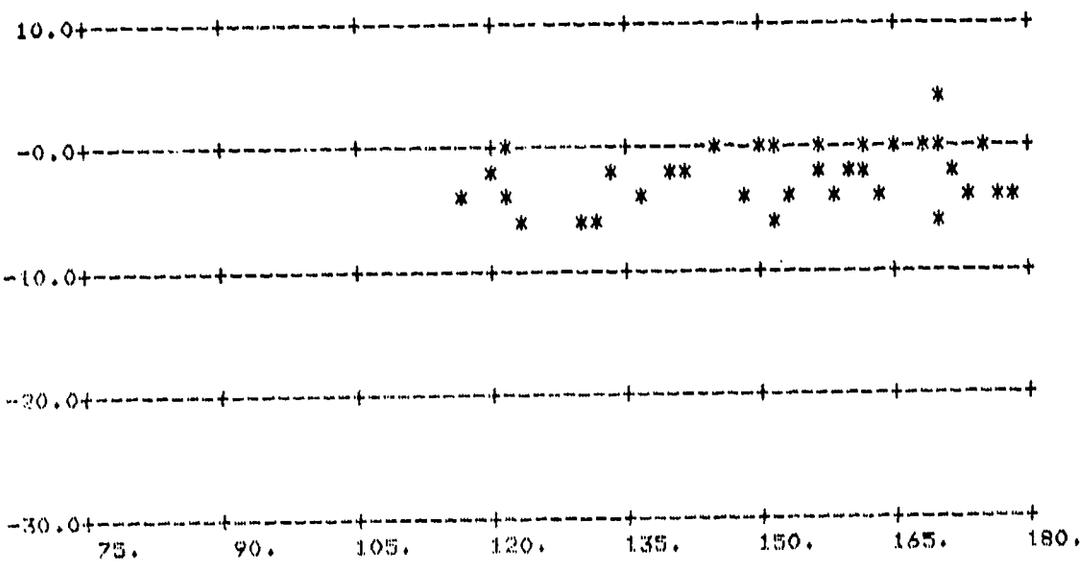

FIGURE A-92. σ_o vs ϕ_s; $\theta_s = 80°$, $\theta_i = 80°$

(Above: All Data; Below: Averages Over 5° Intervals)

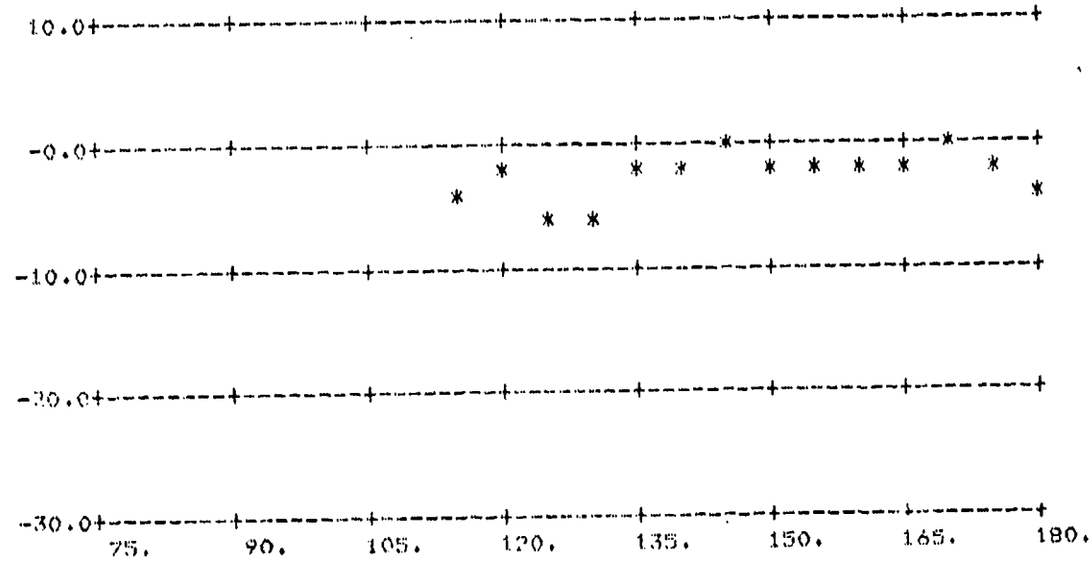

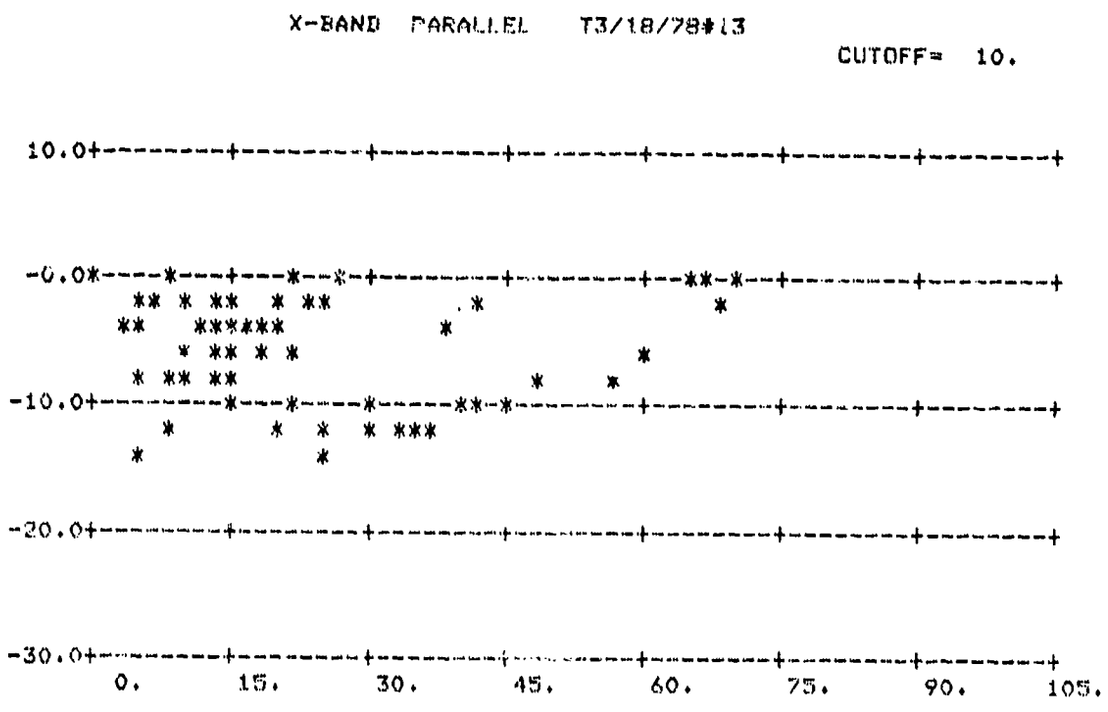

FIGURE A-93. σ_o vs ϕ_s; $\theta_s = 84°$, $\theta_i = 80°$

(Above: All Data; Below: Averages Over 5° Intervals)

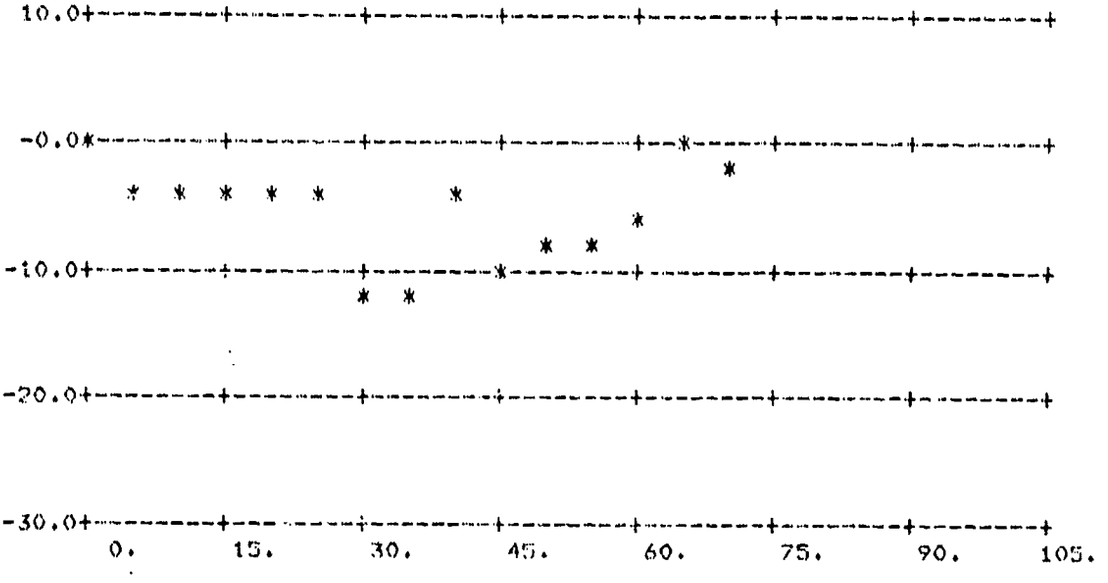

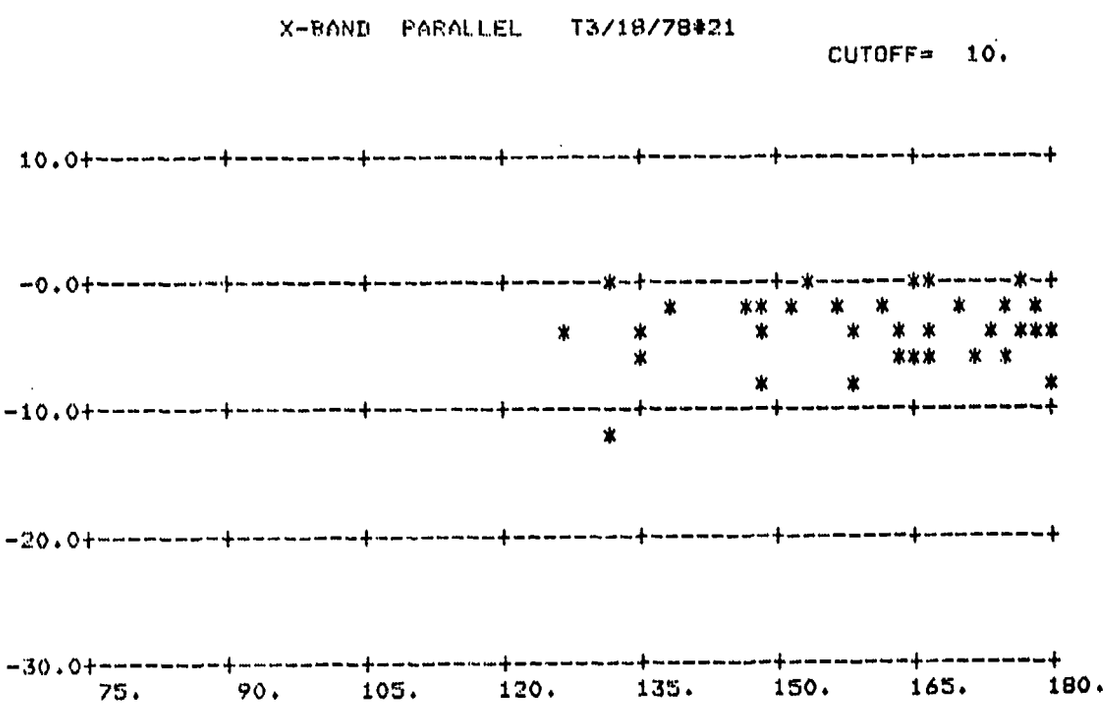

FIGURE A-94. σ_o vs ϕ_s; $\theta_s = 84°$, $\theta_i = 80°$

(Above: All Data; Below: Averages Over 5° Intervals)

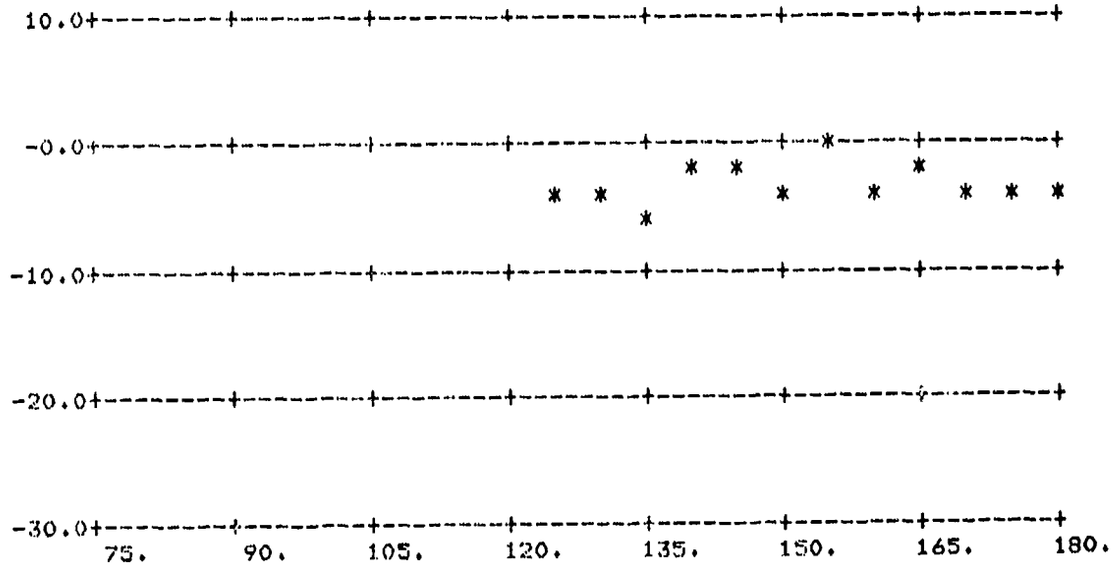

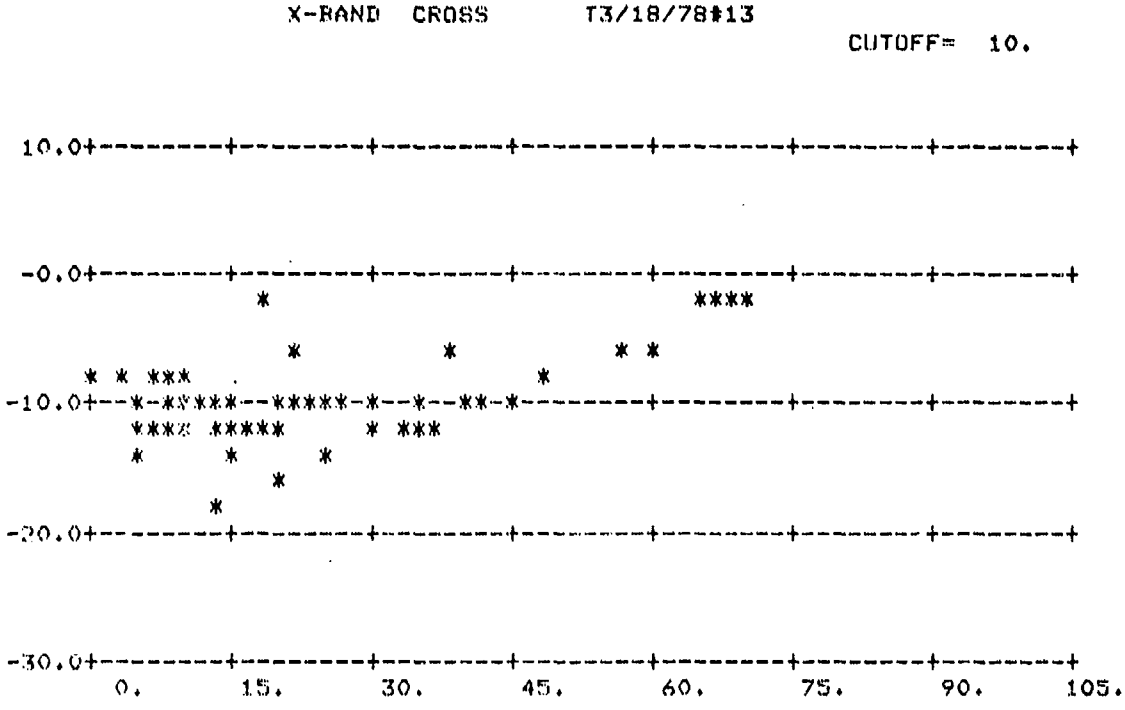

FIGURE A-95. σ_o vs ϕ_s; $\theta_s = 84°$, $\theta_i = 80°$

(Above: All Data; Below: Averages Over 5° Intervals)

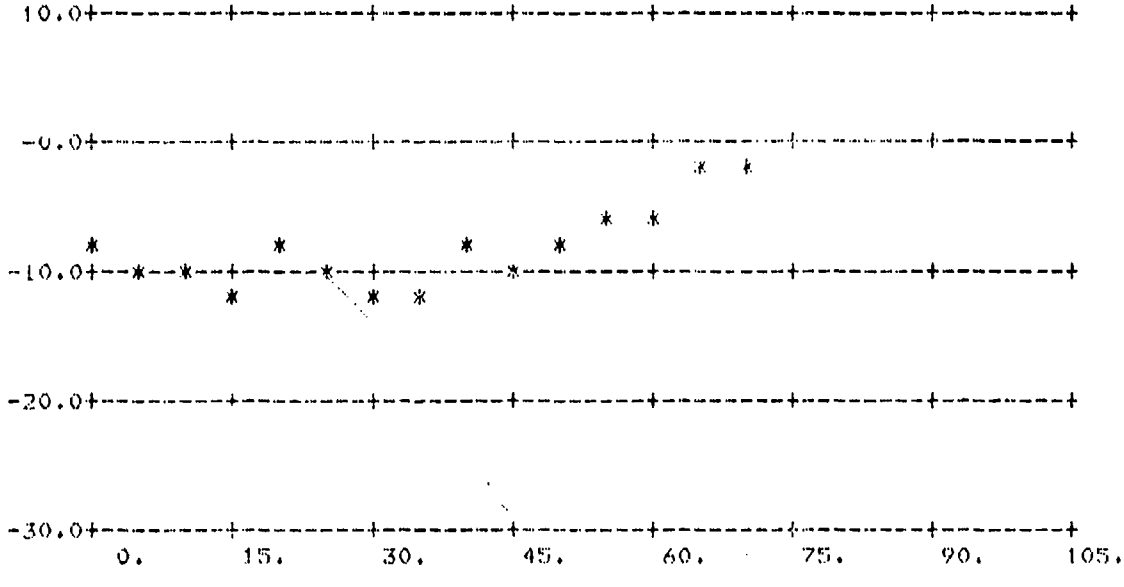

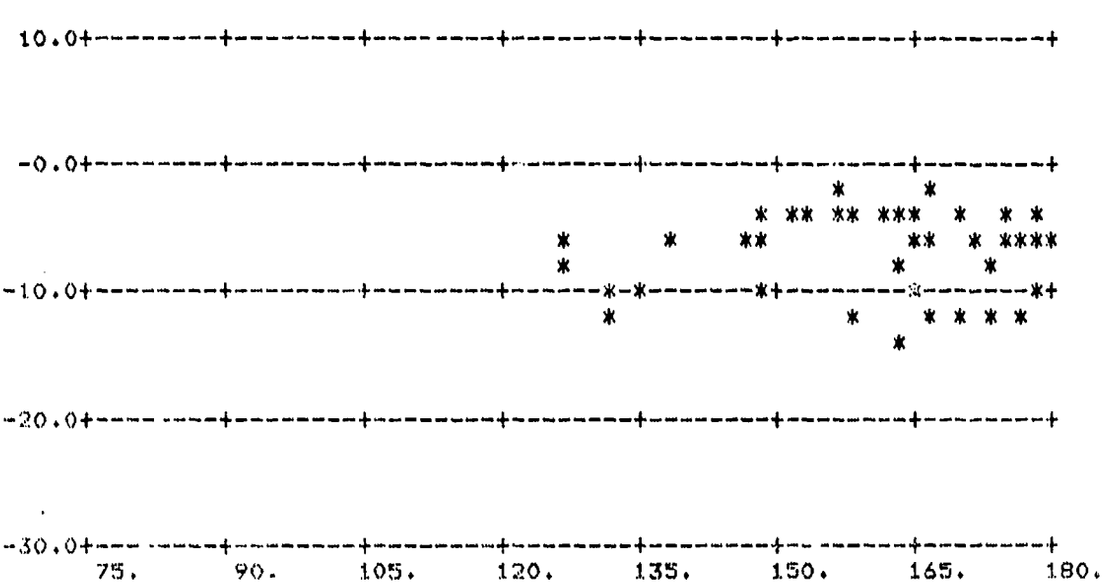

FIGURE A-96. σ_o vs ϕ_s; $\theta_s = 84°$, $\theta_i = 80°$

(Above: All Data; Below: Averages Over 5° Intervals)

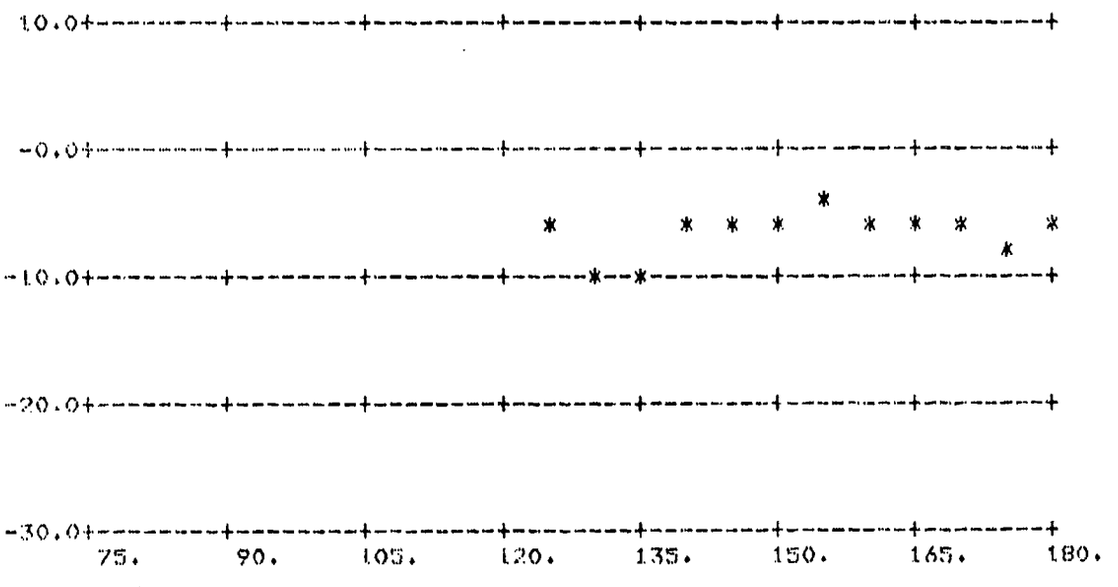

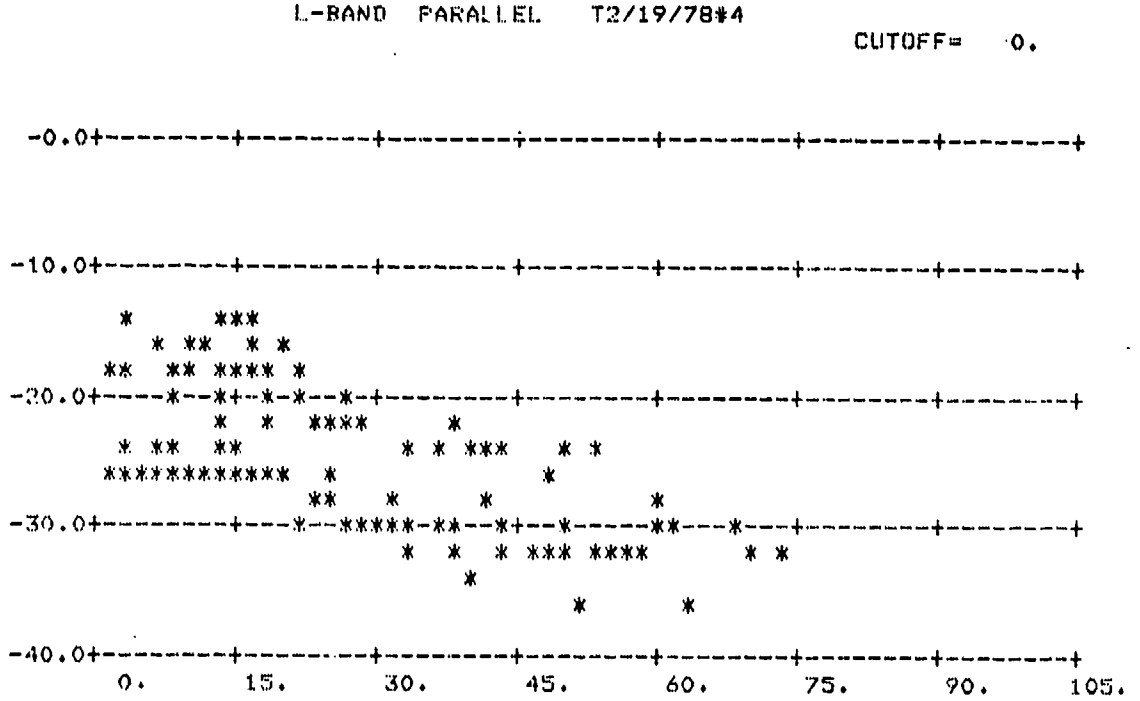

FIGURE A-97. σ_o vs ϕ_s; $\theta_s = 60°$, $\theta_i = 60°$

(Above: All Data; Below: Averages Over 5° Intervals)

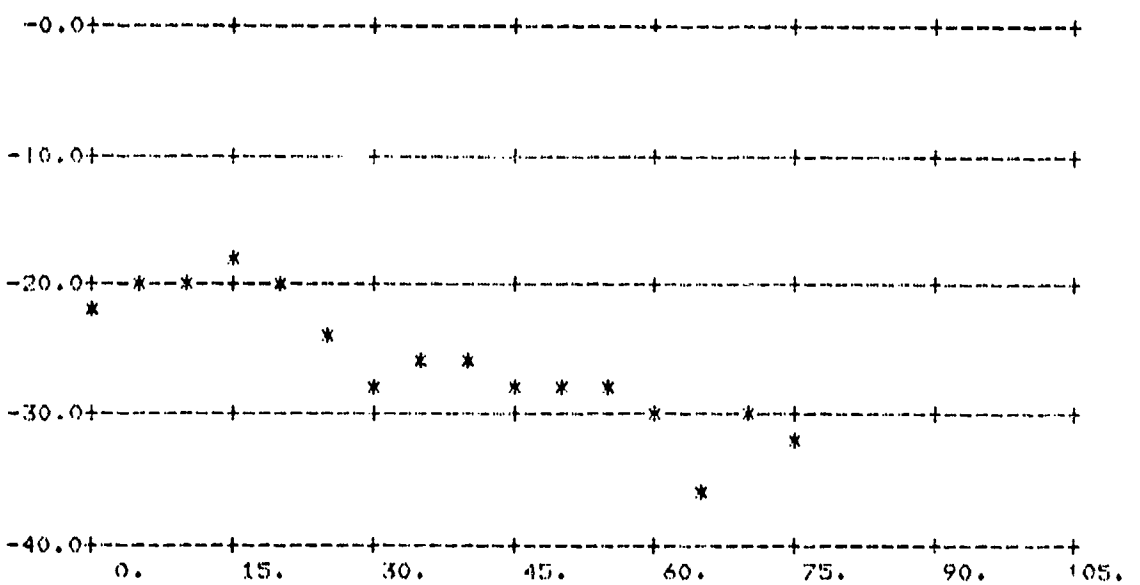

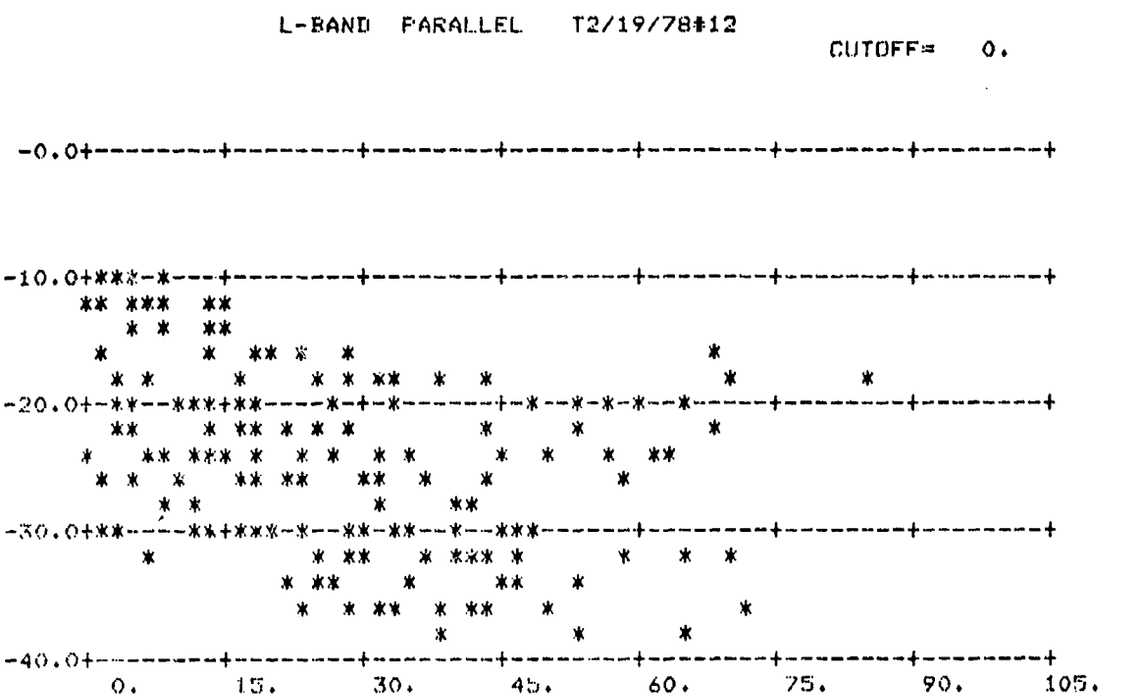

FIGURE A-99. σ_o vs ϕ_s; $\theta_s = 60°$, $\theta_i = 60°$

(Above: All Data; Below: Averages Over 5° Intervals)

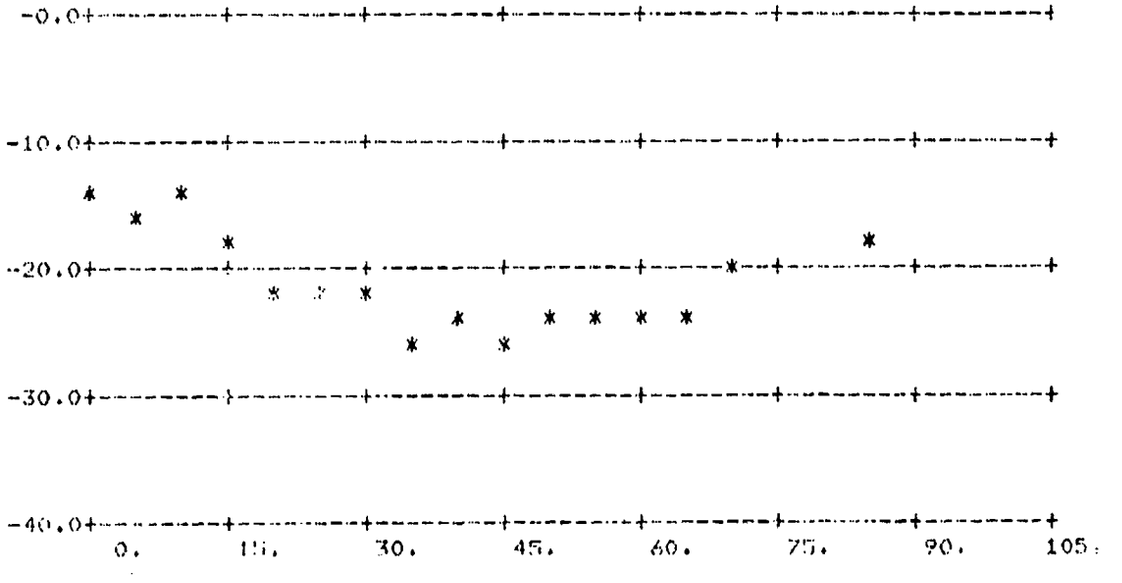

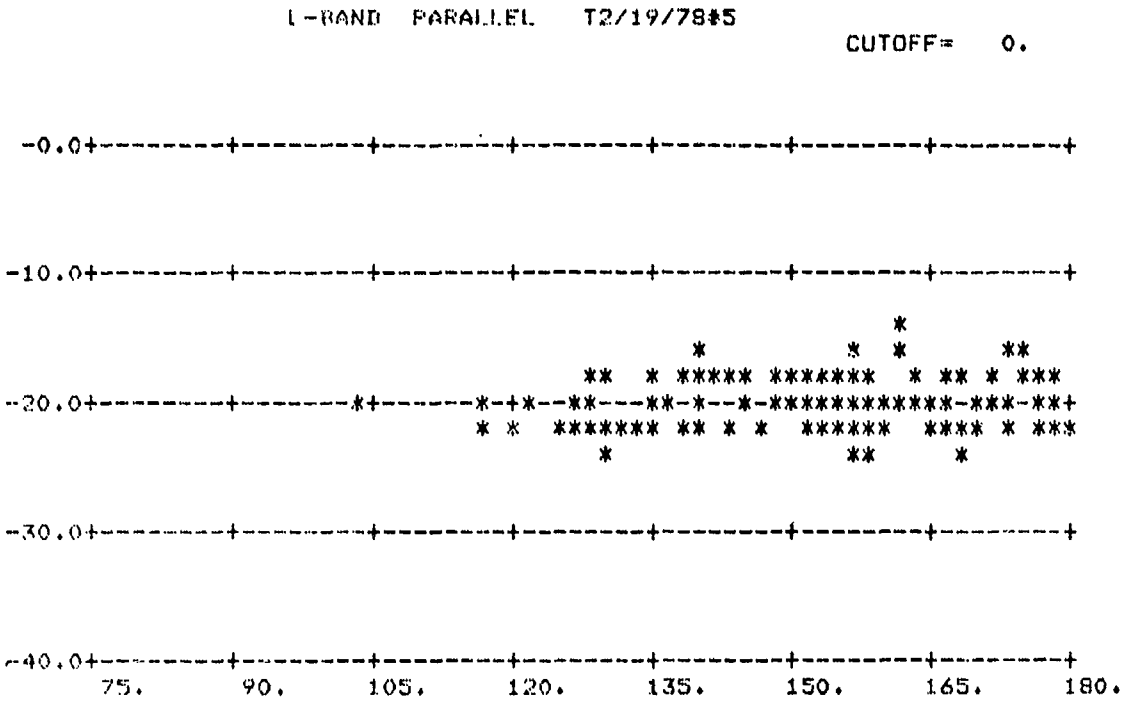

FIGURE A-100. σ_o vs ϕ_s; $\theta_s = 60°$, $\theta_i = 60°$

(Above: All Data; Below: Averages Over 5° Intervals)

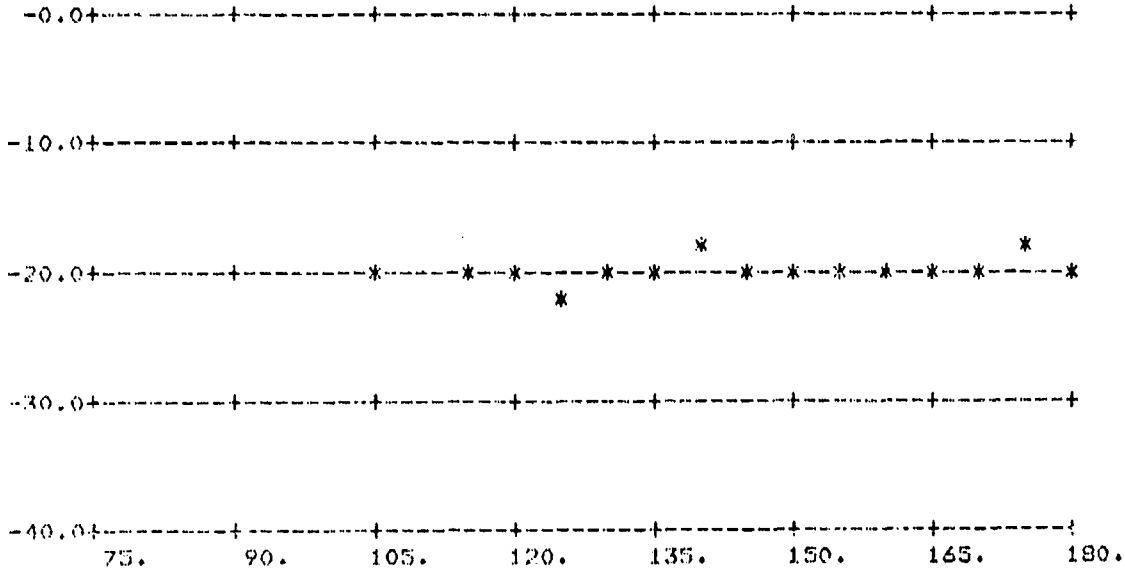

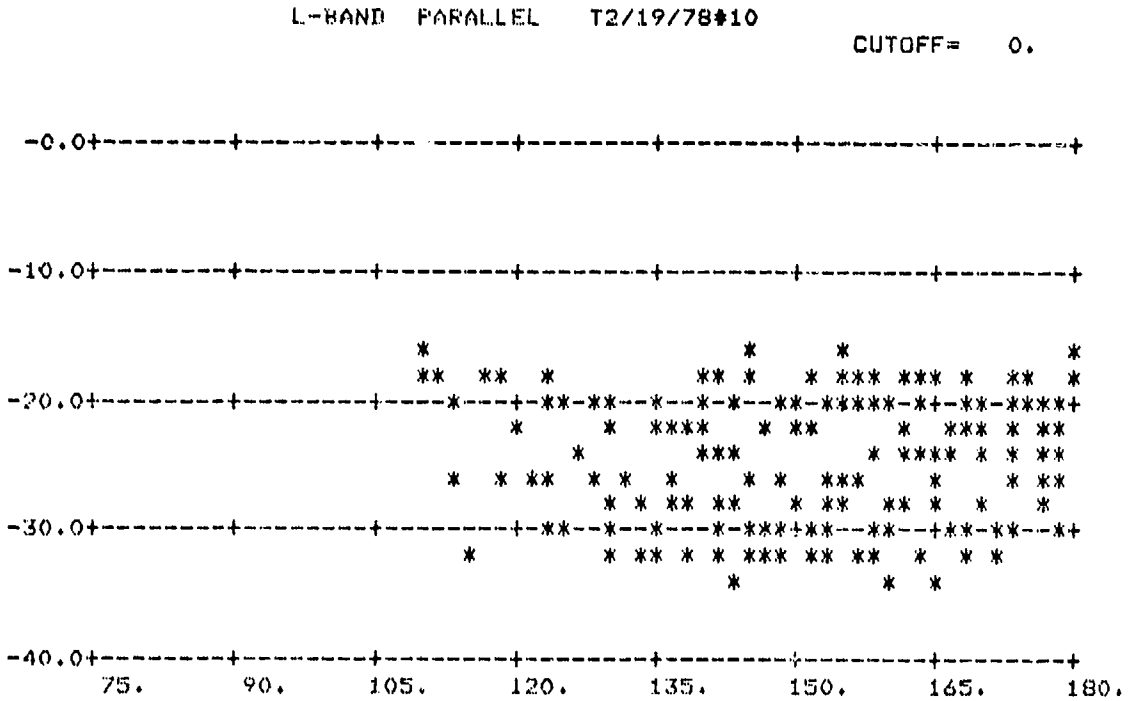

FIGURE A-101. σ_o vs ϕ_s; $\theta_s = 60°$, $\theta_i = 60°$

(Above: All Data; Below: Averages Over 5° Intervals)

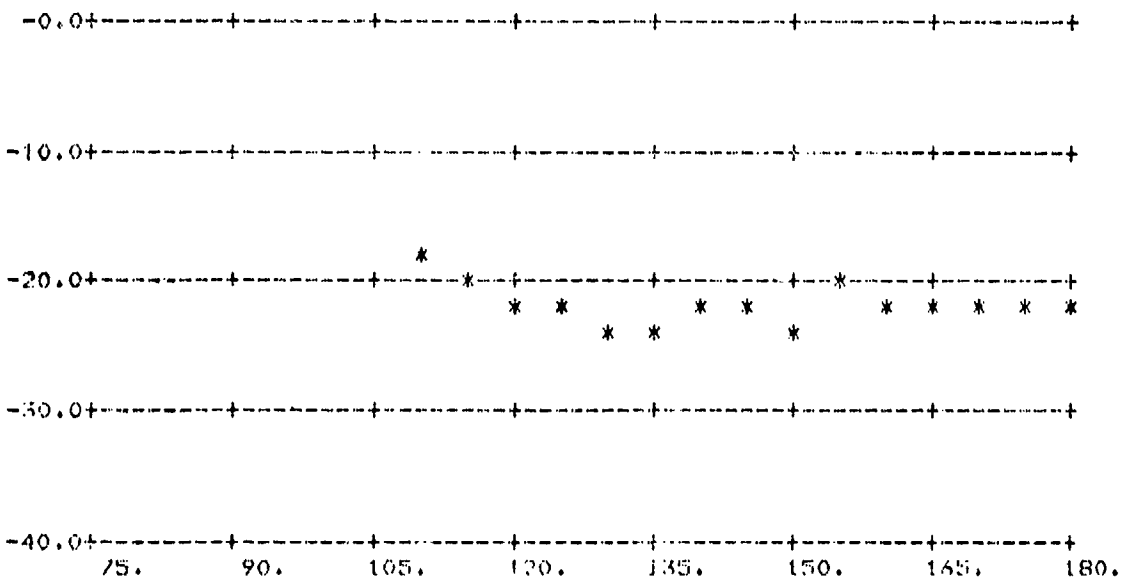

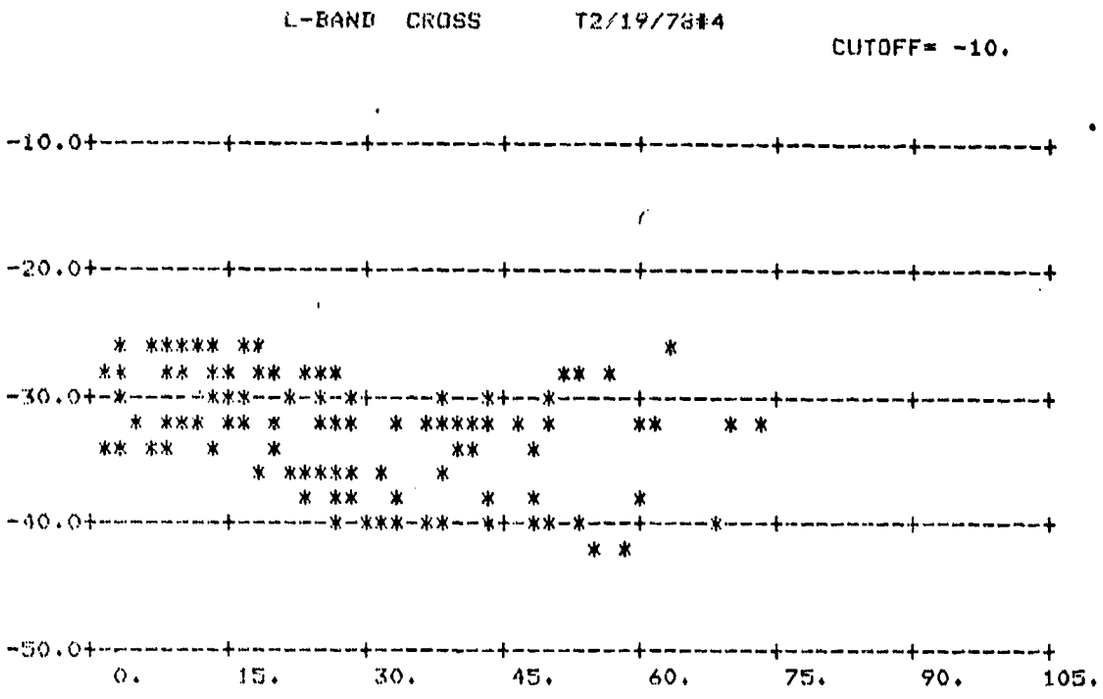

FIGURE A-102. σ_o vs ϕ_s; $\theta_s = 60°$, $\theta_i = 60°$

(Above: All Data; Below: Averages Over 5° Intervals)

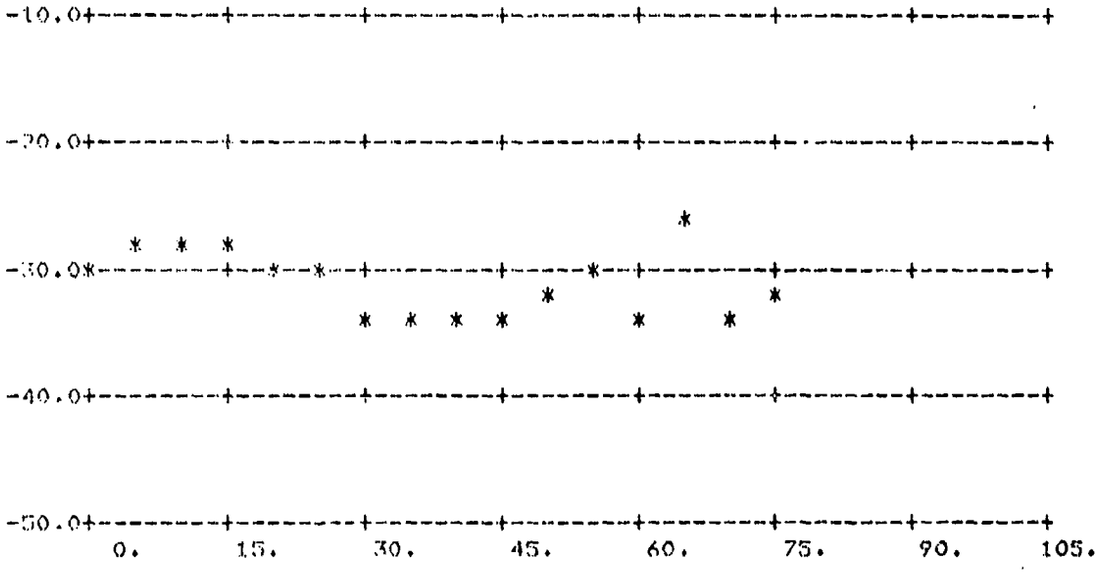

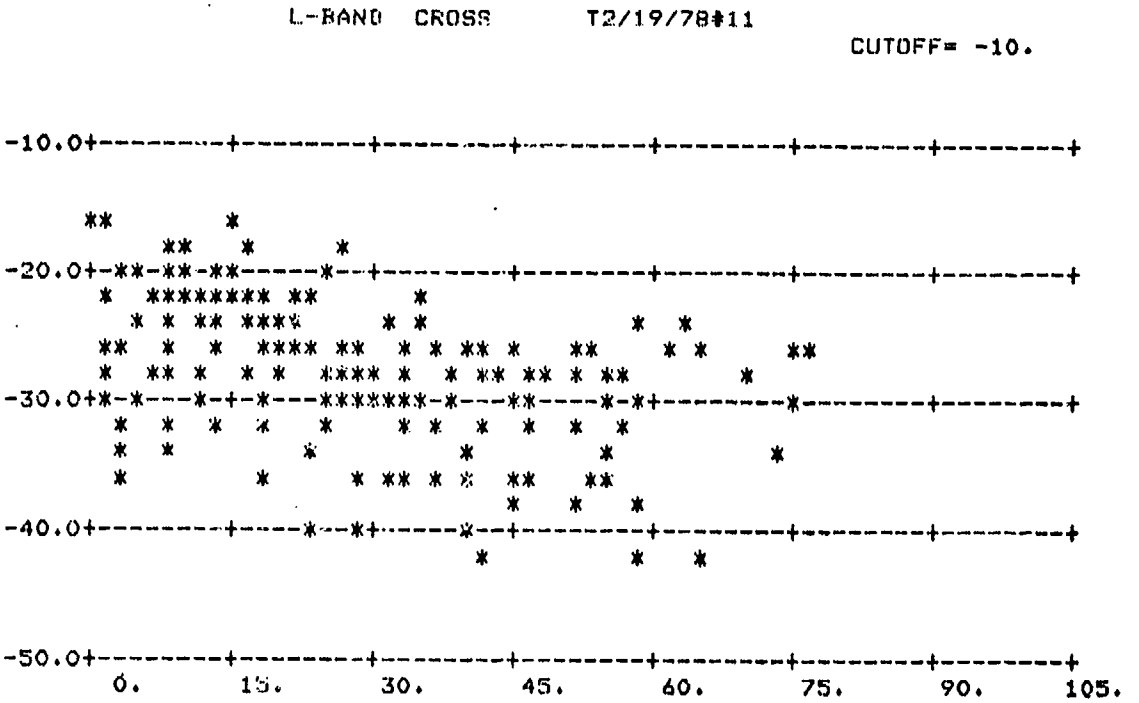

FIGURE A-103. σ_o vs ϕ_s; $\theta_s = 60°$, $\theta_i = 60°$

(Above: All Data; Below: Averages Over 5° Intervals)

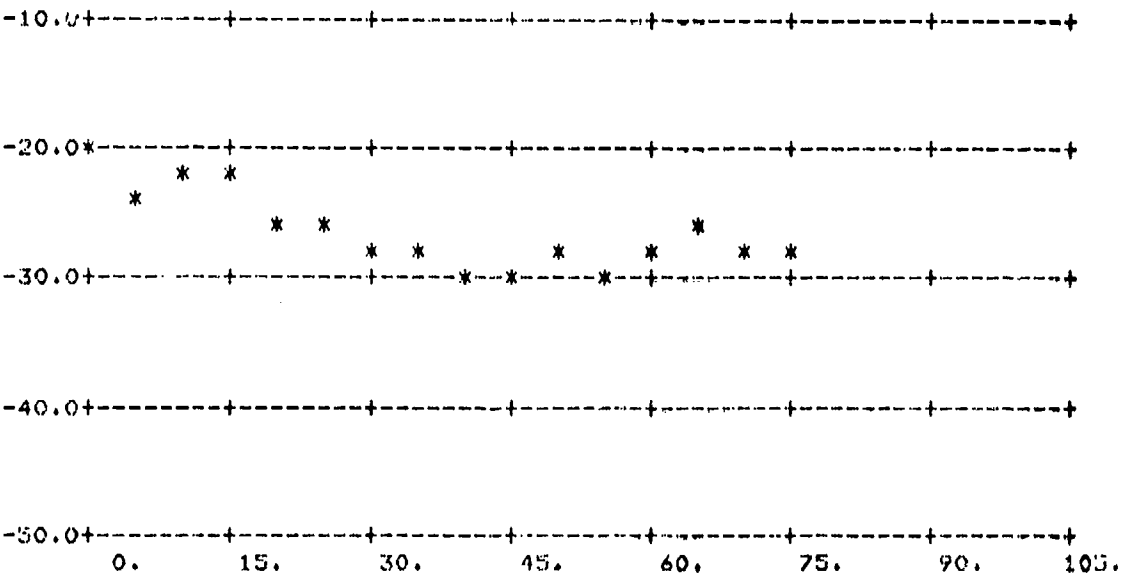

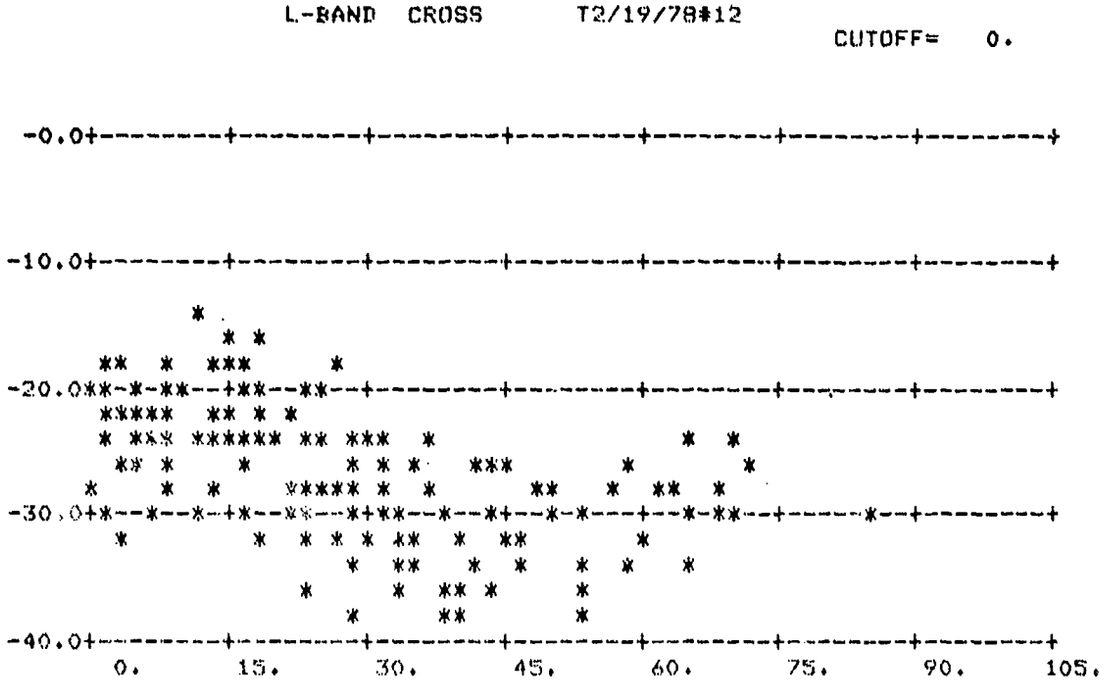

FIGURE A-104. σ_o vs ϕ_s; $\theta_s = 60°$, $\theta_i = 60°$

(Above: All Data; Below: Averages Over 5° Intervals)

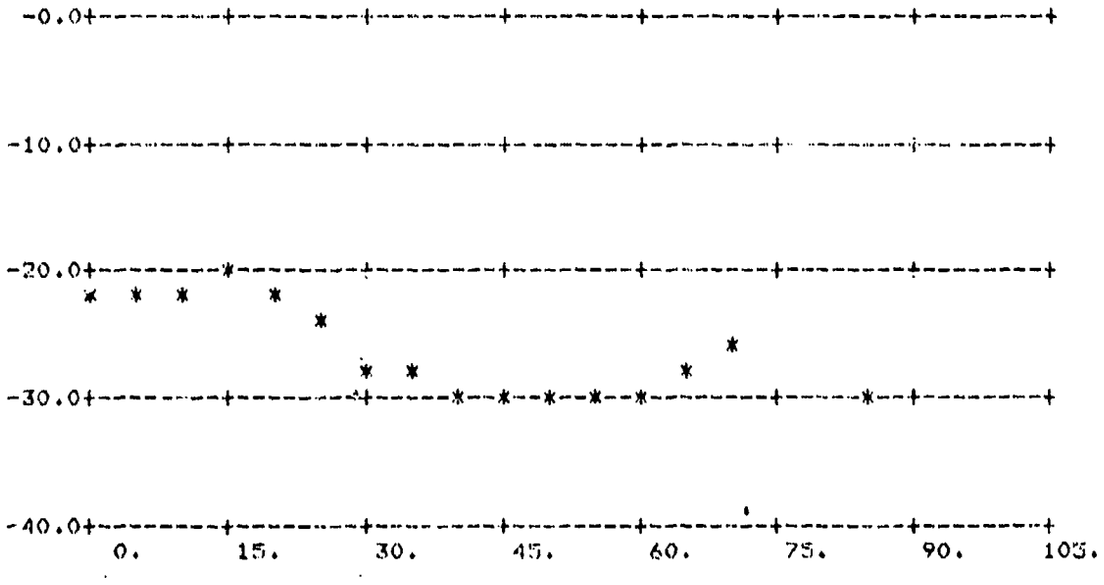

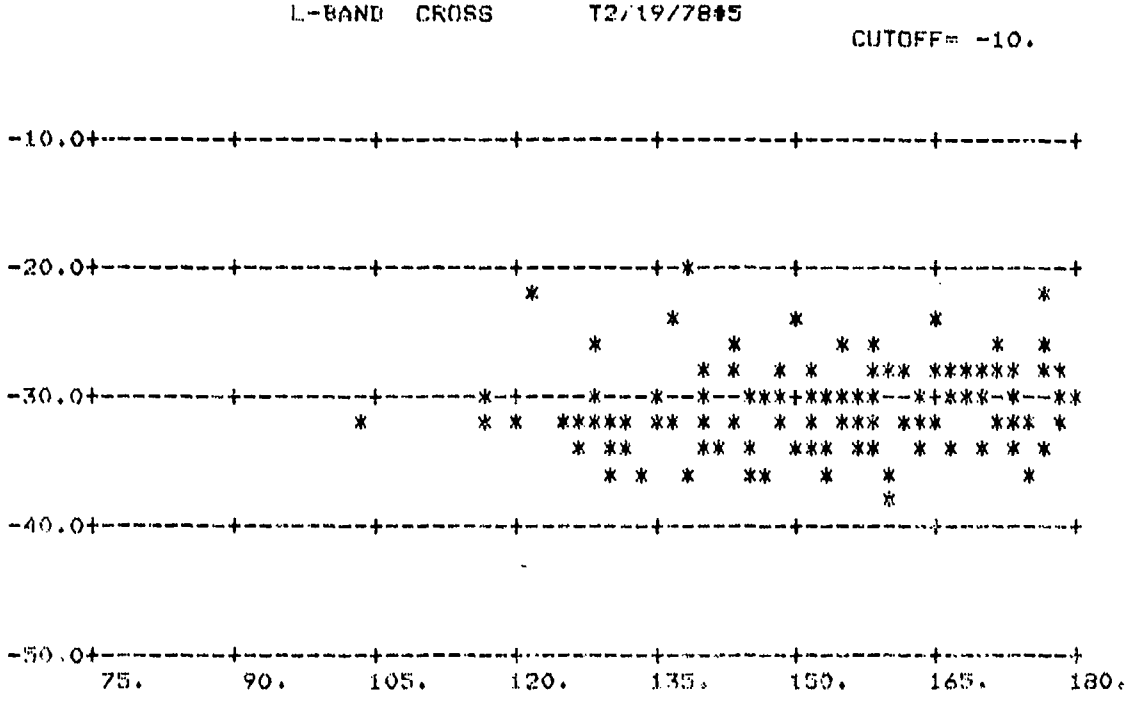

FIGURE A-105. σ_o vs ϕ_s; $\theta_s = 60°$, $\theta_i = 60°$

(Above: All Data; Below: Averages Over 5° Intervals)

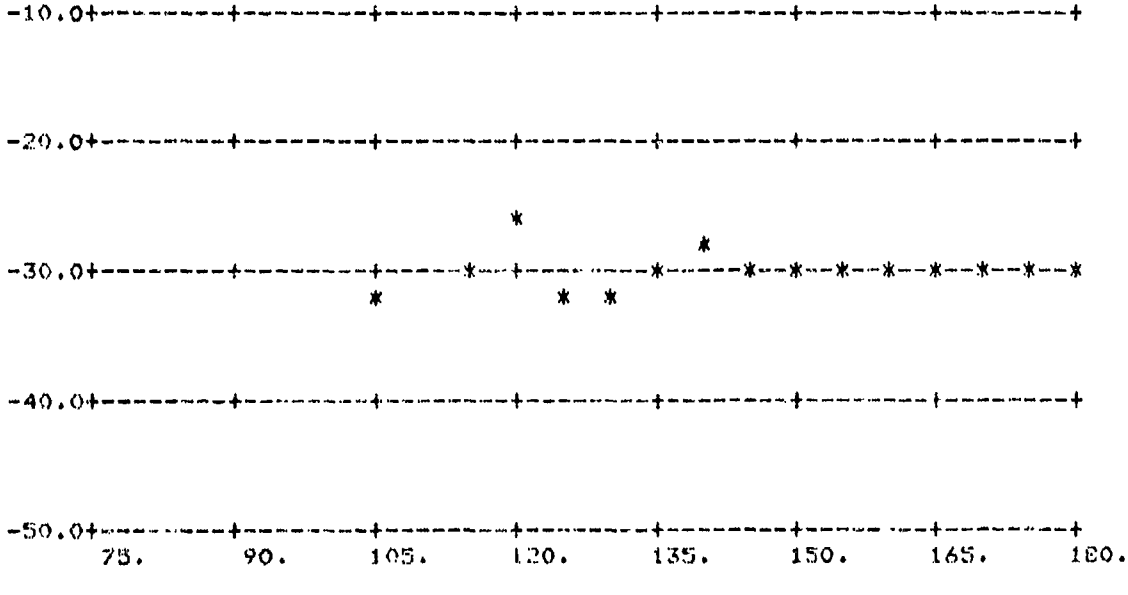

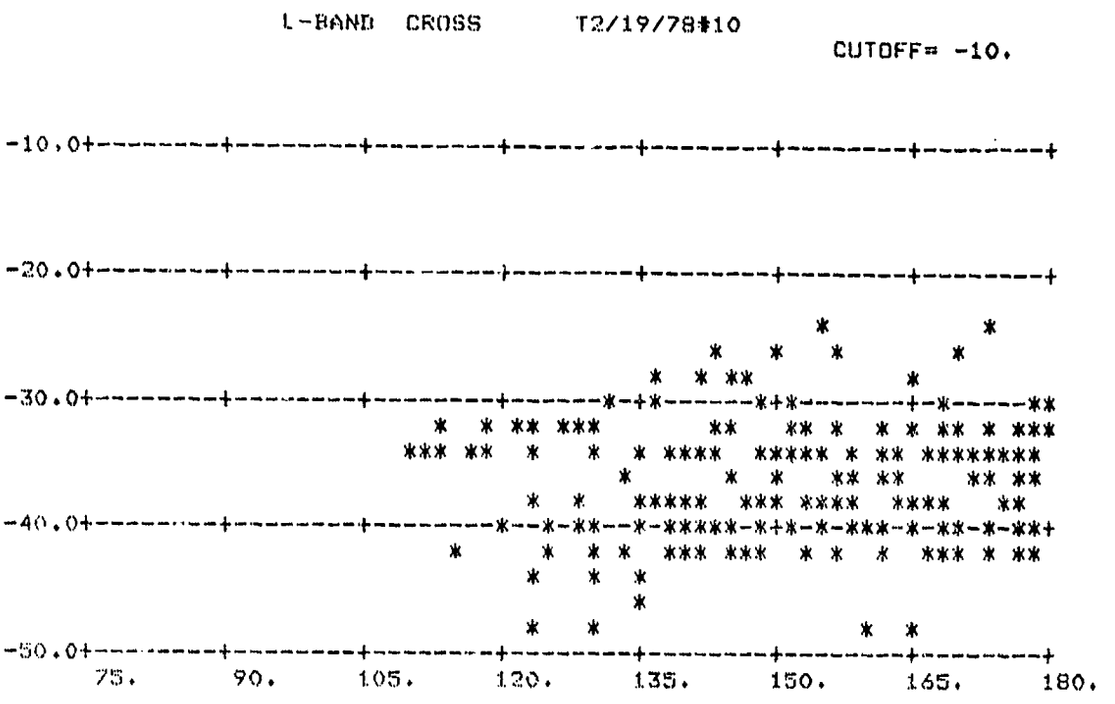

FIGURE A-106. σ_o vs ϕ_s; $\theta_s = 60°$, $\theta_i = 60°$

(Above: All Data; Below: Averages Over 5° Intervals)

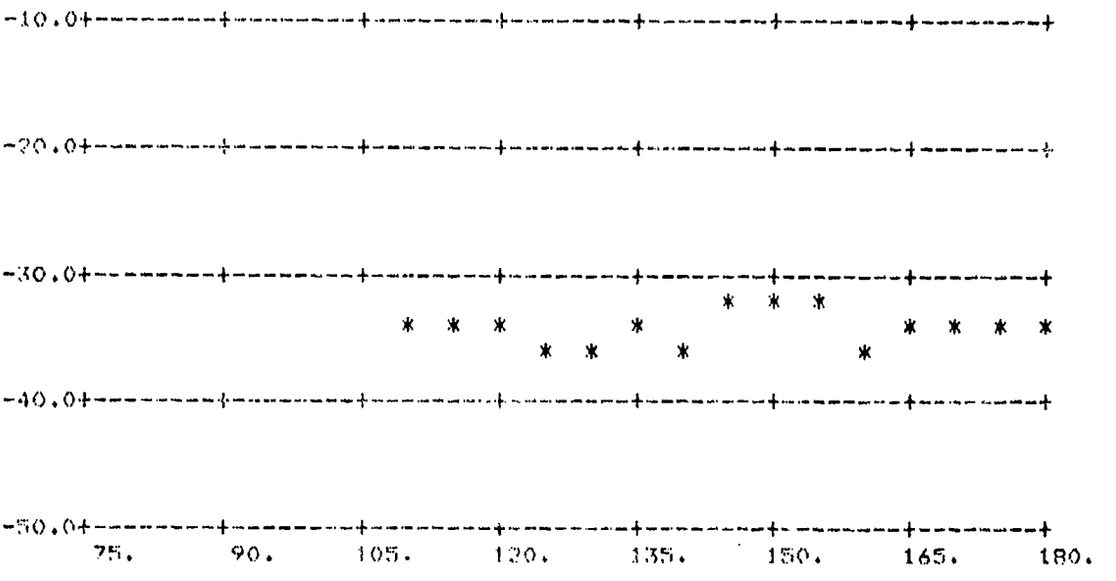

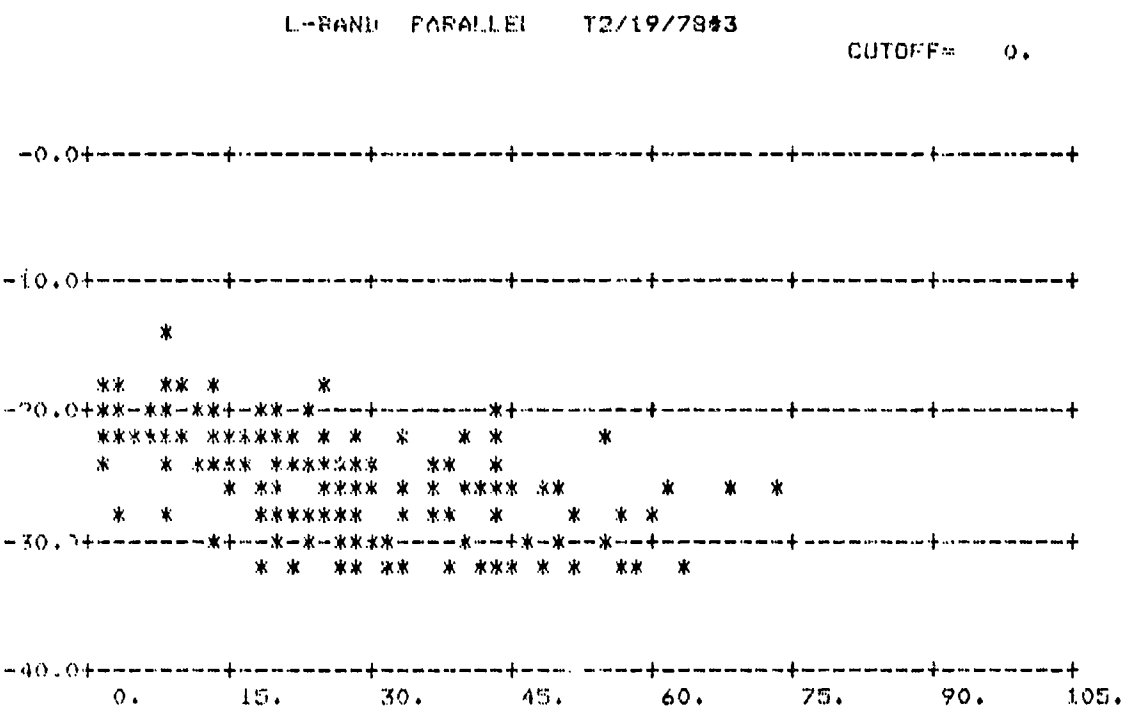

FIGURE A-107. σ_o vs ϕ_s; $\theta_s = 70°$, $\theta_i = 60°$

(Above: All Data; Below: Averages Over 5° Intervals)

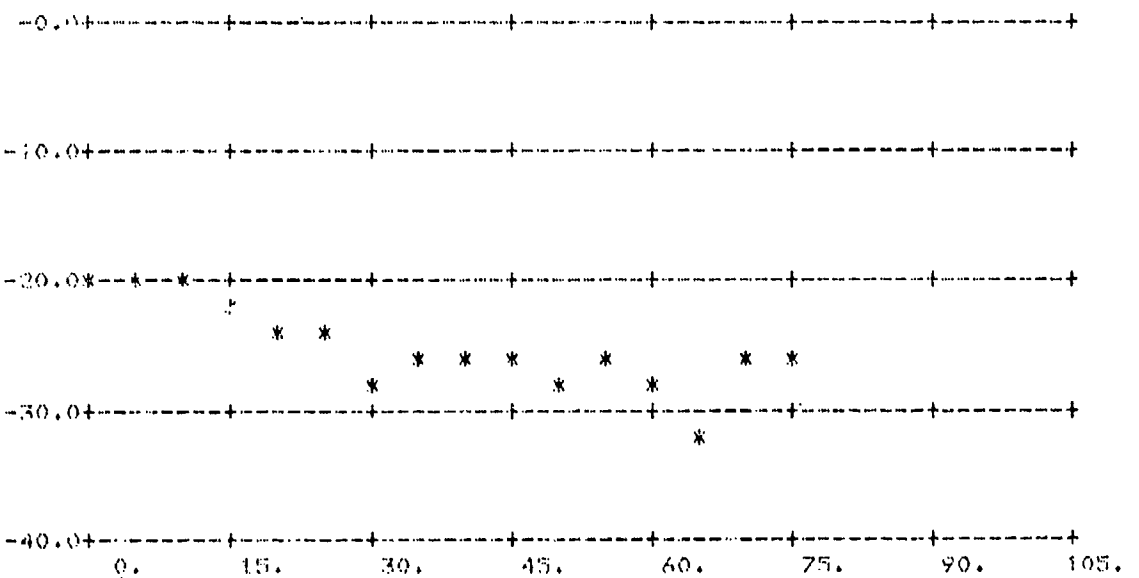

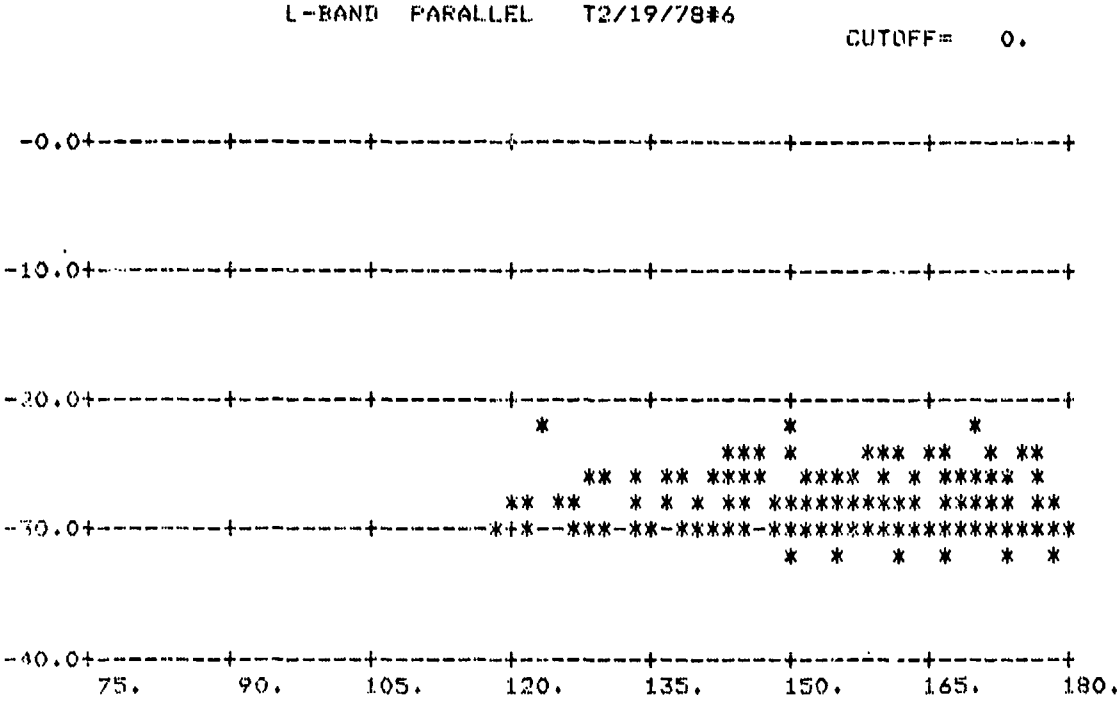

FIGURE A-108. σ_o vs ϕ_s; $\theta_s = 70°$, $\theta_i = 60°$

(Above: All Data; Below: Averages Over 5° Intervals)

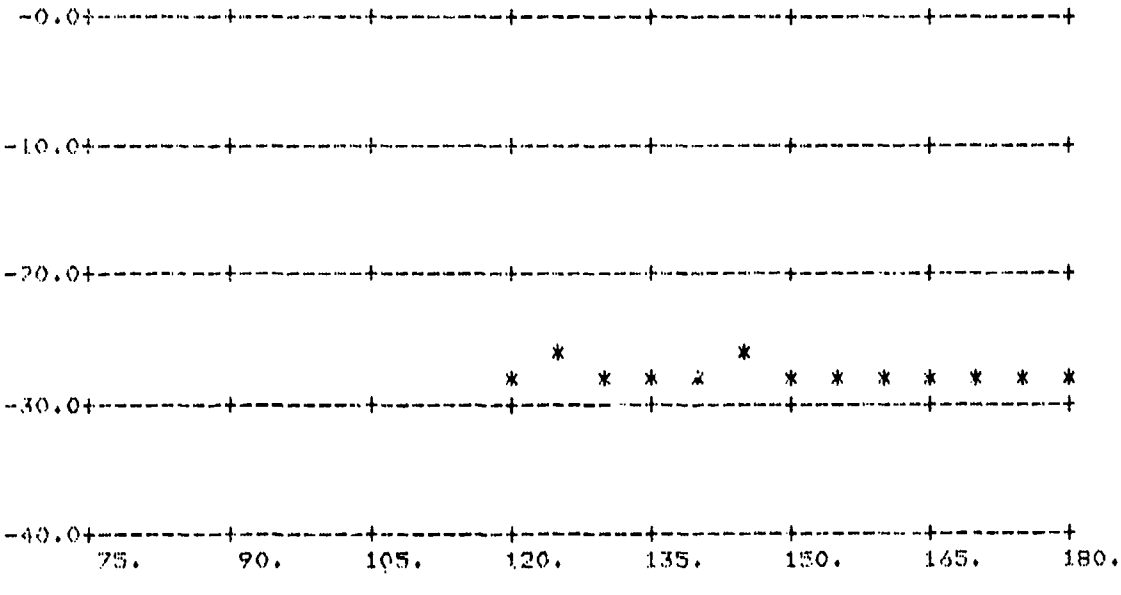

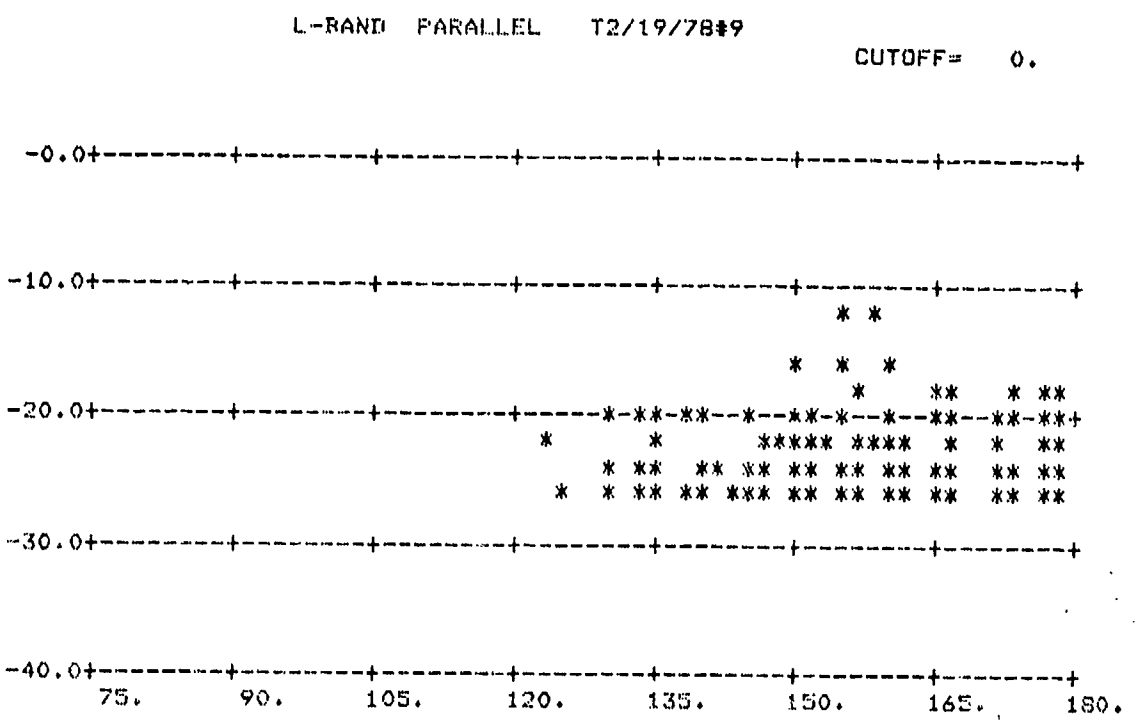

FIGURE A-109. σ_o vs ϕ_s; $\theta_s = 70°$, $\theta_i = 60°$

(Above: All Data; Below: Averages Over 5° Intervals)

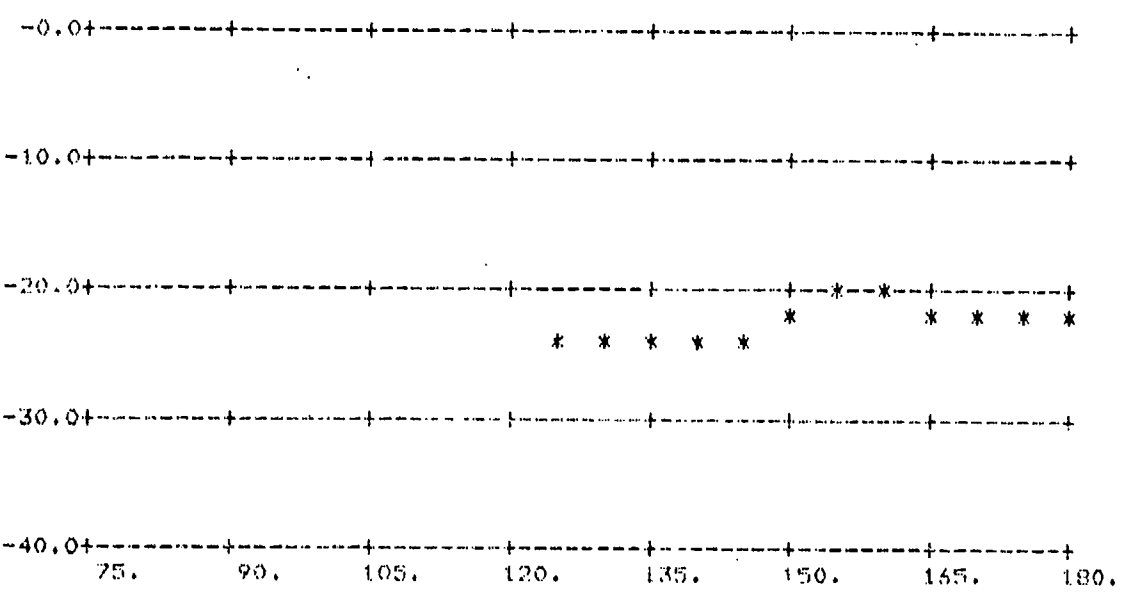

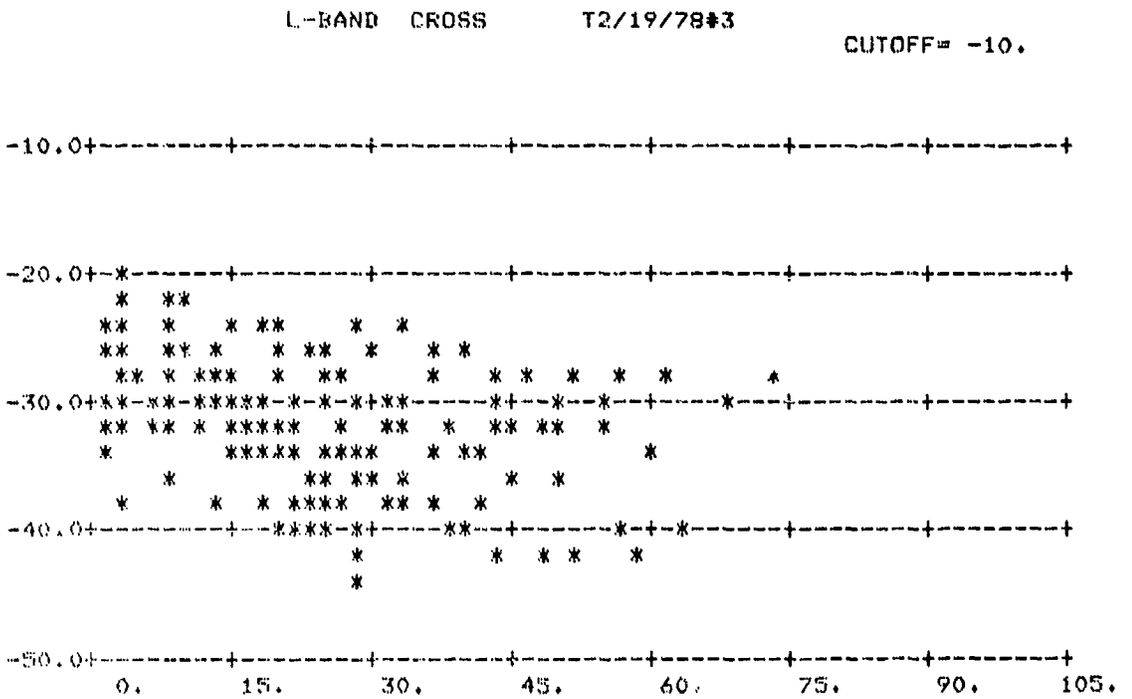

FIGURE A-110. σ_o vs ϕ_s; $\theta_s = 70°$, $\theta_i = 60°$

(Above: All Data; Below: Averages Over 5° Intervals)

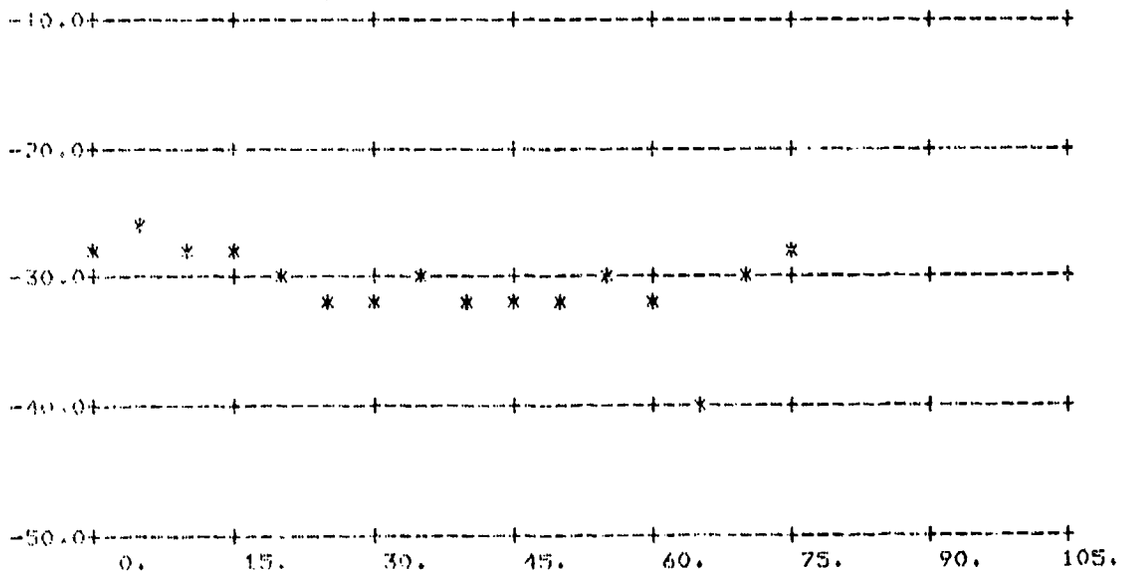

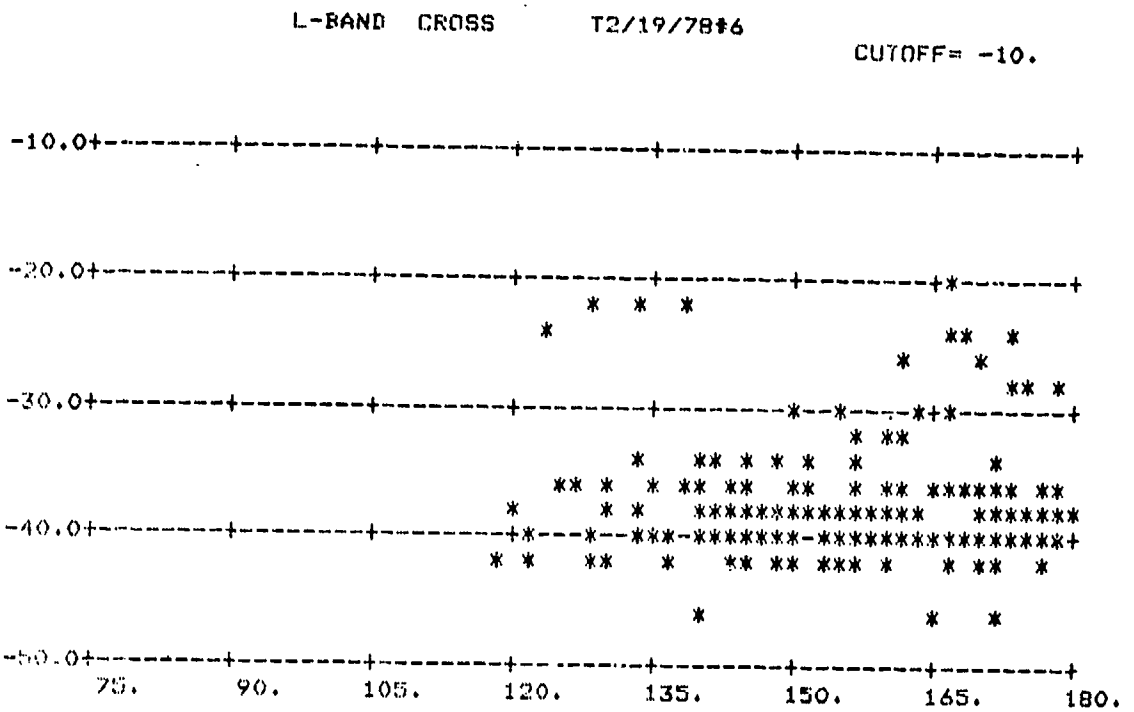

FIGURE A-111. σ_o vs ϕ_s; $\theta_s = 70°$, $\theta_i = 60°$

(Above: All Data; Below: Averages Over 5° Intervals)

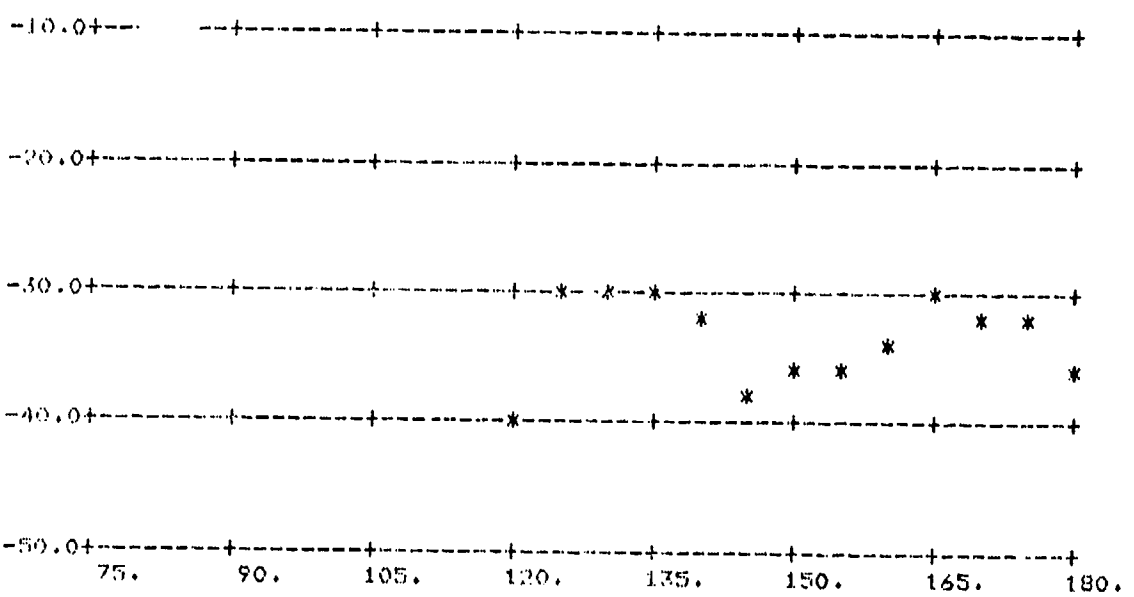

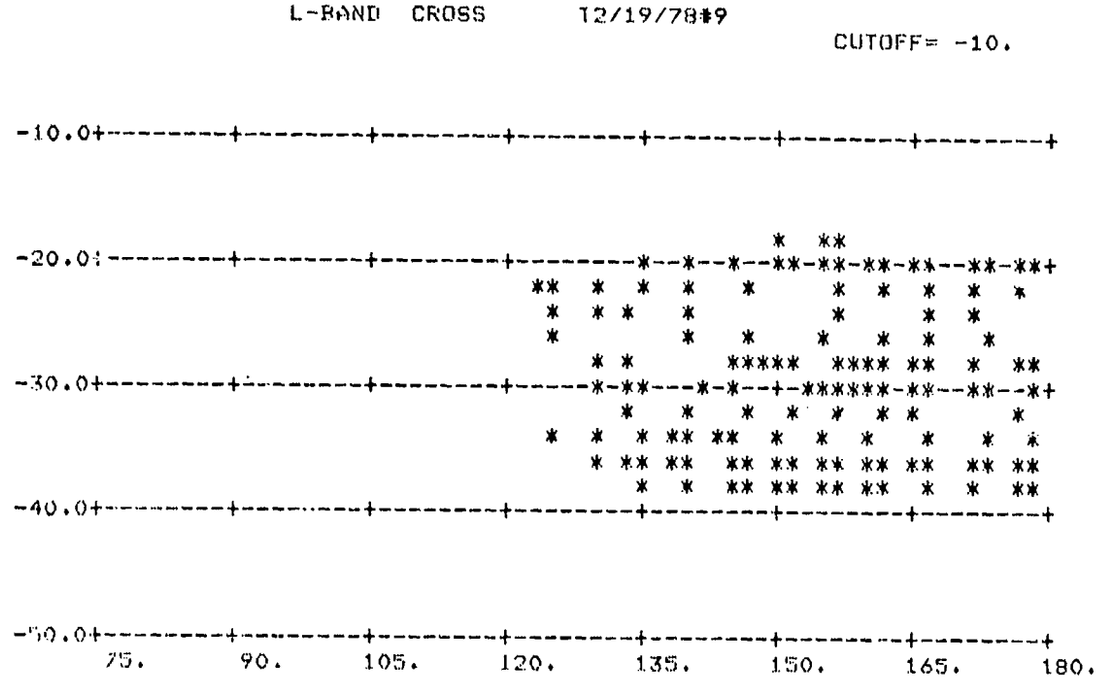

FIGURE A-112. σ_o vs ϕ_s; $\theta_s = 70°$, $\theta_i = 60°$

(Above: All Data; Below: Averages Over 5° Intervals)

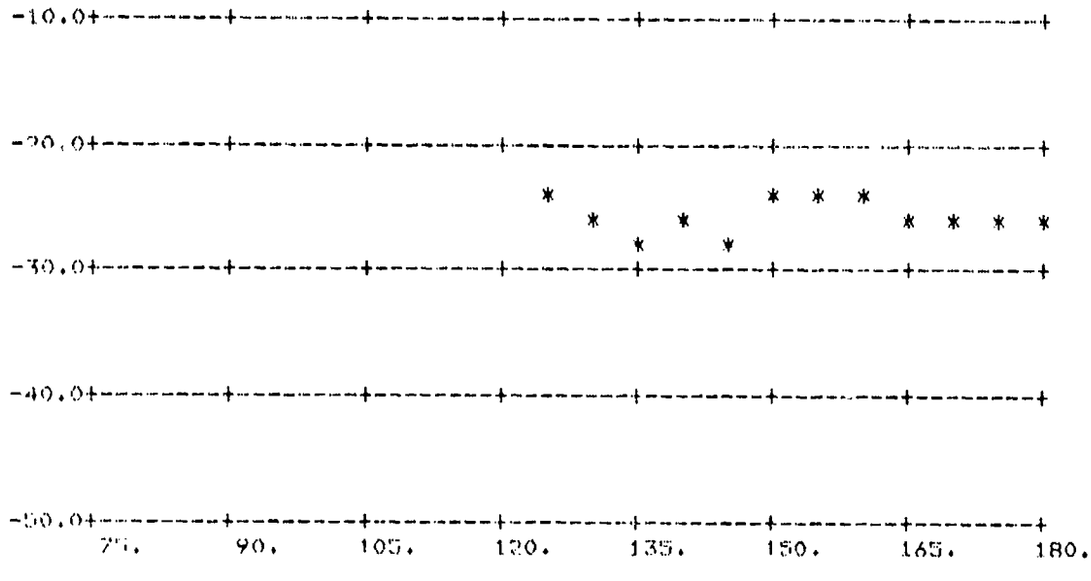

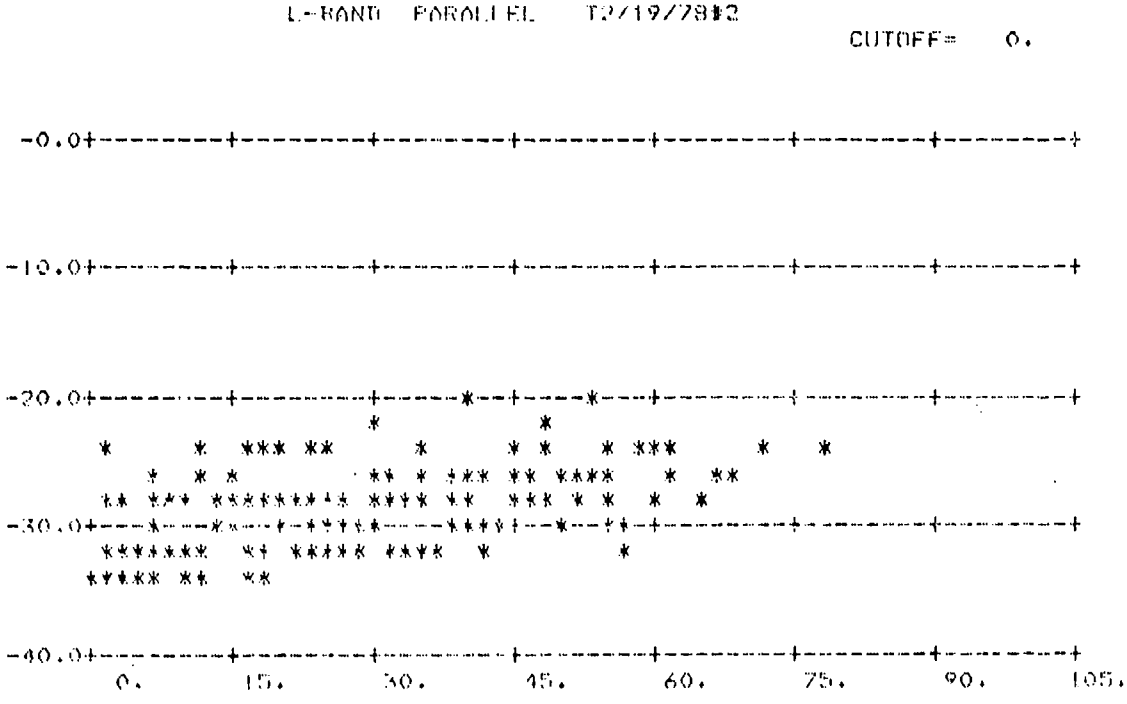

FIGURE A-113. σ_o vs ϕ_s; $\theta_s = 80°$, $\theta_i = 60°$

(Above: All Data; Below: Averages Over 5° Intervals)

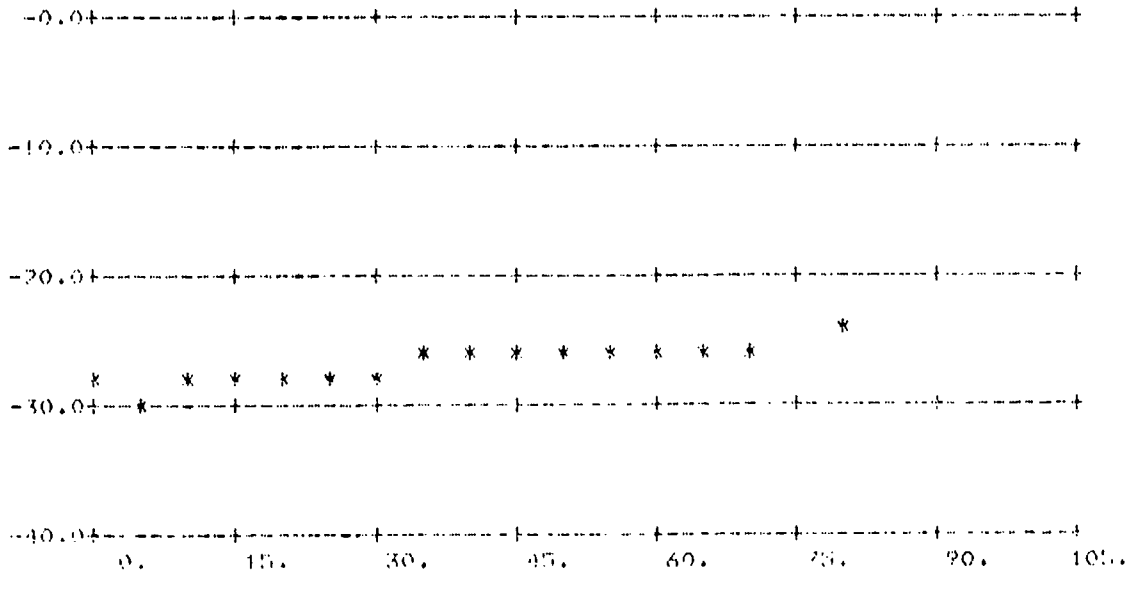

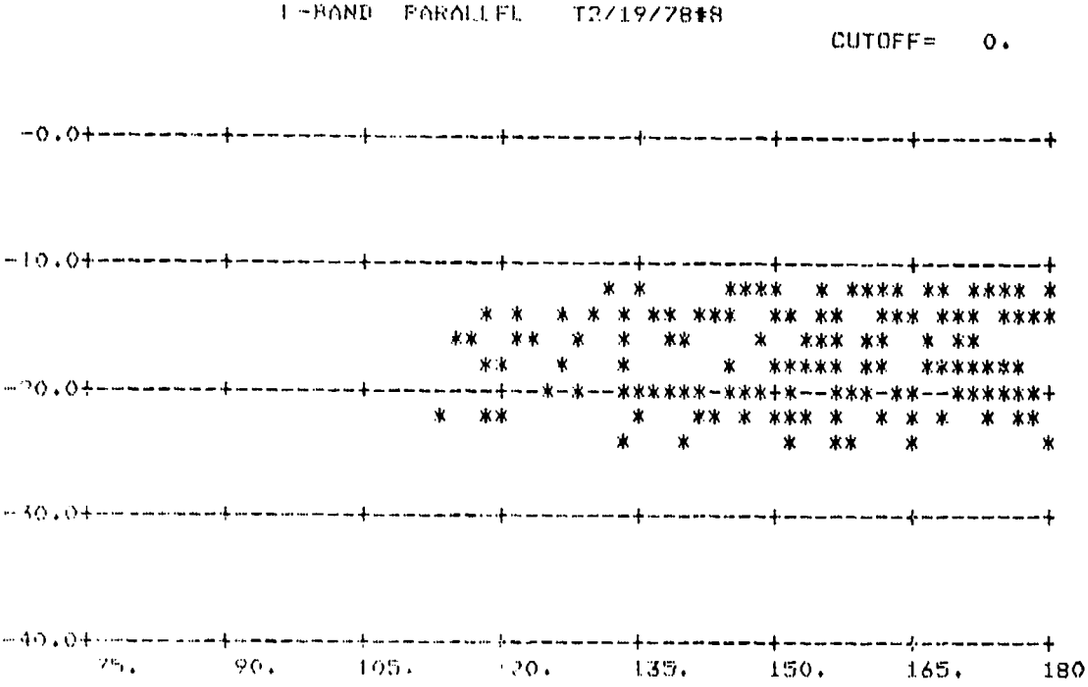

FIGURE A-114. σ_o vs ϕ_s: $\theta_s = 80°$, $\theta_i = 60°$

(Above: All Data; Below: Averages Over 5° Intervals)

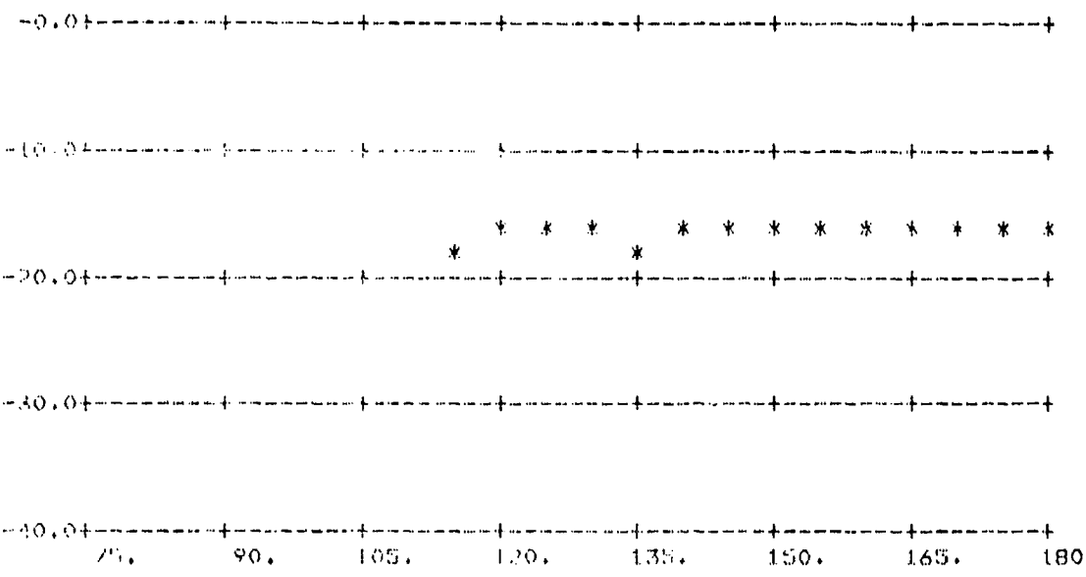

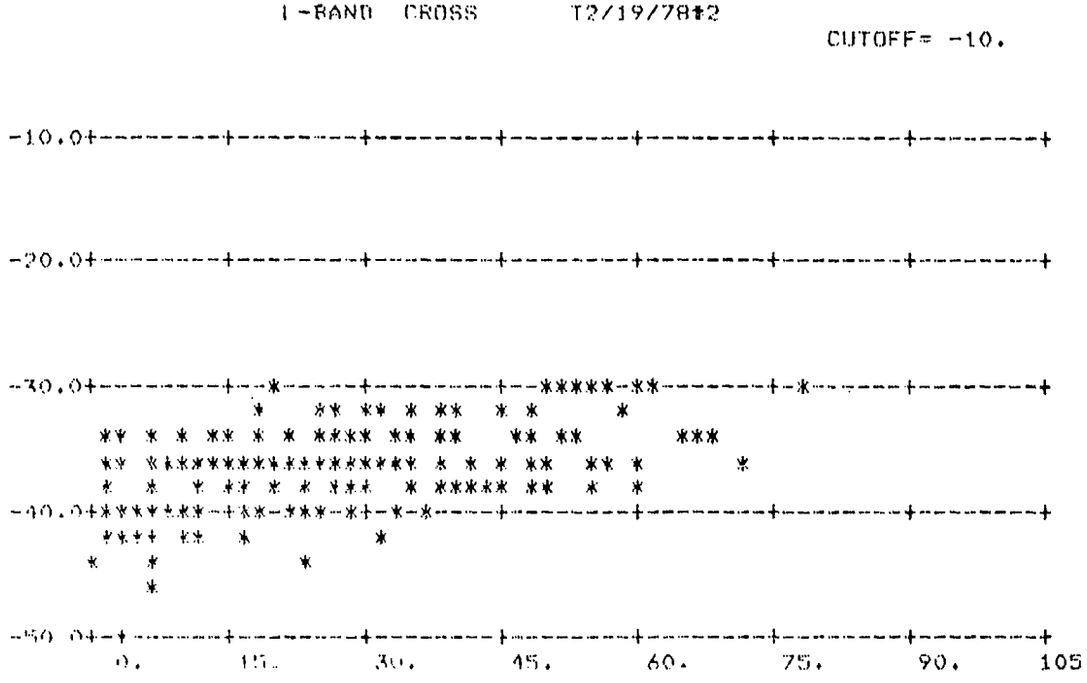

FIGURE A-115. σ_o vs ϕ_s; $\theta_s = 80°$, $\theta_i = 60°$

(Above: All Data; Below: Averages Over 5° Intervals)

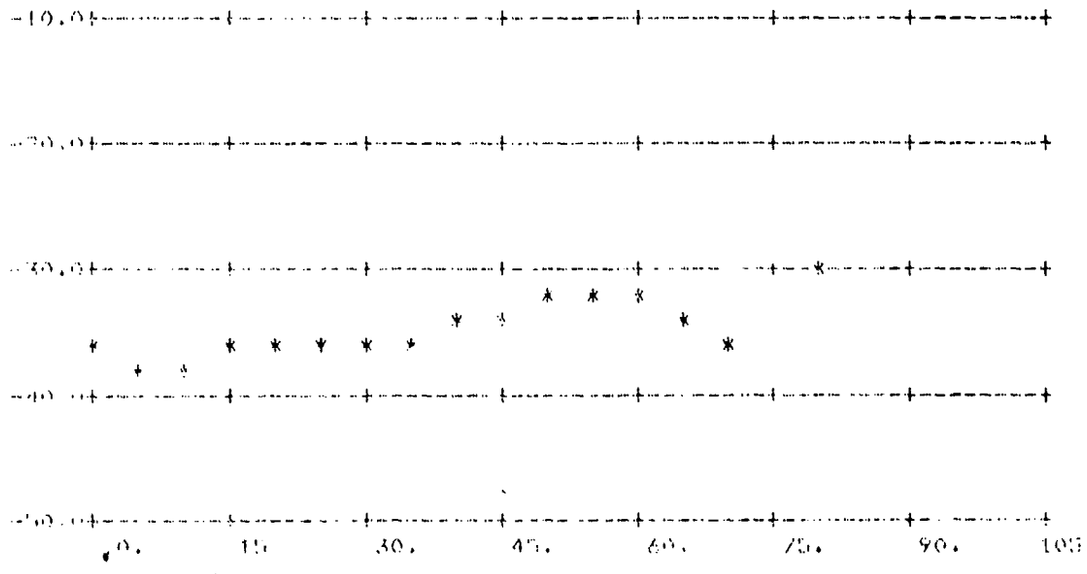

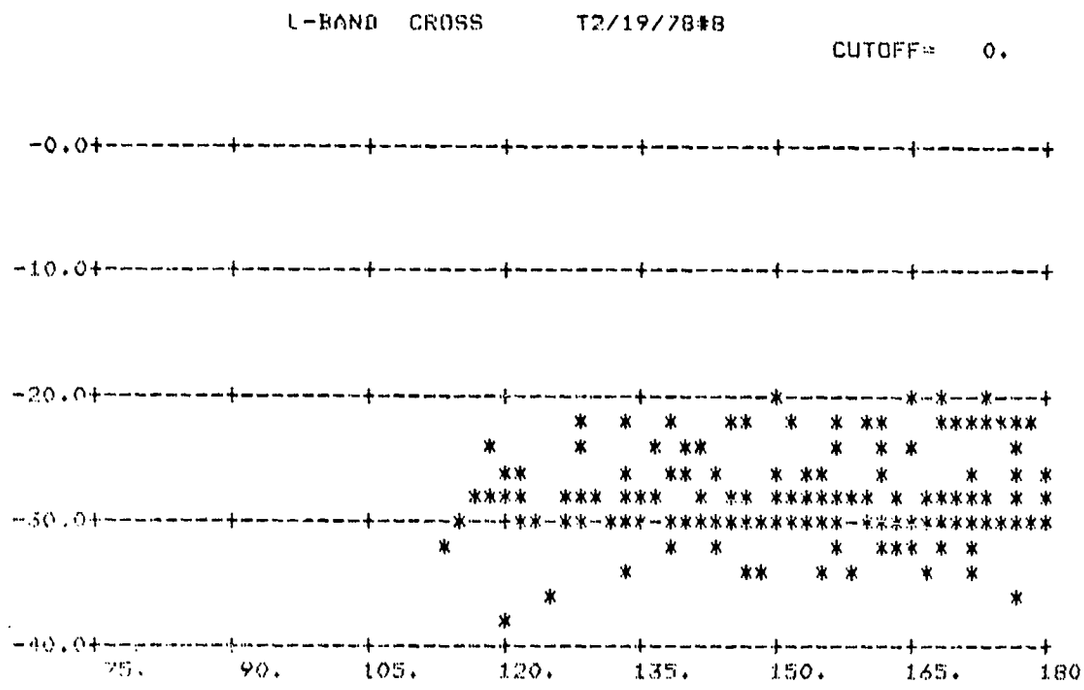

FIGURE A-116. σ_o vs ϕ_s; $\theta_s = 80°$, $\theta_i = 60°$

(Above: All Data; Below: Averages Over 5° Intervals)

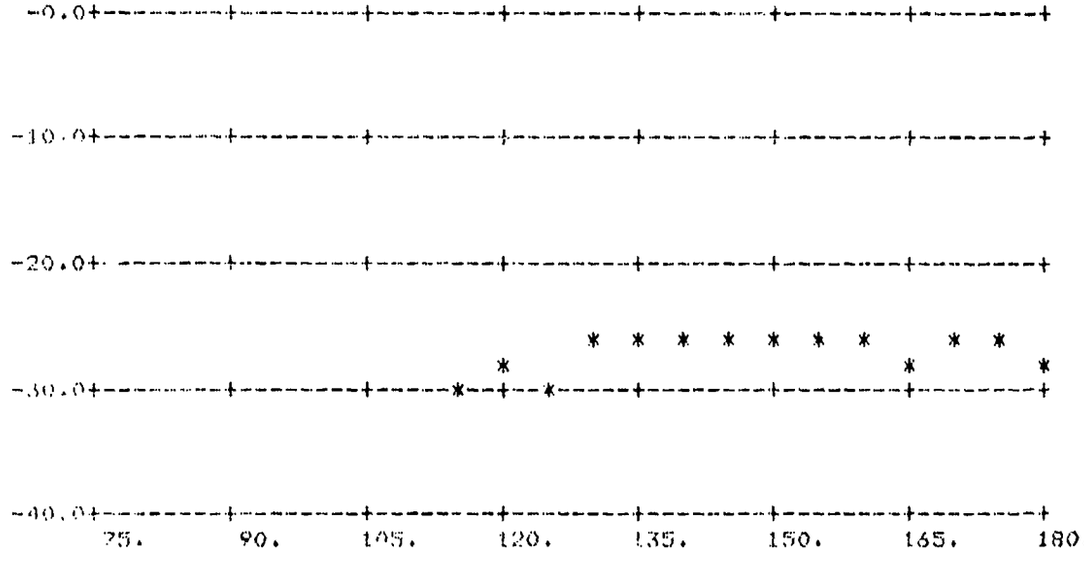

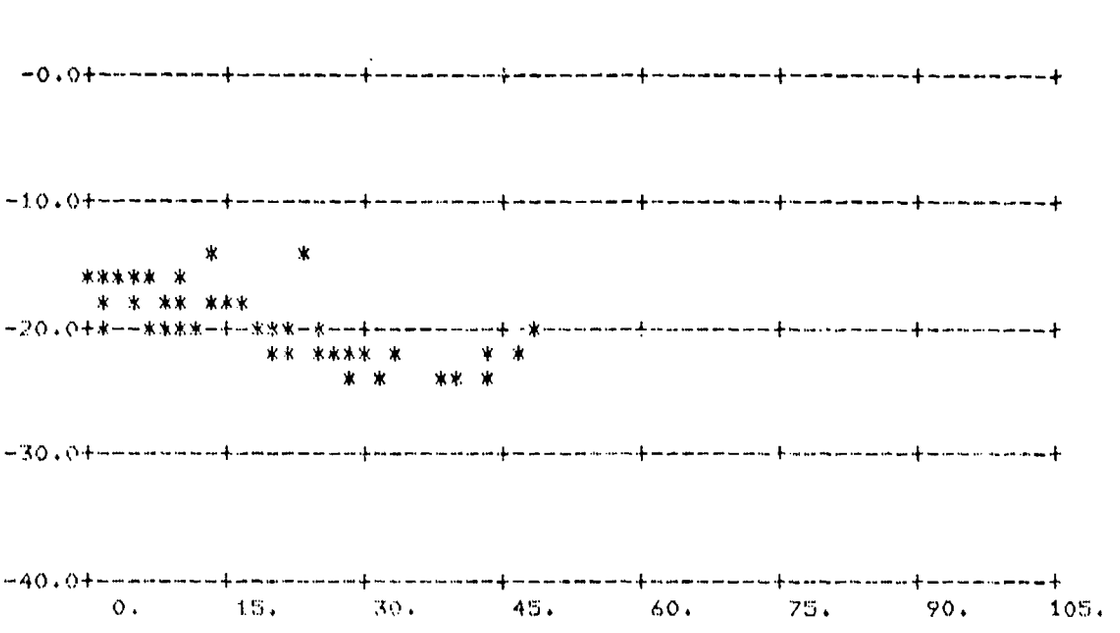

FIGURE A-117. σ_o vs ϕ_s; $\theta_s = 60°$, $\theta_i = 70°$

(Above: All Data; Below: Averages Over 5° Intervals)

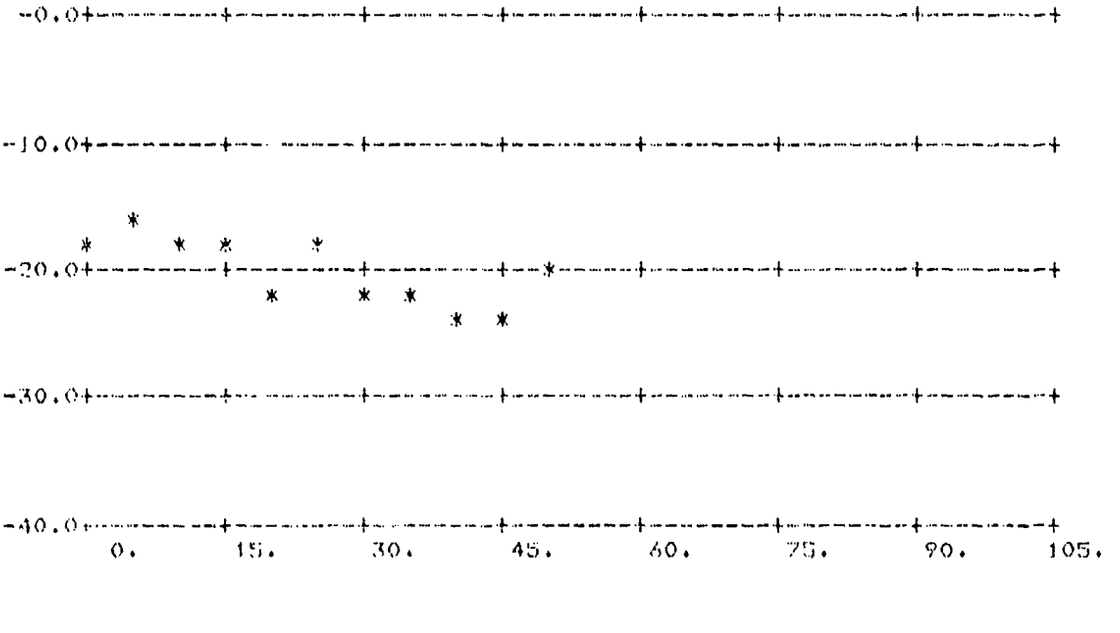

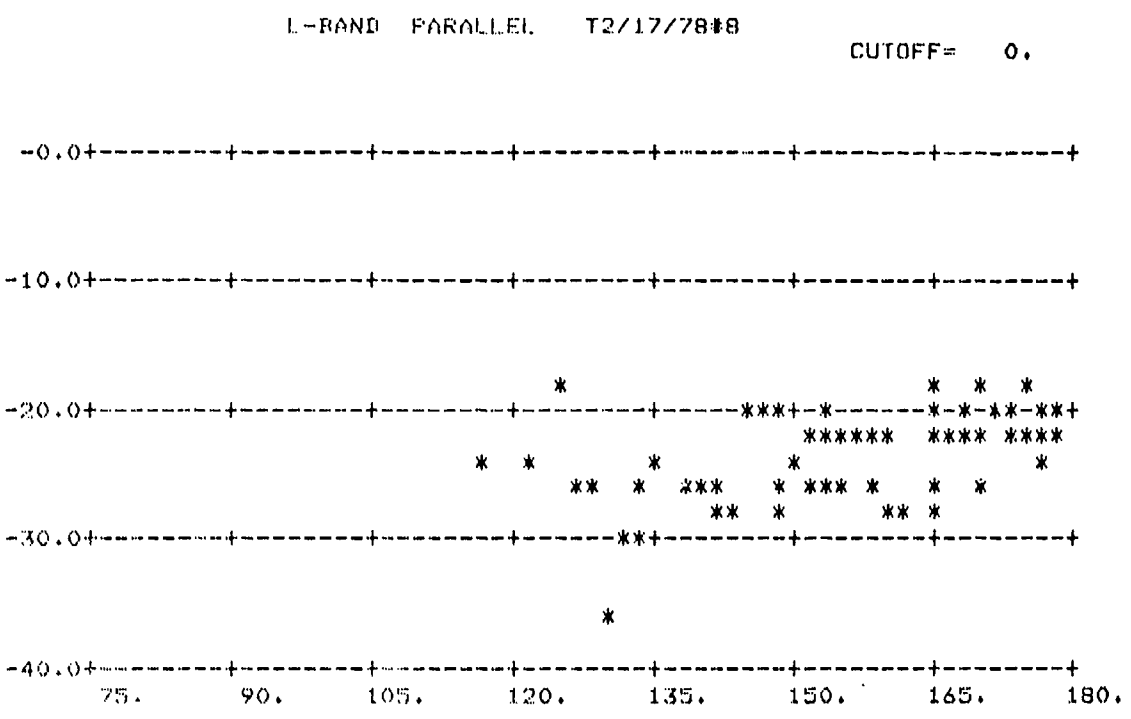

FIGURE A-118. σ_o vs ϕ_s; $\theta_s = 60°$, $\theta_i = 70°$

(Above: All Data; Below: Averages Over 5° Intervals)

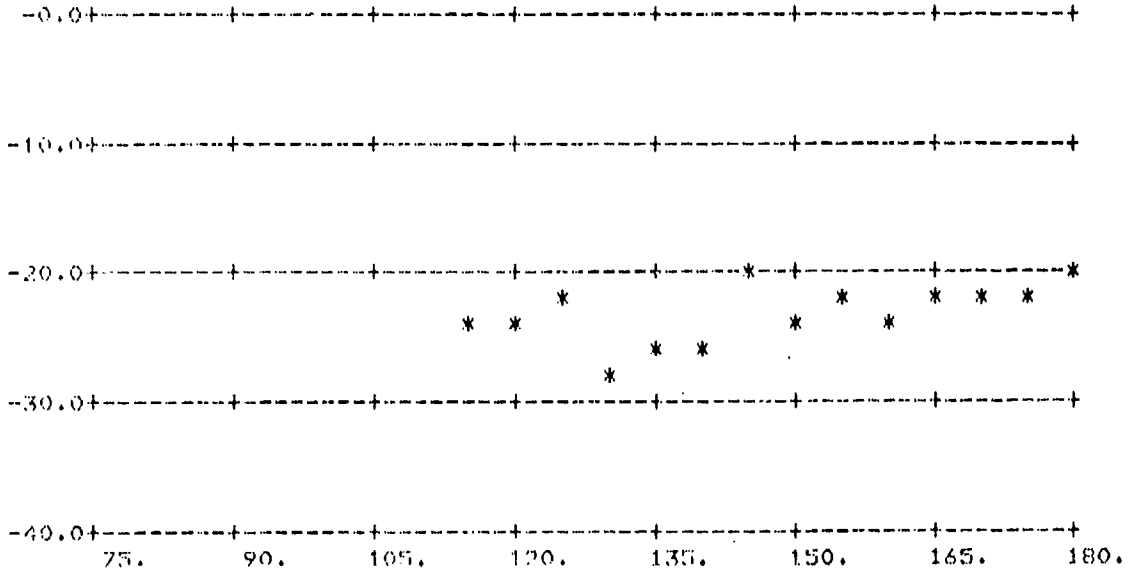

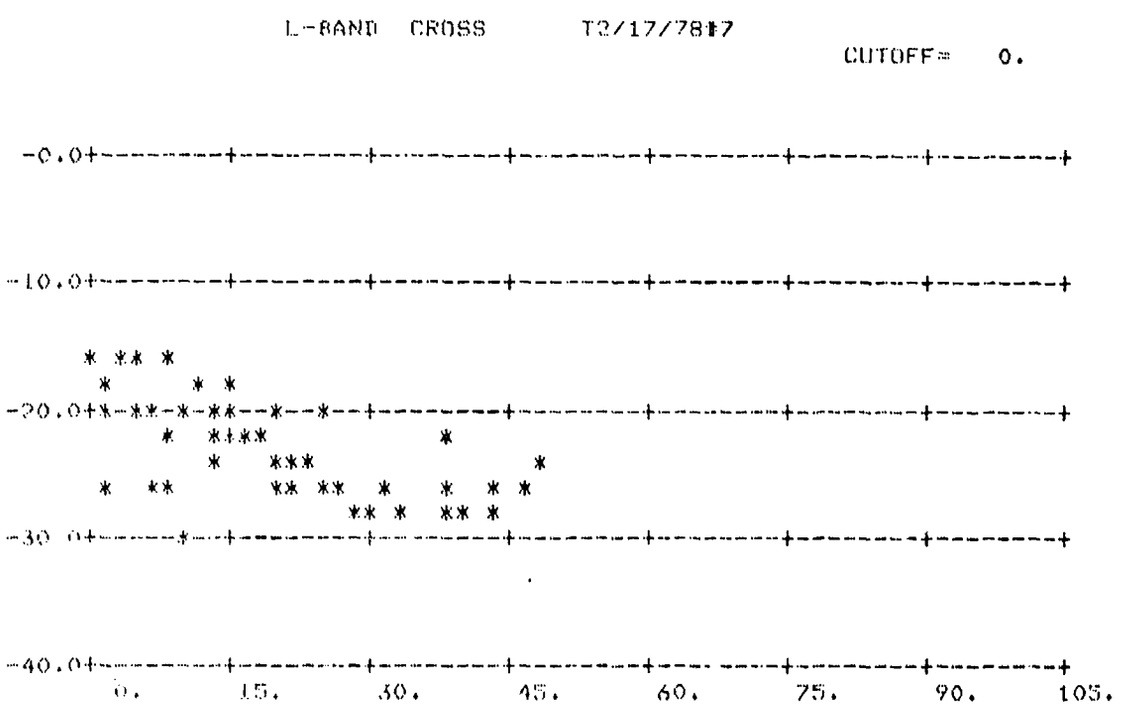

FIGURE A-119: σ_o vs σ_s; $\sigma_s = 60°$, $\sigma_i = 70°$

(Above: All Data; Below: Averages Over 5° Intervals)

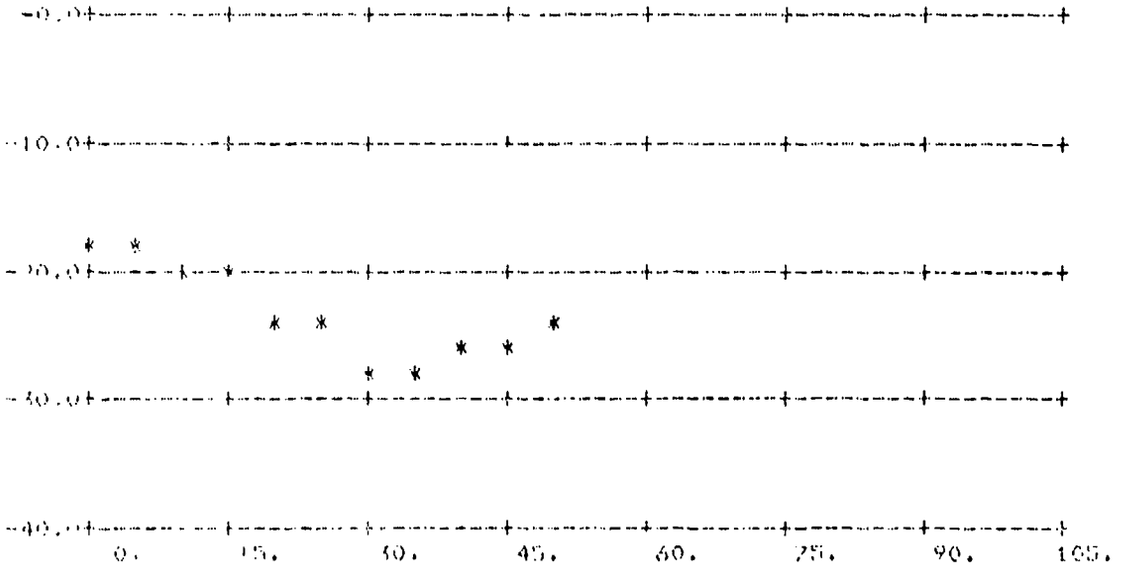

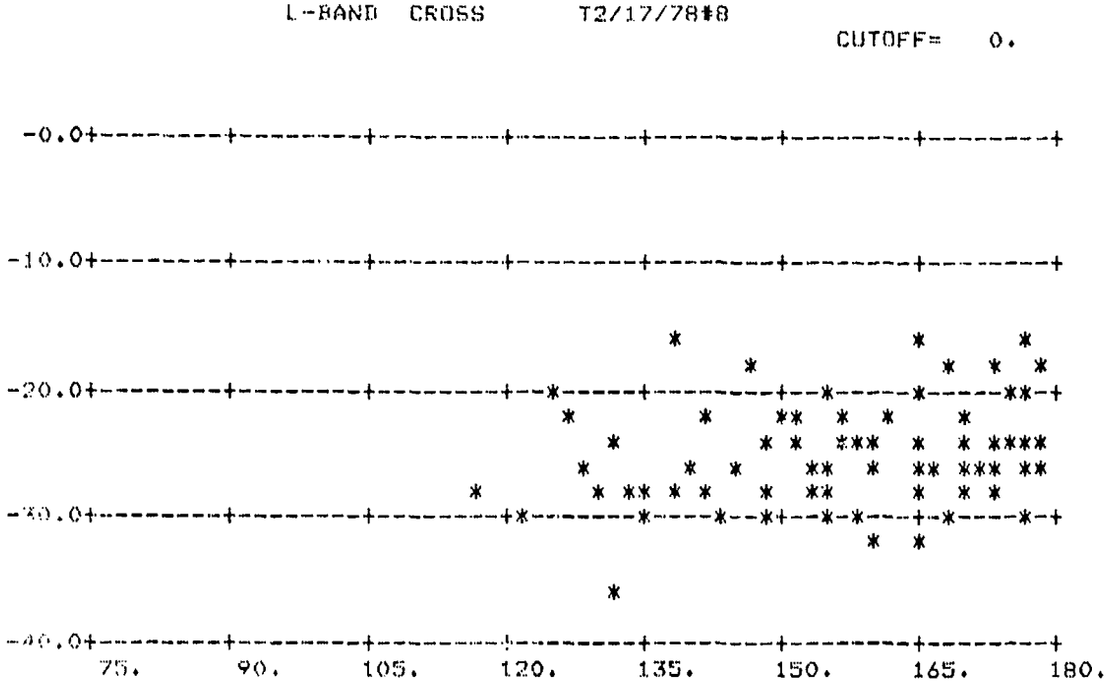

FIGURE A-120. σ_o vs ϕ_s; $\theta_s = 60°$, $\theta_i = 70°$

(Above: All Data; Below: Averages Over 5° Intervals)

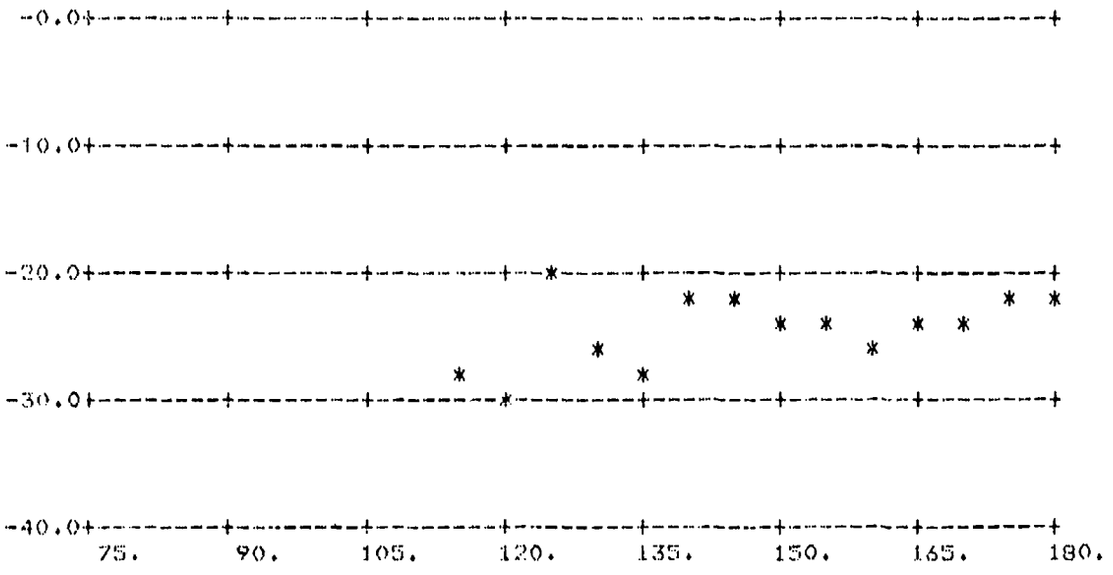

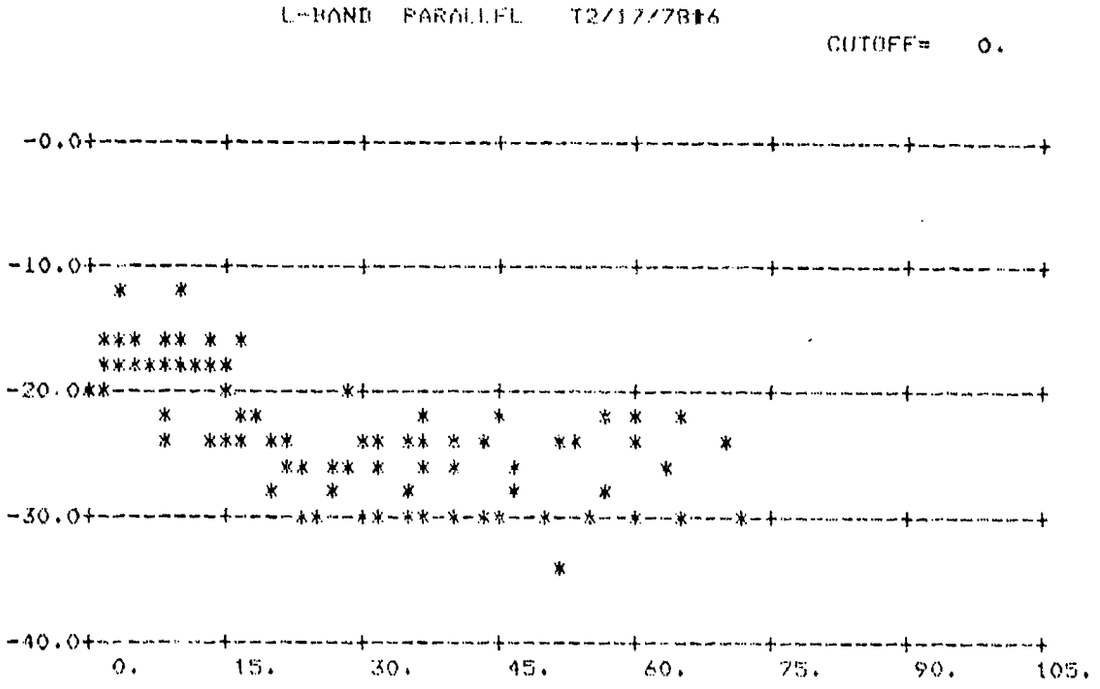

FIGURE A-121. σ_o vs ϕ_s; $\theta_s = 70°$, $\theta_i = 70°$

(Above: All Data; Below: Averages Over 5° Intervals)

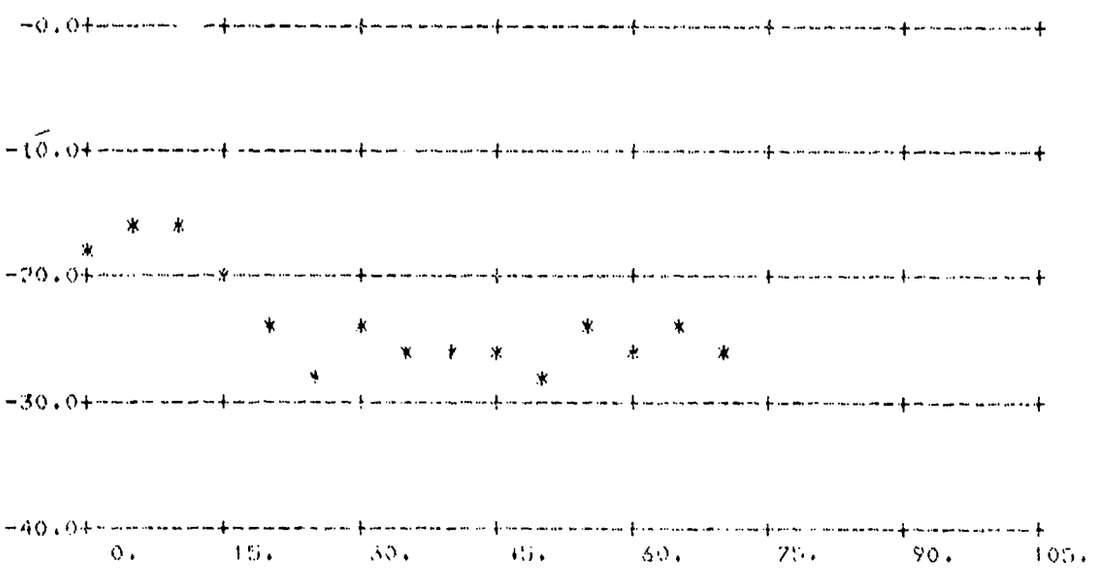

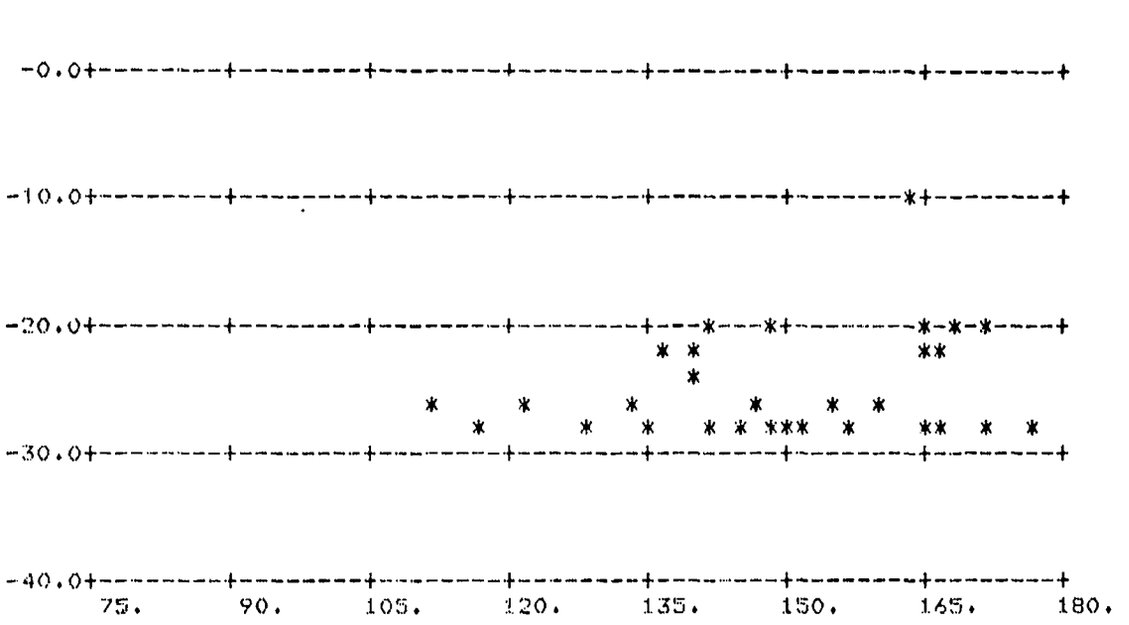

FIGURE A-122. σ_o vs ϕ_s; $\theta_s = 70°$, $\theta_i = 70°$

(Above: All Data; Below: Averages Over 5° Intervals)

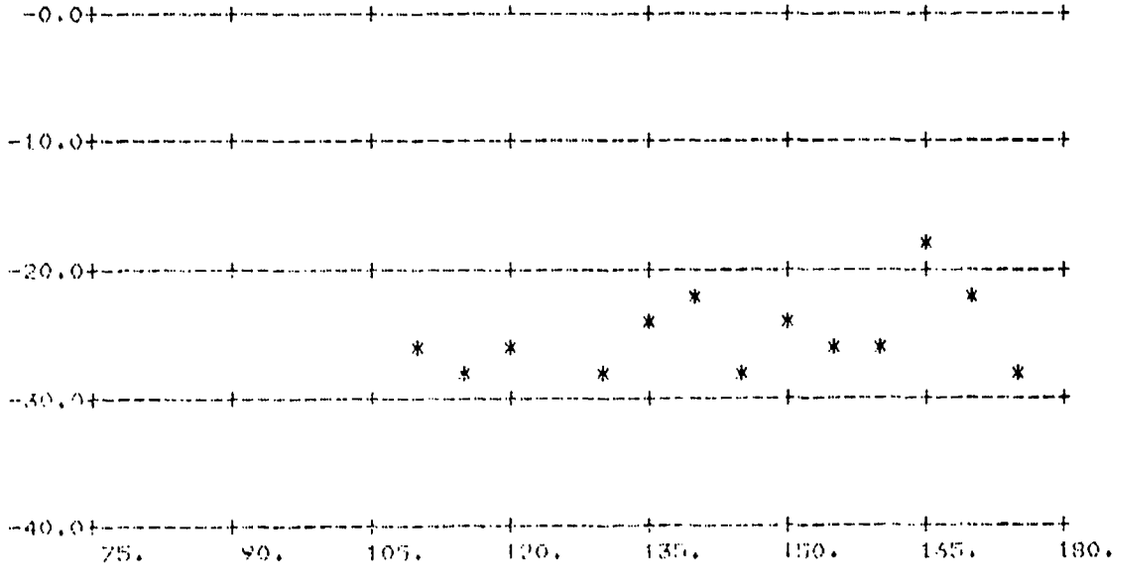

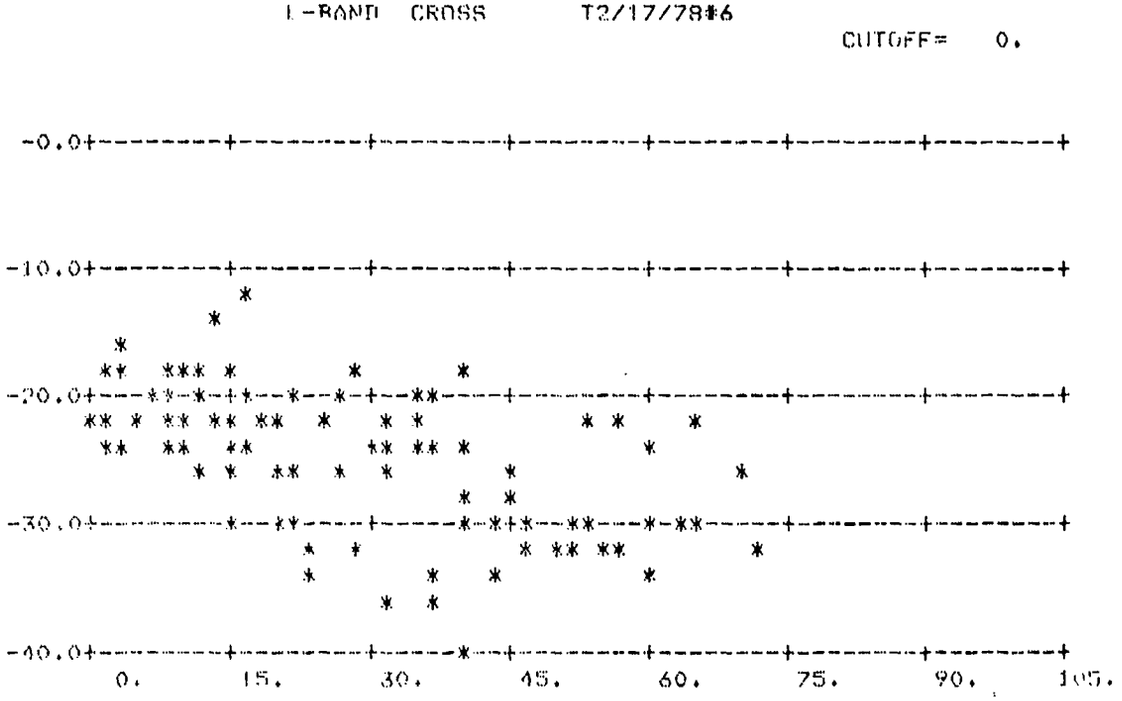

FIGURE A-123. σ_o vs ϕ_s; $\theta_s = 70°$, $\theta_i = 70°$

(Above: All Data; Below: Averages Over 5° Intervals)

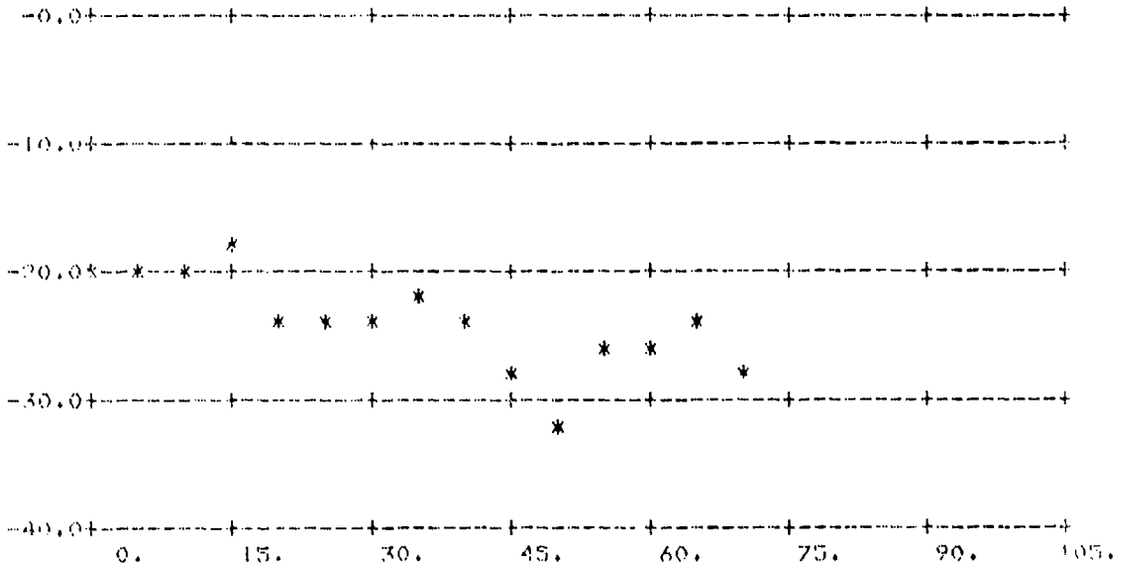

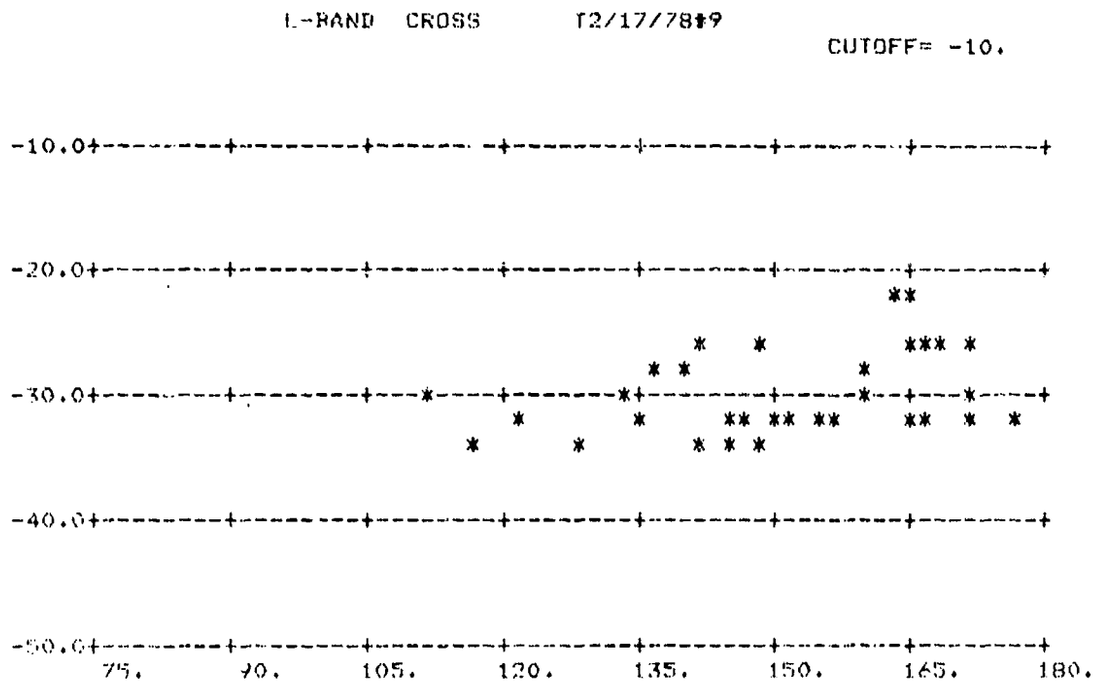

FIGURE A-124. σ_o vs ϕ_s; $\theta_s = 70°$, $\theta_i = 70°$

(Above: All Data; Below: Averages Over 5° Intervals)

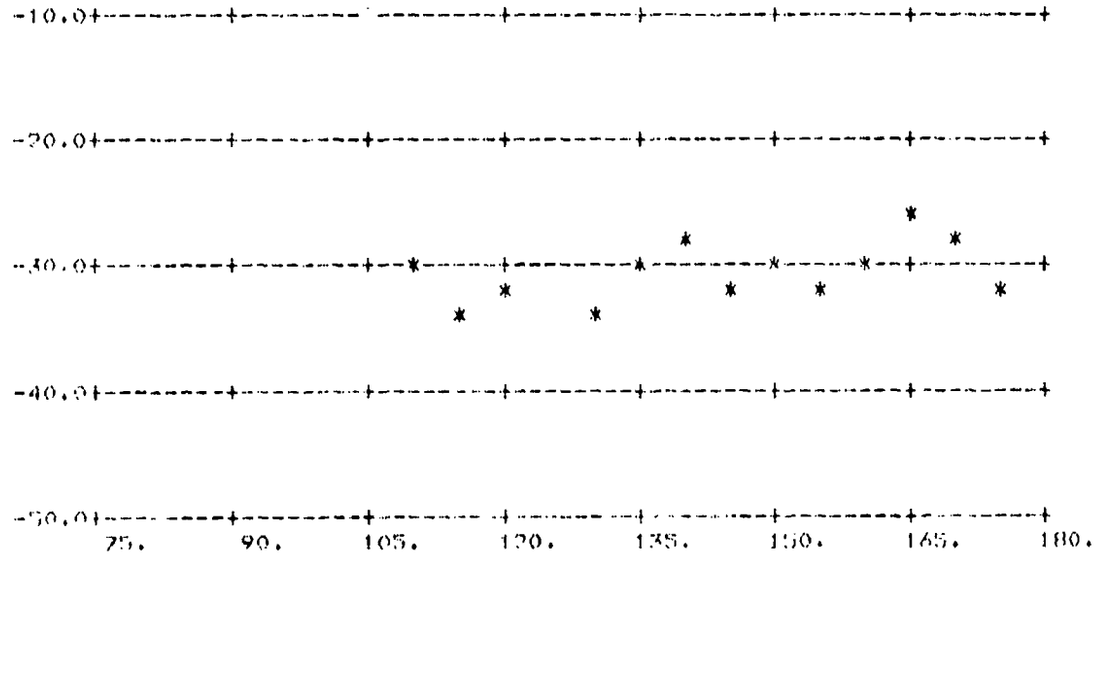

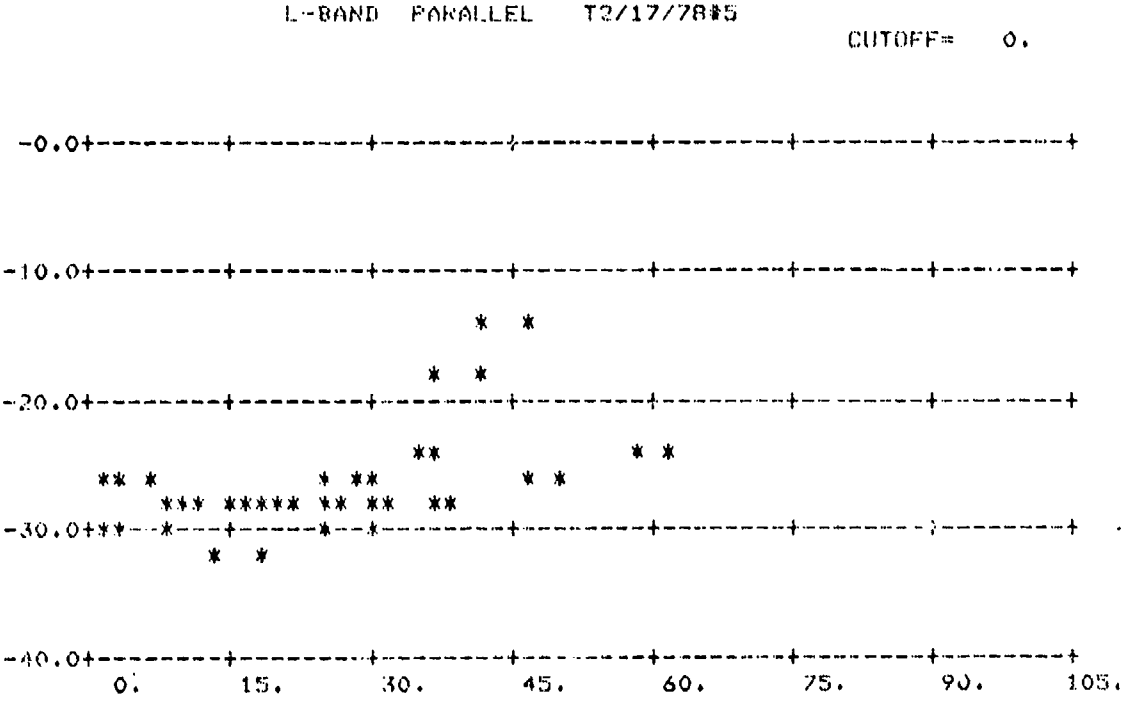

FIGURE A-125. σ_o vs ϕ_s; $\theta_s = 80°$, $\theta_i = 70°$

(Above: All Data; Below: Averages Over 5° Intervals)

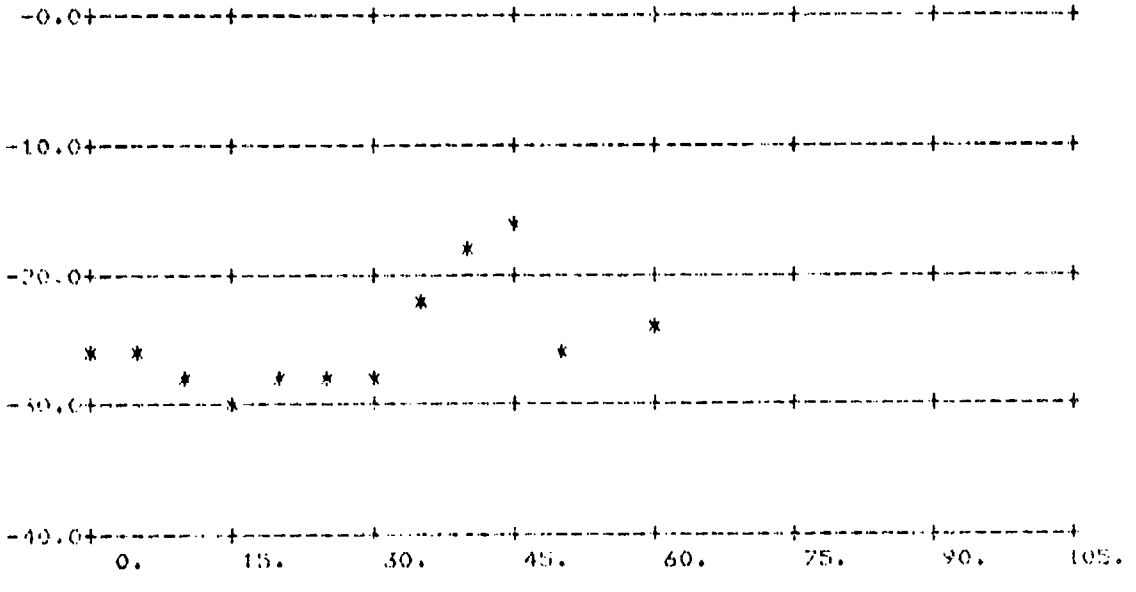

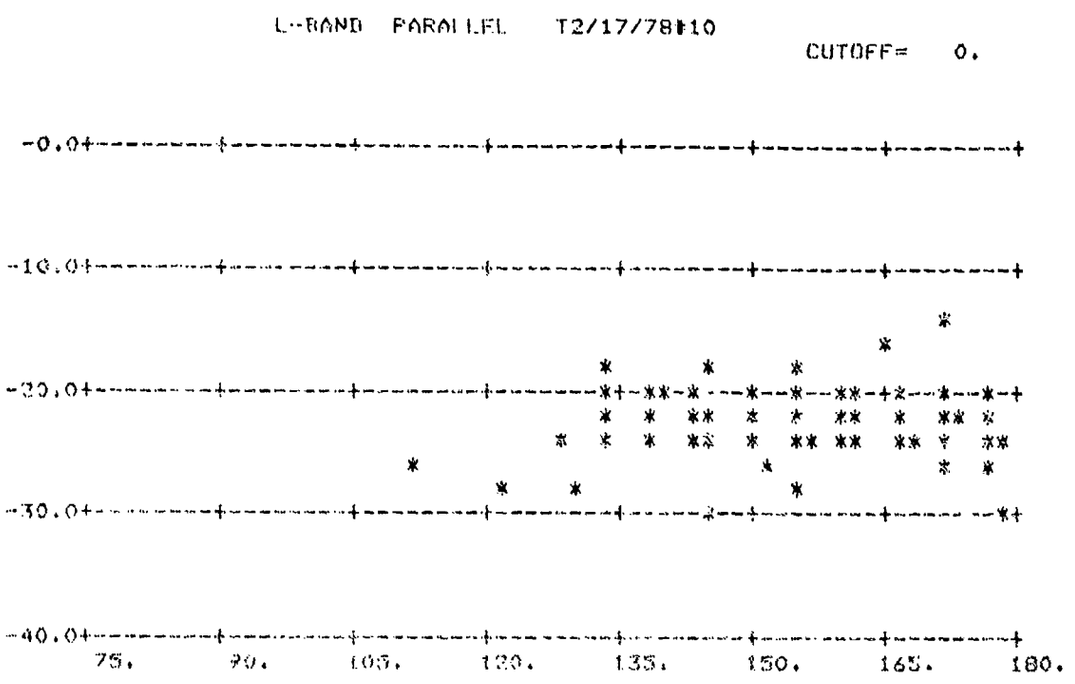

FIGURE A-126. σ_o vs ϕ_s; $\theta_s = 80°$, $\theta_i = 70°$

(Above: All Data; Below: Averages Over 5° Intervals)

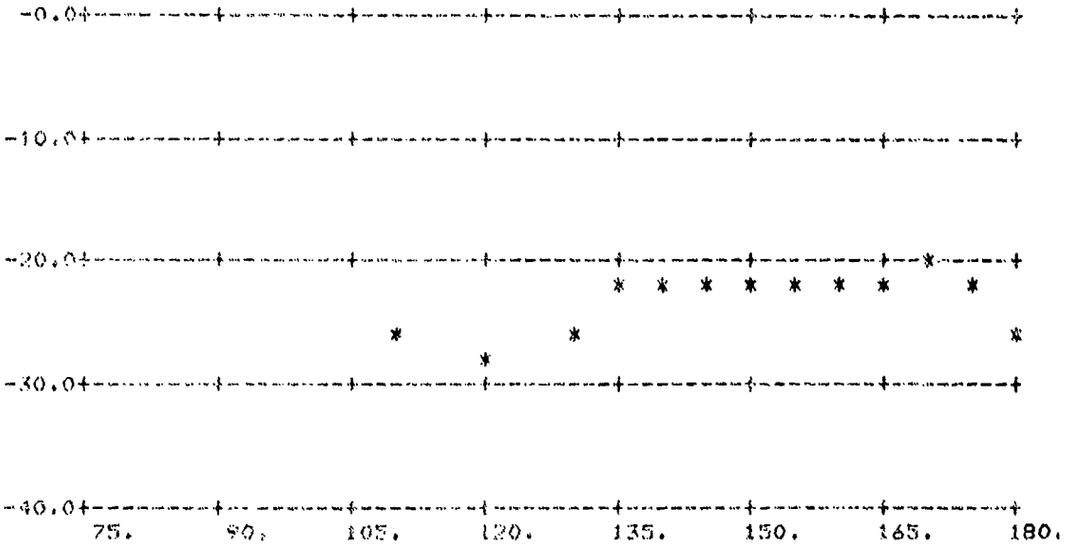

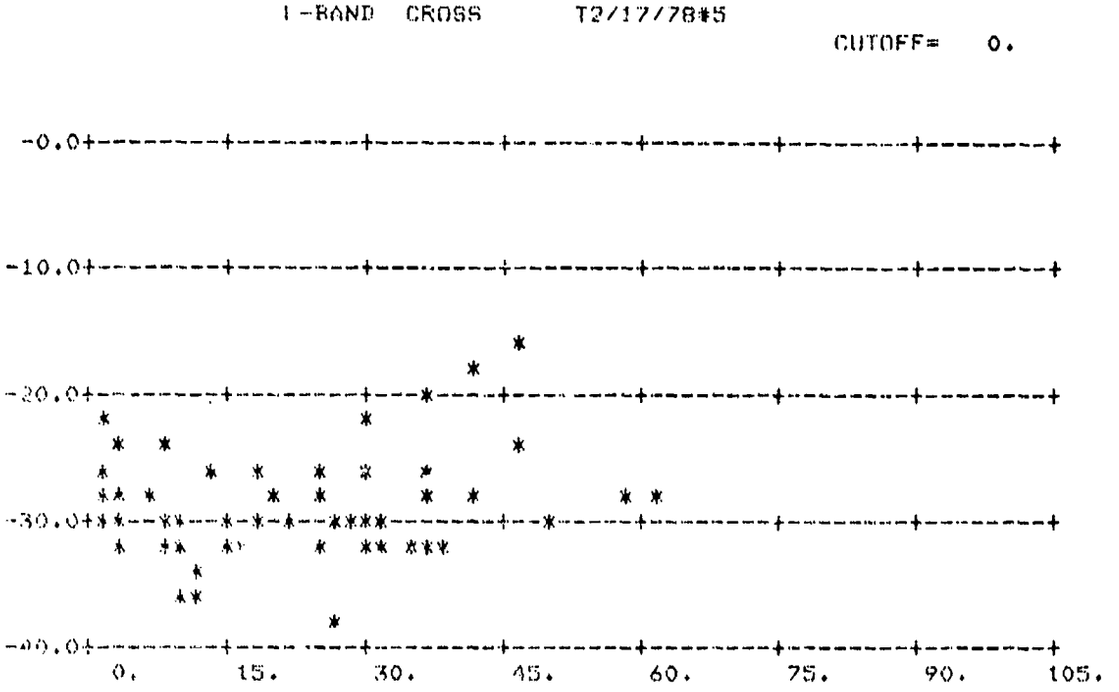

FIGURE A-127. σ_o vs ϕ_s; $\theta_s = 80°$, $\theta_i = 70°$

(Above: All Data; Below: Averages Over 5° Intervals)

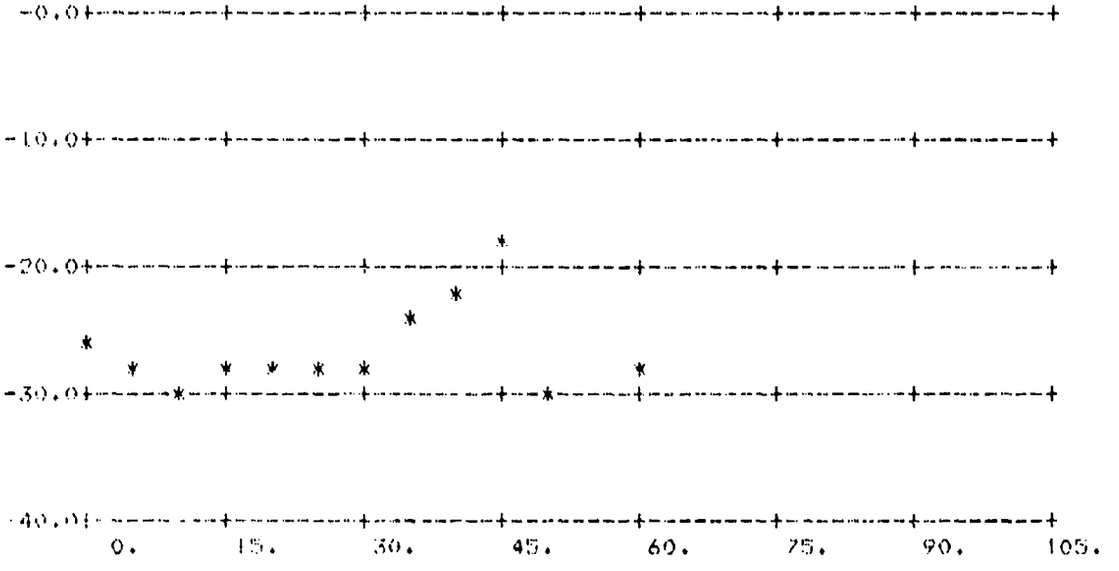

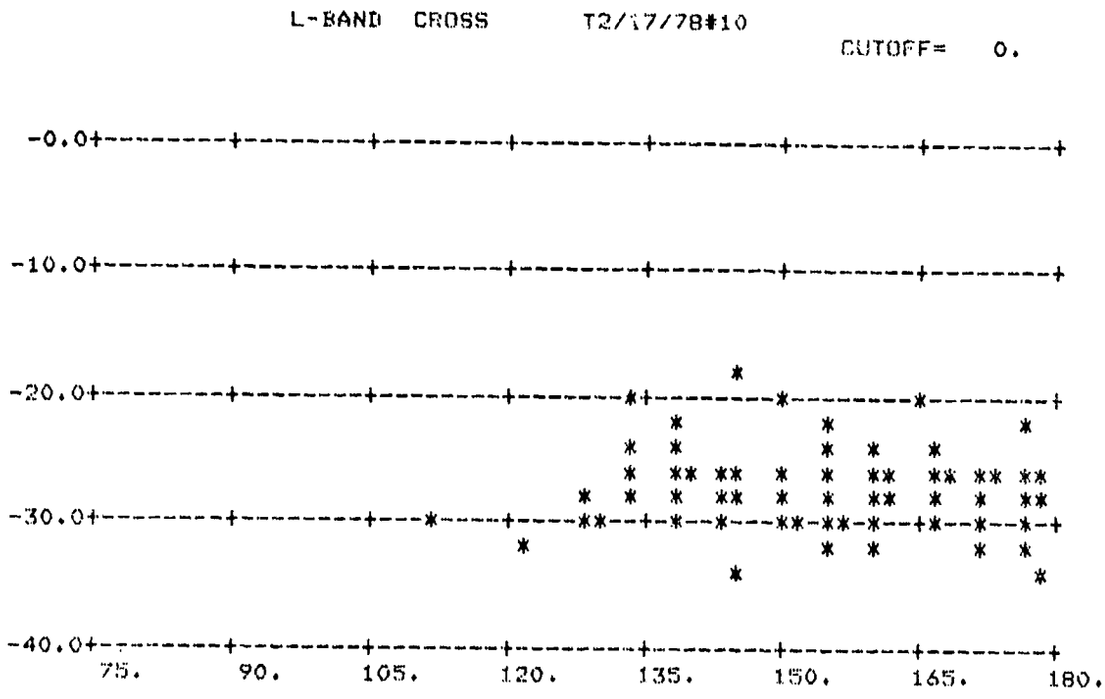

FIGURE A-128. σ_o vs ϕ_s; $\theta_s = 80°$, $\theta_i = 70°$

(Above: All Data; Below: Averages Over 5° Intervals)

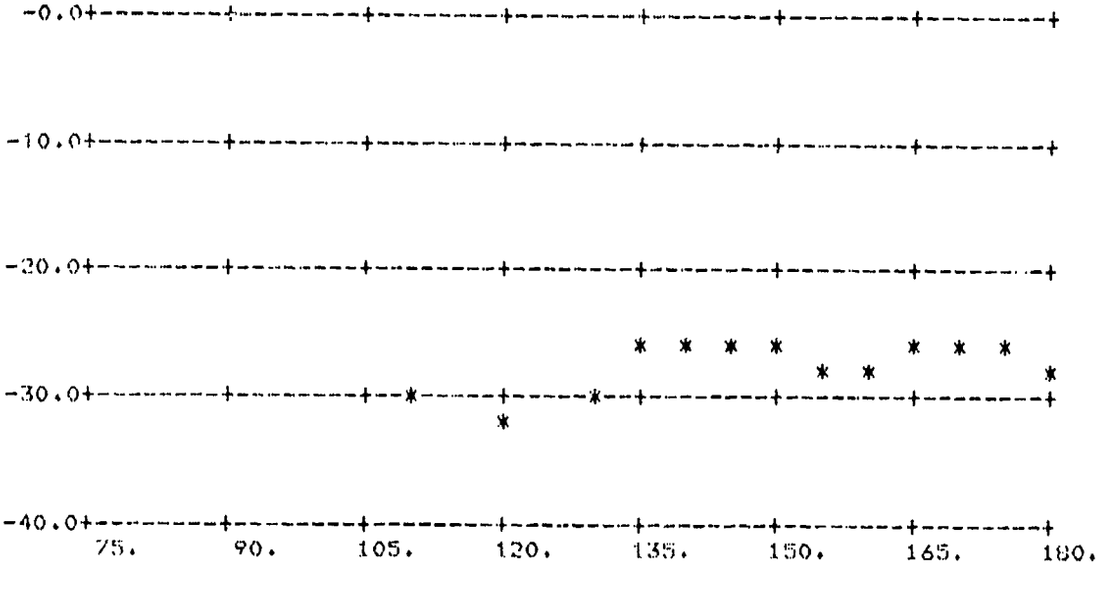

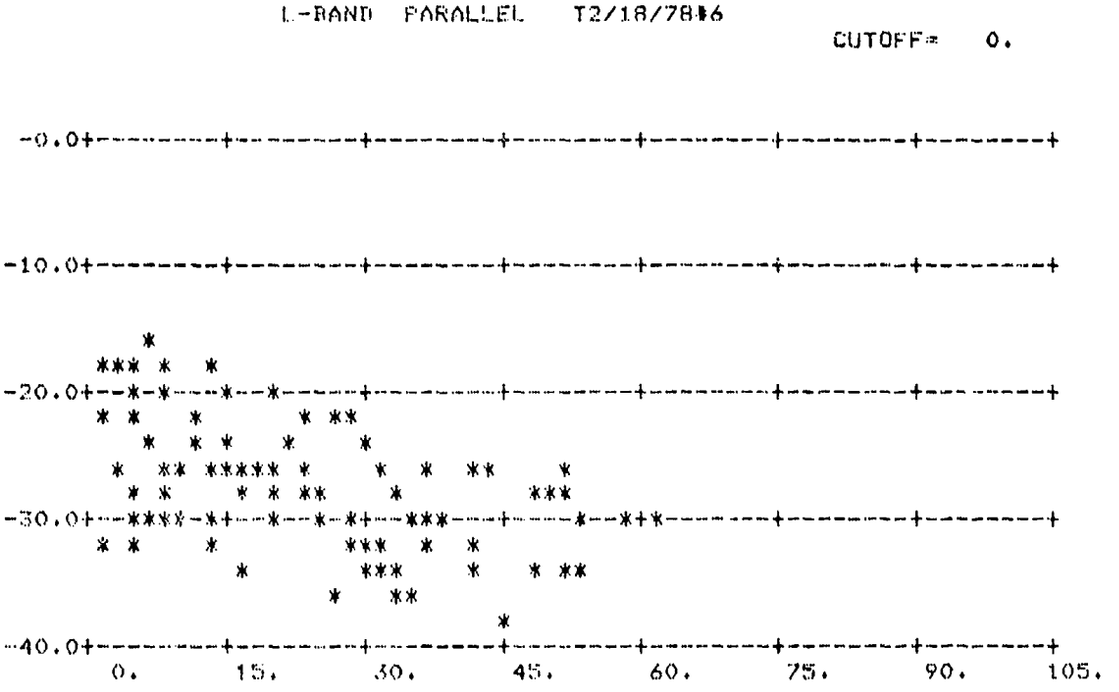

FIGURE A-129. σ_o vs ϕ_s; $\theta_s = 60°$, $\theta_i = 80°$

(Above: All Data; Below: Averages Over 5° Intervals)

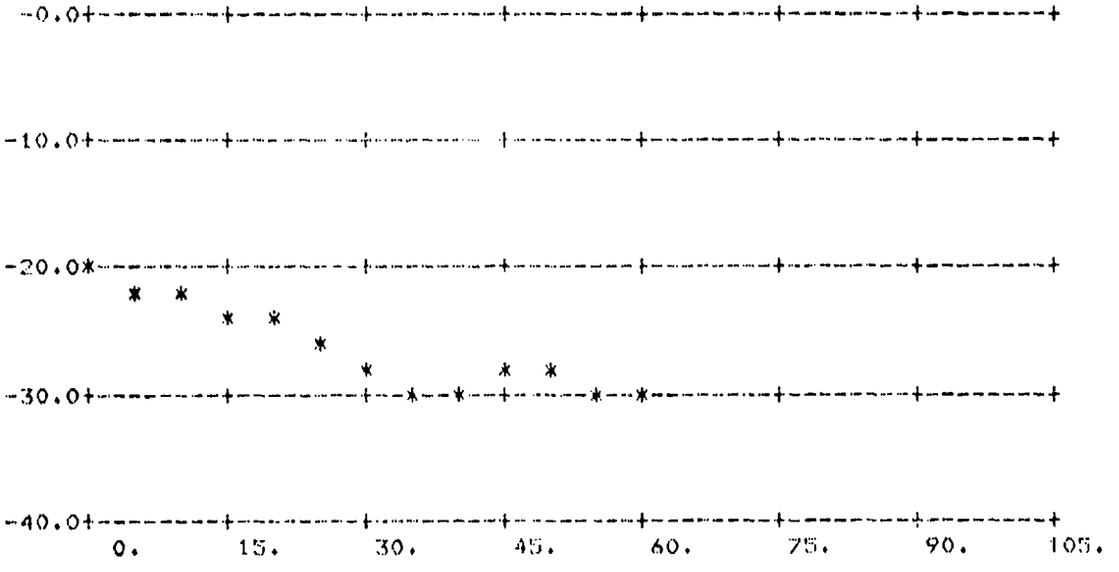

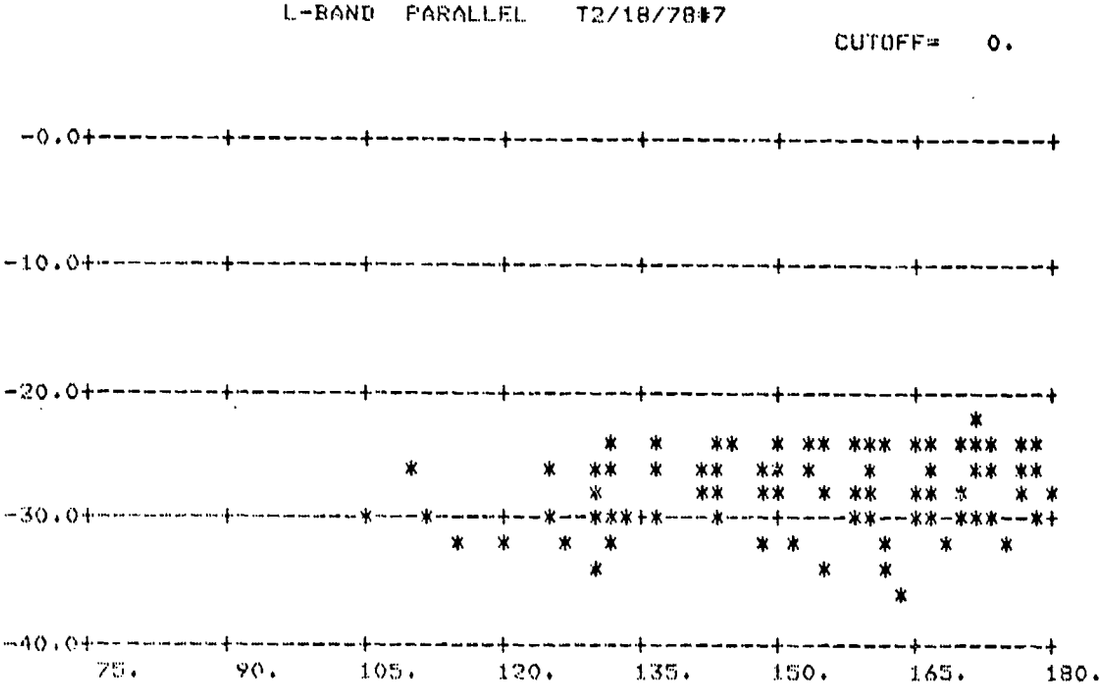

FIGURE A-130. σ_o vs ϕ_s; $\theta_s = 60°$, $\theta_i = 80°$

(Above: All Data; Below: Averages Over 5° Intervals)

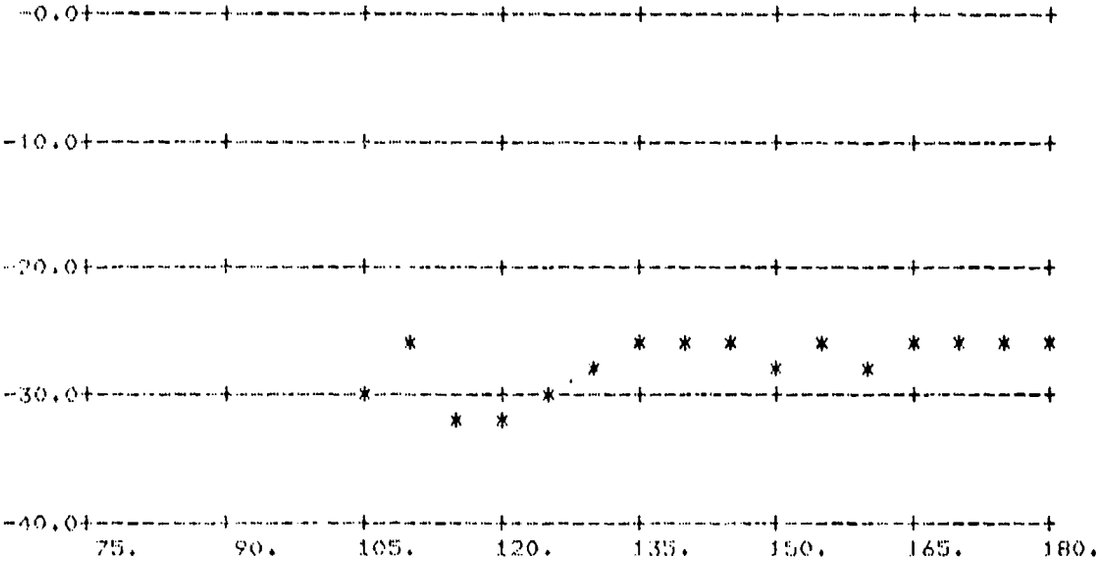

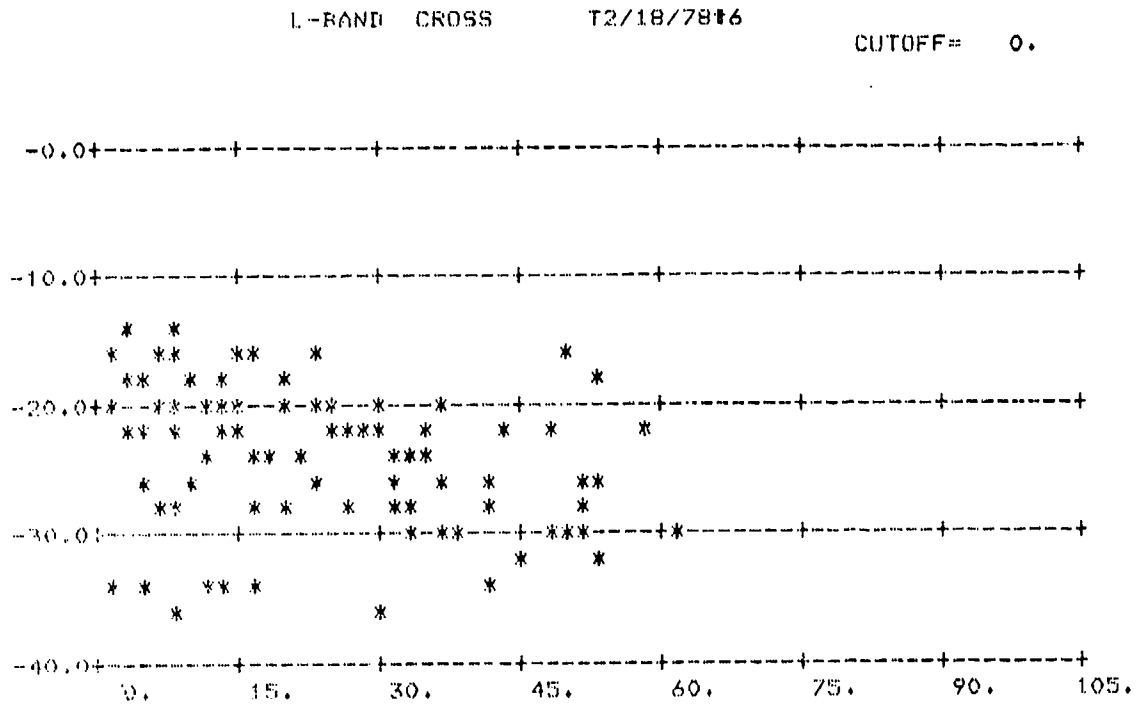

FIGURE A-131. σ_o vs ϕ_s; $\theta_s = 60°$, $\theta_i = 80°$

(Above: All Data; Below: Averages Over 5° Intervals)

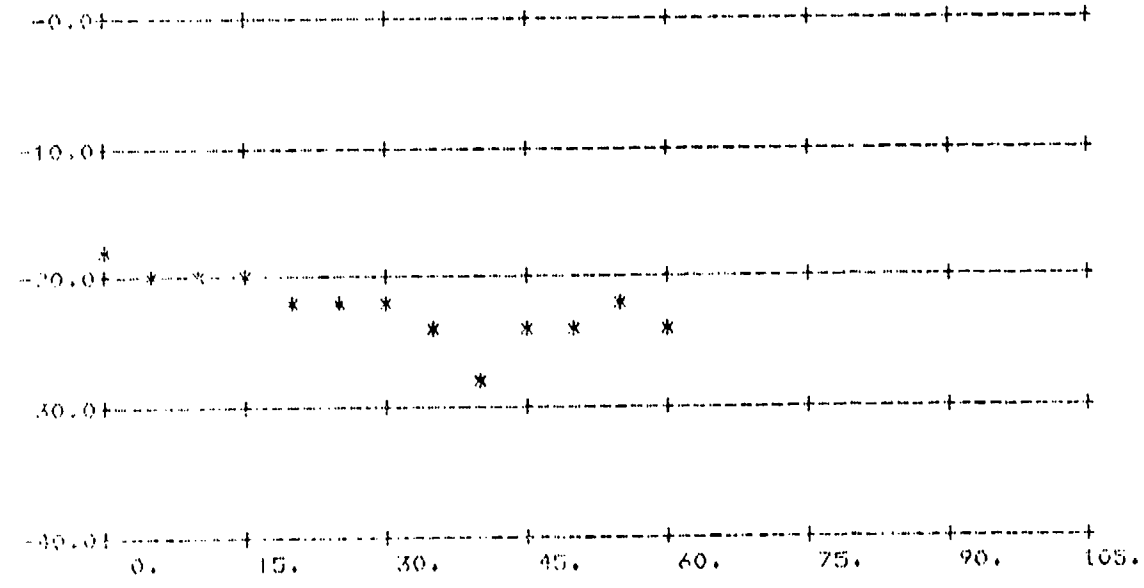

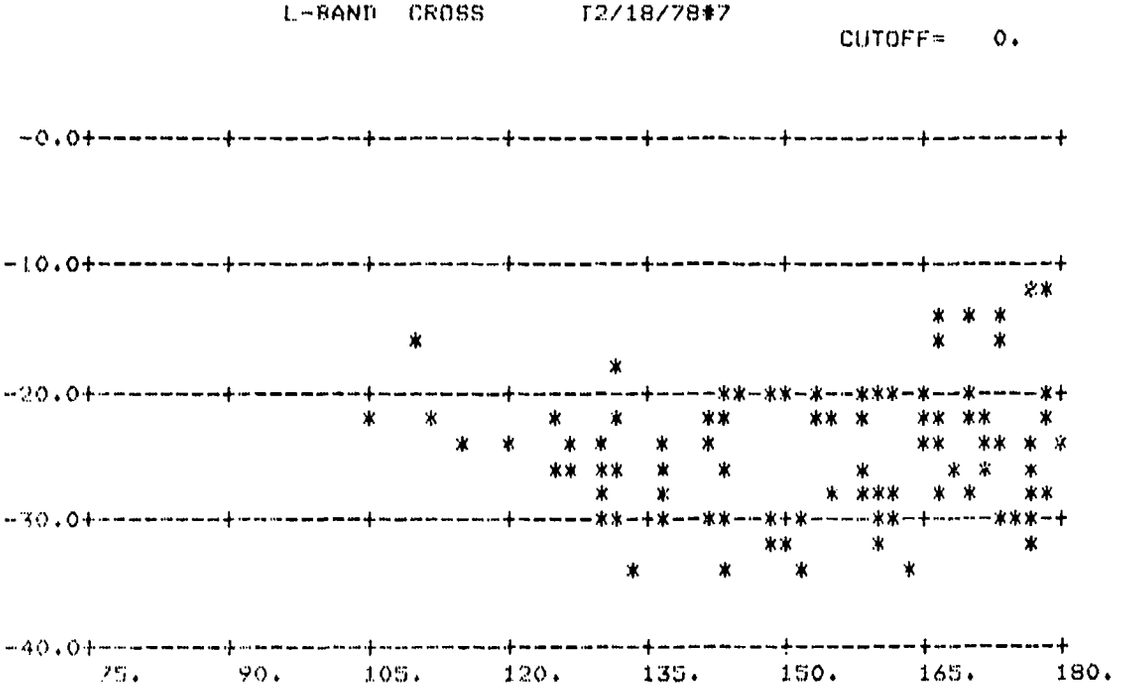

FIGURE A-132. σ_o vs ϕ_s; $\theta_s = 60°$, $\theta_i = 80°$

(Above: All Data; Below: Averages Over 5° Intervals)

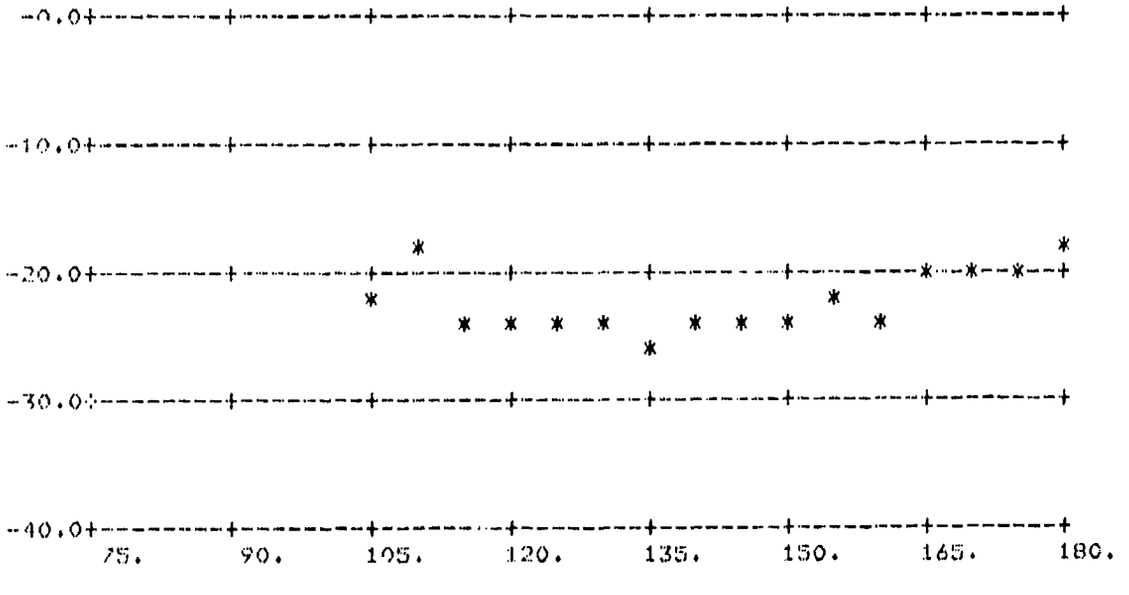

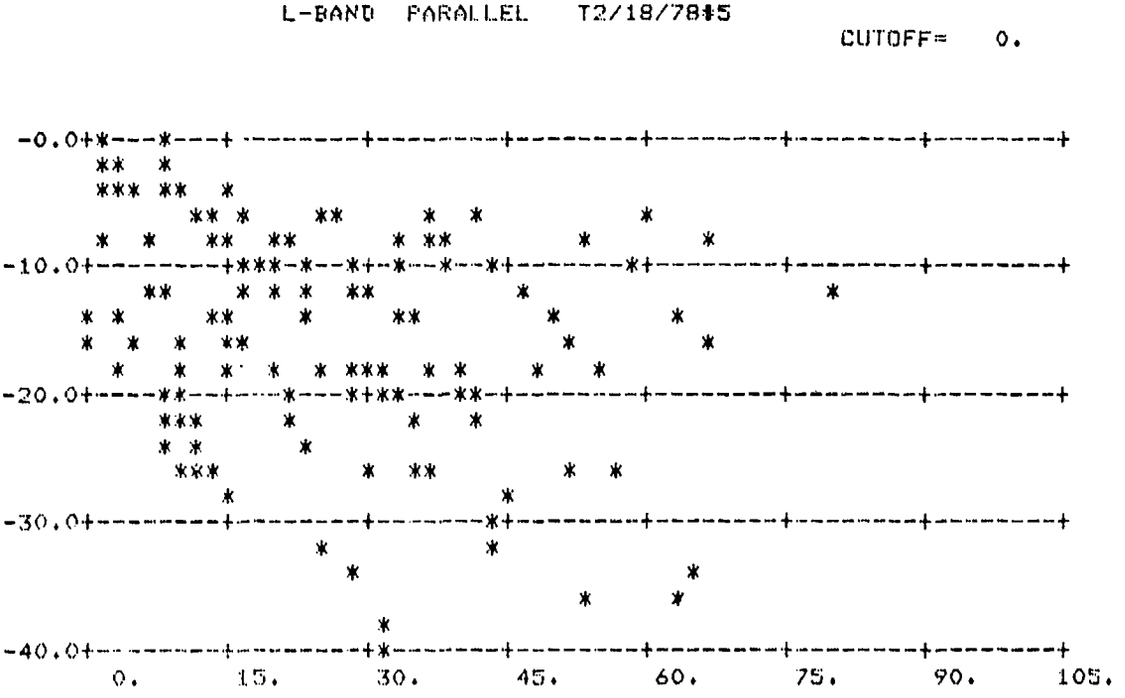

FIGURE A-133. σ_o vs ϕ_s; $\theta_s = 70°$, $\theta_i = 80°$

(Above: All Data; Below: Averages Over 5° Intervals)

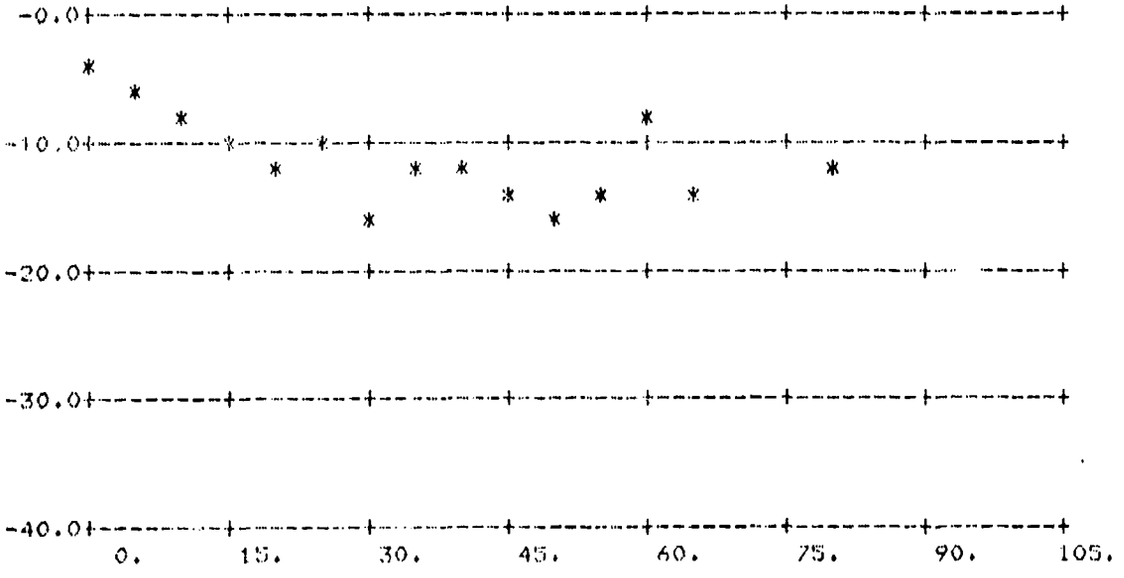

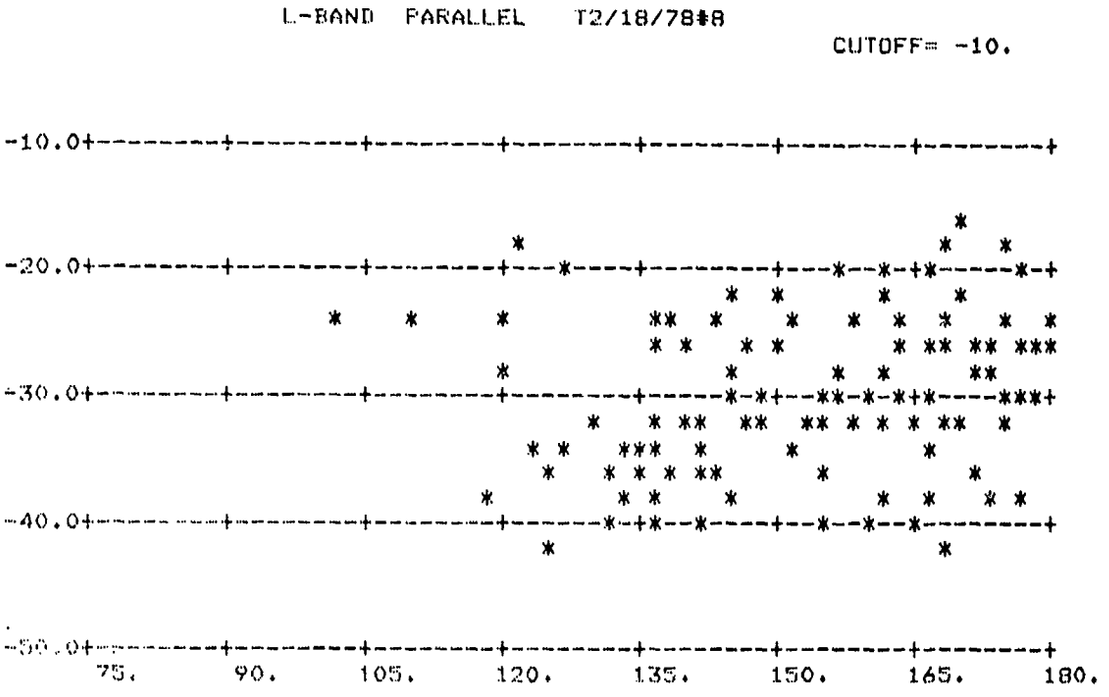

FIGURE A-134. σ_o vs ϕ_s; $\theta_s = 70°$, $\theta_i = 80°$

(Above: All Data; Below: Averages Over 5° Intervals)

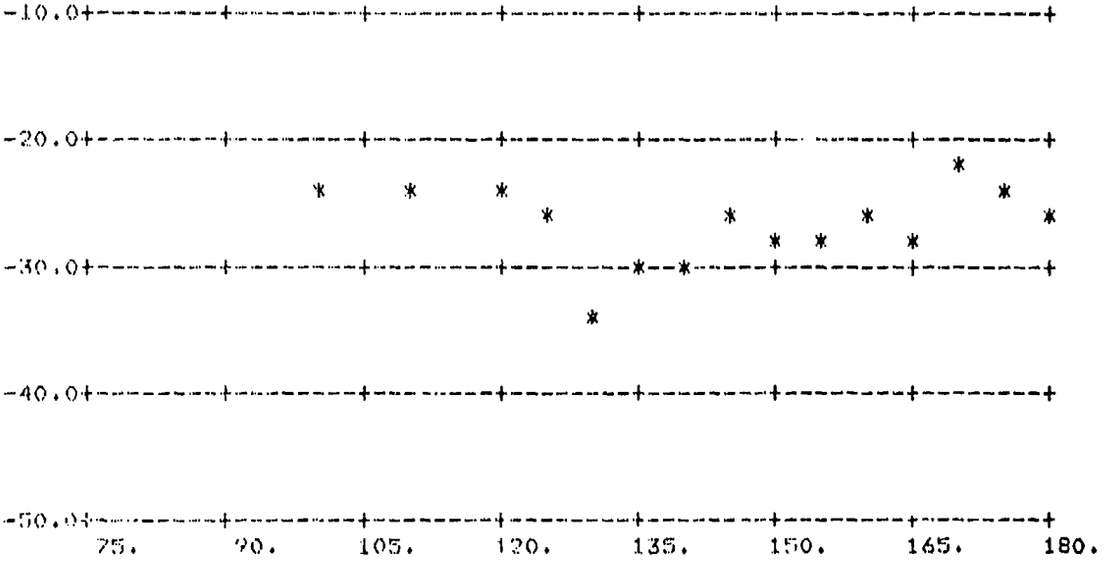

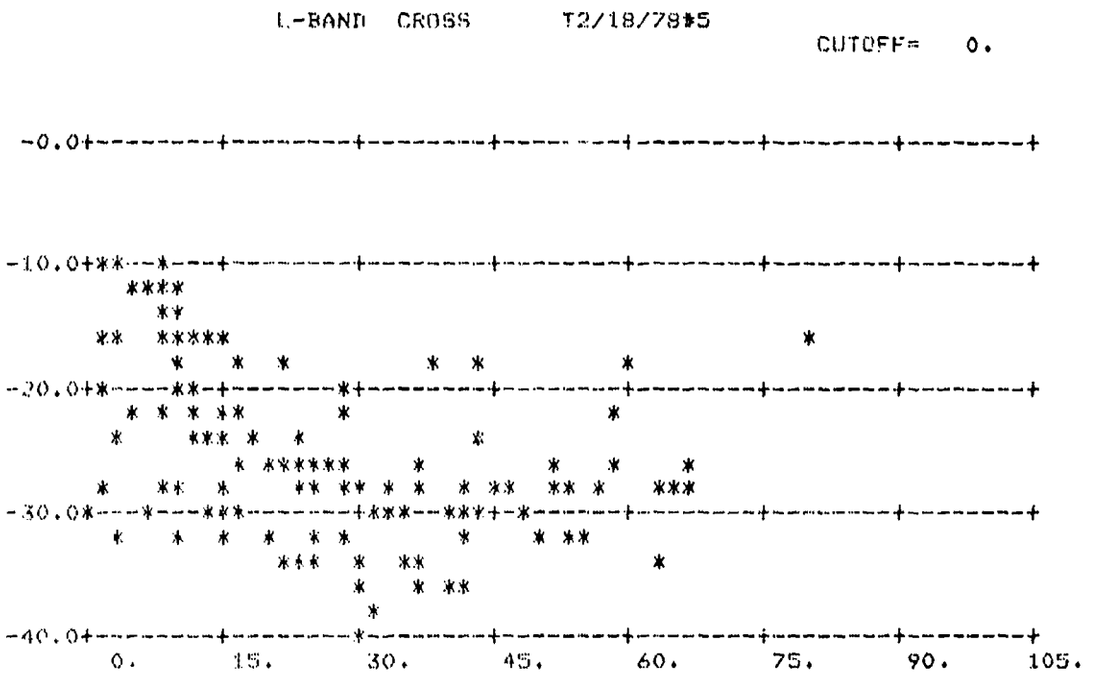

FIGURE A-135. σ_o vs ϕ_s; $\theta_s = 70°$, $\theta_i = 80°$

(Above: All Data; Below: Averages Over 5° Intervals)

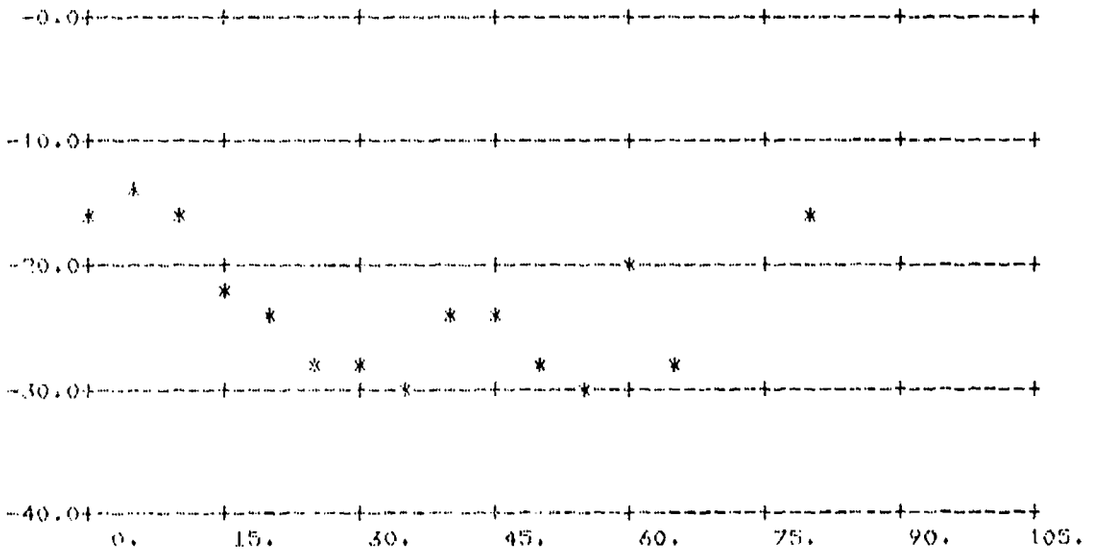

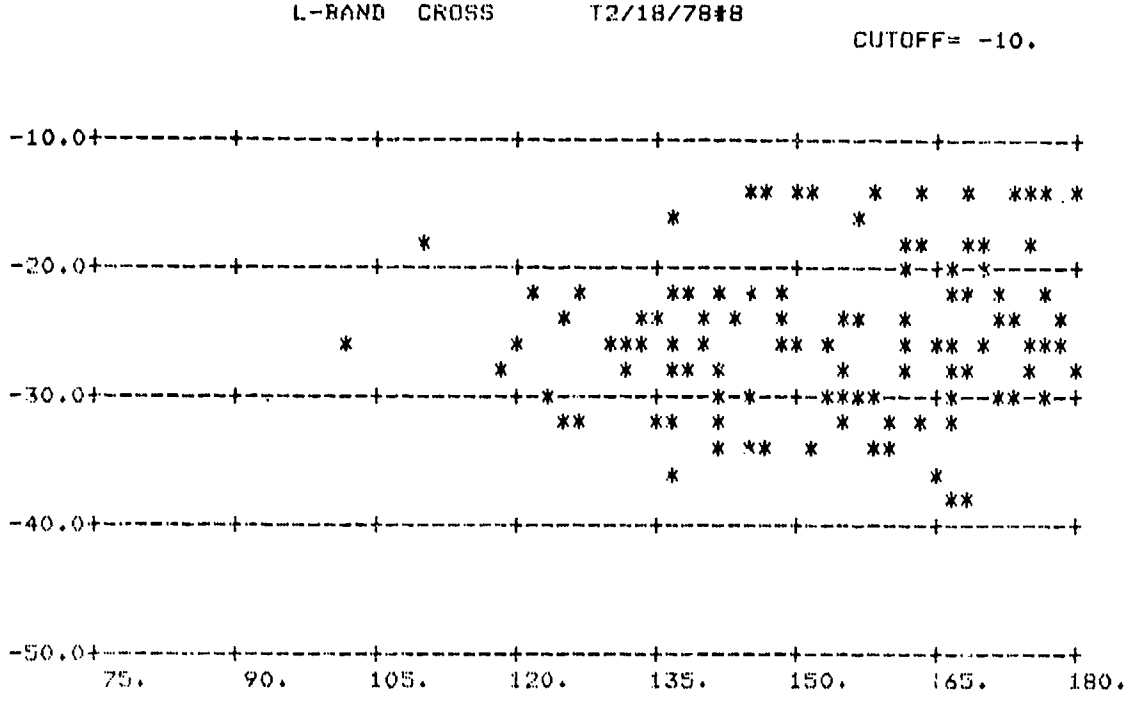

FIGURE A-136. σ_o vs ϕ_s; $\theta_s = 70°$ $\theta_i = 80°$

(Above: All Data; Below: Averages Over 5° Intervals)

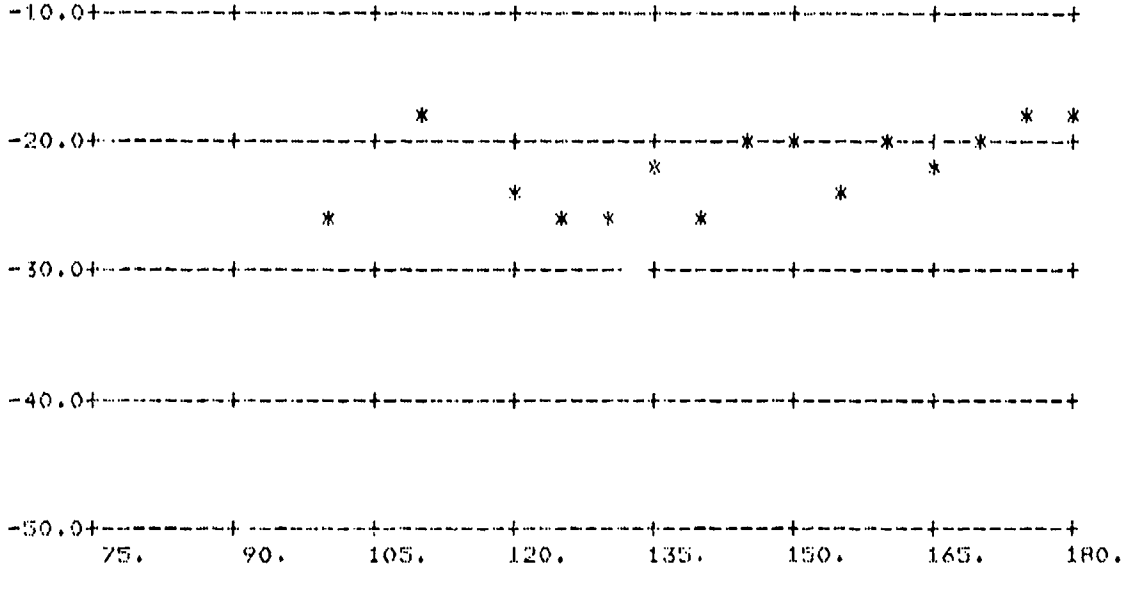

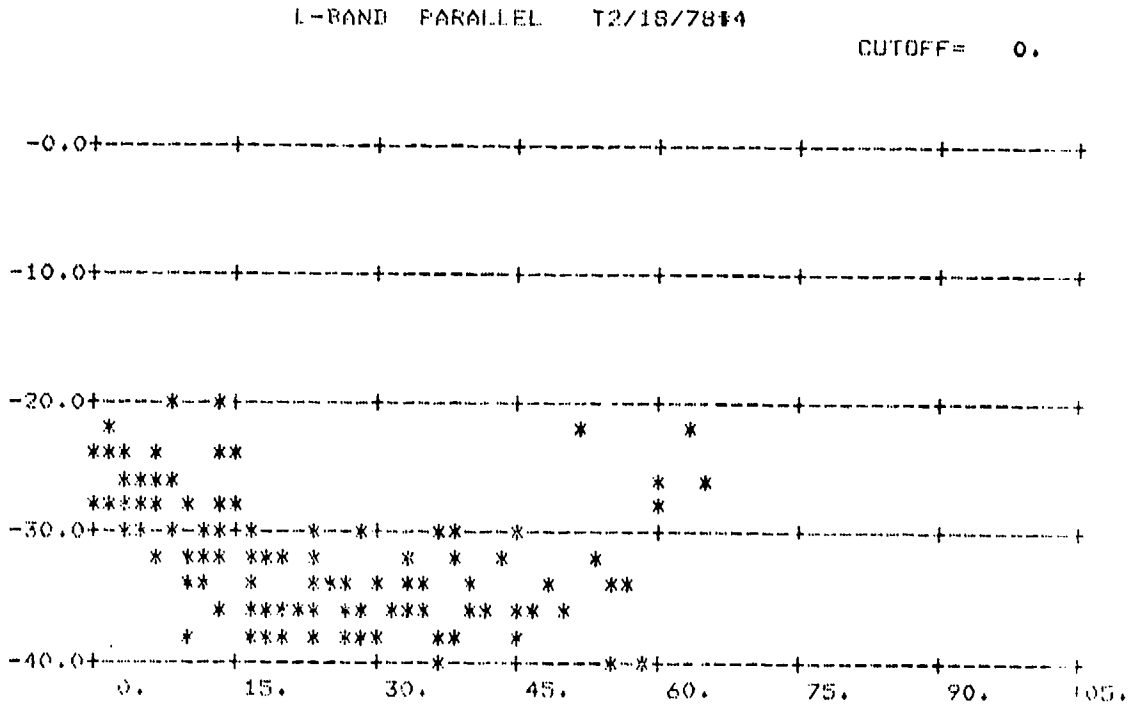

FIGURE A-137. σ_o vs ϕ_s; $\theta_s = 80°$, $\theta_i = 80°$

(Above: All Data; Below: Averages Over 5° Intervals)

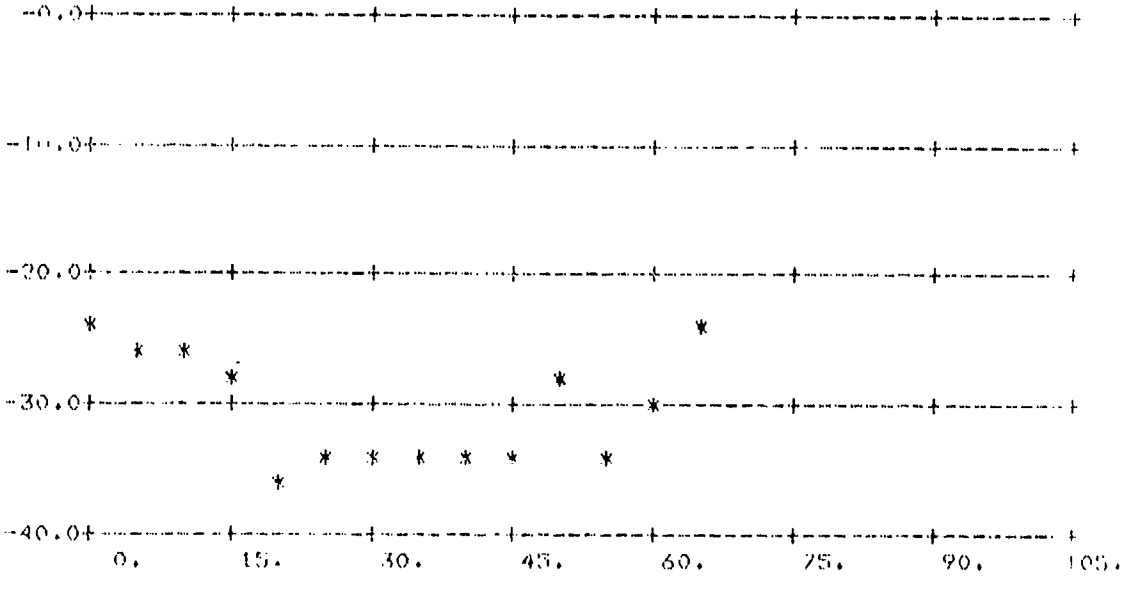

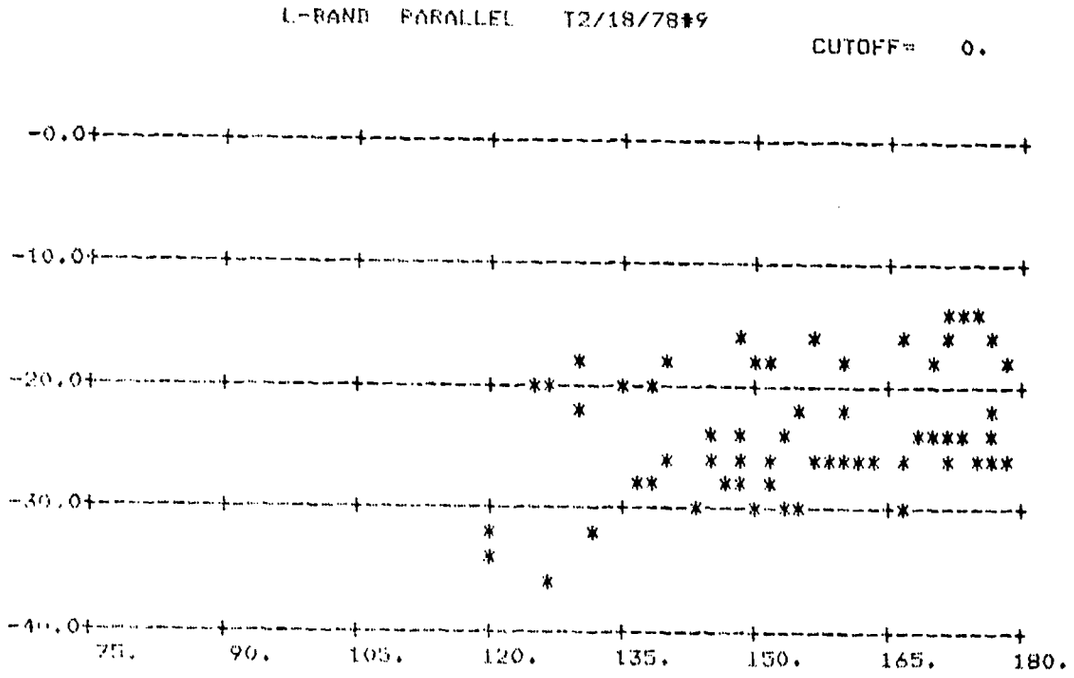

FIGURE A-138. σ_o vs ϕ_s: $\theta_s = 80°$, $\theta_i = 80°$

(Above: All Data; Below: Averages Over 5° Intervals)

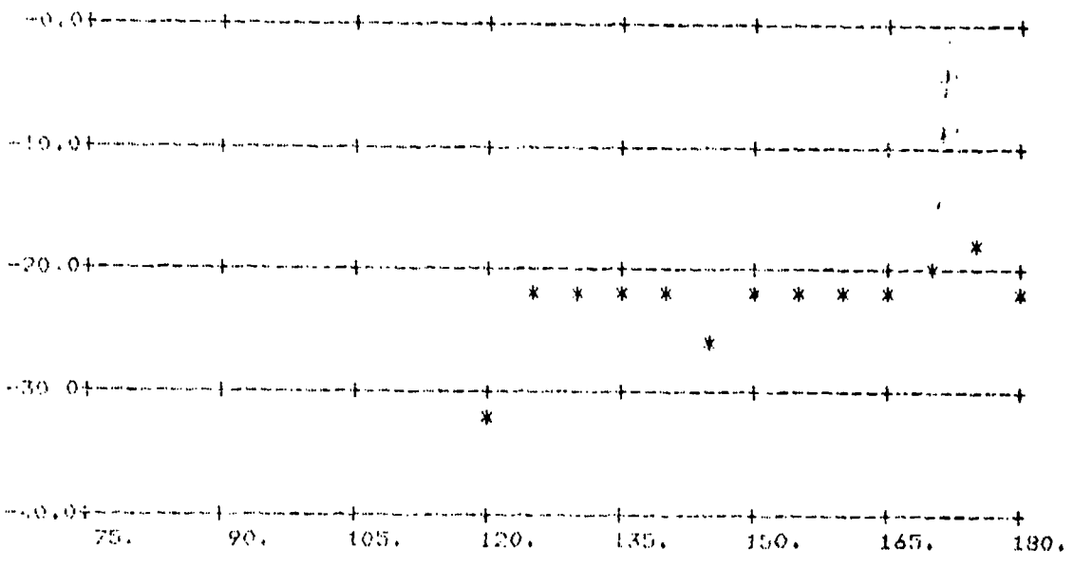

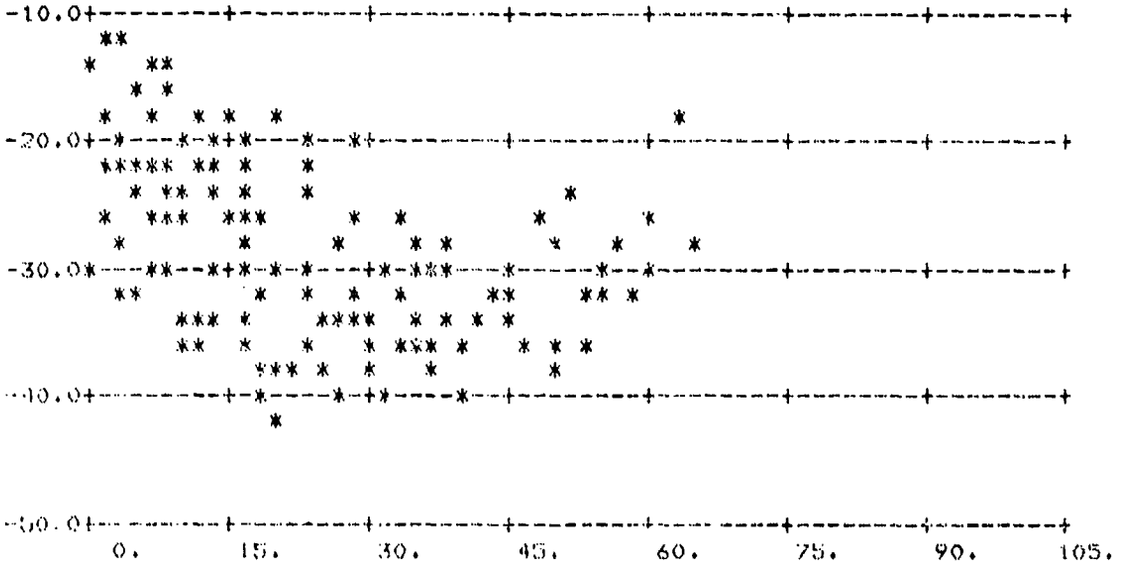

FIGURE A-139. σ_o vs ϕ_s; $\theta_s = 80°$, $\theta_i = 80°$

(Above: All Data; Below: Averages Over 5° Intervals)

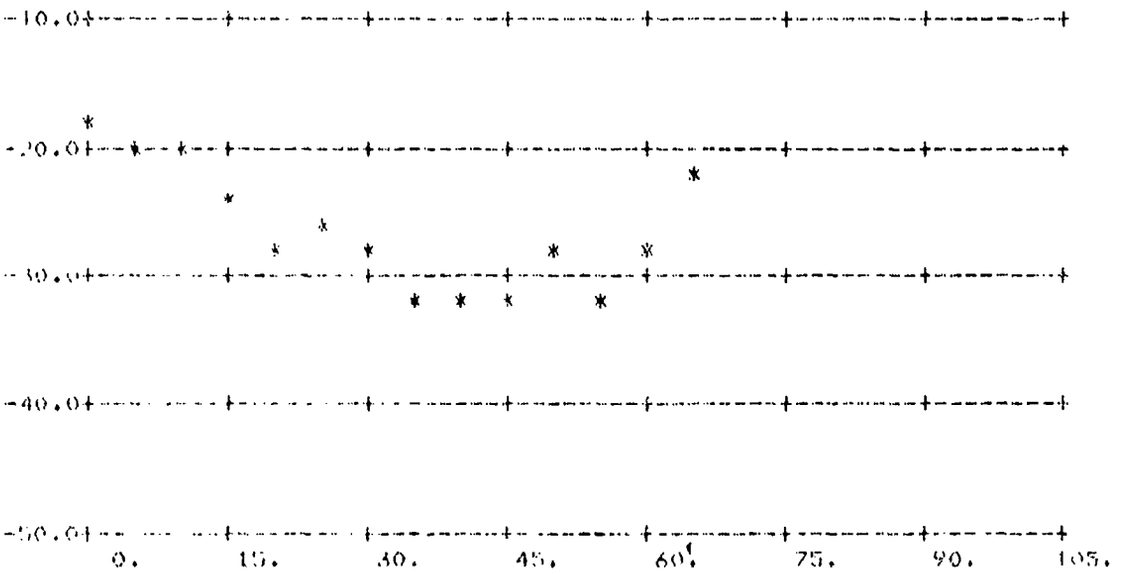

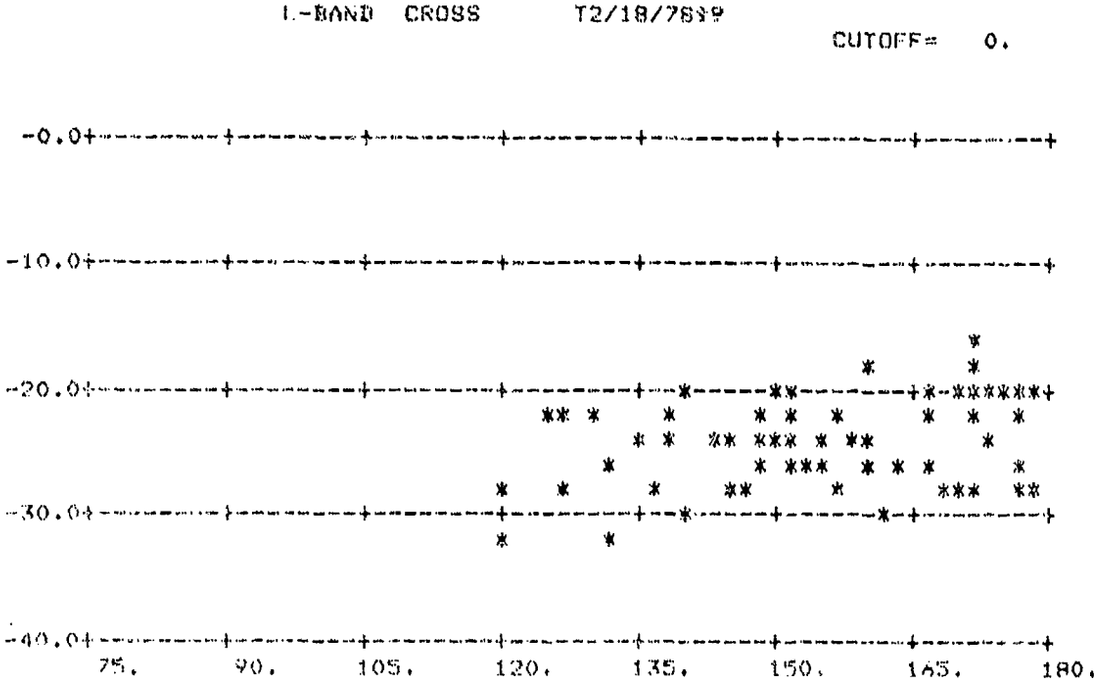

FIGURE A-14C. σ_o vs ϕ_s; $\theta_s = 80°$, $\theta_i = 80°$

(Above: All Data; Below: Averages Over 5° Intervals)

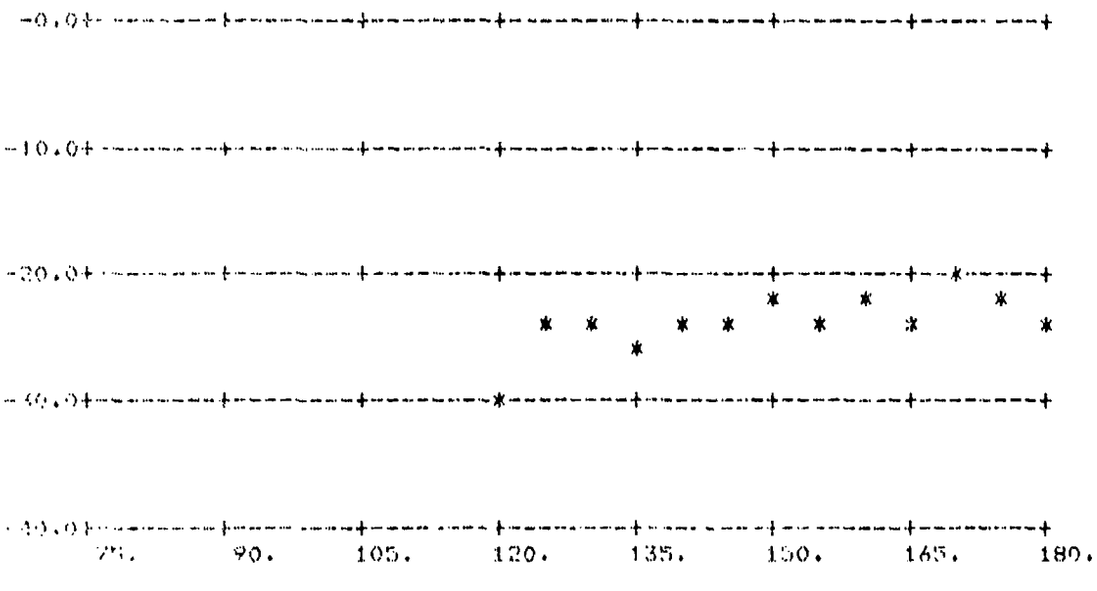

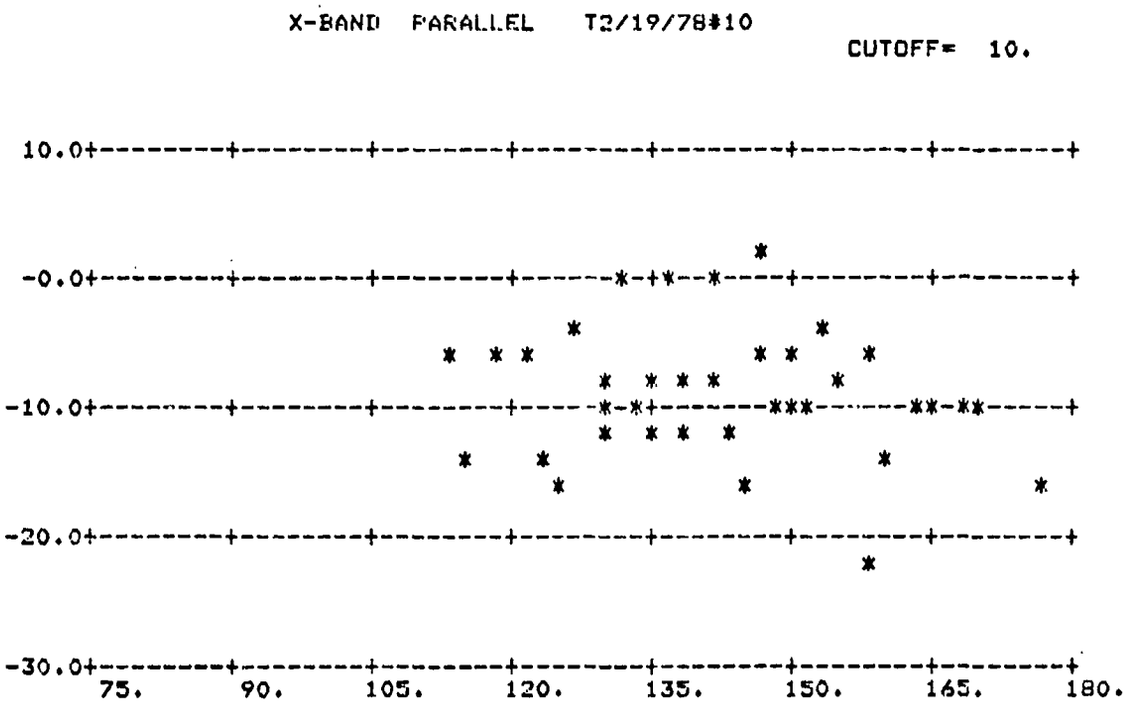

FIGURE A-141. σ_o vs ϕ_s; $\theta_s = 60°$, $\theta_i = 60°$

(Above: All Data; Below: Averages Over 5° Intervals)

Data from first half of pass only

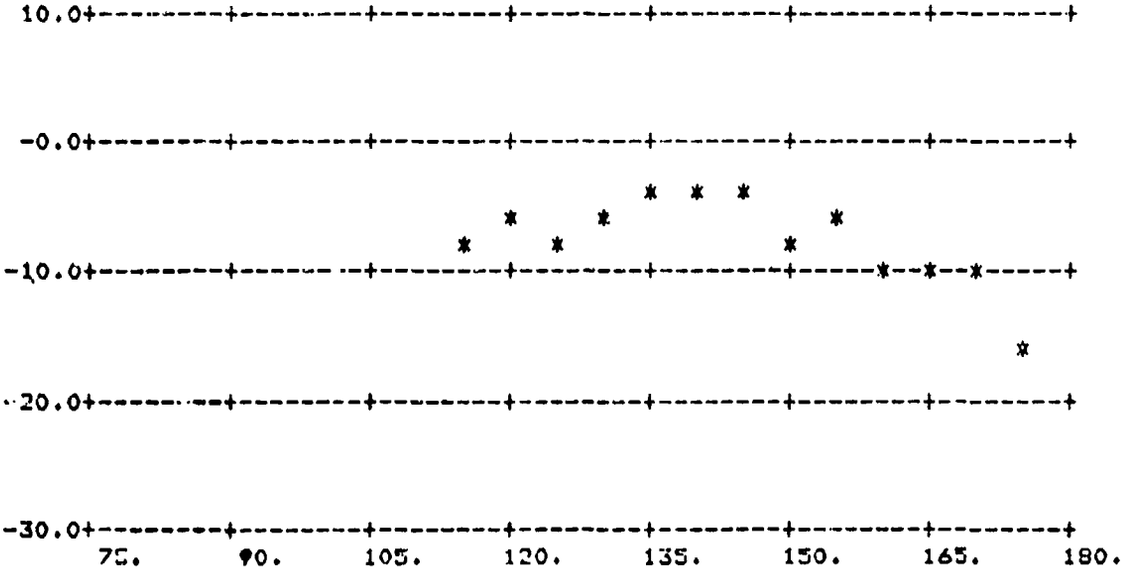

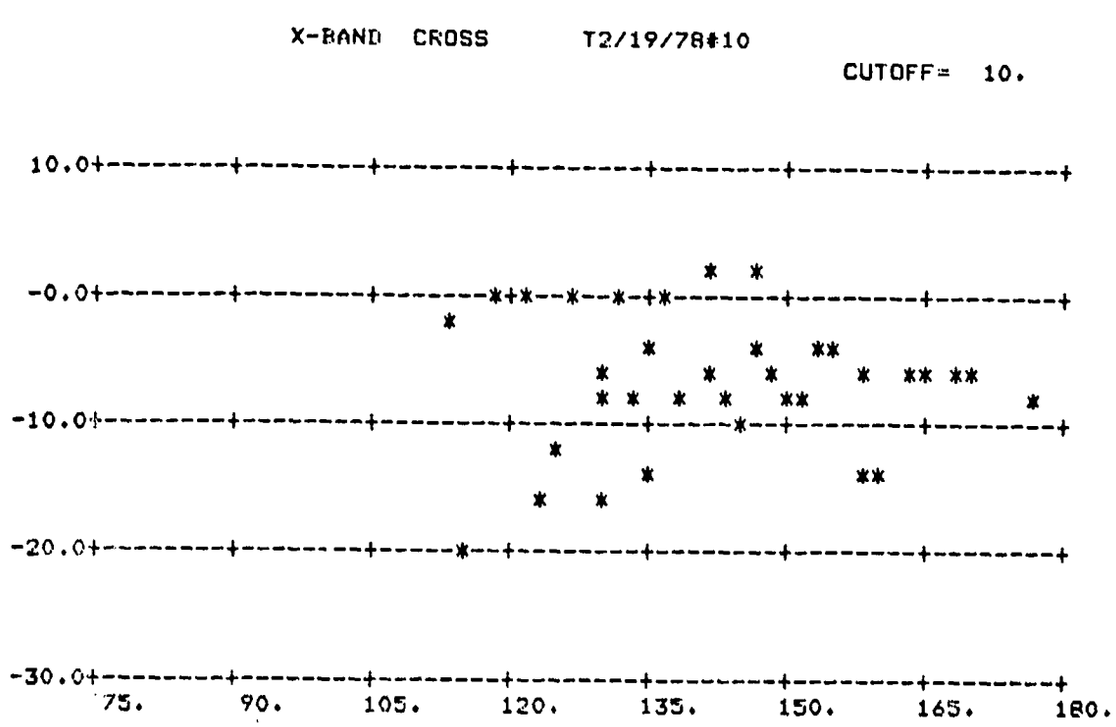

FIGURE A-142. σ_o vs ϕ_s; θ_s = 60°, θ_i = 60°

(Above: All Data; Below: Averages Over 5° Intervals)

Data from first half of pass only

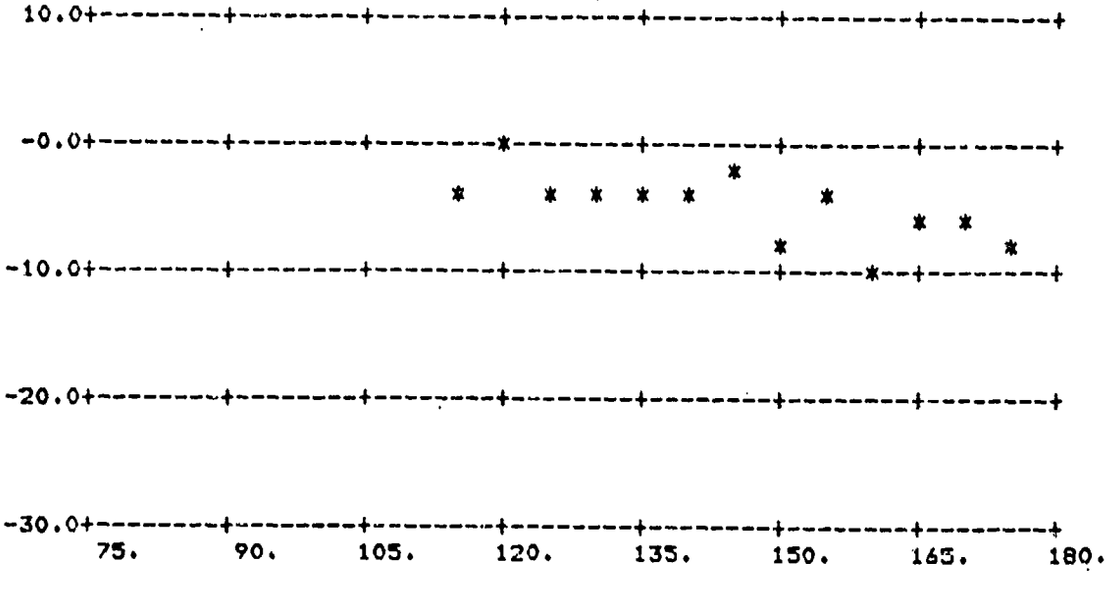

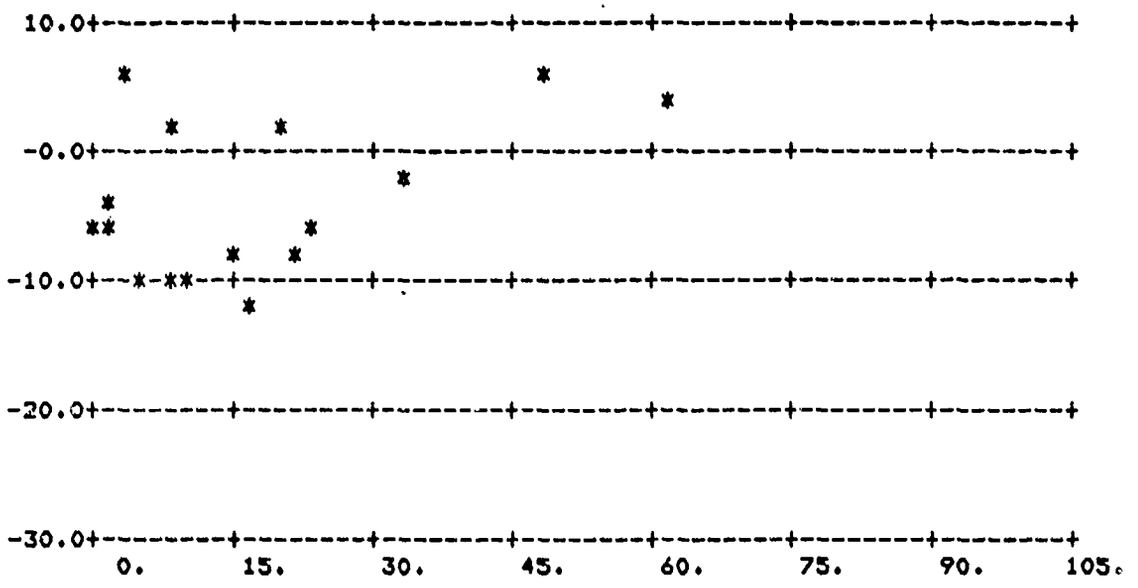

FIGURE A-143. σ_o vs ϕ_s; $\theta_s = 80°$, $\theta_i = 70°$

(Above: All Data; Below: Averages Over 5° Intervals)

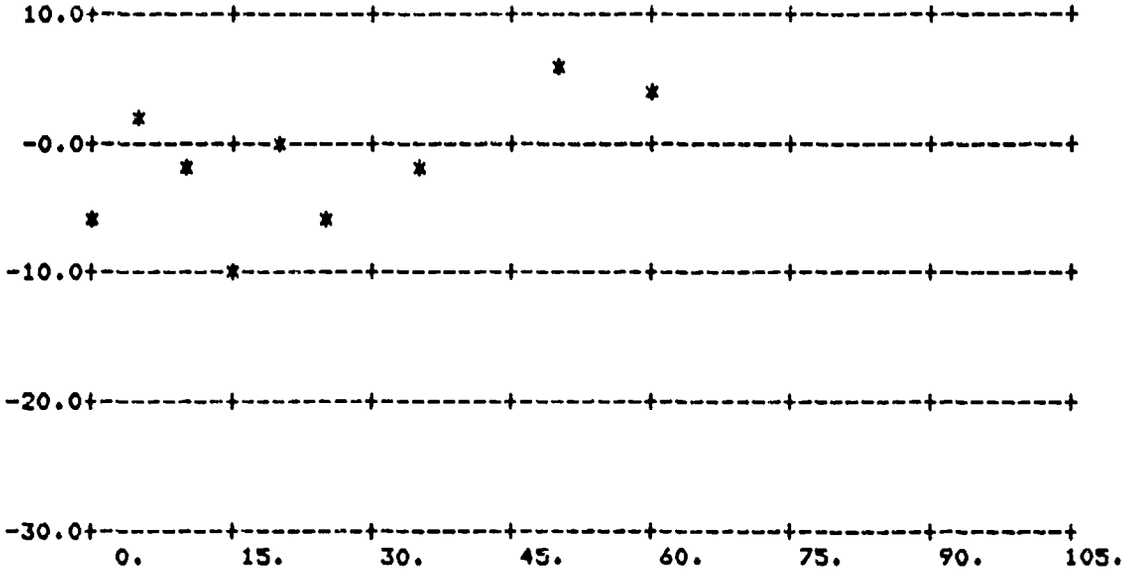

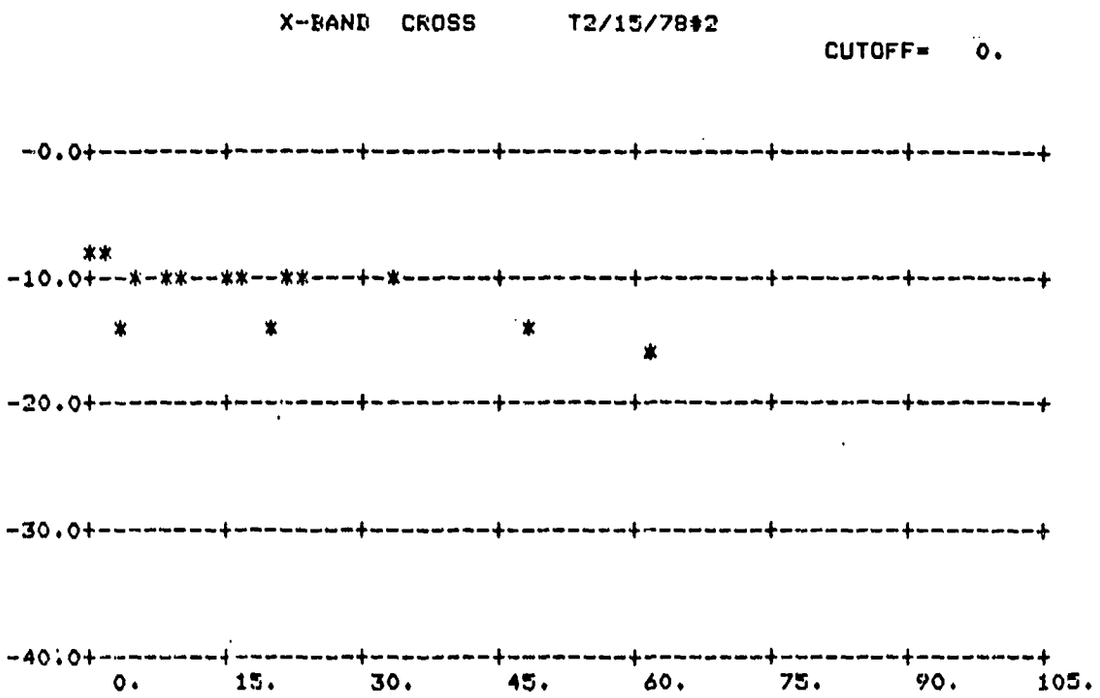

FIGURE A-144. σ_o vs ϕ_s; $\theta_s = 80°$, $\theta_i = 70°$

(Above: All Data; Below: Averages Over 5° Intervals)

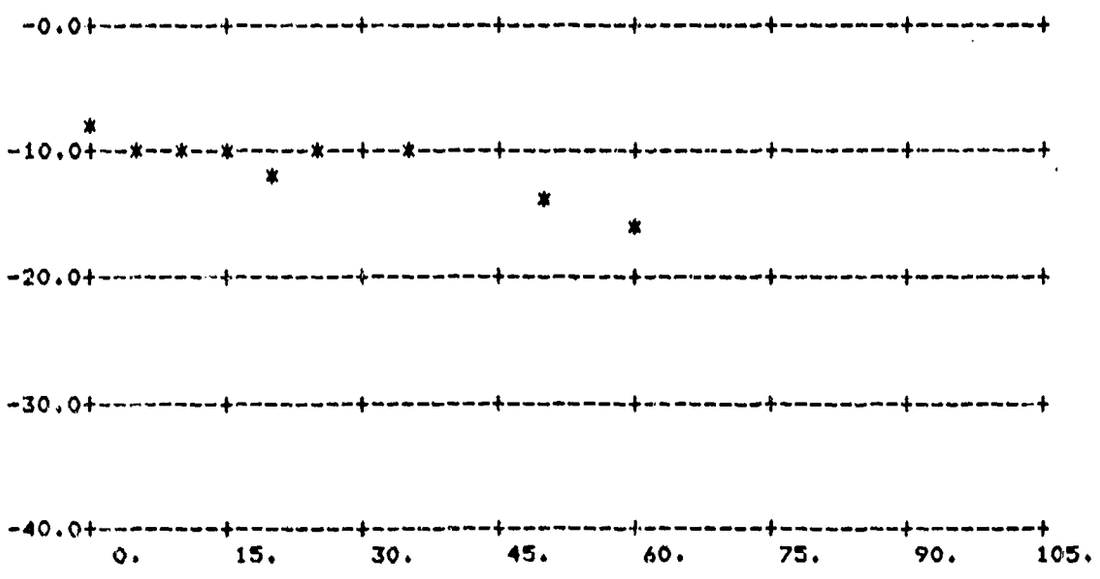

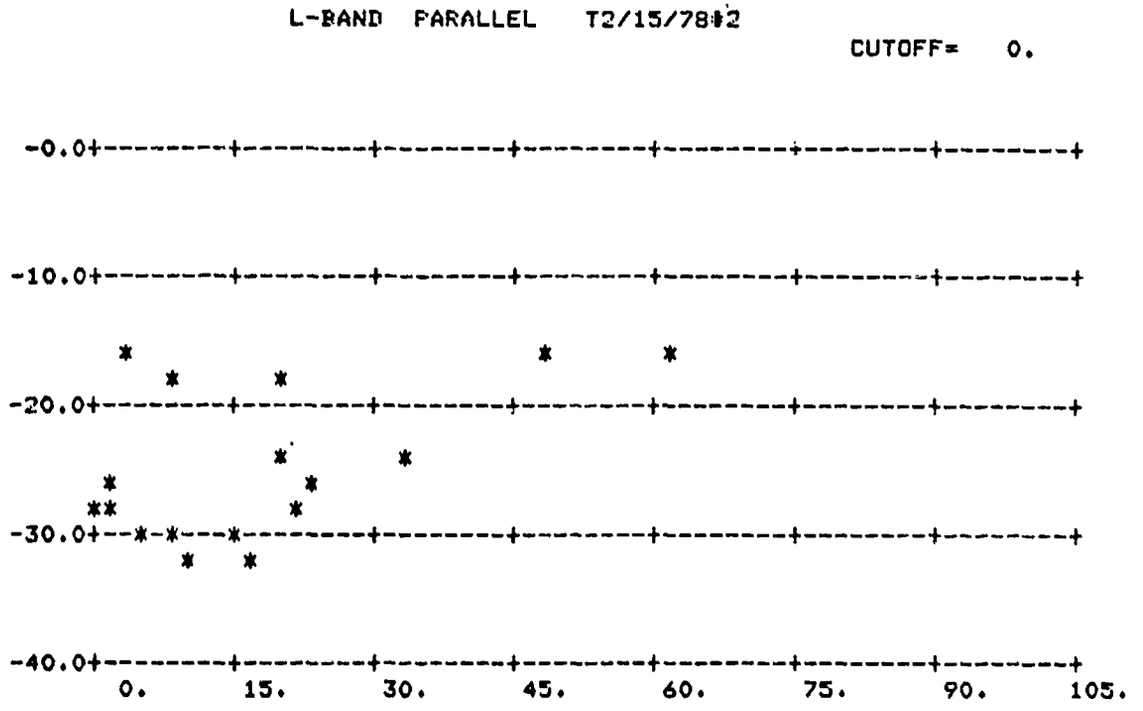

FIGURE A-145. σ_o vs ϕ_s; $\theta_s = 80°$, $\theta_i = 70°$

(Above: All Data; Below: Averages Over 5° Intervals)

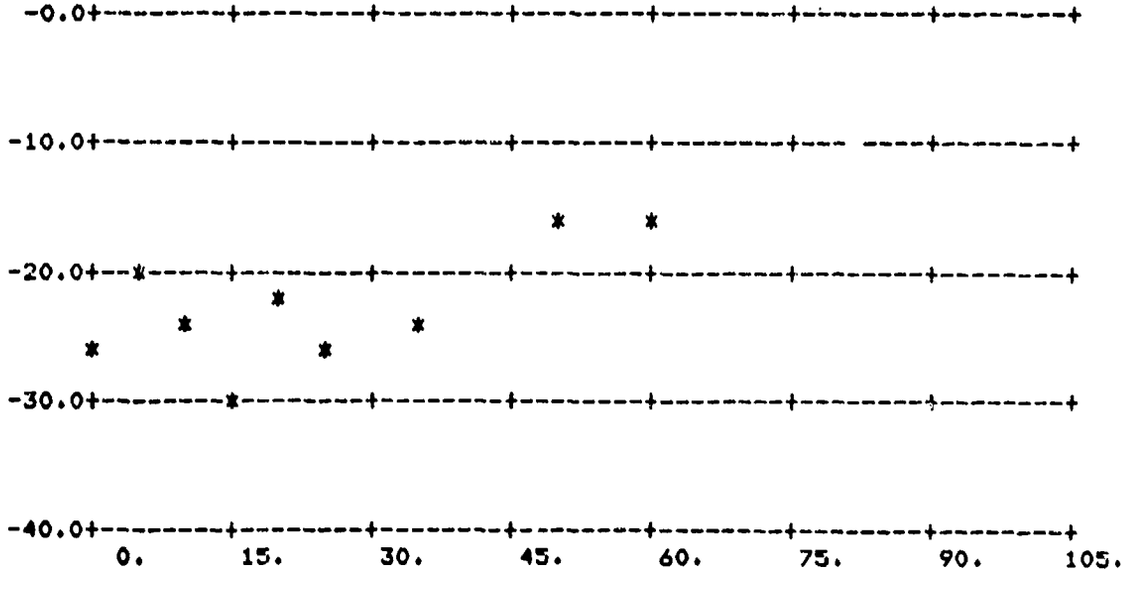

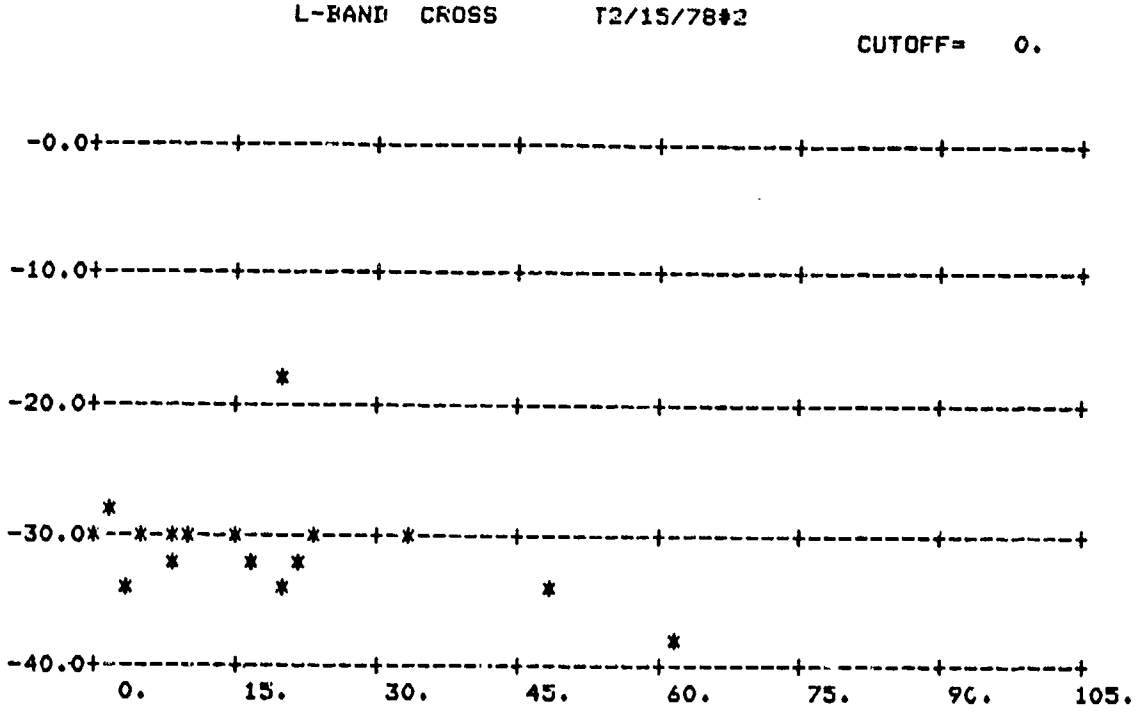

FIGURE A-146. σ_o vs ϕ_s; $\theta_s = 80°$, $\theta_i = 70°$
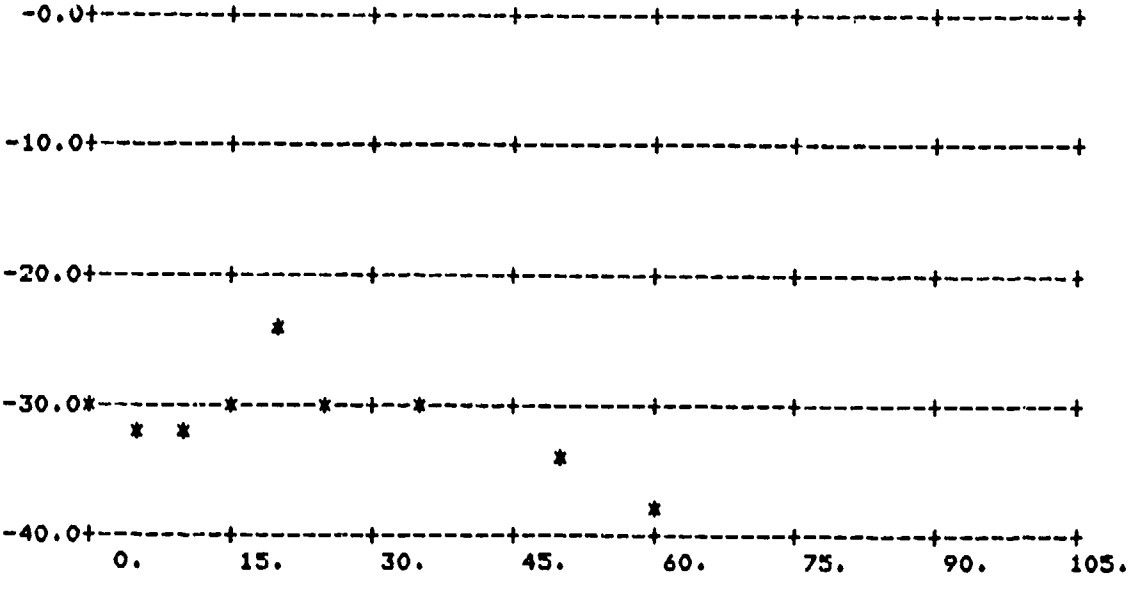
(Above: All Data; Below: Averages Over 5° Intervals)